

Experimental and Numerical Methods for Characterization of
Impact Damage in Titanium-Graphite Laminates

Stefan P. Hovik

A dissertation
submitted in partial fulfillment of the
requirements for the degree of

Doctor of Philosophy

University of Washington

2019

Reading Committee:

Ramulu Mamidala, Chair

Jeffrey Miller

Mark Tuttle

Program Authorized to Offer Degree:

Mechanical Engineering

©Copyright 2019

Stefan P. Hovik

University of Washington

Abstract

Experimental and Numerical Methods for Characterization of
Impact Damage in Titanium-Graphite Laminates

Stefan P. Hovik

Chair of the Supervisory Committee:

Ramulu Mamidala

Mechanical Engineering

TiGr (Titanium-Graphite) is a relatively new aerospace material system composed of layers of titanium alloy and graphite-reinforced thermoplastic. This material is in a class of materials called FMLs (Fiber-Metal-Laminates) which are characterized by high stiffness, fatigue resistance, and strength-to-weight ratios when compared to traditional composites. One of the particularly advantageous properties of TiGr is its damage tolerance; specifically its resistance to impact damage. While traditional graphite composites may sustain significant sub-surface impact damage in the form of delamination, fiber breakage, and matrix cracking that can be very difficult to detect, TiGr sustains damage primarily by absorbing energy in the form of plastic metal deformation and re-direction of impact energy into the plane of the metallic layers. This is useful both in that the damage is readily detectable by visual inspection, characterized by local plastic yielding, and that the mechanism for energy dissipation allows for absorption of greater energy with less effect to residual compressive strength compared to traditional graphite fiber composites. A finite element modelling method has been developed to show failure mechanism dependence on impact energy, layup sequence, and titanium thickness, and have been validated with empirical data. This method uses empirically derived constitutive material models in conjunction with a traction-separation law and applicable geometry to model three-point-bending behavior of TiGr laminates. Results show that dynamic finite element simulation can accurately portray the various

failure mechanisms associated with low-velocity impact. These results demonstrate a valuable tool for comparing and contrasting various TiGr layups, as well as understanding how TiGr's unique properties can be exploited to make aerospace structures stronger, lighter, and more reliable.

TABLE OF CONTENTS

TABLE OF FIGURES	6
TABLE OF TABLES.....	10
CHAPTER 1: INTRODUCTION.....	13
1.1 Development.....	14
1.2 Processing	14
1.3 Structural.....	16
1.4 Damage Tolerance.....	18
1.5 Quasi Static Loading.....	18
1.6 Fatigue Loading	19
1.7 Impact Durability	21
1.8 TiGr Durability Testing	21
CHAPTER 2: REVIEW OF CURRENT KNOWLEDGE.....	25
2.1 Brief History of Fiber Metal Laminates (FMLs)	25
2.2 TiGr Manufacturing and Machining.....	26
2.3 Fatigue	32
2.4 Impact.....	35
2.5 Numerical Modeling of Hybrid Laminates	43
2.5.1 Material Models.....	43
2.5.2 Finite Element Formulation	57
2.5.3 Numerical Modeling Discussion.....	62
2.6 Analytical Modeling	63
2.7 Discussion.....	70
CHAPTER 3: RESEARCH SCOPE AND OBJECTIVES.....	73
3.1 Scope of Research.....	73
3.2 Research Goals & Objectives	74
CHAPTER 4: METHODS OF APPROACH.....	77
4.1 Specimen Preparation.....	77
4.1.1 Industry Standard.....	77
4.1.1 Experimental Specimen Preparation	83
4.2 Experimental Analysis of Impact Panels.....	86
4.2.1 Industry Standard Data Collection	86
4.2.2 Industry Standard Experimental Approach	89
4.2.4 Experimental Approach.....	96
4.3 Numerical Modeling of Low Velocity Impact	99
4.3.1 Typical Model Geometry	99
4.3.3 Post Processing	104

CHAPTER 5: RESULTS	107
5.1 TiGr Laminates with Titanium Face Sheets	107
5.2 Quasi-Static Loading of Thin Laminates & Size Effects	111
5.2.1 Numerical Modeling Data	115
5.2.2 Width Effects	118
5.2.3 Thickness Effects	121
5.3 Static Loading of Thick Laminates	124
5.4 Low-Velocity Impact Loading of Thick Laminates.....	126
CHAPTER 6: DISCUSSION	136
6.1 Laminates with Titanium Face Sheets	136
6.2 Thin Laminates and Size Effects	136
6.3 Static & Low-Velocity Impact Loading of Thick Laminates	138
6.4 Classical Laminate Theory	140
6.5 Metal Volume Fraction	144
CHAPTER 7: CONCLUSIONS AND FUTURE WORK RECOMMENDATIONS	151
7.1 Conclusions.....	151
7.2 Future Work Recommendations	152
REFERENCES	154
APPENDIX I: DAMAGE PROGRESSION IN NUMERICAL MODELS	160
APPENDIX II: CLASSICAL LAMINATE THEORY, CALCULATION OF ELASTIC CONSTANTS	231
APPENDIX III: NUMERICAL MODELING CODE	248

TABLE OF FIGURES

Figure 1. Sol-Gel Layer Structure	15
Figure 2. Ply Replacement using Titanium Layers	16
Figure 3. Axial Structures using TiGr	17
Figure 4. Titanium Face Sheets	17
Figure 5. Titanium used for Abrasion Resistance	18
Figure 6. Aspects of Damage Tolerance in FMLs	18
Figure 7. Impact Test Setup (Instron, Inc)	22
Figure 8. Compression-After-Impact Failed Specimen (Instron, Inc.).....	23
Figure 9. Abaqus Finite Element Model.....	23
Figure 10. Critical fracture energies of different toughed epoxy formulations with and without sol-gel interphase layers at titanium-epoxy interface [33].	28
Figure 11. Nanoporous microstructure of resin fracture surfaces [33].....	29
Figure 12. Tearing in induction-headed specimens caused by bottom titanium ply delamination [19]	30
Figure 14. Fatigue Life of TiGr 2-6-2.....	34
Figure 15. S-N Curve for TiGr 2-6-2	34
Figure 16. Bernhardt Test Apparatus.....	37
Figure 17. Nakatani Delamination Zones After Impact	38
Figure 18. Delamination Area vs. Impact Energy	39
Figure 19. Nakatani Delamination and Titanium Fracture at Different Energy Levels	40
Figure 20. Nakatani Load History and Load vs. Displacement.....	40
Figure 21. Bernhardt Load History and Load vs. Displacement for Mode I and Mode II Impacts	41
Figure 22. Reiner Impact Load History and Energy History	42
Figure 23. Damage Evolution in Finite Elements [77].....	52
Figure 24. Exponential Damage Evolution [77]	53
Figure 25. Traction-Separation with Linear Material Softening [77].....	56
Figure 26. Hexahedral Element Configuration [77].....	59
Figure 27. Spring-Mass Model of Impact to FML Plate	68

Figure 28. Process Methodology for Damage Characterization of TiGr	73
Figure 29. Specimen Preparation Flow Chart.....	77
Figure 30. Impact Specimen Dimensions	78
Figure 31. Layup Schematic	79
Figure 32. Layup Schematic Legend	80
Figure 33. Cure Cycle for Hexply IM7/8552 Epoxy Matrix.....	81
Figure 34. Test Fixture for Impact Testing	87
Figure 35. Impact Test Stand and Hemispherical Impactor Geometry.....	88
Figure 36. Specimen Damage Measurement Locations.....	95
Figure 37. Drop Test Apparatus.....	96
Figure 38. 3-Point Bend Fixture with TiGr Specimen Under Load.....	97
Figure 39. Experimental Setup For Low-Velocity Impact Experiments	98
Figure 40. Finite Element Applied Boundary Conditions	104
Figure 41. Contact Force Time History	105
Figure 42. Impactor Displacement Time History.....	105
Figure 43. Impactor Velocity Time History	106
Figure 44. Laminate Absorbed Energy Time History	106
Figure 45. Bernhardt Drop Test Data [X]	108
Figure 46. Mode 1 Failure Comparison	108
Figure 47. Mode 2 Failure Comparison	109
Figure 48. Mode 1 Failure Comparison	109
Figure 49. Mode 2 Failure Comparison	110
Figure 50. Interlaminar Delamination.....	111
Figure 51. Trimmed Surfaces (a) fine EDM, (b) rough EDM, (c) rough AWJ, and (d) fine AWJ	112
Figure 52. Profile Along Thickness Direction of Machined Surfaces (a) fine EDM, (b) rough EDM, (c) rough AWJ, and (d) fine AWJ.....	113
Figure 53. Stress-Strain Curves for Static TiGr Samples	114
Figure 54. Sample of Specimens after 3-Point Bend Test (a) EDM 4A 25 μ s, (b) EDM 11A 200 μ s, (c) AWJ 720mm/min 3.53g/s, and (d) AWJ 60mm/min 9.78g/s.....	115

Figure 55. Numerical Modelling of TiGr Specimen	116
Figure 56. Stress-Strain Plot of Numerical and Experimental Data	116
Figure 57. Normalized Energy Plot of Numerical and Experimental Data	117
Figure 58. Normalized Energy Rate of Numerical and Experimental Data	117
Figure 59. Width Effect on Fracture Mechanisms of FMLs.....	120
Figure 60. Thickness Effects on Damage Mechanisms of FMLs.....	123
Figure 61. Numerical Model of Quas-Static Specimen	124
Figure 62. Quasi-Static Test Specimens after Loading	124
Figure 63. Load-Displacement of Quasi-Static Loading	125
Figure 64. Load-Displacement Numerical Model Comparison	126
Figure 65. Load-Displacement of 2.5 m/s Impact Loading	127
Figure 66. Absorbed Energy, 2.5 m/s Impact Loading	128
Figure 67. Numerical Comparison, 2.5 m/s Impact Loading.....	129
Figure 68. Delamination Damage Progression, 2.5 m/s Impact Loading	130
Figure 69. Delamination Damage Progression, Crosshead Indentation	131
Figure 70. Load-Displacement of 4 m/s Impact Loading	131
Figure 71. Delamination Damage Progression, 4 m/s Impact Loading	132
Figure 72. Absorbed Energy, 4 m/s Impact Loading	133
Figure 73. TiGr Laminate Damage Types indicating crushing and increased deflection gradient under crosshead (a), (b), titanium compressive buckling (c), (d), titanium buckling and tensile fracture transition (e), (f), and fiber fracture near regions of titanium buckling (g), (h).	134
Figure 74. SEM micrograph for t7 (AWJ machined, $R_z=11.83 \mu\text{m}$) depicting (a) Top ply crushing, (b) Ti first ply buckling, (c) magnified view of Ti buckling, (d) Abrasive wear track, (e) magnified view of wear track and crack initiation site and (f) Ti buckling near the neutral axis of TiGr specimen.....	134
Figure 75. SEM micrograph for t7 (AWJ machined, $R_z=11.83 \mu\text{m}$) depicting (a) lateral cracking (b) lateral crack in striated channel and (c) lateral crack path	135
Figure 76. SEM micrograph for t12 (CNC trimmed, $R_z=31.5 \mu\text{m}$) depicting (a) lateral cracking (b) lateral crack in striated channel and (c) lateral crack path	135
Figure 77. Differences between Quasi-Static and Low-Velocity Impact Loading	139
Figure 78. Internal and Plastic Dissipation Energies for 2.5 and 4 m/s Impact Simulations	140
Figure 79. Bernhardt Laminate CLT Stress Distributions	142

Figure 80. Vara Laminate CLT Stress Distributions	142
Figure 81. Thick Laminate CLT Stress Distributions	143
Figure 82. Force-Displacement of MVF-comparison Models	144
Figure 83. Laminate Max Load Normalized by Flexural Rigidity	147
Figure 84. Laminate Absorbed Energy at Max Load Normalized by Flexural Rigidity	147
Figure 85. Flexural Rigidity vs. Max Load for All Specimens.....	149
Figure 86. Flexural Rigidity vs. Absorbed Energy at Max Load.....	149

TABLE OF TABLES

Table 1. Material Constants for Ti-15-3-3-3.....	43
Table 2. Material Constants for Composite Lamina.....	44
Table 3. Johnson-Cook Plasticity Constants for Ti-6Al-4V	48
Table 4. Johnson-Cook Damage Coefficients for Ti-6Al-4V	51
Table 5. TiGr Specimen Edge Trimming Parameters.....	84
Table 6. Specimen Geometry and Layup	85
Table 7. Properties of Constituent Materials.....	85
Table 8. AWJ Experimental Conditions for TiGr Specimens	85
Table 9. Low Velocity Impact in Flexure and AWJ Process Variables for TiGr Specimens	98
Table 10. Titanium 15-3-3-3 Material Properties	101
Table 11. GFRP/PEEK Material Properties	101
Table 12. Cohesive Surface Properties	102
Table 13. Interlaminar Cohesive Properties.....	102
Table 14. Experimental Results from Quasi-Static 3-Point-Bend Testing.....	113
Table 15. Specimen Flexural Rigidity Comparison Data	146

ACKNOWLEDGEMENTS

I would like to thank Professor Ramulu for his coaching and expertise with this body of work. His dedication to teaching and commitment to this field is reflected in the successes of his students and significant continuing industry influence. His patience and direction made this work possible.

I would like to thank the Boeing Company for the financial support of my continuing education.

I would thank my wife for her unwavering support of this multi-year effort. Her love and patience make her an amazing mom to our children and have enabled me to complete this milestone.

NOMENCLATURE

Fiber Metal Laminate (FML)	A hybrid composite material system composed of metal plies and composite plies co-cured together
Metal Volume Fraction (MVF)	The percentage of overall laminate volume occupied by metal layers.
ARALL	Aramid Reinforced Aluminum Laminate
TiGr	Titanium-Graphite
Coefficient of Thermal Expansion (CTE)	A material property that indicates how much a material will expand or contract with changes in temperature.
GFRP	Graphite Fiber Reinforced Plastic
CFRP	Carbon Fiber Reinforced Plastic
Sol-Gel	Solution-Gelation process for creating solid materials from small molecules, typically used in the formation of metal oxides.
Stringer	A strip of metal or other material to which the skin of an aircraft is fastened.
Strut	Referring to several different components used to strengthen and stiffen aircraft fuselage structures.
Longeron	A longitudinal stringer.
Stress Intensity Factor (SIF)	A material property used to describe the stress state at the tip of a material crack when subject to a far-field load. This parameter can provide failure criterion for brittle materials.

CHAPTER 1: INTRODUCTION

The aerospace industry is continuously looking for new innovative materials to help expand the design space for future vehicles. Composite materials are of particular interest, owing to their high strength-to-weight ratio, adaptability to varied applications, and resistance to environmental degradation. However, aircraft manufacturers have encountered many obstacles in the transition from mostly metal aircraft to composite structures. One such obstacle is the prediction of how composite materials will fail. Traditional composite materials are made up of many ply layers, or lamina, of unidirectional fabric material bonded together using an adhesive. Varying bulk properties can be obtained by changing the orientation of the fabric lamina and the chemical composition of the adhesive, or matrix material. However, this structure leaves composite materials prone to delamination, or separation of the fabric layers. Composite delamination can be very difficult to detect, and can cause serious degradation of the structure. Another obstacle encountered by aircraft manufacturers is the joining of these laminate structures to traditional metal structure. Because composites are generally stiffer than their metal analogs, more load is carried by the composite than the metal structure it is joined to. To accommodate this increased load, the composite joint must be “padded up” with more material, adding weight and thickness to bolted joints.

A new class of hybrid composite materials has been developed to address some of these issues. Fiber-metal laminates (FMLs) are a class of composite materials consisting of thin sheets of metal adhesively bonded to traditional fiber-reinforced polymers. They are characterized by increased fatigue resistance and superior damage tolerance, among other favorable properties. Several FMLs have been investigated extensively for aerospace applications. ARALL is a FML consisting of aluminum alloy bonded to aramid fiber, and was used in the construction of the C-17 military transport vehicle. GLARE is another material consisting of aluminum alloy sheet bonded to fiberglass. This material has been used in several applications by the plane maker Airbus. Finally TiGr is a FML consisting of titanium alloy sheet bonded to graphite-reinforced polymer. This material has been investigated but has not been used in aerospace commercially to this date. However, initial test data indicates potential for increased bearing strength and high strength-to-weight ratio.

1.1 Development

TiGr was first developed by Boeing in the late 1990s. The High Speed Civil Transport (HSCT) program was in development, and engineers were looking for strong, lightweight materials that could withstand the high temperatures associated with supersonic flight. Processing of composite materials was becoming cheaper, and fiber-metal laminates looked like a promising compromise between strength at high temperatures and weight. Two of the main factors when considering materials for fiber-metal-laminates are galvanic corrosion caused by dissimilarity of materials and CTE mismatch. CTE mismatch makes a big difference in processing due to residual stresses created during the cure cycle. For GFRP the two most likely materials are titanium and corrosion-resistant steel. Titanium has excellent galvanic compatibility with carbon, and has high strength with much lower specific weight than steel, therefore it is the best choice for weight-critical aerospace applications. It was this logic that led to the creation of TiGr as a feasible laminate in the aerospace industry. After the HSCT program was abandoned in 1999, Boeing continued development work on TiGr as a possible option for future aircraft design. During this time period, the selection of titanium alloy 15-3-3-3 was made, choosing the most cost-effective alloy that could be readily formed into thin sheets. Various foil thicknesses were tried, however in cases where titanium foil was replacing a CFRP ply it made sense to have the thicknesses match. Therefore most tested foil thicknesses were between 0.15 and 0.25 mm. Most tested layups were quasi-isotropic (Ti-0-90-0-Ti).

During this time period, Boeing collaborated with academic institutions on a testing campaign that looked at many of TiGr's static and fatigue properties. These studies are documented in the literature. However, impact testing and compression-after-impact results were never published. Although some work has been done to characterize impact behavior of TiGr, much more is needed to understand the various failure mechanisms and their impact on residual strength.

1.2 Processing

The processing of fiber metal laminates such as TiGr requires careful consideration of the bonding between metal and fiber layers. Ideally, the bonds between the metal and substrate should be much stronger and more durable than the composite matrix resin. Also, the bonded joint must be compatible with the composite resins, must be applied using a controlled process for good bond reliability, and must be able to withstand the environment for which the component is designed. To this end, Boeing designed a Sol-

Gel process for titanium processing that is the industry-accepted standard for preparing titanium for bonding to composite structure. This process is currently used in titanium spars for the F-35 control surfaces, primary and secondary structure on the Boeing 787 for titanium-composite interfaces as well as rain erosion protection of large 787 parts, and for lightning protection straps on rotorcraft (Fink).

Sol-Gel is a contraction of the terms solution and gelation. This substrate consists of a mixture of different compounds that bind to the metal surface, but allow active bonding sites for bonding to organic primer as well. Components of sol-gel are zirconium compound, a silane compound, glacial acetic acid, a surfactant, and water (Fink). Sol-Gel for this process is commercially available from 3M (AC130) as a kit.

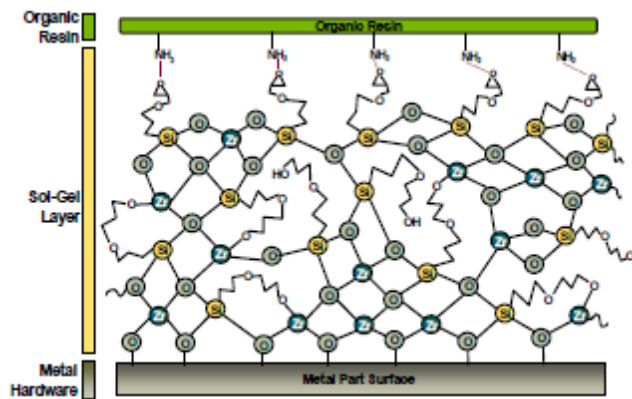


Figure 1. Sol-Gel Layer Structure

The preparation of titanium using the Sol-Gel process involves the following steps:

- Chemical or mechanical etch
- Rinse
- Surface activation (50% hot Turco 5578L)
- Rinse
- Dry
- Sol-Gel drench
- Dry
- Apply BR 6747-1 zero VOC chromated primer (Cytec Engineered Materials)

Titanium prepared using the Sol-Gel process exhibits superior bonding to CFRP plies in a laminate. The process was commercialized at Triumph Fabrications in a joint venture with Boeing. Capability currently exists to process 305mm wide foil that is .025-.254 mm thick at a line speed of 1.52 meters per minute.

With the addition of primer and a protective plastic sheet coating, the treated titanium can be stored for later use in rolls.

Production of the TiGr laminate follows a similar process to fabrication of a traditional CFRP laminate. Plies of unidirectional or woven pre-impregnated CFRP are layered with sheets of Sol-Gel treated titanium foil according to the prescribed layup. Compaction techniques are used to debulk the layup using applied pressure, vacuum, or both. Finally, the laminate is cured using a combination of heat and pressure in an autoclave or between heated platens.

Post-cure processing of the laminate has been researched by Ramulu et al. While machining and drilling techniques are common, abrasive waterjet is the preferred method for developing final shapes, as it has been shown to leave a superior finished surface, with few fiber pull-outs and metal microcracks.

1.3 Structural

From a structural design perspective, TiGr's most valuable properties lie in its high bearing strength, good fatigue resistance, and superior damage tolerance. TiGr does have a higher specific weight than a traditional composite, however, so it has been investigated primarily as a method to locally reinforce a composite part. The figure below shows how ply replacement is used to create a hybrid composite part exhibiting the low specific weight of a composite on one side and the localized superior bearing properties of TiGr on the other, all without changing the thickness of the laminate.



Figure 2. Ply Replacement using Titanium Layers

Composite design traditionally requires “building up” or increasing the thickness of a laminate in areas that interface with bolted joints. Building up a laminate for a bolted joint ensures that the bearing strength of the material is adequate for the applied bolt loads reacted through the thickness of the material, but may add significant weight to large structures such as airplane wing skins or spars. Since TiGr has a significantly

higher bearing strength than traditional CFRP, such building up is not required and ply replacement can be utilized, as illustrated above.

Taking advantage of the high stiffness of TiGr, laminates using unidirectional plies can be formed into axially loaded shapes shown in Figure 3. These structures can be designed to be lighter, stiffer, and stronger with better fatigue properties than either purely titanium or purely composite structures. Examples of aircraft geometry that fit this description are stringers, struts, and longerons.

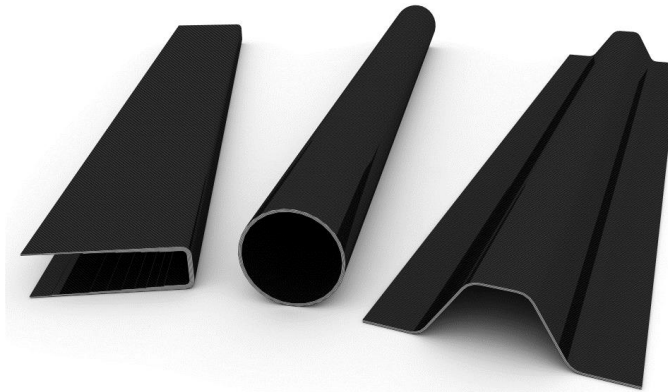


Figure 3. Axial Structures using TiGr

For structures that are regularly exposed to environments that are damaging or corrosive to composite structures, TiGr can be structured by placing the titanium plies on the outer surfaces or face sheets of hybrid composite as shown in Figure 4. Such use of titanium face sheets provides a lighter-weight alternative to a pure titanium part without sacrificing strength or rigidity.

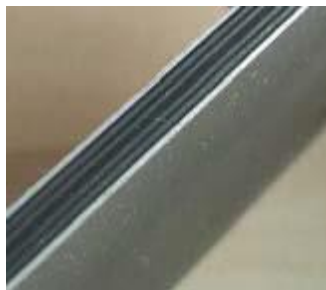


Figure 4. Titanium Face Sheets

Figure 5 shows how titanium skins can be used locally as protection against abrasion or corrosion. Because adding the titanium layers will increase weight, only adding titanium locally will minimize the weight impact while providing protective benefits.



Figure 5. Titanium used for Abrasion Resistance

1.4 Damage Tolerance

A particular field of interest with all FMLs is their resistance to damage, or damage tolerance. Aircraft design criteria include provisions for sustainment of damage over the lifecycle, detectable and repairable within regular inspection intervals. This requirement demands the ability to bear limit loads after the damage occurs, and this in turn requires the residual strength of aircraft materials to be determined. In metallic structures, damage tolerance is driven mainly by usage criteria. That is, fatigue and crack propagation play a major role, due to grain boundary slippage and material plasticity. Environmental degradation such as corrosion may also play a role. In composite materials, damage tolerance is primarily determined by impact loading, although environmental variables affect composite damage tolerance as well. Because FMLs contain both metals and composites, a comprehensive approach must be used to consider all of these factors and their interactions with each other as depicted in Figure 6.

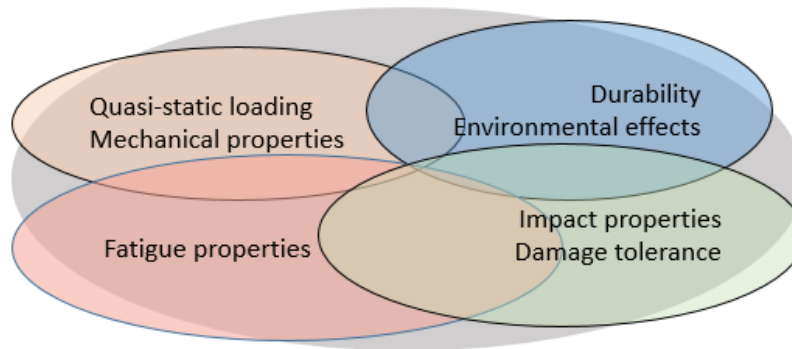


Figure 6. Aspects of Damage Tolerance in FMLs

1.5 Quasi Static Loading

The mechanical properties of FMLs are governed by the individual mechanical properties of the lamina that make up the composite. Metals are approximately isotropic, while composite plies are anisotropic. Because of this, the bulk properties of FMLs are generally anisotropic; however this is dependent on layup and orientation. Metal plies exhibit elastic-plastic behavior when deformed, while

composites are linearly elastic until the point of failure. It is the ductility of metals that cause the composite plies to dictate when the FML fails. Because the strain at which composite fibers fail is usually much less than the strain at which metal plies fail, the strain of the fibers is the same as the strain of the entire laminate. Another difference between FMLs and traditional composites is the degree to which residual stresses are induced during curing. Because metals and composites have different coefficients of thermal expansion (CTE) they deform differently when subjected to the heat of an autoclave. This develops residual stresses both in the material layers and the interlaminar bonding material. An accurate material model must then include these induced residual stresses in order to demonstrate bulk properties. A common approach to such problems is the Metal Volume Fraction method, or MVF. This was a method to use the amount of metal layers in the laminate to approximate bulk properties. The MVF is defined as:

$$MVF = \frac{\sum t_{metal}}{t_{laminate}}$$

With this definition, it is possible to calculate other equivalent material properties using the relation:

$$P_{laminate} = MVF \cdot P_{metal} + (1 - MVF) \cdot P_{composite}$$

In this way, P represents the property of interest. Properties calculated using this method are tensile yield and ultimate strength, modulus of elasticity, bearing yield and ultimate strength, blunt notch strength, shear yield and ultimate strength, compressive yield and ultimate strength, shear modulus, and compressive modulus of elasticity. A major drawback to this method is the inaccuracy of calculated values compared to experimental data, and the fact that accuracy can only be improved with sufficient data. Secondly, yield parameters for a FML are difficult to establish, as this parameter virtually does not exist for most unidirectional composites. As mentioned earlier, most composites exhibit linear elastic behavior until fracture, and do not exhibit yielding. Therefore the notion of bulk yield properties for a FML may have limited practicality.

1.6 Fatigue Loading

This category of damage tolerance characterization is divided into two parts; crack initiation and crack propagation. The first of these pertains to mechanisms involving the initiation of microscopic cracks while the second involves the subsequent transition into macroscopic propagating cracks. The crack

initiation mechanisms are traditionally a function of surface quality and mode of loading, while the crack propagation mechanisms are related to material bulk properties.

The crack initiation phase is predominately concerned with microscopic cracks that are governed by the local stress state at the notch root. Classical laminate theory in conjunction with stress concentration factors is used to describe this stress state. Prediction of fatigue life is the next step, and uses S-N data obtained for metallic sheet. However, the crack transition length must be appropriately modified to account for fibers that bridge the direction of crack propagation. These bridging fibers will limit the transition crack length, and have an increasing influence as the crack propagates. An important clarification is that while bridging fibers do not affect the crack initiation, their influence is important when using classical laminate theory to define the stress state. Although these bridging fibers do not affect initiation, the cut fibers at the notch root are responsible for small stress concentrations. Cracks tend to form at these stress concentrations, and thus are prevalent along more of the notch contour than is observed in homogeneous isotropic metals. Finally, when considering initiation of cracks in FMLs, it is important to remember the residual stresses formed during manufacturing. These residual stresses affect the stress ratio of a cyclic load, as they set a non-zero nominal load about which applied stresses vary.

Crack propagation in FMLs originally relied on the philosophy of assuming homogeneous properties for the laminate and using Stress Intensity Factors (SIF) to correlate to empirical data, similar to an isotropic metallic sheet. The downside of this approach is that a number of correction factors were needed to make the data correlate, and this required acquisition of much test data. Additionally, this approach neglected to consider primary FML damage mechanisms such as delamination and fiber bridging. To improve on this method, Marissen proposed a method by which each mechanism would be considered separately, based on superposition of SIFs. This method was later refined by Guo and Wu, Alderleisten, and Wilson [69-71]. The method can be generalized by:

$$K_{FML} = K_{farfield} - K_{bridging}$$

Where K_{FML} is the stress intensity factor for the FML, $K_{farfield}$ is the stress intensity factor for the monolithic metal layers based on stresses calculated using composite laminate theory, and $K_{bridging}$ represents the reduction in stress intensity factor due to unbroken fibers bridging across the crack tip. This method was

the first method that only required knowledge of the mechanical properties of the individual plies in the laminate along with their damage resistance behavior.

1.7 Impact Durability

Impact damage tolerance of FMLs is often characterized using an energy approach, as there are several mechanisms for damage from an impact, and an energy based approach allows correct appropriation of contribution to each mechanism. The three primary mechanisms for damage are i) membrane stretching, ii) flexural deformation, and iii) transverse shear deformation [1]. The flexural deformation energy is absorbed according to the bending stiffness of the FML, while the transverse shear and membrane stretching are defined by the interlaminar fracture and constituent properties, respectively. To simplify the flexural deformation portion of the energy balance, quasi-static loading is assumed, as the mass ratio of the impactor and FML is generally greater than 2 [72]. Another finding from experimental studies is that the extent of interlaminar fracture ie. ply delamination does not extend beyond the visibly yielded damage zone, when the FML is constructed with metallic face-sheets. This discovery suggests that visual inspection could provide a reasonable assessment of internal damage after an impact. However, this does not necessarily hold true for cases where the metallic layer is intermediate in the layup. Morinier [73] observed that regardless of metallic ply location in the stackup, these layers absorb up to 90% of the energy from an impact. Because the metallic layers absorb such a large percentage of the impact energy, there must be energy transferred from the composite to the metallic plies, resulting in high impact tolerance for FMLs. The composite plies, due to their linear elastic properties and high stiffness, serve to redirect energy into the plane of the metallic plies. This allows the metallic plies to deform more globally, directing energy away from the point of impact and plastically deforming under flexure. The ductility of the metallic plies governs how much the material will plastically deform, and thus how much energy can be absorbed. Final fracture is still governed by the last fiber to reach fracture strain, however, as discussed earlier.

1.8 TiGr Durability Testing

As mentioned above, TiGr consists of titanium metallic plies and graphite composite plies impregnated with resin. The material properties of TiGr have been investigated both in academia and industry recently. However, as with most new materials, an exhaustive study of all material characteristics must be completed before the material is deemed ready for a commercial application. The manufacturing

challenges and quality control standards associated with TiGr have so far outweighed the projected weight savings in the few detailed applications for which the material has been studied. Thus, further data is needed to support selection of the highest value applications for weight savings and manufacturing efficiency.

A significant component of the quality control standards that must be imposed for TiGr to be considered application-ready is the characterization of damage. Because delamination has such a significant effect on the strength of any composite structure, acceptance standards must be established. The impact test is commonly used in the characterization of damage in composites, and test standards and procedures follow well-documented guidelines. The testing consists of dropping a heavy mass with a spherical impacting tip called a tup onto a stationary test specimen. The energy of impact can be calculated using the mass of the impactor and the height of the drop. Data is collected measuring the impact energy and the response of the sample. The impact energy is quantified using the standard expression for potential energy:

$$P = mgh$$

Where P is the energy of impact, m is the mass of the tup, g is the gravitational constant, and h is the drop height.

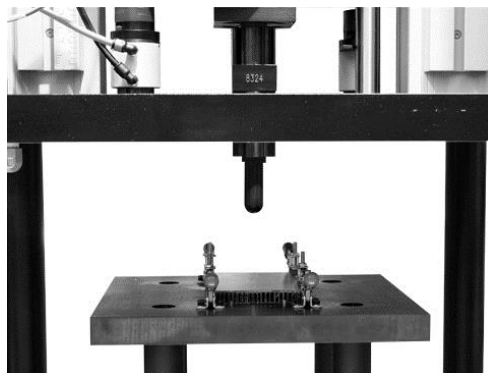


Figure 7. Impact Test Setup (Instron, Inc)

Following the drop test, a non-destructive inspection of the sample is done using through-transmission ultrasonic (TTU) techniques. This inspection allows identification and measurement of delamination regions inside the composite without destroying the sample. Finally, the compression-after-impact (CAI) testing is done on the specimens, subjecting them to buckling compression load until the specimens fail.



Figure 8. Compression-After-Impact Failed Specimen (Instron, Inc.)

The next major component of validation involves modeling the impact specimen using finite element software and building a dynamic simulation of the impact event. Once the model is adjusted to replicate actual impact results, parametric studies can be run quickly to predict performance of different layups, ply thicknesses, processing variables, and material types. The commercial finite element software ABAQUS (Dassault Systemes) is capable of modeling both static and dynamic responses of composite materials, and includes damage models to simulate failure and delamination.

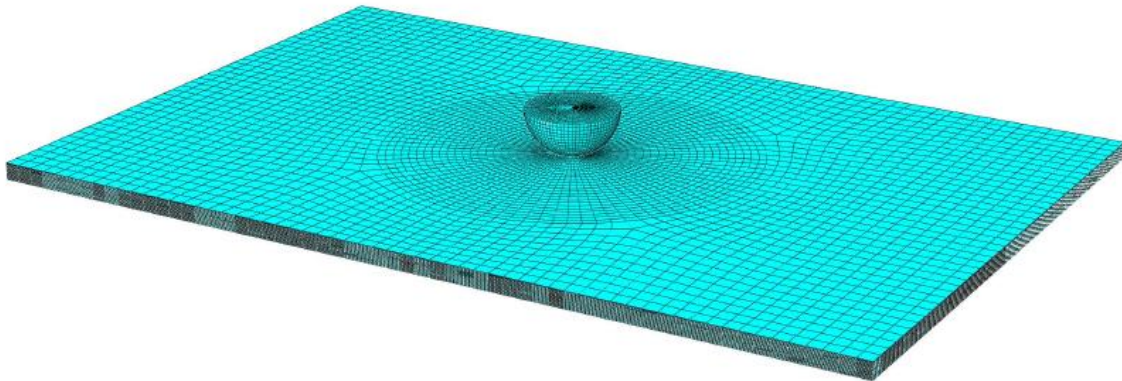


Figure 9. Abaqus Finite Element Model

Several modeling techniques can be employed when modeling composites in Abaqus. These will be discussed in greater detail in coming sections. The model shown in figure 9 represents an assembly of layers of solid elements. Each layer represents a ply, and has material properties and orientations assigned to represent either titanium foil or unidirectional graphite composite. These layers of solid elements are bound together using cohesive elements representing the interlaminar bonds between composite plies.

These cohesive elements are given failure conditions corresponding to the delamination properties acquired from testing. Finally, the impacting tup is modeled using rigid elements. In a static simulation a load is applied to the tup and the material deforms accordingly. For a dynamic simulation the tup is given an initial velocity corresponding to the impact velocity for a specified impact energy.

Other modeling techniques include using 2-dimensional shell elements to construct each ply layer. This technique leads to faster processing times, however the plane stress condition is assumed for all layers. Though this is a valid assumption for this geometry, the material failure models for isotropic metallic require 3-dimensional geometry.

Finally, ABAQUS includes a composites analysis tool that builds a representative laminate within a workbench out of virtual plies. The plies are not visualized, but stacking geometry, orientation, and material properties are applied correctly, giving the representative bulk response. This tool is useful for analysis of composite structures, but lacks the ability to model interlaminar damage behavior.

In the following chapter the evolution of manufacturing, testing, and impact simulation of TiGr will be discussed in the larger context of fiber-metal-laminate (FML) development. The incorporation of simulation tools such as ABAQUS will be shown to be vital to the continued advancement of this unique material system.

CHAPTER 2: REVIEW OF CURRENT KNOWLEDGE

2.1 Brief History of Fiber Metal Laminates (FMLs)

FMLs were first considered by Fokker in the mid 1940's, as several Dutch engineers considered ways to bond wood to metal, allowing construction of strong, lightweight structures for airplanes. At the time, the British airplane company De Havilland had considerable experience with wood bonded construction of airplanes, and had begun experimenting with metal bonding as well. Norman de Bruijne, a dean at Cambridge University, had discovered an effective adhesive for metals and had worked with his contacts at De Havilland to introduce this concept to the aircraft industry. De Bruijne was also friends with Anthony Fokker, and it was a young trainee at De Havilland named Rob Schliekelmann who would later bring metal bonding technology to Fokker and eventually implement various metal bonding techniques on production aircraft [14]. Over the next decades as composites technology developed and plastics embedded with fibers found uses in aerospace applications, several entities continued to look at bonded combinations of metal and composite. The University of Delft and NLR, both Dutch entities, developed ARALL (Aramid Reinforced Aluminum Laminate) in the mid-1970s. In the US, the NASA Langley Research Center investigated various fiber-metal combinations for Space Shuttle components. It wasn't until the 1980's however, that continuing research on FMLs at Delft led to the final patenting of ARALL as a commercially available material, with the Dutch company AKZO holding the rights [15]. In 1987 AKZO filed a patent for a new FML called GLARE (Glass Laminate Aluminum Reinforced Epoxy). This new material had superior impact properties compared to ARALL, and was also found to have excellent burn-through resistance. Several aerospace applications have since used GLARE, including cargo liners [16], the front radome bulkhead of the Bombardier Learjet 45 business jet, and most notably on the upper fuselage of the Airbus A380 [14]. In the mid 1990's Boeing began experimenting with a new FML called TiGr (Titanium Graphite). The motivation for this research was the necessity of a lightweight structural material that could withstand high temperatures associated with supersonic flight. Boeing was running the HSCT (High Speed Civil Transport) program and estimated wing skin temperatures were higher than aluminum wing skins could withstand due to creep. TiGr laminates were a promising solution, offering lightweight performance with high temperature resistance [17]. Previous work on the characterization of low-velocity impact and

fatigue resistance of GLARE boosted confidence in a FML as a potential solution. After the HSCT program was canceled in 1999 [18] research on TiGr continued in the academic sphere.

To create an effective bond between titanium and carbon lamina, a process had to be developed to pre-treat titanium to have better cohesion with the organic polyamide resins used in thermoplastic layers. Research at Stanford University yielded a sol-gel (solution-gelation) process using ZrO₂/epoxysilane applied to titanium that enables adequate bond strength [33]. This was a key enabler for TiGr manufacturing, and allowed further mechanical property investigation. Drilling processes on TiGr laminates were investigated by Kim at the University of Washington, characterizing exit damage and attempting to optimize feed and spindle speeds [19]. Spaulding investigated drilling TiGr laminates using EDM (Electrical Discharge Machining) to determine the impacts of peak current, pulse time, and percent-on time on the material removal rate, tool wear, and cut quality. Pahuja studied abrasive waterjet cutting of TiGr laminates characterizing the surface finish and kerf quality in both thick and thin laminates with different traverse speeds and flow velocities [21]. At the Massachusetts Institute of Technology (MIT) Burianek [22-23] studied the fatigue mechanics of TiGr, where others including Shim and Alderliesten [24] did other work on fatigue properties of other fiber metal laminates including GLARE. At the University of California Los Angeles (UCLA) work was done to develop constitutive multi-scale models for simulating the metal-composite interfaces in TiGr laminates by Hundley, Hahn, and Yang [25-28], as well as analysis of bolted joints and TiGr bearing strength. Because FMLs had been shown to exhibit favorable impact properties compared with conventional composites, low-velocity impact damage was characterized by Bernhardt [2], Nakatani [6, 30-31], and Reiner [32]. Nakatani [6, 30-31] and Reiner [32] focused on flat-plate specimens impacted by hemispherical impactors, demonstrating membrane deformation & associated damage, while Bernhardt's impact specimens were in a 3-point-bend configuration using by a cylindrical impactor. This allowed Bernhardt [2] to study how edge quality may affect damage propagation during impact. All three of these impact tests used TiGr constructed as quasi-isotropic carbon composites with titanium face sheets.

2.2 TiGr Manufacturing and Machining

Before effective investigation could be done on the mechanical properties of TiGr, a methodology had to be created for bonding the titanium and composite layers together. Simply co-curing the materials

together using an autoclave or hot-press resulted in poor bond strength due to the dissimilarity of the titanium and composite. Because in almost all tested cases delamination was the biggest precursor to catastrophic damage of the laminate, improving the bond strength became a critical factor in the development of TiGr. Research at Stanford University led by Reinhold Dauskardt [33] focused on development of a thin film interphase layer that would act as an intermediary between the dissimilar metals. This metal/epoxysilane sol-gel could be applied to the titanium as a coating, and would act as a coupling agent between titanium oxide and epoxy. The research team experimented with different formulation precursors, solvents, and process variables, attempting to optimize this sol-gel layer to get the best adhesion, eventually standardizing a ZrO₂/epoxysilane formulation and spray application process for continued work. In the second phase of the research, different methods for toughening a Bis-A epoxy resin were investigated, including rubber particles of different sizes, silica nanoparticles, hard core shells, and different epoxy cross-linking agents. Double-cantilever beam specimens were then tested to determine the critical fracture energy and fracture surface characterization. Specimens for each of several different toughened epoxy formulations were compared to specimens employing sol-gel interphase layers. Notably, sol-gel specimens generally outperformed specimens lacking the interphase layers, in some cases by a factor of three. Also, Dauskardt observed that when sol-gel was not applied failures were often by adhesive debonding at the titanium-epoxy interface. With the sol-gel film applied the failures were generally cohesive fracture in the epoxy layer, and had fracture energies higher than the adhesively bonded specimens [33].

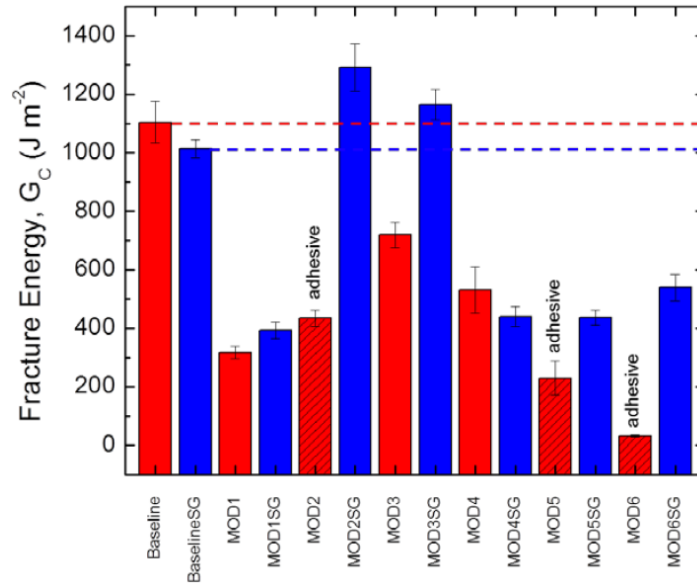
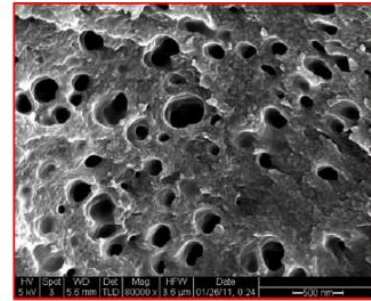
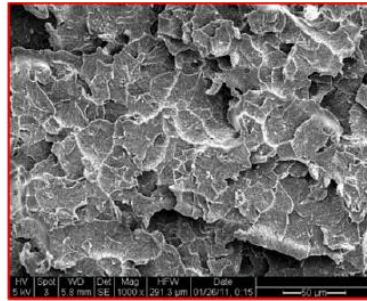


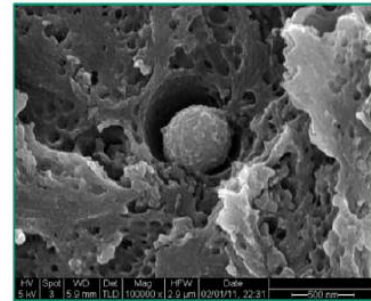
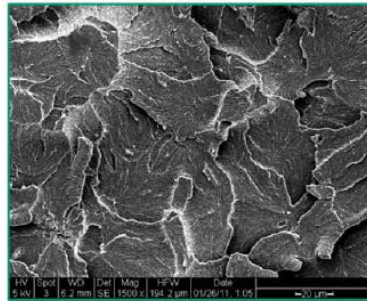
Figure 10. Critical fracture energies of different toughed epoxy formulations with and without sol-gel interphase layers at titanium-epoxy interface [33].

The best performing specimens were the MOD2SG, which outperformed the baseline with the addition of the interphase layer. This epoxy formulation was toughed with 0.4 μm butadiene/acrylic hard core shells. SEM imagery of the fracture surface indicates a nanoporous microstructure with channels roughly 100-250 nm in diameter for the baseline resin.

MSR355 Baseline
• nanoporous
channeled structure



MOD 2
• 0.4 μm hard core
shells



MOD 4
• combination of 3M
silica nanoparticles
and 5-10 μm
polybutadiene
rubber

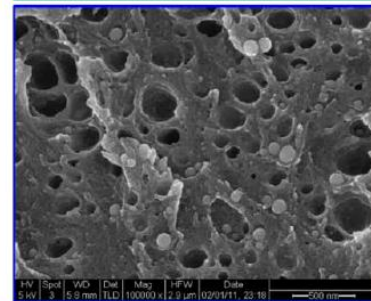
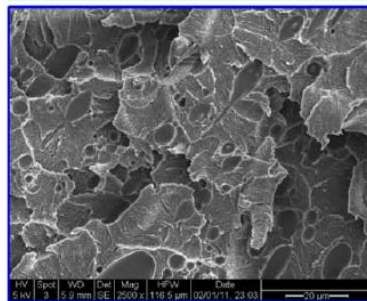


Figure 11. Nanoporous microstructure of resin fracture surfaces [33].

With the development of a process to effectively bond titanium and composite layers together, the macro scale properties of different laminates could be investigated, developing bulk characterizations of TiGr as an engineering material.

As with most laminated structures, the intention for future applications is that FMLs would be molded and cured to a net shape near their final form. Conventional machining operations would then be minimized; however it's reasonable to assume some follow-on processing such as drilling holes or trimming edges would still be needed. In order to consider FMLs for production applications, investigation of these techniques is required. Researchers at the University of Washington have experimented with different methods for these follow-on operations.

Kim looked into drilling processes in titanium/thermoplastic laminates [19]. He investigated the effect of different consolidation methods on tool wear, heat induced damage, hole size and roundness, surface texture, and presence of metallic burrs. The two consolidation methods used were autoclaving and induction heating using a ceramic hot press. Kim's specimens used a Ti, PIXA-M (0, 90, 0, 0, 0, 0, 90, 0), Ti layup with 140 μm titanium foil thickness on the top and bottom faces. A drill press was instrumented to provide torque and speed data as holes were drilled through the laminate using a standard carbide drill bit. Kim noted that drill head thrust and torque parameters were linearly related to feed speed in autoclaved specimens, but that these parameters had a nonlinear relationship in the induction heated specimens. As the laminate is drilled, cutting energy increases rapidly with depth. The cut surface was smoother in induction heated specimens due to matrix smearing. Notably for layups with titanium face sheets, drilling the exit hole through the bottom titanium layer causes large compressive and bending forces, and can cause the titanium to be pushed away from the neighboring composite in the vicinity of the hole [19]. In a production application this must be considered, as any delamination damage from drilling may not be easily visible and may erode local bearing strength of the laminate.

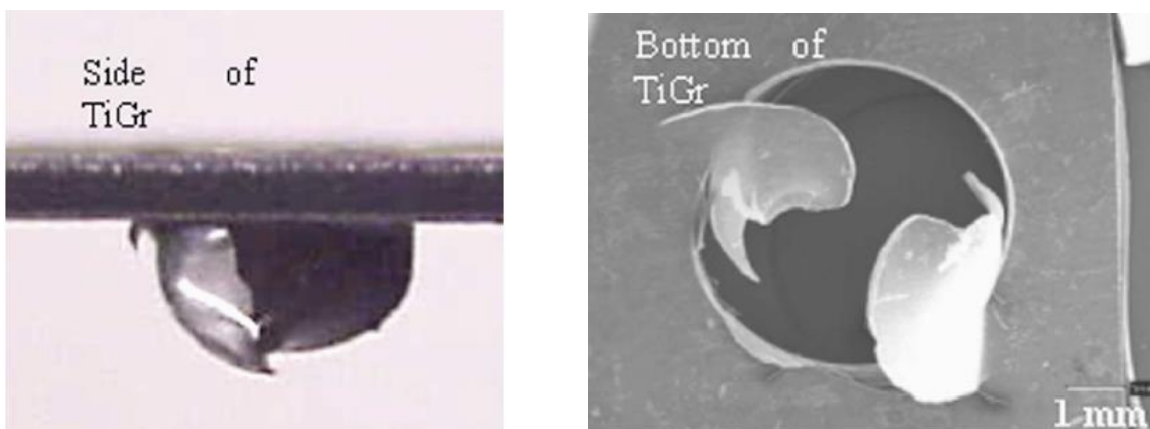


Figure 12. Tearing in induction-heated specimens caused by bottom titanium ply delamination [19]

Continuing to evaluate drilling techniques, Spaulding [20] investigated using electrical discharge machining (EDM) techniques with TiGr laminates of the same composition as Kim. Because EDM machining imparts no force on the work piece as material is removed, it has the ability to mitigate many of the challenges of conventional machining of composites, including those highlighted by Kim and shown in Figure 13. Typically EDM techniques require that the material to be removed is conductive, which would present a

problem for most non-conductive epoxies; however if the fibers are conductive it is possible for them to generate sparks, enabling material removal with EDM. Inclusive of the standard EDM machine settings, Spaulding included 3 variables in his investigation; pulse time, percent on-time, and peak current in Amperes. Output variables being studied were material removal rate (MRR), tool wear rate (TWR), and cut surface characterization using SEM imaging and surface topography [20].

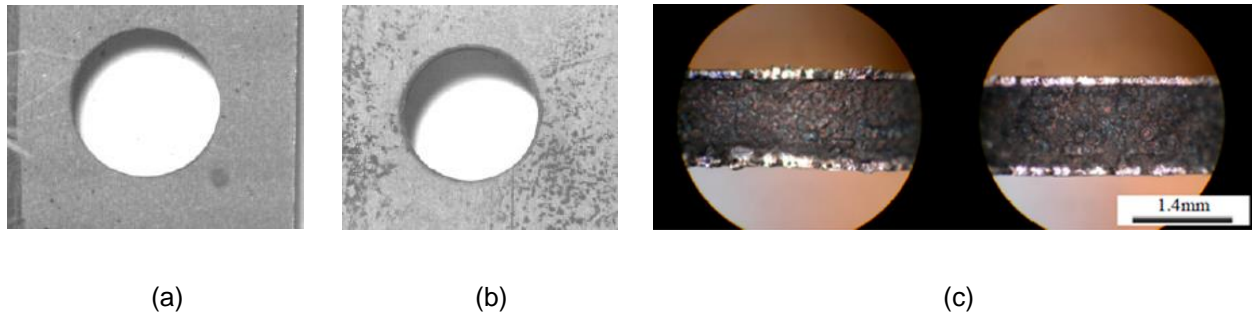


Figure 13. Top Surface (a), Bottom Surface (b), and Section View (c) of EDM holes in TiGr laminate [20]

Spaulding found that higher MRR values corresponded with higher amperage settings, and that with lower peak currents, MRR is very low. Also, a longer pulse time led to more material being removed. In all cases TWR was very low regardless of the other input variables. Average surface roughness also increased with higher peak current and higher percentage time-on. The observed mechanisms impacting surface roughness were globules of melted matrix material that solidified, as well as craters, matrix cracks, and debonded plies. In general, the best quality holes were made using lower peak current and shorter pulses; as current and on time increased the MRR increased, but the surface roughness and associated damage increased dramatically as well. This leads to a conflict between the desire for faster manufacturing times and the quality of the finished product. Spaulding used a multi-factor optimization scheme to evaluate the effects of current, pulse time, and percent on time to determine the optimal parameters. Spaulding's work confirmed the efficacy of EDM as an option for TiGr, but its use in a manufacturing environment would have to be evaluated through the lens of productivity and finished quality. One of the challenges of this manufacturing method is that the optimal settings for machining composite are different from those for titanium; composite requires lower current and shorter pulses and titanium requires higher currents or machining time increases dramatically. Future research will expand on titanium face-sheet construction to

include laminates with more than two titanium layers; a condition that may further complicate use of EDM techniques with FMLs [20].

Also at the University of Washington Pahuja studied the use of abrasive waterjet (AWJ) machining on both thick and thin TiGr laminates [21]. This machining technique has the advantages of not causing thermal damage to the work piece and providing a fast cutting speed. Paul et al. had studied the use of AWJ for GLARE laminates, setting a precedent for investigation [34]. Pahuja investigated cut quality in terms of MRR and kerf characteristics, then optimized AWJ parameters such as abrasive flow rate (AFR) and traverse speed using analysis of variance (ANOVA) techniques. Observations of the kerf quality using different machining parameters indicated that specimens cut with high traverse speed and low AFR exhibited more irregular surfaces, with little entry damage in the top titanium ply. With low traverse speed and high AFR the cut surface was more smooth and regular, with lower surface roughness. Damage mechanisms observed under magnification included ductile shearing, abrasive plowing, and scratching of titanium layers, while matrix material in the composite was damaged by shearing and plastic deformation. Fibers were cut by micro chipping, brittle fracture, and bending fracture. Overall machinability of TiGr by AWJ was determined using MRR, overcut, taper, and damage as output variables. Statistically, it was found that traverse speed had the biggest impact on these parameters [21].

2.3 Fatigue

Research at the Massachusetts Institute of Technology (MIT) centered on the fatigue properties of TiGr laminates. Burianek and Spearing [22-23] measured the fatigue life of TiGr specimens at elevated temperatures and under different load conditions, investigating the both the propagation of damage and consequent reduction of stiffness over the lifetime of the specimens. Material was supplied by Boeing for the testing in the form of 305 mm x 38.1 mm rectangular coupons with 6.35 mm diameter holes in the center. The layup was [Ti/0/90/0₂]_s, and used .127 mm thick Ti-15-3 beta titanium alloy with IM7 fibers and PIXA polyimide resin. The specimens were loaded into a servo-hydraulic load frame with a digital controller for applying the cyclic loads. The entire assembly was enclosed in a cabinet that was then heated to the prescribed test temperatures using a heat gun with thermocouple feedback control. An extensometer mounted across the hole in the center of the specimen provided stiffness measurements.

Burianek noted that previous work on modeling of fatigue crack growth in TiGr laminates showed that crack growth rates remained stable after initiation, compared with rising growth rates in monolithic metals. In TiGr laminates the fibers bridge the cracks in titanium face sheets and act to slow growth rate. In an attempt to further understand how damage propagates in the laminate, a series of experiments were conducted where specimens were stopped after a prescribed number of cycles to destructively analyze the extent of damage. At 1000 cycles no titanium face sheet damage was evident, but some minimal delamination was present, as well as ply cracking in the 90 degree plies in the vicinity of the holes. At 10,000 cycles, although there was still no face sheet damage visible, there were splits in the 0 degree plies and delamination between 0 and 90 degree plies. Transverse ply cracking was also advanced. At 30,000 cycles face sheet cracking was evident, along with further 0 degree ply splits. Finally at 100,000 cycles the titanium cracks extended all the way across the specimen and extensive delamination was present. The length of original ply splits had increased, and new splits had formed in areas away from the hole locations. Interestingly, the number and length of ply splits near the holes hadn't increased significantly, indicating reduced local stress due to advancing damage. These tests served to demonstrate the complex sequence of damage mechanisms that determine TiGr laminate performance. Because many of the mechanisms occur in the composite layer underneath the titanium face sheets, it's critical to understand their contribution to the life of the laminate.

To simplify construction of an S-N curve for TiGr laminate, a convention had to be adopted to identify when a specimen had "failed". Burianek suggested using 50% reduction in stiffness as a reference point for "failure" and constructed the plot from the experimental data. From observation, this stiffness drop corresponded to when face sheets were cracked all the way through and delamination had progressed to over one inch away from the hole in all directions.

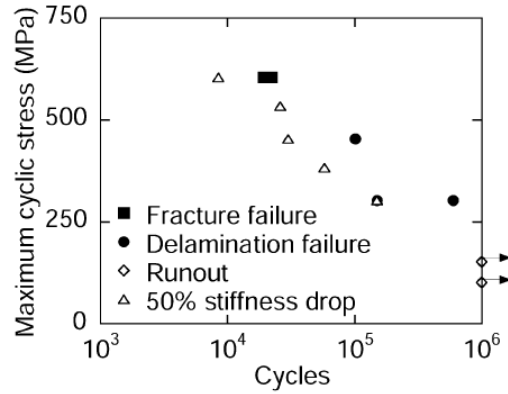


Figure 14. Fatigue Life of TiGr 2-6-2

Other work on the fatigue life of TiGr laminates was conducted by Rhymer and Johnson [74] to characterize how the bond strength between composite and titanium layers influences fatigue life. Using an advanced formulation of PETI-5 polyimide for the matrix surrounding the IM7 fibers and an alkaline-perborate titanium surface treatment, an advanced TiGr laminate was created to compare with the traditional sol-gel formulation being optimized at Stanford. This laminate was tested and compared to traditional TiGr to obtain the following S-N curves:

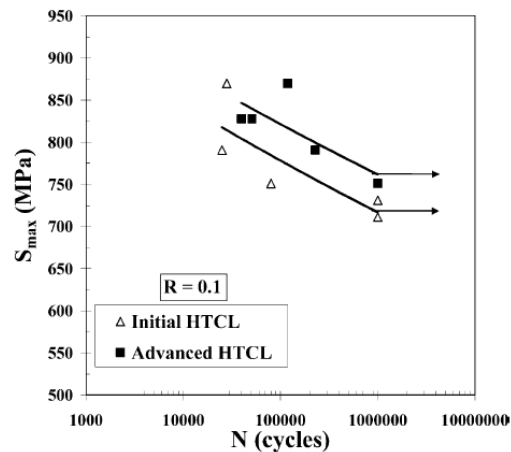


Figure 15. S-N Curve for TiGr 2-6-2

As the laminates were in all other respects identical, it's clear that increasing bond strength plays a measurable role in laminate fatigue performance. Rhymer and Johnson also saw a different progression of damage in their specimens, which had internal as well as external titanium plies. In their experiments damage began with cracking of the titanium plies, followed by delamination in the crack vicinity along the

bond line. In the advanced laminate the bond strength was higher, causing higher stress intensity on the fibers near a titanium crack. In these instances the fibers themselves fractured. Rhymer notes that this may be an undesirable result, as the effects of fiber bridging on extending fatigue life can't be realized if the fibers are fractured near the crack. Ideally the optimal laminate would have a toughened interface resulting in high fatigue life but would allow crack propagation and delamination simultaneously without fiber fracture [74].

Because of the many forms TiGr can take with different interfacial chemistry, different layups, and different metal volume fractions much more work is needed to catalog and understand the fatigue life of these laminates. The advantages of fiber bridging offer a tantalizing benefit of steady-state crack growth that is seemingly unaffected by crack length. This is an advantage over homogenous metals, which experience typically accelerating crack growth rates highly dependent on crack length. Further experimental data coupled with constitutive modeling development offer potential for future laminate designs with superior damage tolerance.

2.4 Impact

Composite materials are susceptible to impact damage both during manufacturing and during their service life. During manufacturing, common impacts occur from dropped tools, mishandling during transfer in an assembly line, during shipping to the final assembly locations, and after final assembly to the finished product. In aerospace applications, in-service impacts can occur during maintenance, ground operations, or in flight as a result of hail or bird strike. All of these impacts can have a detrimental effect on the strength of the composite material, and due to the linear elastic nature of most composites, subsurface damage due to fiber delamination may go largely unnoticed. Therefore, it is necessary to understand the magnitude to which these low-speed impacts may cause subsurface damage, and to quantify this damage as a function of impact kinetic energy.

Drop tests conducted by Bernhardt [2], Nakatani [6, 30-31], and Reiner [32], focused on the effect of titanium face sheets on the impact behavior of composites. The layups were typically [Ti/0/90] (Reiner), or symmetric layups consisting of titanium sheet, 0 degree plies, and 90 degree plies such as [Ti/0/90/0/0/0/0/90/0/Ti] (Bernhardt) or [Ti/0/90/0/Ti] (Nakatani). Titanium face sheets were preferred

because the primary mechanism for energy dissipation in the low-velocity impact test is plastic deformation of the titanium layers. Having these layers on the outside of the laminate makes characterization of this energy dissipation easier. The other TiGr failure modes during impact include debonding between the titanium and GFRP plies, matrix cracking, fiber fracture, and interlaminar delamination. The interface between 0 degree plies and 90 degree plies serves to demonstrate the effect of titanium plastic deformation on interlaminar delamination, as well as to illustrate the “fiber bridging” effect of fibers running transverse to titanium crack propagation.

A number of different fibers and matrix materials were used for the graphite plies. Bernhardt et al. used IM-6 graphite fibers with PIXA-M, a high-temperature thermoplastic similar to many used in the aerospace industry. Nakatani used a proprietary prepreg tape developed by Mitsubishi Rayon Co, LTD., and Reiner used Hexcel G947/M18 unidirectional prepreg tape. While all of these graphite fiber thermoplastic composites have slightly different properties, their behavior during impact follows the same basic failure modes. Contribution of each mode to the overall damage of the laminate is highly dependent on specimen geometry, layup sequence, and impact energy. Two different titanium alloys were investigated for TiGr impact behavior. Ti-6Al-4V, used by Nakatani et al. is the most common titanium alloy and is readily available in many different forms, including thin sheets. Bernhardt and Reiner used Ti-15V-3Cr-3Al-3Sn, a metastable beta alloy of titanium that is primarily used in sheet metal and thin-rolled forms. This alloy was chosen due to its high strength and cold formability. Also, the cost of producing thin sheets of this alloy was found to be almost half that of Ti-6Al-4V at the time of the research. Specimen dimensions were different for each set of tests as well. Bernhardt used rectangular specimens measuring 76.2 x 12.7 mm, cut parallel to the zero-degree ply orientation. Nakatani used square specimens measuring 100 x 100 mm, however the specimens were clamped between two steel panels with a circular opening 80 mm in diameter in the center, and fixed in place using epoxy adhesive. In this configuration the unsupported specimen shape is circular rather than rectangular. Reiner used larger specimen geometry 300 x 300 mm, and secured the specimens around the edges. This resulted in a much larger square unsupported area.

In general, test equipment for low velocity impact testing is similar. The apparatus consists of an impactor with known mass and a hemispherical or hemicylindrical contacting head, often affixed to a guide

rail to ensure linear translation. The test rig also usually contains some method for measuring drop height, as well as a brake system to catch the falling weight after initial impact to prevent multiple strikes. Various instrumentation may measure force-time history, impact velocity, and deflection after impact. Post impact inspection was most successfully conducted using sectioning and scanning-electron-microscopy (SEM). Other methods of non-destructive inspection (NDI) were attempted, however the authors of these experiments had little success with being able to identify failure modes and interlaminar damage.

Both Reiner and Nakatani used a traditional drop test employing a weighted rod with a hemispherical end. Reiner's drop weight had a hemispherical radius of 12.7 mm and a mass of 3.0223 kg, while Nakatani used an impactor with a radius of 10 mm and mass 2 kg. Bernhardt used a different configuration with a hemicylindrical impactor that applied a line load across the specimen, rather than a point load in the center. His impactor was 5.59 mm in diameter, and the mass of the falling weight and sensors was 2.013 kg. This apparatus is shown below:

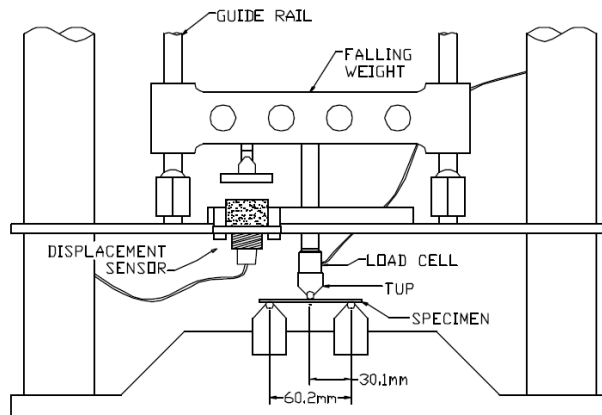


Figure 16. Bernhardt Test Apparatus

It is interesting to note that these two drop test configurations may produce different results due to the loading geometry. Bernhardt's apparatus is essentially a 3-point-bend setup, and thus all ply interaction effects through interlaminar transition zones are normal to the axis of bending. This results in experimental data that is easier to relate to a closed form solution, however this type of loading is less representative of many of the impacts seen in the real world.

The testing procedure quite simply consisted of securing the specimen using appropriate clamping (although Bernhardt's samples were simply supported) and releasing the drop weight from a prescribed height to achieve the desired impact energy. Force transducers were attached between the falling weight and the impacting head, and measured the force of impact through the duration of contact. This data, along with displacement sensor data, was fed through a data acquisition system and scaled to appropriate engineering units. Slight differences in data acquisition and sensor technology existed between experiments, but overall the procedures were similar. After impact, samples were inspected first visually, then using destructively sectioned and examined using optical microscopy or SEM. This level of inspection was necessary to determine the contribution of each failure mode and extent of the damage for a given impact energy.

Nakatani et al. noted the following damage for drop tests done on GFRP and TiGr panels. The TiGr image was created from the impacted side after the titanium ply had been physically removed.

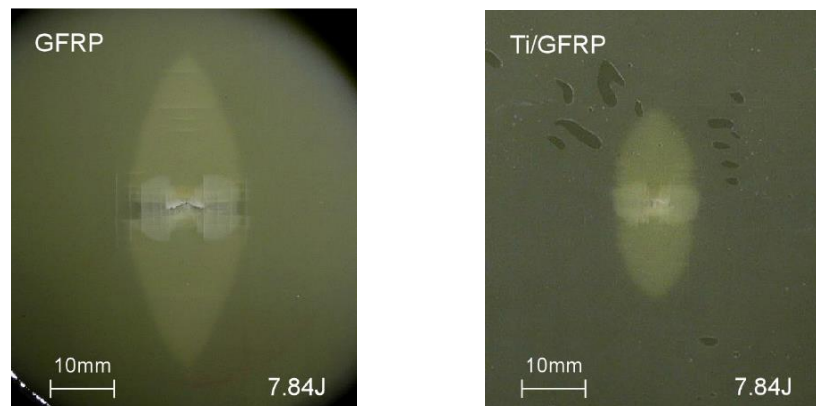


Figure 17. Nakatani Delamination Zones After Impact

From this view on the impacted side, delamination zones are clearly visible as the lighter colored areas around the locus of impact. Because of increased stiffness due to the titanium and adhesive, as well as the energy absorption via plastic dissipation in the titanium layers, the delamination zone in the TiGr laminate is significantly smaller than the delmination zone in the GFRP laminate for the same energy impact. These zones represent areas of separation between zero and 90-degree GFRP.

The following figure shows delamination area as a function of impact energy for both GFRP and TiGR plies, as tested by Nakatani et al.

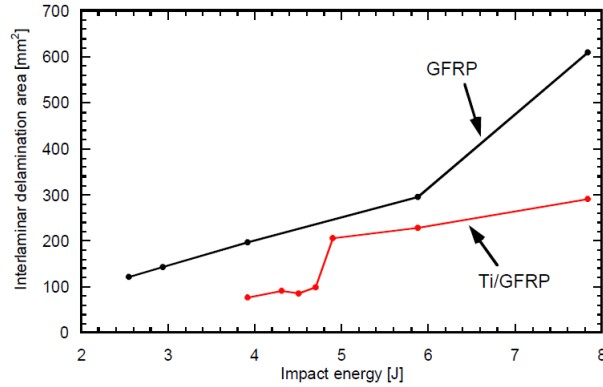
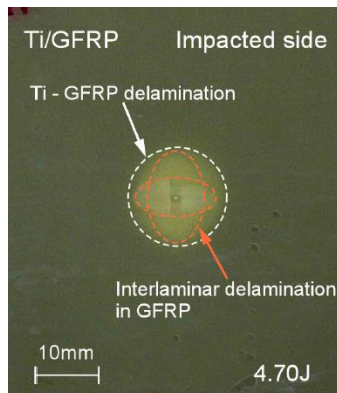


Figure 18. Delamination Area vs. Impact Energy

As shown, the interlaminar delamination area for GFRP increases fairly linearly for increasing energy levels. At a certain impact energy, additional failure mechanisms such as fiber breakage or matrix cracking are initiated, resulting in a steep increase in delamination area. For the TiGr specimens, delamination area is fairly stable below 4.7J. In this region, titanium opposite the side being impact is plastically deformed in a convex shape, however interlaminar delamination between GFRP plies is contained to within the area of titanium debonding, or separation from the adjacent GFRP plies. At impacts higher than 4.7 J, cracks were observed in the lower titanium layer, and this corresponded with the area of GFRP delamination extending beyond the area of titanium debonding. This describes the “jump” in the data at 4.7J impacts. The following pictures show Nakatani’s impacted TiGr specimens at impact energies below and above this jump.



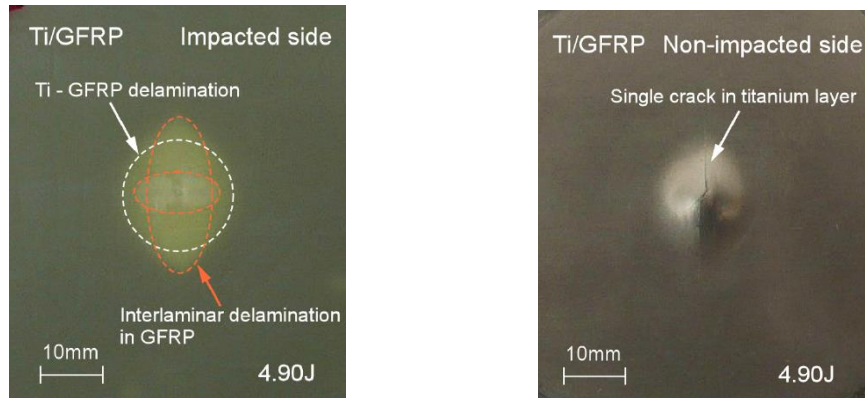


Figure 19. Nakatani Delamination and Titanium Fracture at Different Energy Levels

Load-vs-time and load-vs-displacement curves are shown below for these two impact energies. For the 4.7 J impact, a smooth load-time curve is present, while at 4.9 J the crack initiation in the titanium layer causes local fluctuations in stiffness at peak load. This results in the load oscillations visible after 2.5 msec. This effect can also be seen in the load-displacement curves, the crack initiation causing fluctuations in load at peak displacement as the crack propagated. These load fluctuations corresponded with the wider propagation of interlaminar delamination.

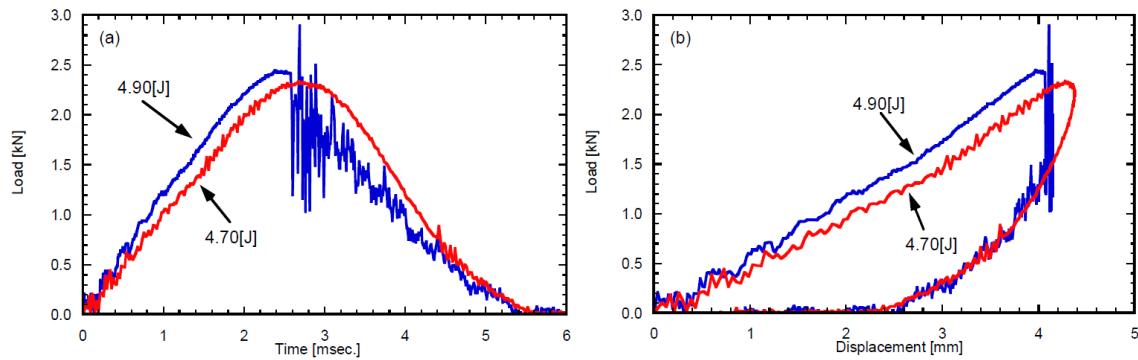


Figure 20. Nakatani Load History and Load vs. Displacement

Bernhardt et al. investigated the differences between two failure modes of TiGr laminates. The first failure mode is characterized by the lower titanium face sheet remaining intact, while the second failure mode is characterized by the lower titanium face sheet failing in tension, similar to Nakatani. These two modes exhibit different force-time behavior, as illustrated by the following plots:

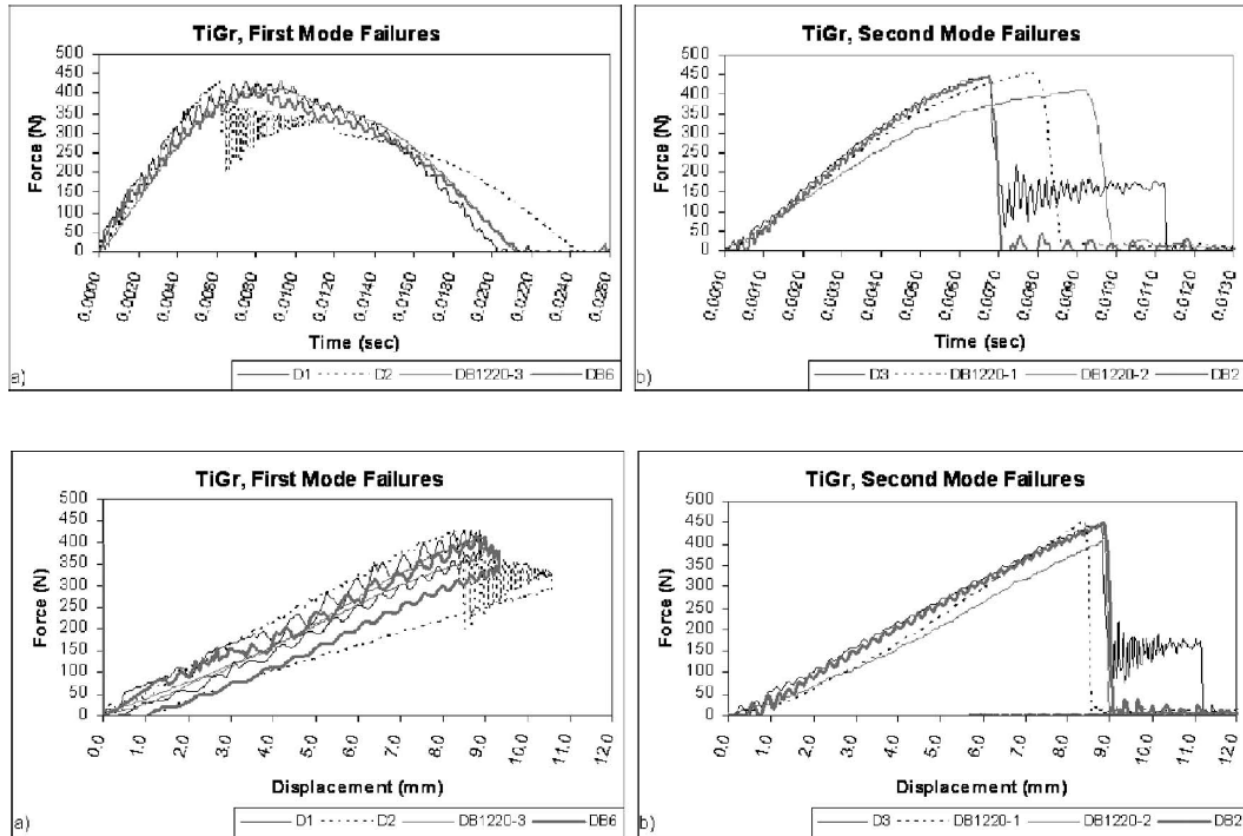


Figure 21. Bernhardt Load History and Load vs. Displacement for Mode I and Mode II Impacts

Comparing these plots to those generated by Nakatani et al., it is clear that the impact energies used by Bernhardt were much higher. While the Nakatani plots exhibited elastic rebound in the force-displacement curves, these force displacement curves show increasing displacement until failure. For the first mode with no tensile failure of the bottom titanium ply, the force-displacement curve shows smooth increase even after the force curve dropped. This corresponds to buckling of the uppermost titanium layer and compression failure of the uppermost GFRP ply. In the Mode 2 case with tensile failure of the bottom titanium sheet, the force-displacement curve shows a sharp drop where the titanium ply fails in tension. This was closely followed by significant damage to the rest of the laminate, including matrix cracking, delaminations between GFRP plies, buckling fracture of the upper GFRP plies, and buckling failure of the uppermost titanium sheet. Reiner conducted experiments with much higher impact energies and much larger unsupported specimen geometry, resulting in different force-time curves.

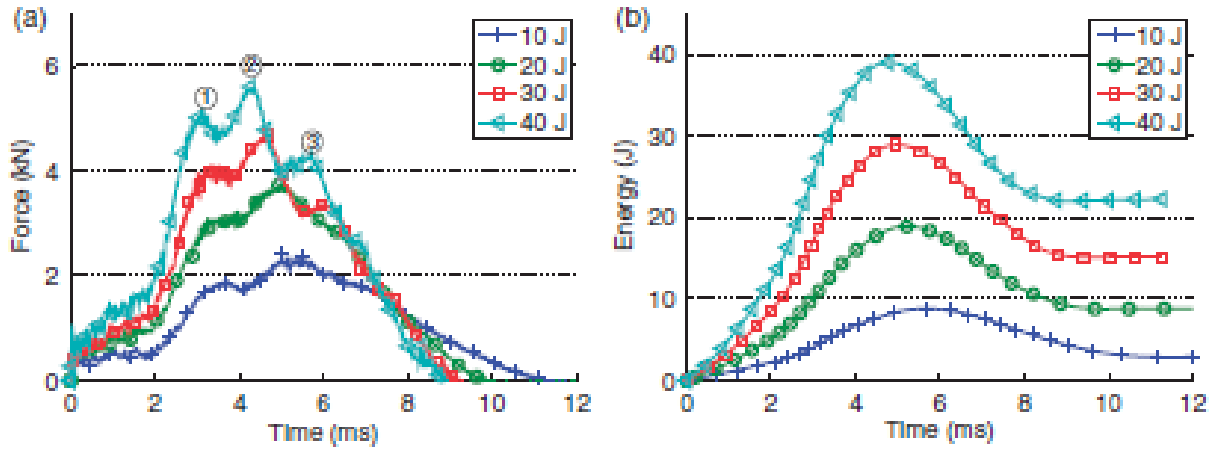


Figure 22. Reiner Impact Load History and Energy History

The experiments conducted by Reiner resulted in delamination, debonding, matrix cracking, and fiber fracture, but did not include titanium cracking as observed by Nakatani and Bernhardt. This can be observed by the lack of spurious oscillations in the force-time curves, indicative of titanium crack propagation. One reason for this difference could be the size of the specimens; more energy was absorbed by out-of-plane bending than by localized plastic deformation, as seen in the smaller samples. As a result, the titanium plies absorbed less of the energy locally and this resulted in greater delamination area and more matrix damage.

Although there have been significant differences in the specimen geometry, methods, and results of previous low-velocity impact tests, a few common conclusions can be drawn about the impact behavior of TiGr. First, in laminates where titanium is used as a face sheet on the bottom and top layers, damage of the laminate is governed by plastic deformation and tensile failure of the titanium face sheets. Two principle modes have been identified for this case. The first mode when the bottom titanium ply remains intact is described by top titanium ply buckling and damage to the uppermost GFRP ply, accompanied by significant delamination of the GFRP plies. The second mode when the bottom titanium ply fails in tension is described by buckling of the top titanium ply, significant fiber breakage and matrix cracking through the GFRP layers, and delamination. In this failure mode final fracture is governed by fiber breakage. The second conclusion drawn is that the sequence of damage for TiGr laminates is typically begun with buckling of the uppermost GFRP ply, immediately followed by buckling of the upper titanium surface. Damage

propagation continues as a mix of intra and inter-laminar delamination through the thickness of the GFRP plies, until local deflection causes tensile failure of the lower titanium surface. Once the titanium surface has failed, the remaining GFRP fibers fail in tension, instigating final failure through the thickness. Because failure of the lowest titanium surface directly results in failure of the remaining composite, the damage resistance of the laminate is directly tied to the ability of the composite to absorb energy through delamination rather than directing the energy through the zone of localized plasticity. Finally, because the first indication of damage is the buckling failure of the uppermost GFRP ply and the uppermost titanium layer, visual inspection for impact damage is much easier with TiGr than with a traditional GFRP composite.

2.5 Numerical Modeling of Hybrid Laminates

Conducting accurate simulation of low-velocity impact of FMLs is complicated by the fact that multiple damage modes occur simultaneously and are highly sensitive to specimen geometry, boundary conditions, and impactor size and shape. Appropriate constitutive models must be employed for accurate representation of each material and interaction, as the overall simulated impact behavior is an amalgamation of unique element formulations. Factors such as laminate geometry, boundary conditions, and impactor geometry have been shown to influence the relative appropriateness of different material models, based on assumptions about stress state during the impact event. However, numerical models provide an invaluable representation of the internal stresses and modes of damage propagation within a laminate, often invisible in experimental work and not accurately represented in an analytical model. Literature reviewed indicates significant advancement in the individual formulations with many comparisons to experimental data showing good agreement. These are briefly highlighted below.

2.5.1 Material Models

Material behaviors in Abaqus are defined in cards that describe the physical, linear elastic, plastic, and damage characteristics for a given material. The physical parameters for each material consist only of the density, and the linear elastic variables are the Young's Modulus and Poisson's ratio.

Table 1. Material Constants for Ti-15-3-3-3

Material	Young's Modulus	Poisson's Ratio
Ti-15-3-3-3	82 GPa	0.38

Since unidirectional fiber-reinforced composite plies are nominally orthotropic, their elastic behavior must include stiffness definitions in both of their in-plane principal directions.

Table 2. Material Constants for Composite Lamina

Material	E1	E2	Nu12	G12	G13	G23
HexPly8552	134 GPa	10 GPa	0.32	3.3 GPa	3.3 GPa	3.3 GPa

2.5.1.1 Elasticity

Elasticity in general is defined according to Hooke's law by $\sigma = \mathbf{D}^{el} \varepsilon^{el}$, where σ is the Cauchy stress, \mathbf{D}^{el} is the fourth-order elasticity tensor, and ε^{el} is the elastic strain. For problems involving traditional linear-elasticity, it is assumed that the elastic strain is a very small value. Materials exhibiting such traits are known as Hookean, and describe most metals, including titanium, as well as unidirectional CFRP. Formulation of the elasticity tensor is directionally dependent, with the simplest formulation being that of an isotropic material. For the sake of analysis, it is assumed that titanium is an isotropic solid, therefore its elasticity model is given as:

$$\begin{pmatrix} \varepsilon_{11} \\ \varepsilon_{22} \\ \varepsilon_{33} \\ \gamma_{12} \\ \gamma_{13} \\ \gamma_{23} \end{pmatrix} = \begin{bmatrix} 1/E & -\nu/E & -\nu/E & 0 & 0 & 0 \\ -\nu/E & 1/E & -\nu/E & 0 & 0 & 0 \\ -\nu/E & -\nu/E & 1/E & 0 & 0 & 0 \\ 0 & 0 & 0 & 1/G & 0 & 0 \\ 0 & 0 & 0 & 0 & 1/G & 0 \\ 0 & 0 & 0 & 0 & 0 & 1/G \end{bmatrix} \begin{pmatrix} \sigma_{11} \\ \sigma_{22} \\ \sigma_{33} \\ \sigma_{12} \\ \sigma_{13} \\ \sigma_{23} \end{pmatrix}$$

where the shear modulus, G , is given a default value of $G = E/2(1 + \nu)$.

For a unidirectional lamina, the elasticity formulation is complicated by the fact that the material is orthotropic. That is, the elasticity values are different in the 0 and 90 degree orientations. However, if an assumption of plane stress is made for CFRP lamina, the stiffness formulation can be reduced to:

$$\begin{pmatrix} \varepsilon_1 \\ \varepsilon_2 \\ \gamma_{12} \end{pmatrix} = \begin{bmatrix} 1/E_1 & -\nu/E_1 & 0 \\ -\nu/E_1 & 1/E_2 & 0 \\ 0 & 0 & 1/G_{12} \end{bmatrix} \begin{pmatrix} \sigma_{11} \\ \sigma_{22} \\ \tau_{12} \end{pmatrix}$$

This formulation assumes no stress in the σ_{33} direction, however the Abaqus formulation does include inputs for G_{13} and G_{23} because some plane stress element types allow consideration of transverse shear deformation.

2.5.1.2 Plasticity

Plasticity is generally explained by the additive strain rate decomposition, according to the following explanation. It is assumed that for a material exhibiting linear elasticity and subject to a deformation gradient \mathbf{F} there exists an elastic component of the deformation that, if the material were frozen in its deformed state, forces were removed, and the material allowed to unload, would cause a “reverse” deformation equal to $(\mathbf{F}^{el})^{-1}$. This reverse deformation would leave the material in a state deformed from its original state, and this left over deformation would be equal to \mathbf{F}^{pl} , the inelastic deformation.

$$\mathbf{F}^{pl} = (\mathbf{F}^{el})^{-1} \cdot \mathbf{F}$$

Rearranging to express the total deformation,

$$\mathbf{F} = \mathbf{F}^{el} \cdot \mathbf{F}^{pl}$$

The velocity gradient can be defined by $\mathbf{L} = \dot{\mathbf{F}} \cdot \mathbf{F}^{-1}$,

$$\mathbf{L} = \dot{\mathbf{F}}^{el} \cdot (\mathbf{F}^{el})^{-1} + \mathbf{F}^{el} \cdot \dot{\mathbf{F}}^{pl} \cdot (\mathbf{F}^{pl})^{-1} \cdot (\mathbf{F}^{el})^{-1}$$

Now if we define the elastic and plastic velocity gradients as $\mathbf{L}^{el} = \dot{\mathbf{F}}^{el} \cdot (\mathbf{F}^{el})^{-1}$ and $\bar{\mathbf{L}}^{pl} = \dot{\mathbf{F}}^{pl} \cdot (\mathbf{F}^{pl})^{-1}$, the velocity gradient can be re-written as

$$\mathbf{L} = \mathbf{L}^{el} + \mathbf{F}^{el} \cdot \bar{\mathbf{L}}^{pl} \cdot (\mathbf{F}^{el})^{-1}$$

In the plasticity model, it is now assumed that the elastic strains are very small compared to unity. This holds true for many traditional elastic-plastic materials, including most metals and the titanium of interest here. Using this assumption and the left polar decomposition of the elastic deformation,

$$\mathbf{F}^{el} = \mathbf{V}^{el} \cdot \mathbf{R}^{el} = (\mathbf{I} + \vartheta \mathbf{A}) \cdot \mathbf{R}^{el}, \quad \vartheta \ll 1, \quad \mathbf{A} = \mathbf{A}^T, \quad \sup \|\mathbf{A}\| = 1$$

Then,

$$\mathbf{L} = \mathbf{L}^{el} + (\mathbf{I} + \vartheta \mathbf{A}) \cdot \mathbf{R}^{el} \cdot \bar{\mathbf{L}}^{pl} \cdot \mathbf{R}^{elT} \cdot (\mathbf{I} - \vartheta \mathbf{A})$$

$$\mathbf{L} = \mathbf{L}^{el} + \mathbf{R}^{el} \cdot \bar{\mathbf{L}}^{pl} \cdot \mathbf{R}^{elT} + \vartheta \mathbf{A} \cdot \mathbf{R}^{el} \cdot \bar{\mathbf{L}}^{pl} \cdot \mathbf{R}^{elT} - \vartheta \mathbf{R}^{el} \cdot \bar{\mathbf{L}}^{pl} \cdot \mathbf{R}^{elT} \cdot \mathbf{A} - \vartheta^2 \mathbf{A} \cdot \mathbf{R}^{el} \cdot \bar{\mathbf{L}}^{pl} \cdot \mathbf{R}^{elT} \cdot \mathbf{A}$$

Now we can define \mathbf{D} and \mathbf{W} as the symmetric and antisymmetric parts of each velocity gradient, respectively, and can write them in terms of \mathbf{L} .

$$\mathbf{L} = \mathbf{D} + \mathbf{W}$$

$$\mathbf{L}^{el} = \mathbf{D}^{el} + \mathbf{W}^{el}, \quad \bar{\mathbf{L}}^{pl} = \bar{\mathbf{D}}^{pl} + \bar{\mathbf{W}}^{pl}$$

Substituting into the velocity gradient equation and neglecting higher-order terms,

$$\mathbf{L} = \mathbf{D}^{el} + \mathbf{W}^{el} + \mathbf{R}^{el} \cdot (\bar{\mathbf{D}}^{pl} + \bar{\mathbf{W}}^{pl}) \cdot \mathbf{R}^{elT} + \vartheta \mathbf{A} \cdot \mathbf{R}^{el} \cdot (\bar{\mathbf{D}}^{pl} + \bar{\mathbf{W}}^{pl}) \cdot \mathbf{R}^{elT} - \vartheta \mathbf{R}^{el} \cdot (\bar{\mathbf{D}}^{pl} + \bar{\mathbf{W}}^{pl}) \cdot \mathbf{R}^{elT} \cdot \mathbf{A}$$

Since the antisymmetric part of the velocity gradient constitutes rigid body motion, and therefore does not contribute to the relative deformation of an isotropic solid, it is ignored and only the symmetric part of the velocity gradient is considered.

$$\mathbf{D} = \mathbf{D}^{el} + \mathbf{R}^{el} \cdot \bar{\mathbf{D}}^{pl} \cdot \mathbf{R}^{el} + \vartheta \mathbf{A} \cdot \mathbf{R}^{el} \cdot \bar{\mathbf{W}}^{pl} \cdot \mathbf{R}^{elT} - \vartheta \mathbf{R}^{el} \cdot \bar{\mathbf{W}}^{pl} \cdot \mathbf{R}^{elT} \cdot \mathbf{A}$$

The antisymmetric part of the plasticity component of the expression, $\bar{\mathbf{W}}^{pl} = 0$ for isotropic materials, therefore the expression can be simplified to

$$\mathbf{D} = \mathbf{D}^{el} + \mathbf{D}^{pl}, \quad \mathbf{D}^{pl} = \mathbf{R}^{el} \cdot \bar{\mathbf{D}}^{pl} \cdot \mathbf{R}^{el}$$

This decomposition shows how general expression for deformation of a body can be decomposed by only considering the symmetric part of the velocity gradient, and by assuming that the total elastic strain is always small compared to 1. The rate of deformation decomposition is denoted otherwise as:

This decomposition shows how general expression for deformation of a body can be decomposed by only considering the symmetric part of the velocity gradient, and by assuming that the total elastic strain is always small compared to 1. The rate of deformation decomposition is denoted otherwise as:

$$\dot{\boldsymbol{\varepsilon}} = \dot{\boldsymbol{\varepsilon}}^{el} + \dot{\boldsymbol{\varepsilon}}^{pl}$$

where $\dot{\boldsymbol{\varepsilon}}$, $\dot{\boldsymbol{\varepsilon}}^{el}$, and $\dot{\boldsymbol{\varepsilon}}^{pl}$ are the total strain rate, elastic strain rate, and plastic strain rate, respectively.

2.5.1.3 Johnson-Cook Strain Hardening

After a material has reached its yield strain, it will begin to deform in an inelastic manner, and the stress-strain curve will deviate from the linear-elastic relationship. As described above, the total plastic deformation rate can be described as the sum of elastic and plastic strain rates. Because stress and strain do not hold a linear relationship in this region, a model is needed to describe the plastic strain rate contribution, $\dot{\varepsilon}^{pl}$ as the material elongates. The Johnson-Cook model uses a strain-hardening model to approximate the stress-strain relationship after the onset of yielding, and is appropriate for describing the ductile behavior of most metals.

The Johnson-Cook model is a Mises plasticity model that is formulated with static yield stress in the form

$$\sigma^0 = [A + B(\bar{\varepsilon}^p)^n](1 - (\hat{\theta})^m)$$

where $\bar{\varepsilon}^p$ is the equivalent plastic strain and A, B, n, and m are material properties obtained from empirical test data obtained at or below the transition temperature, $\theta_{transition}$, the temperature below which there is no temperature dependence of the yield stress. $\hat{\theta}$ is a quantity known as the non-dimensional temperature, and is described by the following:

$$\hat{\theta} \equiv \begin{cases} 0 & , \quad \theta < \theta_{transition} \\ (\theta - \theta_{transition}) / (\theta_{melt} - \theta_{transition}) & , \quad \theta_{transition} \leq \theta \leq \theta_{melt} \\ 1 & , \quad \theta > \theta_{melt} \end{cases}$$

This model will only consider test temperatures at room temperature, so the effective value of $\hat{\theta}$ will always be 0. Therefore the static yield stress can be simplified to $\sigma^0 = [A + B(\bar{\varepsilon}^p)^n]$. Equivalent plastic strain,

$\bar{\varepsilon}^p$, can be described by $\bar{\varepsilon}^p = \bar{\varepsilon}^p|_0 + \int_0^t \sqrt{\frac{2}{3}} \dot{\varepsilon}^{pl} dt$, where $\bar{\varepsilon}^p|_0$ is the initial amount of equivalent plastic strain, or work hardening. In the case of the impact test, no initial strain exists, so this value will be zero.

The Johnson-Cook model also has the capability to include strain rate dependence of a material. Because impact testing involves high strain rates, it is necessary to modify the strain hardening accordingly. Abaqus calculates strain rate dependence by assuming that yield stress, $\bar{\sigma}$ at any given strain rate is a function the static yield stress, σ^0 (which is a function of static plastic strain $\bar{\varepsilon}^p$ and temperature θ) multiplied by the ratio of the nonzero strain rate to the static yield stress, $R(\dot{\varepsilon}^{pl})$.

$$\bar{\sigma} = \sigma^0(\bar{\varepsilon}^p, \theta)R(\dot{\varepsilon}^{pl})$$

The equivalent plastic strain rate is assumed to be

$$\dot{\varepsilon}^{pl} = \dot{\varepsilon}_0 \exp \left[\frac{1}{C} (R - 1) \right] \quad \text{for } \bar{\sigma} \geq \sigma^0$$

where $\dot{\varepsilon}_0$ is a reference strain rate and C is a material constant measured at or below the transition temperature $\theta_{transition}$. The inclusion of strain rate dependence in the Johnson-Cook strain hardening plasticity model modifies the yield stress equation to

$$\bar{\sigma} = [A + B(\bar{\varepsilon}^p)^n] \left[1 + C \cdot \ln \left(\frac{\dot{\varepsilon}^{pl}}{\dot{\varepsilon}_0} \right) \right] (1 - (\hat{\theta})^m)$$

which can be simplified to

$$\bar{\sigma} = [A + B(\bar{\varepsilon}^p)^n] \left(1 + C \cdot \ln \left(\frac{\dot{\varepsilon}^{pl}}{\dot{\varepsilon}_0} \right) \right)$$

since all experiments will be performed at room temperature.

Material parameters were selected from a number of experiments performed at the U.S. Army Research Laboratory [9] using the Split-Hopkinson pressure bar technique.

Table 3. Johnson-Cook Plasticity Constants for Ti-6Al-4V

Parameter	A (MPa)	B (MPa)	n	C	m
Ti-6AL-4V	896	331.2	0.34	0.012	0.80

The process for determining these parameters employs both static and dynamic data, as well as a least-squares curve fit technique to minimize the error between the effective stress function and the empirical data. Determination of the individual parameters follows the methods described by Meyer [9, 11].

Parameter A is defined as the static yield strength at room temperature, determined using a strain rate of 1/s. This parameter can be established based on quasi-static tensile test data at room temperature. The value is cited from Dandekar and Spletzer [75] as 896 MPa.

Parameter B and n are found using the least squares technique described by Meyer [11]. To simplify the effective stress equation, data obtained at room temperature and a strain rate of 1/s is considered. If empirical data is not available for this strain rate, it may be interpolated by considering strain rate data above and below 1/s. This makes the second two terms of the effective stress equation equal to 1, and simplifies the equation to $\sigma^0 = [A + B(\bar{\varepsilon}^{pl})^n]$. Rearrangement yields

$$\sigma^0 - A = B\varepsilon^n$$

Now let

$$\varphi = \ln(\sigma^0 - A)$$

$$\varphi = n \cdot \ln(\varepsilon) + b$$

where $b = \ln(B)$.

Assuming the logarithmic curve-fit data at a strain rate of 1/s is given in the form $\sigma = \beta\varepsilon^\alpha$, the effect of the static yield stress must be subtracted from the overall stress to only consider the portion of the stress-strain curve related to post-yield deformation. Therefore A is subtracted from both sides of the logarithmic representation equations, and a new term, Ψ is introduced.

$$\Psi = \ln(\sigma - A) = \ln(\beta\varepsilon^\alpha - A)$$

The error is the measure between the theoretical line plotted by the Johnson-Cook coefficients and the data approximation equation. If a discrete set of k reference strains is used to represent the range across the data, the minimization of the summation of errors can be represented by

$$\sum_{i=1}^k (\varphi_i - \Psi_i)^2 = \text{minimum}$$

which can be evaluated by setting the derivatives with respect to b and n equal to 0:

$$\frac{\partial}{\partial b} \sum_{i=1}^k (\varphi_i - \Psi_i)^2 = 0,$$

$$\frac{\partial}{\partial n} \sum_{i=1}^k (\varphi_i - \Psi_i)^2 = 0.$$

Substituting the expression for φ and performing the differentiation, the following two expressions are obtained for b and n:

$$b = \ln(B) = \frac{\sum \Psi_i \ln \varepsilon_i \sum \ln \varepsilon_i - \sum \Psi_i \sum (\ln \varepsilon_i)^2}{(\sum \ln \varepsilon_i)^2 - 7 \sum (\ln \varepsilon_i)^2},$$

$$n = \frac{\sum \Psi_i - 7b}{\sum \ln \varepsilon_i}$$

In this way, by using these equations to calculate values for B and n, values of 0.656 GPa and 0.106 are obtained, respectively [cite].

Parameter C is found by simplifying the effective stress equation, considering only strain rates at room temperature. The equation takes the form:

$$\bar{\sigma} = [A + B(\bar{\epsilon}^p)^n][1 + C \cdot \ln(\dot{\epsilon}^*)]$$

where $\dot{\epsilon}^*$ is the effective strain rate divided by the reference strain rate of 1/s.

If the first term is simplified by $S_i = [A + B(\bar{\epsilon}^p)^n]$ this equation becomes

$$\bar{\sigma} = S_i + S_i C \ln(\dot{\epsilon}^*)$$

Now there must be an equivalent expression constructed from the empirical data. Split-Hopkinson pressure bar tests were conducted at a number of different strain rates. These tests resulted in sets of stress-strain data, for which logarithmic functions were fit, as described above. Taking a discrete set of representative strains over the range of data, these strains were substituted into the logarithmic fit curves, and the resulting stresses were plotted against $\ln(\dot{\epsilon}^*)$. This resulted in a curve representing strain rate dependence for each representative strain. The family of curves shows how strain rate dependence evolves with increasing strain. Analytical expressions were fit to each curve, described in the form:

$$y_i = s_i + s_i k_i \ln \dot{\epsilon}^*$$

Now this expression can be used with the familiar least-squares function

$$\frac{\partial}{\partial C} \sum (\bar{\sigma}_i - y_i)^2 = 0$$

Differentiation yields the following expression for C:

$$C = \frac{\sum s_i^2 k_i}{\sum s_i^2}$$

Using room temperature strain rate data obtained from the Split-Hopkinson pressure bar testing conducted by T. Weerasooriya and cited by Meyer [9], the value of C was obtained as 0.012.

Parameter m is the exponent to the non-dimensional temperature $\hat{\theta}$, and serves to modify the effective stress equation for conditions at elevated temperatures above $\theta_{transition}$. Because all low-velocity impact testing will be conducted at room temperature, $\hat{\theta}$ will be equal to zero, and the value of m is irrelevant for this work. Derivation of this value is outlined by Johnson and Cook (1983) [64].

2.5.1.4 Johnson-Cook Damage

This model for damage initiation in a material is based on the equivalent plastic strain calculated at the integration points of the elements in a finite-element model. The model is designed to use the Johnson-

Cook plasticity model, and assumes dynamic, high strain rate behavior of ductile metals. Damage is assumed to occur when the damage parameter w exceeds unity, defined by:

$$w = \sum \frac{\Delta \bar{\epsilon}^{pl}}{\bar{\epsilon}_f^{pl}} \geq 1$$

In this description, $\Delta \bar{\epsilon}^{pl}$ is the plastic strain for one time increment in a dynamic analysis, measured at an integration point, and $\bar{\epsilon}_f^{pl}$ is the failure strain, calculated from the Johnson-Cook damage parameters described below. The summation represents the collection of all the incremental damage for an integration point over the analysis time increment, and when the value equals unity damage has occurred and the element will either be deleted or retained, according to the preferences specified. Once an element has failed, the deviatoric stress components are set to zero for the remainder of the analysis. The hydrostatic stress tensor may be retained if the user wants to keep the elements in the analysis, or may be set to zero, with the affected elements deleted from the global stiffness matrix.

The failure strain $\bar{\epsilon}_f^{pl}$ is calculated from the following expression from Johnson and Cook.

$$\bar{\epsilon}_f^{pl} = \left[D_1 + D_2 \exp\left(D_3 \frac{P}{\bar{\sigma}_{JC}}\right) \right] \times \left[1 + D_4 \ln\left(\frac{\dot{\bar{\epsilon}}}{\dot{\bar{\epsilon}}_0}\right) \right] \left[1 + D_5 \left(\frac{\theta_w - \theta_0}{\theta_m - \theta_0}\right) \right]$$

In this equation, P is equal to pressure and $\bar{\sigma}_{JC}$ is the von Mises stress, and their ratio describes the stress triaxiality. The initial failure strain D_1 , exponential factor D_2 , triaxiality factor D_3 , strain rate factor D_4 , and temperature factor D_5 are material parameters calibrated from empirical test data.

Table 4. Johnson-Cook Damage Coefficients for Ti-6Al-4V

Parameter	D ₁	D ₂	D ₃	D ₄	D ₅
Ti-6AL-4V	-0.09	0.27	-0.48	0.014	3.87

Calibration of these material parameters follows a similar least-squares methodology to the Johnson-Cook plasticity parameter evaluation.

Damage Evolution:

Once an element has failed, the stress in the surrounding elements must be adjusted to account for the overall loss of stiffness. A material experiencing damage may have a stress-strain curve similar to that shown below. After the onset of damage there is a softening of the yield stress coupled with a

degradation of elasticity. These two mechanisms can be simulated using a damage law; that is, a macromechanical mathematical representation of the material's response.

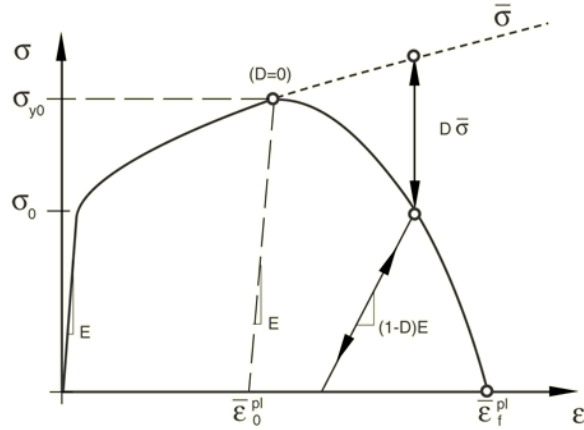


Figure 23. Damage Evolution in Finite Elements [77]

In this figure, damage initiation occurs at stress σ_{y0} , at which point the material begins to soften. The dashed line represents a material experiencing strain hardening and plastic deformation without damage, while the solid line shows how overall damage variable D evolves with increasing strain from $D=0$ at damage initiation to $D=1$ at the failure strain $\bar{\epsilon}_f^{pl}$, when stress is back to zero. The overall damage variable D is introduced as the combined effect of all damage mechanisms, and is defined such that

$$D = \max_{j \in N_{max}} (d_j)$$

Multiple failure mechanisms may be contained in a finite element model, with individual damage mechanisms denoted d_i . In the above equation, N_{max} represents the set of active mechanisms that contribute to the overall damage.

After the onset of failure, the above figure shows a deviation from the classic stress-strain curve defined by the material plasticity. To follow this curve, Hillerborg [76] introduced a fracture energy approach utilizing the material parameter G_f , the material strain energy release rate. To use this model, however, a stress-displacement relationship must be used, rather than the stress-strain curve used for the model prior to damage initiation. This is partially due to the fact that using a stress-strain relationship for a damage model would introduce a strain localization-based mesh dependency that could yield inaccurate results, as mesh refinement would decrease the amount of energy dissipation. Instead, Hillerborg suggested a model

based on Griffith's brittle fracture theory, where strain energy release rate or equivalent plastic displacement could be used to specify damage evolution.

$$G_f = \int_{\bar{\varepsilon}_0^{pl}}^{\bar{\varepsilon}_f^{pl}} L \sigma_y d\bar{\varepsilon}^{pl} = \int_0^{\bar{u}_f^{pl}} \sigma_y d\bar{u}^{pl}$$

This description of the stress-displacement relationship defines \bar{u}^{pl} as the equivalent plastic displacement, such that before damage initiation $\dot{\bar{u}}^{pl} = 0$, and after damage initiation $\dot{\bar{u}}^{pl} = L\dot{\bar{\varepsilon}}^{pl}$. The parameter L is the characteristic length of the element, which is defined based on element formulation, and is addressed in the next section. Characteristic length is important because the direction of damage propagation is not pre-determined; this parameter serves to normalize response across elements with different aspect ratios and topologies, thereby reducing mesh dependency.

Multiple methods are available for specifying how the damage evolves according to the fracture energy. The exponential form shown below ensures that the energy dissipation during evolution is equal to the strain energy release rate.

$$d_i = 1 - \exp\left(-\int_0^{\bar{u}^{pl}} \frac{\bar{\sigma}_y \dot{\bar{u}}^{pl}}{G_f}\right)$$

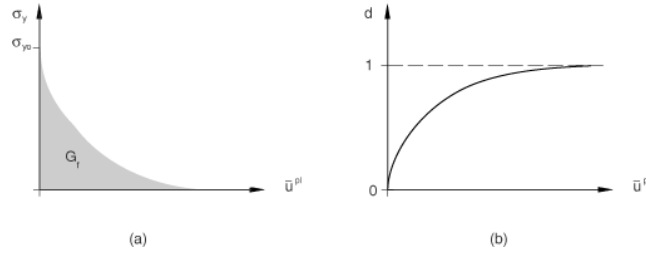


Figure 24. Exponential Damage Evolution [77]

When the overall damage variable D reaches a value of 1 at any element integration point, this corresponds to the failure strain $\bar{\varepsilon}_f^{pl}$, and the element has completely failed. At this point the element is removed from the mesh and an appropriate damage is applied to the stiffness components of all elements to which damage may propagate. This damage is applied according to $\sigma = (1 - D)\bar{\sigma}$.

2.5.1.5 Hashin Damage

This damage criteria was developed out of the need for a damage model that described the individual failure mechanisms of unidirectional fiber-reinforced composites. Prior to its conception, Tsai [78] had made the assumption that the failure criterion of a unidirectional fiber composite could be described in a similar form to Hill's [79] description of an ideal orthotropic plastic:

$$A(\sigma_{11} - \sigma_{22})^2 + B(\sigma_{22} - \sigma_{33})^2 + C(\sigma_{33} - \sigma_{11})^2 + 2D\sigma_{12}^2 + 2E\sigma_{23}^2 + 2F\sigma_{31}^2 = 1$$

However, this form assumes no contribution from isotropic stress, and fails to account for the unequal failure strengths of matrix and composite when loaded in axial tension and compression. A damage model that accurately describes failure of a unidirectional fiber laminate must consider four distinct failure modes; fiber breakage in tension, fiber buckling in compression, matrix cracking in transverse tension and shear, and matrix crushing due to transverse compression and shear. The failure model must consider each failure mode separately, as the initial mode of failure will affect subsequent damage evolution in the material. This is the formulation that was employed in nearly all cases employing commercial finite-element software for which damage was considered. Hashagen [65], being the exception, looked at the performance of both continuum shell and solid brick elements using the Hoffman [80] yield criteria for orthotropic materials. He concluded that shell elements could adequately predict laminate behavior and didn't suffer from shear-locking effects seen in solid elements.

In a general sense, the Hashin post-damage material response is of the form:

$$\sigma = C_d \varepsilon$$

where C_d represents the damaged stiffness matrix of the transversely isotropic unidirectional lamina, given by:

$$C_d = \frac{1}{D} \begin{bmatrix} (1 - d_f)E_1 & (1 - d_f)(1 - d_m)v_{21}E_1 & 0 \\ (1 - d_f)(1 - d_m)v_{12}E_2 & (1 - d_m)E_2 & 0 \\ 0 & 0 & (1 - d_s)GD \end{bmatrix}$$

In this expression, D is calculated as:

$$D = 1 - (1 - d_f)(1 - d_m)v_{12}v_{21}$$

and d_f , d_m , and d_s represent fiber damage, matrix damage, and shear damage, respectively. Hashin's failure criteria considers each of these damages separately, and uses quadratic representations of the

stresses to create a piecewise-smooth quadratic failure surface in stress space. The initiation criteria for each failure mode are given by:

Fiber Tension ($\hat{\sigma}_{11} \geq 0$):

$$d_f^t = \left(\frac{\hat{\sigma}_{11}}{X^T} \right)^2 + \alpha \left(\frac{\hat{\tau}_{12}}{S^L} \right)^2$$

Fiber Compression ($\hat{\sigma}_{11} < 0$):

$$d_f^c = \left(\frac{\hat{\sigma}_{11}}{X^C} \right)^2$$

Matrix Tension ($\hat{\sigma}_{22} \geq 0$):

$$d_m^t = \left(\frac{\hat{\sigma}_{22}}{Y^T} \right)^2 + \alpha \left(\frac{\hat{\tau}_{12}}{S^L} \right)^2$$

Matrix Compression ($\hat{\sigma}_{22} < 0$):

$$d_m^c = \left(\frac{\hat{\sigma}_{22}}{S^C} \right)^2 + \left[\left(\frac{Y^C}{2S^T} \right)^2 - 1 \right] \frac{\hat{\sigma}_{22}}{Y^C} + \left(\frac{\hat{\tau}_{12}}{S^L} \right)^2$$

In these equations, X^T is the longitudinal tensile strength, X^C is the longitudinal compressive strength, Y^T is the transverse tensile strength, Y^C is the transverse compressive strength, S^L is the longitudinal shear strength, and S^T is the transverse shear strength. These values are determined experimentally. Once damage variables d_f^t , d_f^c , d_m^t , and d_m^c reach a value of 1, damage initiation is assumed to have occurred for that particular failure mode. Once damage initiation has occurred, the effect of the damaged failure mode is incorporated into the effective stress matrix via the damage operator M through the following relation:

Damage Operator $\hat{\sigma} = M\sigma$

Prior to any of the damage variables reaching a value of 1, the damage operator M has the value of the identity matrix, therefore $\hat{\sigma} = \sigma$. After one of the failure modes has experienced damage initiation and evolution, the damage operator can be written:

$$M = \begin{bmatrix} \frac{1}{(1-d_f)} & 0 & 0 \\ 0 & \frac{1}{(1-d_m)} & 0 \\ 0 & 0 & \frac{1}{(1-d_s)} \end{bmatrix}$$

where the calculated effective stress is assumed to apply to the damaged internal region affected by the damaged element. The internal damage variables d_f , d_m , and d_s are derived from the failure mode damage variables through the following relations:

$$d_f = \begin{cases} d_f^t, & \hat{\sigma}_{11} \geq 0 \\ d_f^c, & \hat{\sigma}_{11} < 0 \end{cases}$$

$$d_m = \begin{cases} d_m^t, & \hat{\sigma}_{22} \geq 0 \\ d_m^c, & \hat{\sigma}_{22} < 0 \end{cases}$$

$$d_s = 1 - (1 - d_f^t)(1 - d_f^c)(1 - d_m^t)(1 - d_m^c)$$

Once the damage initiation has been satisfied, material behavior follows a damage evolution behavior investigated by Lapczyk [13]. This damage evolution takes the form of linear material softening from the progressive damage in the material. This relationship is described graphically by:

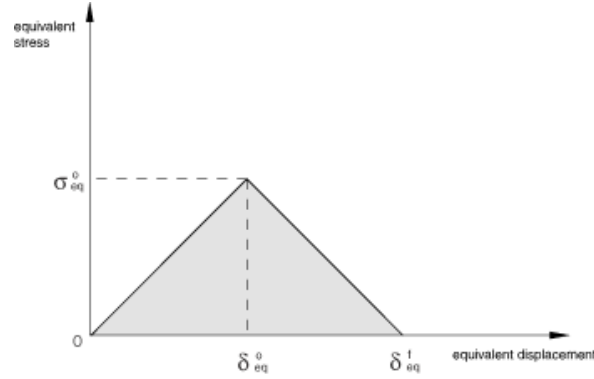


Figure 25. Traction-Separation with Linear Material Softening [77]

The linearly increasing stress-displacement relationship demonstrates the linear elastic behavior of the material prior to damage initiation, which occurs at a stress σ_{eq}^0 and strain δ_{eq}^0 . This is followed by damage evolution by one or a combination of the four modes discussed above, until damage is complete at failure displacement δ_{eq}^f . Determination of the failure displacement parameter again includes the element characteristic length, included to reduce mesh dependency. Failure displacements and stresses are given for each failure mode by

Fiber Tension ($\hat{\sigma}_{11} \geq 0$):

$$\delta_{eq}^{ft} = L^c \sqrt{\langle \varepsilon_{11} \rangle^2 + \alpha \varepsilon_{12}^2},$$

$$\sigma_{eq}^{ft} = \frac{\langle \sigma_{11} \rangle \langle \varepsilon_{11} \rangle + \alpha \tau_{12} \varepsilon_{12}}{\delta_{eq}^{ft} / L^c}$$

Fiber Compression ($\hat{\sigma}_{11} < 0$):

$$\delta_{eq}^{fc} = L^c \langle -\varepsilon_{11} \rangle,$$

$$\sigma_{eq}^{fc} = \frac{\langle -\sigma_{11} \rangle \langle -\varepsilon_{11} \rangle}{\delta_{eq}^{fc} / L^c}$$

Matrix Tension ($\hat{\sigma}_{22} \geq 0$):

$$\delta_{eq}^{mt} = L^c \sqrt{\langle \varepsilon_{22} \rangle^2 + \varepsilon_{12}^2},$$

$$\sigma_{eq}^{mt} = \frac{\langle \sigma_{22} \rangle \langle \varepsilon_{22} \rangle + \tau_{12} \varepsilon_{12}}{\delta_{eq}^{mt} / L^c}$$

Matrix Compression ($\hat{\sigma}_{22} < 0$):

$$\delta_{eq}^{mc} = L^c \sqrt{\langle -\varepsilon_{22} \rangle^2 + \varepsilon_{12}^2},$$

$$\sigma_{eq}^{mc} = \frac{\langle -\sigma_{22} \rangle \langle -\varepsilon_{22} \rangle + \tau_{12} \varepsilon_{12}}{\delta_{eq}^{mc} / L^c}$$

where the $\langle \ \rangle$ brackets denote the Macaulay operator, such that $\langle \alpha \rangle = (\alpha + |\alpha|)/2$.

When the material has reached the point of damage initiation, and $\delta_{eq} > \delta_{eq}^0$, the damage variable is calculated as a function of displacement, relative to the initiation displacement and the failure displacement along a linear path for one of the four modes mentioned above. This expression is:

$$d = \frac{\delta_{eq}^f (\delta_{eq} - \delta_{eq}^0)}{\delta_{eq} (\delta_{eq}^f - \delta_{eq}^0)}$$

The user inputs for this damage evolution criteria are the strain energy release rates for each failure mode. The strain energy release rate represents the area under the stress-displacement curve (Figure 25) and determines the value of δ_{eq}^f used in the evolution determination.

Once a single integration point in an element has reached the failure displacement δ_{eq}^f the element will be removed from the mesh according to the set user preferences.

2.5.2 Finite Element Formulation

Early numerical formulations of FMLs used 3D, linear, 8-noded, solid brick elements (C3D8) to represent metal layers in fiber-metal laminates. These formulations were often either elastic or elastic-plastic and included the 3-dimensional state to model through-thickness stress distributions. Later

formulations were able to realize computational efficiency gains by using a reduced integration scheme which only considers nodal strains relative to the element centroid. Composite layers were represented by quadrilateral, full integration S4 shell elements, for which usage assumes a state of plane stress. These elements contain the geometry of a 3D brick element, but are formulated with a 2D stress state, thus ignoring thru-thickness distributions. Seo, Hundley, Hahn, and Yang [81] conducted an extensive investigation on the use of continuum shell elements for impact loading, comparing outcomes to use of 3D solid elements. Using a new 3D formulation of the 2D Hashin failure criteria they were able to show that under certain conditions the 3D formulation for composite elements provides a more accurate representation of laminate impact behavior than the 2D Hashin criteria used with continuum shell elements. The difference between the two methods is highlighted in cases where thru-thickness effects are not negligible and the plane-stress assumption is no longer valid. The commercial finite element code ABAQUS contains an extensive library of elements and integration options that are beyond the scope of this work, therefore only the element formulations and options used for modeling low-velocity impact of TiGr will be outlined here. Since this is a dynamic test, ABAQUS/Explicit will be used. This version of the software is time history-based and solution dependent. That is, the integrated solution for a particular time period is dependent on the time period directly preceding it. This integration follows the algorithm defined by Hughes and Winget [82], and begins with the assumption of a Lagrangian frame, with stresses calculated at specific points coinciding with material quanta. The Explicit version of Abaqus uses a rate constitutive equation written in terms of a material time derivative, making time-discretization of the result a matter of simple integration [77]. The theory and constitutive models for integrating finite elements are beyond the scope of this research; however the element formulations specific to the numerical model of TiGr will be summarized.

2.5.2.1 Solid Elements

The 3-dimensional solid elements composing all of the materials used in this study are defined by 8-node hexahedral bricks. These bricks use interpolation functions to define elemental properties between nodes. Nodes are defined by their normalized coordinates relative to a centroidal point as shown

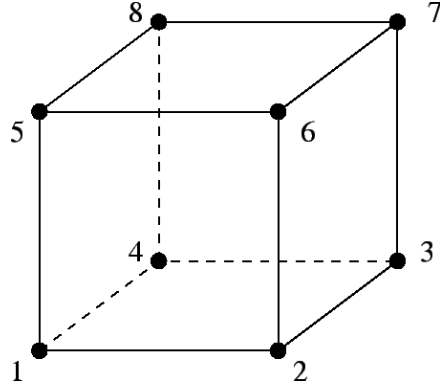


Figure 26. Hexahedral Element Configuration [77]

The interpolation function is given by:

$$\mathbf{u} = N^I(g, h, r)\mathbf{u}^I$$

where \mathbf{u} is the displacement vector, g , h , and r are the isoparametric elemental coordinates, and N^I is the isoparametric shape function:

$$N^I(g, h, r) = \frac{1}{8}\Sigma^I + \frac{1}{4}g\Lambda_1^I + \frac{1}{4}h\Lambda_2^I + \frac{1}{4}r\Lambda_3^I + \frac{1}{2}hr\Gamma_1^I + \frac{1}{2}gr\Gamma_2^I + \frac{1}{2}gh\Gamma_3^I + \frac{1}{2}ghr\Gamma_4^I$$

where

$$\Sigma^I = [+1, +1, +1, +1, +1, +1, +1, +1]$$

$$\Lambda_1^I = [-1, +1, +1, -1, -1, +1, +1, -1]$$

$$\Lambda_2^I = [-1, -1, +1, +1, -1, -1, +1, +1]$$

$$\Lambda_3^I = [-1, -1, -1, -1, +1, +1, +1, +1]$$

$$\Gamma_1^I = [+1, +1, -1, -1, -1, -1, +1, +1]$$

$$\Gamma_2^I = [+1, -1, -1, +1, -1, +1, +1, -1]$$

$$\Gamma_3^I = [+1, -1, +1, -1, +1, -1, +1, -1]$$

$$\Gamma_4^I = [-1, +1, -1, +1, +1, -1, +1, -1]$$

and I signifies the node of the element. The centroidal strain formulation only considers strain at the element center, then extrapolates this result to the element nodes using the following method. The gradient matrix, B^I , is given by:

$$B_i^I = N_i^I(0,0,0)$$

where the I denotes the element node, and i signifies the dimension with a range of 3. The element nodes are assumed to exhibit anti-symmetry according to the following arrangement:

$$B_i^1 = -B_i^7$$

$$B_i^3 = -B_i^5$$

$$B_i^2 = -B_i^8$$

$$B_i^4 = -B_i^6$$

This method of calculating the strains at the nodes of an element reduces computational expense, but also reduces the accuracy of the solution, as each nodal strain is not calculated explicitly, but is assumed based on the centroidal strains and material constitutive model. This loss of accuracy is most pronounced in elements with skewed geometry; therefore hexahedral parallelepiped geometry is recommended for elements using this integration scheme.

2.5.2.2 Cohesive Interactions

The constitutive formulation of cohesive elements can be described either in terms of a continuum, wherein the three-dimensional elements are described with a finite thickness and use similar material models to other solid continuum elements in Abaqus, or may use a traction-separation approach. This approach is useful for cases where the cohesive zone is very thin, or assumed to have zero thickness. Because this model uses cohesive elements to simulate bonding between graphite layers, the traction-separation approach is most appropriate for this work. These models are assumed to have linear elastic behavior prior to damage initiation, then assumes a progressive damage model similar to other material models.

The traction vector \mathbf{t} has components t_n , t_s , and t_t representing the normal, 1-direction shear, and 2-direction shear, respectively. If T_0 is the initial thickness of the cohesive element, nominal strains can be written:

$$\varepsilon_n = \frac{\delta_n}{T_0},$$

$$\varepsilon_s = \frac{\delta_s}{T_0},$$

$$\varepsilon_t = \frac{\delta_t}{T_0}.$$

Variables δ_n , δ_s , and δ_t represent measured displacements, or separations, in the normal, 1, and 2 directions, respectively.

Elastic behavior for these tractions can be described by the familiar matrix equation:

$$\mathbf{t} = \begin{Bmatrix} t_n \\ t_s \\ t_t \end{Bmatrix} = \begin{bmatrix} E_{nn} & E_{ns} & E_{nt} \\ E_{ns} & E_{ss} & E_{st} \\ E_{nt} & E_{st} & E_{tt} \end{bmatrix} \begin{Bmatrix} \varepsilon_n \\ \varepsilon_s \\ \varepsilon_t \end{Bmatrix} = \mathbf{E}\boldsymbol{\varepsilon}$$

This linear elastic behavior describes cohesive element behavior prior to damage initiation. The criteria for initiation of damage is described by the following equation, where t_n^0 , t_s^0 , and t_t^0 are the failure stresses in the normal, 1-direction shear, or 2-direction shear, respectively. The expression states that when the measured traction is equal to any one of the corresponding failure stresses, the damage initiation criteria is met.

$$\max \left\{ \frac{t_n}{t_n^0}, \frac{t_s}{t_s^0}, \frac{t_t}{t_t^0} \right\} = 1$$

After the initiation criteria is met, damage evolves according to the following set of expressions. These expressions describe the decrease in joint stiffness through the cohesive elements. The damage variable D represents the accumulation of all damage, and is described below.

$$t_n = \begin{cases} (1 - D)\bar{t}_n, & \bar{t}_n \geq 0 \\ \bar{t}_n, & \bar{t}_n < 0 \end{cases}$$

$$t_s = (1 - D)\bar{t}_s,$$

$$t_t = (1 - D)\bar{t}_t,$$

where

$$D = \frac{\delta_m^f (\delta_m^{max} - \delta_m^0)}{\delta_m^{max} (\delta_m^f - \delta_m^0)}$$

The effective displacement variable, δ_m , is given by

$$\delta_m = \sqrt{\langle \delta_n \rangle^2 + \delta_s^2 + \delta_t^2}$$

and this leads to δ_m^f as the failure value for effective separation, δ_m^{max} as the maximum measured effective separation, and δ_m^0 as the effective separation measured at damage initiation. In the expressions for damage evolution, \bar{t}_n , \bar{t}_s , and \bar{t}_t represent the stress components predicted by the linear-elastic behavior of the traction-separation law if damage were not considered.

In the above expression, the failure value for effective separation, δ_m^f is calculated using the Benzeggagh-Kenane method [66], which considers fracture energy (or strain energy release rate) in the constitutive directions by the expression:

$$\delta_m^f = \frac{2G^C}{T_{eff}^0}$$

where T_{eff}^0 is the effective traction at damage initiation, and G^C is described by

$$G^C = G_n^C + (G_s^C - G_n^C) \left\{ \frac{G_s}{G_T} \right\}^\eta$$

Where $G_S = G_s + G_t$, $G_T = G_n + G_S$, and η is an empirically determined material parameter. Strain energy release rates in the normal, 1-direction shear, and 2-direction shear are given by G_n , G_s , and G_t , respectively. These values are input by the user in the material definition card.

2.5.3 Numerical Modeling Discussion

Conducting accurate simulation of low-velocity impact of FMLs is complicated by the fact that multiple damage modes occur simultaneously and are highly sensitive to specimen geometry, boundary conditions, and impactor size and shape. Appropriate constitutive models must be employed for accurate representation of each material and interaction, as the overall simulated impact behavior is an amalgamation of unique element formulations. Factors such as laminate geometry, boundary conditions, and impactor geometry have been shown to influence the relative appropriateness of different material models, based on assumptions about stress state during the impact event. However, numerical models provide an invaluable representation of the internal stresses and modes of damage propagation within a laminate, often invisible in experimental work and not accurately represented in an analytical model. Literature reviewed indicates significant advancement in the individual formulations with many comparisons to experimental data showing good agreement. These are briefly highlighted below.

Nearly every author reviewed employed a combination of the above models for FML numerical models. Based on computational cost, the overall FML formulations can be broadly categorized into three groups [35]:

- Elastic-plastic metal formulation and composite lamina with no failure models
- Elastic-plastic continuum solid element metal formulation with continuum shell 2D (plane stress) Hashin failure model for composite layers.
- Elastic plastic continuum solid element metal formulation with continuum solid composite behavior employing user-defined 3D Hashin failure criteria.

These models are in order of computational cost, from least to most.

To determine appropriate material parameters to input for the above formulations, most authors relied on experimental data [6, 25-26, 30-32, 55]. Bulk material properties for aluminum or titanium metal layers as well as most fiber-reinforced thermoplastics or epoxies have been developed through rigorous experimentation. However, inputs for the interfacial bonds between the two materials are not always well known, as the manufacturing processes for some FMLs have not been standardized. Hundley, Hahn, Yang, and Facciano [25-26] conducted an extensive study on multi-scale modeling of the interfacial bonds between metal and composite surfaces, specifically between titanium and graphite fiber-reinforced polymer laminae. This study first investigated the surface chemistry and morphology of the titanium foils, subjected to a chromium-free sequential acid-base surface treatment. This process creates a uniform layer of titanium oxide on the surface of the metal, enhancing bond strength by providing increased surface area for bonding. The presence of this oxide layer was validated using spectral analysis, then modeled using the commercially available MD (Materials Studio) simulation program. The cross-linking interaction with composite layers was modeled at the molecular level to determine fracture energy, interfacial bond strength, and interfacial elastic parameters which are inputs to the traction-separation model described above. Once the interfacial parameters were estimated using the molecular simulation they were input into a larger continuum-scale model which could be compared to experimental data [25]. Using a similar formulation to the models described above, the model showed good correlation with experimental short-beam-shear data.

2.6 Analytical Modeling

In order to design real-world hardware using fiber metal laminates, it is necessary to have methods to predict behavior that can easily be extended to different materials, layups, thicknesses, and metal volume fractions. While classical laminate theory (CLT) provides a cursory look at laminate stiffness, predicting impact behavior is a more involved proposition. The major benefit of analytical impact models is that they are far less computationally expensive than numerical simulations. While they cannot provide the discretized details about damage initiation and propagation and their relative contribution to laminate degradation, they can provide initial results about laminate optimization or factors such as minimum thickness to prevent perforation. Having good analytical models of the nonlinear impact dynamics problem

with fiber metal laminates is one of the tools that will enable rapid prototyping of fiber-metal-laminate trade studies and use-case comparisons with other materials.

As discussed earlier, impacts occurring in real-world situations are roughly categorized into low-velocity and high-velocity (ballistic) impacts. From a morphological standpoint, low velocity impacts are assumed to occur over a longer period of time than the first mode shape of the impacted structure. Thus the stress wave propagation and higher-order vibration modes are ignored, and the material response can be approximated by quasi-static models. High-velocity impacts are characterized by three-dimensional stress waves that propagate through the thickness of the material as well as laterally from the point of impact. Since the time of contact is likely longer than the transition time for the through-thickness waves, the response is dominated by the lateral two-dimensional transverse shear waves. These waves propagate outward and become bending or membrane stress waves. They may not reach the material boundary before the panel is perforated by the projectile, since the time of contact is considered to be brief. The distinction between these two analytical types is significant, as the solution will be dependent on material variables that may be strain-rate dependent. Incorporation of the correct parameters will impact the validity of the analytical approximation.

Abrate [83] identifies four primary solution types for analytical impacts. Each type represents a mathematical approximation of the physical phenomena assumed to have morphological significance, and may give more or less accurate results depending on the loads and boundary conditions. The types are spring-mass models, energy-balance models, models based on Classical Plate Theory (CPT), and Mindlin's First Order Shear Deformation Theory (FSDT).

One of the first researchers to propose analytical model for FMLs was Vlot [37] who proposed a model for low-velocity impacts. The proposed model was a spring-mass model, based on governing differential equations of motion for an impactor of mass m_p impacting a plate of equivalent mass m_{eq} . Several simplifying assumptions were made about the model, the first being that contact was assumed to be rigid and constant. Another assumption was that the stiffness of the plate was constant regardless of deflection. This assumption was found to be valid as long as plate deflections are small. First the plate equivalent mass was calculated by considering the experimentally measured kinetic energy of the plate:

$$KE_{plate} = \frac{1}{2} m_{eq} \dot{w}_0^2$$

where w_0 is the deflection of the plate at the point of impact. It was found from experimentation that the equivalent mass of the plate was $\frac{7}{54}$ the total plate mass. With this ratio, it was now possible to solve the differential equation of motion:

$$m_{tot} \ddot{w}_0 + C w_0 = 0$$

where m_{tot} is equal to the sum of the impactor mass and the equivalent plate mass and C is the plate stiffness, calculated using CPT. Simple spring-mass models of this type were extended by Tan and Sun [42] to include a Hertz contact model to better represent transient contact stiffness between the impactor and laminate. For the quasi-static assumption, Hertz contact force as a function of time is represented by:

$$F(t) = k_c \alpha^{\frac{3}{2}}(t)$$

where α is the indentation as a function of time and k_c is the Hertz contact stiffness. Indentation is described as the measurement between the tip of the impactor and the surface of the laminate. Modified Hertz stiffness is given by $k_c = \frac{4}{3} E R^{\frac{1}{2}}$ with $\frac{1}{R} = \frac{1}{R_1} + \frac{1}{R_2}$ and $\frac{1}{E} = \frac{1-\nu_1^2}{E_1} + \frac{1-\nu_2^2}{E_2}$. Variables R_1 , E_1 , ν_1 and R_2 , E_2 , ν_2 represent the radius of curvature, modulus of elasticity, and Poisson's ratio of the impactor and laminate respectively. A shortcoming of this method is that it is only valid for initial impact of a laminate from the moment of impact until the time of maximum laminate deformation. Subsequent impacts after permanent indentation is already present are not considered. Thus a modified Hertz contact proposed by Sun and Tan [42] offered a way to consider existing indentation. During unloading the contact force would be represented as

$$F = F_m \left[\frac{(\alpha - \alpha_0)}{(\alpha_m - \alpha_0)} \right]^{2.5}$$

and during re-loading at the same point as the original indentation

$$F = F_m \left[\frac{(\alpha - \alpha_0)}{(\alpha_m - \alpha_0)} \right]^{1.5}$$

where F_m is the maximum contact force, α_0 is the permanent indentation, and α_m is the maximum indentation before the laminate begins to rebound after impact. Using this definition for contact between the impactor and laminate, Vlot [37] was able to use Von Karman strain displacement relations and the Newmark [43] numerical algorithm to demonstrate a nonlinear elastic model for low-velocity impact on an FML plate. It should be noted that in Vlot's work the Von Karman strains are simplified by ignoring in-plane contributions and assuming transverse strains are small compared to out-of-plane displacements. This is an accurate assumption for thin plates.

Energy balance models for low-velocity impacts of FMLs were investigated by Tsamasphyros [45, 48-49], who developed an analytical model for GLARE under quasi-static loading using a hemispherical impactor striking a circular laminate clamped at the edges. The impactor strikes the laminate and deflects the center of the plate downward until its velocity reaches zero, at which point due to the elastic strain of the laminate the impactor begins to move in the opposite direction until the load on the impactor is zero. This model assumes that the impact energy is high enough to cause large deformation of the laminate in the out-of-plane direction, yet not so large as to cause failure of the lamina due to tensile fracture. It also assumes that the aspect ratio of laminate thickness to width is sufficiently high that bending energy is considered negligible and all impact energy is absorbed by membrane resistance. This model also assumes shear deformation and local indentation are negligible. Tsamasphyros [48] identifies three stages of impact; loading before onset of delamination, loading after onset of delamination, and unloading. Each of these stages can be described by a governing differential equation of motion and associated initial conditions.

Loading stage prior to delamination:

$$(M_0 + m_e)\ddot{w}_0 + K_p w_0 + K_{el} w_0^3 = 0 \quad \text{initial conditions:} \quad w_0(0) = 0, \quad \dot{w}_0(0) = v$$

Loading stage after delamination onset until velocity of impactor reaches zero:

$$(M_0 + m_e)\ddot{w}_0 + K_p w_0 + K_{el} w_0^3 = 0 \quad \text{initial conditions:} \quad w_0(0) = w_0^d, \quad \dot{w}_0(0) = \dot{w}_{02}$$

Unloading:

$$(M_0 + m_e)\ddot{w}_0 + 2K_p w_0 + K_{el} w_0^3 - K_p w_0^{max} = 0 \quad \text{initial conditions:} \quad w_0(0) = w_0^{max}, \quad \dot{w}_0(0) = 0$$

In these equations, M_0 and m_e are the mass of the impactor and effective plate mass, respectively. The stiffness terms are derived from a Ritz method by Tsamasphyros [48] as:

$$K_p = 0.576N_x + 0.576N_y + 0.734N_{xy}$$

$$K_{el} = \frac{1}{\alpha^2} [0.62A_{11} + 0.62A_{22} + 0.412(A_{12} + 2A_{66})]$$

These stiffness are dependent on material parameters, where N_x , N_y , and N_{xy} are the in-plane forces in aluminum plies, derived from material parameters, and A_{ij} are stiffnesses of the graphite lamina. By solving these three initial value problems the three physical phenomena described can construct load and deflection history for the impact event. Each equation can be written in the form of a Duffing equation, which can be solved analytically using appropriate change of variables. Proceeding from this construct, the unknown variables w_0^d , \dot{w}_{02} , and w_0^{max} can be determined, allowing the differential equations of motion to be solved. Advantages of the method presented by Tsamasphyros are that delamination damage (or any such damage affecting extensional stiffness of the laminate) are considered in the analytical solution. Thus it is one of the only methods that considers a nonlinear solution without complete rebound from impact. This allows prediction of indentation damage in a purely analytical form.

Malekzadeh [44, 85] performed a similar analysis, assuming a spring-mass model with two degrees of freedom. In this case the two masses represent the impactor and the plate, respectively; x_1 and x_2 represent the displacements of each, and k_1 and k_2 represent the contact stiffness and the shear-bending stiffness.

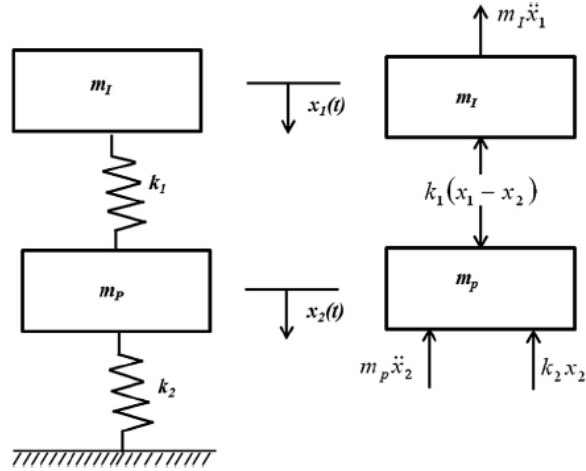


Figure 27. Spring-Mass Model of Impact to FML Plate

To determine the contact force, Malekzadeh [85] used Choi's [53] linearized model instead of the nonlinear Hertz contact used by Tan and Sun [42]. This model is as follows:

The force history is given as a linear relationship between contact force and indentation:

$$F = k_1 \alpha$$

where $k_1 = F_m^{1/3} k_c^{2/3}$

$$k_c = \frac{4}{3} \frac{R_2^{1/2}}{\left(1 - \frac{\nu_2^2}{E}\right) + \left(\frac{1}{E_{22}}\right)}$$

and R_2 is the radius of curvature, E is the elastic modulus of the impactor, E_{22} is the transverse elastic modulus of the top layer of the FML, and ν_2 is its Poisson's ratio. From the previous Hertz model, α is the measure of indentation as a function of time, also described by $(x_2 - x_1)$. With the contact force history, the equations of motion can be constructed from the free-body diagram of the 2 DOF system:

$$m_1 \ddot{x}_1 + k_1(x_1 - x_2) = 0$$

$$m_p \ddot{x}_2 + k_2 x_2 - k_1(x_1 - x_2) = 0$$

To solve for k_2 , the shear-bending stiffness of the plate, Malekzadeh [85] used the plate equations of Whitney and Pagano [86], with the shear correction factor suggested by Mindlin [87]. This results in a

stiffness matrix representing the specific layup, orientation, and thickness of the FML, along with the boundary conditions affecting shear-bending stiffness of the impact target. With this information, the system of differential equations can be solved using a numerical solver such as Matlab using the Runge-Kutta method. In his research Malekzadeh [44, 85] explored the effect of different layup sequences, different impact velocities for constant energy, and different laminate aspect ratios. However, this method neglects permanent damage from impacts and subsequent loss of laminate stiffness. Rotary inertia is also ignored, as well as membrane effect. These factors coupled with the linearization of the Hertz contact law limit the accuracy of this analytical method.

Abatan [54] proposed an analytical solution similar in many ways to the method proposed by Malekzadeh [85] using shear deformation theory and Mindlin's [87] shear correction factor to determine the stiffness of the laminate. However rather than using a spring-mass model with associated differential equations of motion Abatan proposed a double Fourier series representation of the applied impact force. By expressing this applied load as a rectangular wave, a sine wave, and a dirac delta function Abatan compared the response of the plate to different impact mathematical representations. These results were compared to numerical simulations using Ansys to verify their validity. It was found that the rectangular wave and sine wave compared favorably with numerical results, but that the Dirac Delta function differed significantly in predicted deflection of the laminate. It was therefore determined that this function is not a good representation of impact behavior. This numerical model only considered elastic behavior of the laminate, and fails once more to account for damage associated with impact.

These four analytical methods for describing impact behavior of FMLs are useful for describing differences in layup sequence, laminate thickness, metal volume fraction, and impactor energy and geometry. Because they are far less computationally intensive compared to numerical solutions, these trades can be made quickly and efficiently. Analytical modeling is a useful tool for optimization of laminates for a given condition, however the current analytical techniques fall far short from being able to model the actual physical phenomena associated with low-velocity impact. Most of these models are only valid in the elastic region of the impacted material, and most require assumptions to be made about displacement functions, contact formulation, and stress or strain components. Understanding the benefits and limitations

of current analytical techniques is vital to understanding how FMLs can be integrated into designs as engineered materials.

2.7 Discussion

FMLs have shown promise as a versatile new material system for composite part design. Their high specific strength, durability, and damage tolerance have been demonstrated through extensive testing in the laboratory environment. Through a long history of experimentation and iteration on lamina material selection and processing variables several FMLs have been qualified for commercial use in several aerospace applications. Industry confidence in these new material systems is reliant on continual progression on the body of knowledge supporting purported advantages of FMLs for specific design applications. To this end, analytical and numerical techniques are essential to the augmentation of experimental data. As material systems are designed, tested, modeled, and simulated, standardization of process becomes vital to their commercialization. As demonstrated by numerical modeling comparisons to experimental impact data, damage mechanisms and peak loads vary widely depending on specimen curing methods, edge trimming methods, and experimental setup. Fortunately, advances in numerical modeling methods have shown to be effective at predicting peak loads and damage propagation during impact events. These and other simulations will continue to be integral to the development of FML systems.

One of the challenges inherent to all FML systems is the duality of material parameters in close proximity, acting together as a single bulk material. Thin metal sheets are nominally isotropic, ductile, and have significantly positive coefficients of thermal expansion (CTEs). Composites, on the other hand, are highly orthotropic, brittle, and have much lower CTEs, or, in the case of graphite fibers, negative CTE values. Co-curing processes with laminates containing both of these materials thus necessarily induce thermal residual stresses in the laminate, complicating material behavior predictions. Additionally, metals have the advantageous property of being able to re-distribute stresses in areas of localized stress intensity, such as in the plastic zone ahead of a crack tip or near a localized stress concentration. This leads to greater impact resistance and decreased notch sensitivity under static loading. Composites, on the other hand, have higher notch sensitivity and are susceptible to delamination during out-of-plane loading, such as under impact. This exemplifies how FMLs attempt to leverage favorable properties of each of these

systems; the “fiber-bridging” effect of adjacent composites provides improved fatigue crack growth resistance compared to isotropic metal structures, while the metallic layers lend their increased energy absorption and plastic deformation properties to superior impact damage tolerance, relative to traditional composites.

While experimental efforts remain the principal source of new published data on different FML systems, rapidly evolving analysis techniques are improving the efficiency and speed at which different systems can be validated. Analytical techniques remain constrained by closed-form solutions that fail to consider the progression of damage that begins nearly at the onset of contact during impact events, yet remain useful as a low (computational) cost, efficient way to perform trade studies on different layups, lamina thicknesses, or materials. These methods all involve assumptions about displacement functions, linearization of contact laws, or states of plane stress in order to develop solutions that can be solved analytically. Depending on the geometry and conditions being considered, these assumptions may adversely impact the prediction. Recent developments by Moriniere [68] have begun to consider damage in a complex analytical form, yet still involve assumption of a deflection profile and neglect to consider transverse stress components, restricting its usefulness to thin laminates. Numerical methods, though they suffer from computational cost, offer a comprehensive view of damage progression during impact loading. Varying degrees of constitutive model complexity may yield differing results, and as with any numerical techniques the correct application of these models is key to developing numerical models that match experimental data. Nevertheless, established individual methods for modeling metal strain-rate dependency, composite fracture, and interfacial cohesion have shown good agreement in both meso and continuum scales. These favorable results have been extended to investigate effects of boundary conditions, impactor geometry, and impact velocity.

As the aerospace industry continues to develop materials that can satisfy the ever-increasing demands for increased strength and durability, decreased weight, and improved manufacturability, FMLs have seen increasing interest and applicability. Numerous experimental [2, 6, 19, 21-24, 30-33], analytical [37, 42, 44-45, 48-49, 53-54, 83, 85], and numerical [6, 25-28, 30-32] studies have been carried out over the last two decades to better understand the broad range of options available with this unique material

system. As niche applications seek out high-performance materials with superior impact resistance and high specific strength the development of analysis techniques for FMLs will be vital to their commercialization. Low-velocity impact damage tolerance is a property of considerable importance to the aerospace industry, and complete understanding of each damage mechanism's initiation and propagation will continue to be a topic of great importance with any new material. This review summarizes much of the current work in low-velocity impact characterization and indicates that as new numerical tools are developed and integrated into commercial FEA codes the use of these models will gain widespread applicability to FML design and analysis.

CHAPTER 3: RESEARCH SCOPE AND OBJECTIVES

3.1 Scope of Research

Out of the many favorable properties of TiGr, the characterization of damage tolerance is least covered by existing literature. The scope of this research is to conduct a controlled set of low-velocity impact tests on TiGr specimens, then use visual inspection as well as impact force and displacement data to investigate damage propagation. Then, numerical modeling techniques will be used to simulate the experimental impact tests, using force and displacement as well as published material data to tune the model so the force-displacement plots match. By investigating different damage mechanisms in the numerical model that are otherwise not visible inside experimental specimens, more will be learned about how TiGr specimens behave under impact loading and how visible damage correlates to internal or non-visible damage. The following process map defines how experiments will be conducted, and how the information will be synthesized.

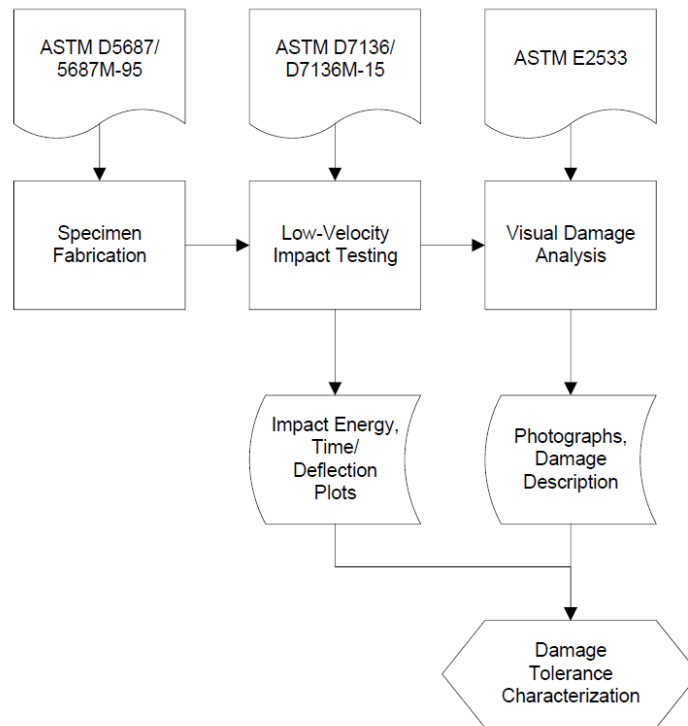


Figure 28. Process Methodology for Damage Characterization of TiGr

Final characterization of damage tolerance will include both qualitative and quantitative measures. Different failure mechanisms will be illuminated by the inspection data and described in terms of delamination area, metal fracture, metallic plastic deformation, matrix cracking, and fiber breakage. Compression data will yield measures of strength degradation compared to an un-impacted plate, and will seek to draw conclusions about how different damage contributes to this reduction in strength. The totality of these observations will inform the engineering community about TiGr's strengths and shortfalls in the area of damage tolerance, and will aid in TiGr's selection for specific engineering applications.

3.2 Research Goals & Objectives

Goal: Develop design space for study of TiGr low-velocity impact behavior.

Objective: The intent of this research is to characterize the failure mechanisms of TiGr when subjected to low velocity impacts. Ply sequence, titanium thickness, and impact energy may all affect these mechanisms. This work will seek to measure the effect of each major variable on the overall damage when a range of different impact energies are experienced.

It is expected that fracture behavior will differ significantly based on the percentage of titanium used in the laminate. For this reason, Metal Volume Fraction (MVF) as defined in Chapter 1 will be used as a metric for different material system configurations. First, laminates with titanium face sheets only will be investigated. Then, internal titanium plies will be added and the effects of scale and dimension will be investigated. Finally thick laminates using multiple plies of titanium and composite will be simulated to differentiate between thick and thin material systems. Of particular interest is the transition from membrane-effect dominated fracture behavior to shear-dominated failure modes. It is expected that the relative contributions of different damage mechanisms will shift as laminates get thicker and incorporate more metal layers; this will be demonstrated using numerical modeling techniques.

Goal: Manufacture test specimens according to test plan

Objective: The following activity will be to establish a process by which the samples should be manufactured. To reduce testing variance, all samples should be prepared in the same facility using the same materials and methods. ASTM D5687/5687M-95 entitled "Standard Guide for Preparation of Flat

Composite Panels with Processing Guidelines for Specimen Preparation” provides a step-by-step guide for preparing specimens for testing. Though the specification is technically limited to fiber-reinforced organic matrix composite prepregs, the methodology will be identical for TiGr, with the addition of preprocessing steps of titanium sheets for good adhesion to the polymer matrix. This document will thus be used as a reference when fabricating the composite specimens.

Goal: Develop a numerical model simulating TiGr impact behavior

Objective: In parallel with the physical testing of the samples, a finite element model has been created to predict the behavior of TiGr under different impact energies. This code can be easily manipulated to vary the properties of the laminate plies and their sequence, thereby providing a reference and comparative constitutive context for description of the experimental results. A representative benchmark sample of the specimens will be numerically modeled to prove the accuracy of the model. These results will be directly compared to the results of the physical testing, and will show the extent to which a numerical simulation can predict behavior of fiber-metal-laminate impact behavior. Preliminary results of such numerical simulations will be presented in the next section. As test data becomes available, the material models for the numerical model components will be adjusted and results compared with test data.

Goal: Test samples in accordance with established procedures for composite impact testing

Objectives: ASTM D7136/D7136-M-15 entitled “Standard Test Method for Measuring the Damage Resistance of a Fiber-Reinforced Polymer Matrix Composite to a Drop-Weight Impact Event” provides a step-by-step guide for impact testing of composite specimens. Although this specification is limited to testing of fiber-reinforced composites only, the methodology is easily applied to hybrid fiber-metal laminates. Reasonable modifications to this test method will be made to utilize available drop-testing equipment at the University of Washington.

Goal: Compile test results, compare with numerical models, and present findings.

Objective: Because the damage behavior of TiGr is described by a number of complex interacting mechanisms, the results of the impact testing must be examined by considering both inspection data and residual strength data. Failure modes will be identified in the inspection data, and the residual strength

data will be coupled with these modes to understand the contribution of each particular failure mode to the overall impact resistance of the laminate. The numerical model will provide an additional tool to fill in any gaps in the experimental data and to provide additional information about trends in impact performance that were not explicitly tested. Because additional titanium thicknesses and ply sequences can be quickly modeled and simulated, more data can be generated at low cost once the model has been validated against the experimental results.

CHAPTER 4: METHODS OF APPROACH

In this chapter, tests conducted are analogous to industry-accepted standard tests for traditional composite materials. Therefore, these very industry standards will be used as the general model for testing of TiGr. The idea is to minimize bias and the improve repeatability of these tests, providing the industry standards are accurately followed. The standards are cited as references to this research, but their content is summarized here, highlighting the material pertinent to these specific experiments. In some instances experimental data from literature was used as a basis for simulation; in these cases the experimental procedures used in the literature reference are summarized, as are the general numerical methods used for simulation.

4.1 Specimen Preparation

4.1.1 Industry Standard

The process for preparation of flat composite panels is outlined in ASTM D5687/D5687M-95. This document describes the needed equipment and steps taken to ensure uniformity and repeatability of specimens. The process is described in eight steps, according to the following flow chart:

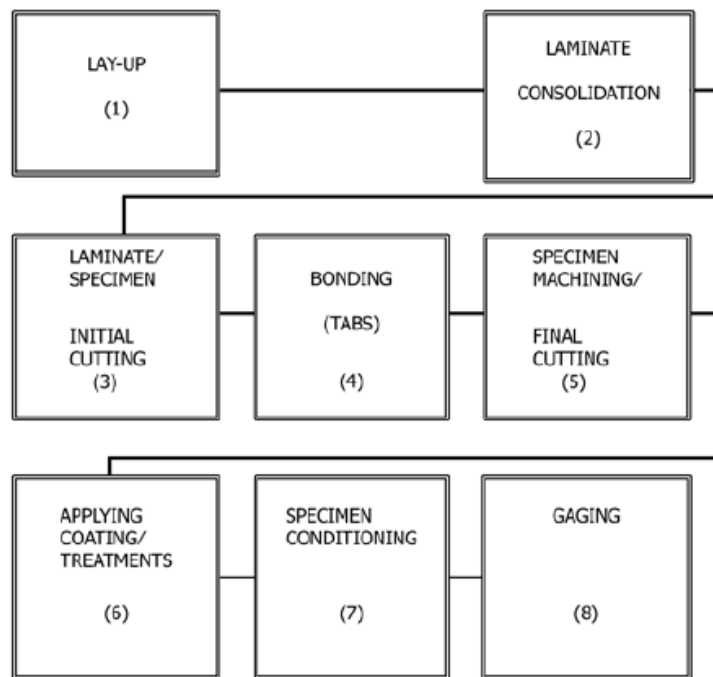


Figure 29. Specimen Preparation Flow Chart

The first step is the layup of the laminate in the ply stacking sequence specified. The ASTM specification stresses the importance of cleanliness in the work area. No dirt or dust shall be visible on the work surface, and care shall be taken to not contaminate the materials with oils or other contaminants on hands or tools. Next, the dimensions of the panel shall be considered. To minimize differences between samples, it is desirable to make all specimens of a particular stacking sequence from the same laminate panel. Additionally, the specimens should be randomized within the panel area, and the outermost edges of the panel should be discarded. ASTM D5687 recommends that the outermost 15 mm be discarded from each panel, therefore this should be considered when determining panel size. The specimen dimensions for impact testing are specified in ASTM D7136, and comprise a rectangle 100 x 150 mm as shown in the graphic below:

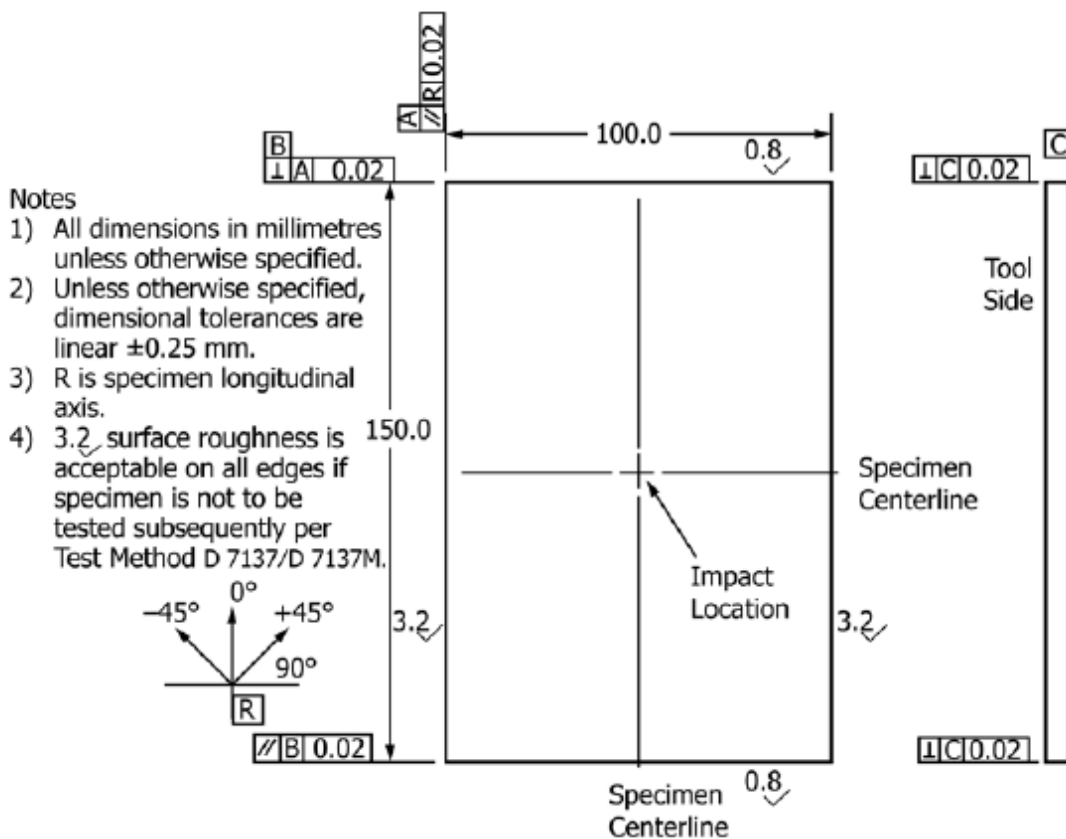


Figure 30. Impact Specimen Dimensions

The laminate layup shall be done according to the following instructions. The base plate shall be flat to a tolerance of 0.05 mm / mm² and a surface roughness of 0.8 μm. The plate shall be coated with

a mold release agent to prevent the laminate from sticking, and shall be large enough so that the laminate and other layup materials are completely supported, with adequate margin around the edges. The general technique used to control resin flow in the laminate is illustrated below:

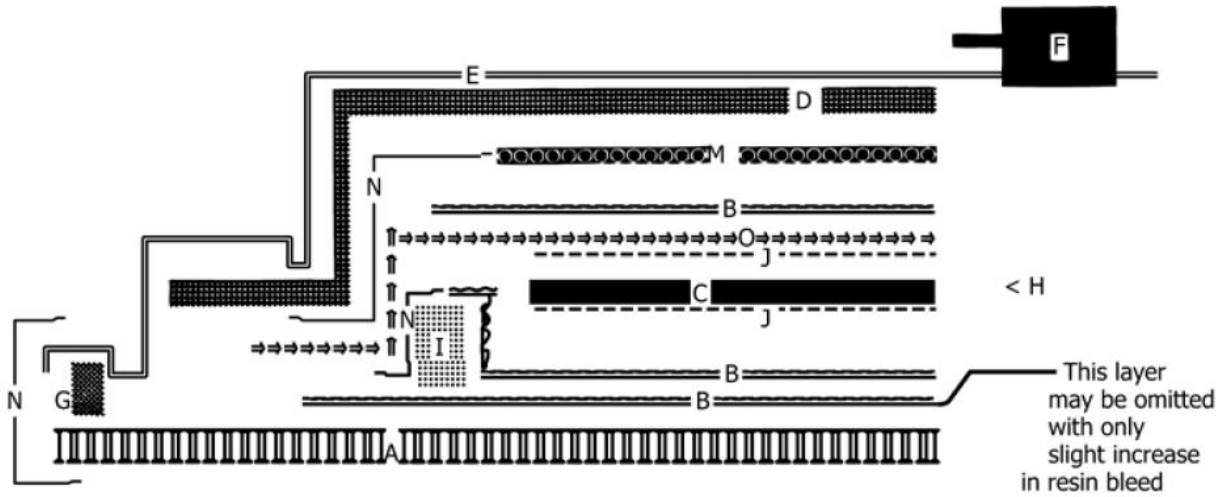


Figure 31. Layup Schematic

A	Base Plate
B	TFE Film
C	Laminate
D	Air Breather
E	Vacuum Bag
F	Vacuum Coupling
G	Sealant
H	Thermocouple
I	Dam
J	Peel Ply
M	Caul Plate
N	High Temperature Tape
O	Breather String

Figure 32. Layup Schematic Legend

Several layup techniques are illustrated in ASTM D5687, however the technique shown above is the only configuration that allows minimum horizontal resin flow from the panel, while providing thickness consistency using the caul plate. The titanium layers prevent vertical resin flow, therefore all resin flow will be in the lateral direction, and will be restricted by the dams.

As the plies are stacked in sequence with the other layup materials, each ply shall be checked for defects including fiber breaks, drags, or pulls. These defects have an effect on the final properties of the laminate, and must be avoided. As each ply is added to the stack, bubbles or voids can be avoided by using a roller or spatula to make sure contact is even between each successive ply. Defects that may be recurring, such as may occur in a roll of unidirectional tape, may be distributed by flip-flopping the ply layers 180 degrees so the recurring defect doesn't fall in the same spot in the stacking sequence. As plies are stacked, the debulking process must be used to ensure uniform fiber density and to discourage porosity. Debulking is the process of compacting a stack of plies using vacuum pressure so that interlaminar voids are reduced. A caul plate is placed on top of the stacked laminate on the base plate with a top sheet of rubber or nylon. Vacuum pressure pulls the caul plate down onto the laminate, squeezing plies together. This process should be done once for each 2.5 mm of laminate thickness.

The layup process for TiGr is slightly different than that of traditional CFRP due to the impervious layer of titanium on the top surface of the laminate. For this reason some features of the CFRP layup may be irrelevant or need to have their configuration altered. Breather strings allow gasses and other volatile materials to escape from the laminate during curing, however placing a breather string along the top of a TiGr laminate may be unnecessary. This feature may be more useful at the periphery of the laminate to allow volatile compounds to escape from the middle CFRP layers. Similarly, the flow of resin in TiGr will be primarily lateral, therefore any layup techniques involving bleeders that would allow vertical flow are irrelevant. Instead, dams and non-porous TFE should be used to control lateral flow at the perimeter. When dams are used, their height should be such that they border the edges of the caul plate. Any mismatch in height between the dams and the caul plate can cause concavity in the laminate, leading to unequal specimen geometry.

The next step in the specimen preparation process is the laminate consolidation. This process involves applying pressure to the laminate using either a press or vacuum bag and autoclave. The exact recipe for pressure and heat applied to the laminate varies by material. For Hexply IM7/8552 as an example, the cure cycle is shown in the following graphic:

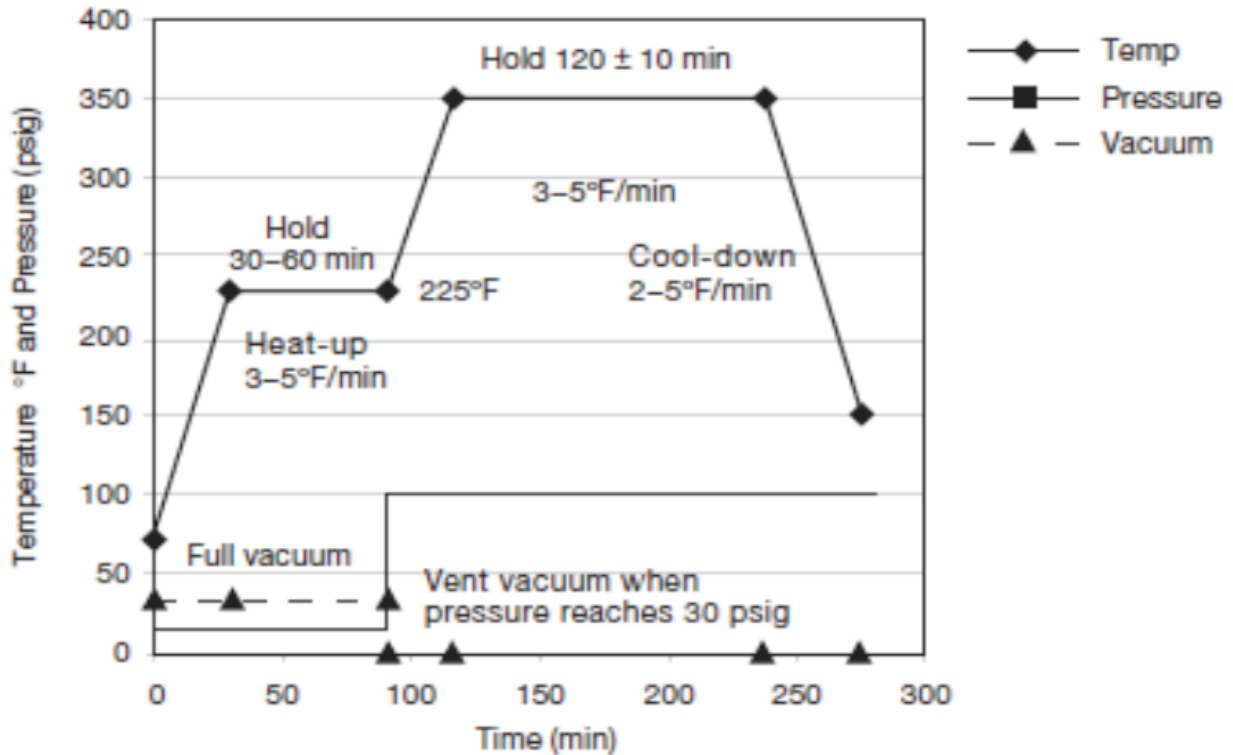


Figure 33. Cure Cycle for Hexply IM7/8552 Epoxy Matrix

The specific autoclave instructions are:

1. Apply full vacuum and 15 psig pressure
2. Heat at 3 – 5°F/min to 225°F
3. Hold at 225°F for 30 – 60 minutes
4. Raise pressure to 85-100 psig;
5. Vent vacuum when pressure reaches 30 psig
6. Hold at 350°F for 120 ± 10 minutes
7. Cool at 2 – 5°F/min to 150°F and vent pressure

During consolidation one of the most important aspects that determine the quality of the finished product is the flatness of the baseplate, caul plate, or press platens such that the laminate thickness is constant and smooth. Parallelism tolerance between the caul plate and base plate shall be 0.3 mm over the area of the laminate. Vacuum ports shall not be placed over any part of the laminate. If it is necessary to position a vacuum port over the laminate, material within a 25.4 mm radius of the port shall be discarded.

The third step in specimen preparation is the cutting of the laminate into individual specimens. Because no tabs will be bonded to these specimens, the initial cutting is also the final machining step in the preparation process. The preferred method of initial cutting is abrasive waterjet, followed by an inspection of the specimen edges to determine edge quality. Because edge effects are not expected to play a significant role in either low-velocity impact resistance or compression-after-impact testing, tight tolerances suggested by the ASTM specification can be relaxed to those of initial cutting (taper of less than 0.015 mm/mm of specimen length and microcracking evident by no more than 0.2 cracks/mm at a magnification of 50x on the cut edge).

No coatings or surface treatments will be used with the TiGr specimens.

No specimen conditioning requirement exists for these specimens.

No strain gauging requirement exists for these specimens.

The report generated during the manufacture of these test specimens shall include the following components:

- The date(s) and location(s) of the preparation steps.
- The name(s) of the individual(s) involved in specimen preparation.
- Any variations to the practice outlined in ASTM D5687/D5687M-95, anomalies noted, or equipment problems experienced.
- Identification of the material including: material type, material designation, age of material, manufacturer or other source, manufacturer's lot or material tracking number, tow or yarn filament count, sizing, form or weave, fiber areal weight, matrix type, and prepreg matrix content.

- Description of the fabrication steps including: fabrication start date, fabrication end date, ply orientation stacking sequence, laminate consolidation cycle, consolidation method, and equipment used.
- Average ply thickness of the consolidated laminate.
- Method of preparing the test specimen, including specimen geometry, coupon cutting method, and fixtures or equipment used.
- Calibration dates and methods for measurement devices.
- Results of any process checks including both destructive and non-destructive evaluation.
- Method of specimen identification.

[ASTM D5687/D5687M-95]

4.1.1 Experimental Specimen Preparation

For this body of work the specimen material (laminate) had been fabricated at an aerospace company at a prior date. Specific layups and specimen preparation methods of different laminates cited and simulated in this research are summarized below:

Drop tests conducted by Bernhardt [16] at the University of Washington focused on the effect of titanium face sheets on the impact behavior of composites. The layups were symmetric, consisting of titanium sheet, 0 degree plies, and 90 degree plies in the following order: [Ti/0/90/0/0/0/0/90/0/Ti]. Titanium Ti6Al4V was used, along with unidirectional IM6 graphite fibers pre-impregnated with PIXA-M high temperature thermoplastic resin. All layers of this laminate were nominally 125-130 μm thick. Titanium face sheets were preferred because the primary mechanism for energy dissipation in the low-velocity impact test is plastic deformation of the titanium layers. Having these layers on the outside of the laminate made characterization of this energy dissipation easier. The other TiGr failure modes during impact included debonding between the titanium and GFRP plies, matrix cracking, fiber fracture, and interlaminar delamination. The interface between 0 degree plies and 90 degree plies served to demonstrate the effect of titanium plastic deformation on interlaminar delamination, as well as to illustrate the “fiber bridging” effect of fibers running transverse to titanium crack propagation [2].

The next body of experimental data focused on evaluating the effect of different edge trimming operations on the flexural properties of TiGr laminates. V. Isvilanonda conducted this study using EDM (electrical discharge machining) and AWJ (abrasive water jet) processes to trim specimens prior to 3-point bend flexural testing. Specimens were fabricated according to the following layup: {Ti, 90, Ti, 0, 0, Ti, 90, Ti} resulting in a laminate that was approximately 1.00 mm thick. The titanium alloy used was 15-3-3-3, and the thermoplastic composite lamina used IM7 carbon fibers with PIXA-M resin. Specimens were trimmed to final dimensions of 9.55 mm x 70.00 mm using either EDM or AWJ, and using either rough or fine parameters for each method. In all, 6 specimens were fabricated using each method, resulting in a total of 12 specimens tested. The following table highlights the machining parameters used to prepare EDM and AWJ specimens using either rough or fine parameters.

Table 5. TiGr Specimen Edge Trimming Parameters

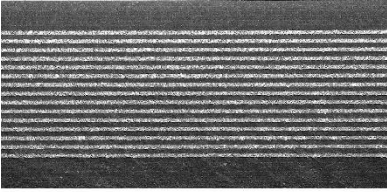
Die-sinker EDM	AWJ
Model: Hansvedt Benchman Die-sinker EDM Machining Parameters: Percent on-time: 50% Gap spacing: 4 Servo speed: 1 Cut off: 3 Fault retract: 5 Cycle EDM: 8 Cycle retract: 8 Capacitor: 0 Generator type: M-pulse Positive tool: Copper Work piece: Titanium	Model: Flow Waterjet Pro Machining Parameters: Abrasive grit size: 80 Orifice diameter: 0.381 mm Nozzle diameter: 1.02 mm Nozzle length: 76.2 mm Water pressure: 276 MPa (40 ksi)
Rough machining: Peak current 11A, pulse on-time 200 μ s (cutting time: 55 minutes) Fine machining: Peak current 4A, pulse on-time 25 μ s (cutting time: 230 minutes)	Rough machining: Traverse speed 720mm/min, abrasive flow rate 3.53g/s (cutting time: 13.3 s) Fine machining: Traverse speed 60mm/min, abrasive flow rate 9.78g/s (cutting time: 159 s)

Finally, the specimens used for the experimental portion of this work were supplied by an aerospace company. A total of 15 specimens were cut from the same laminate using several edge trimming methods as described in [] and were labeled t1 thru 15. Specimens were 70 x 12.5 mm, and were approximately 7.56 mm thick. The following tables contain information about the layup and constituent materials.

Table 6. Specimen Geometry and Layup

Thickness (mm)	Ply designation	Ply thickness (μm)	Number of plies	Layup
7.56	Ti	140	24	[(45/0/-45/45/0/-45/Ti/0/Ti/45/Ti/-45/Ti/45/Ti/0/Ti/-45/Ti/45)/Ti] _s
	0	210	12	
	45	210	10	
	-45	210	12	

Table 7. Properties of Constituent Materials

Optical micrograph	Material	Properties
	Titanium alloy (Ti-15V-3Cr-3Al-3Sn)	33.75 GPa (Shear modulus) 875 MPa (Shear strength)
	Graphite/PEEK	8.9 GPa (Transverse modulus) 80 MPa (Transverse strength)

The specimens were trimmed using an abrasive water jet (AWJ) system with pressure levels set at either 200 MPa or 350 MPa. Cutting traverse speed was also varied at 3 different rates; 2.12, 10.58, and 21.17 mm/s. These parameters were varied to determine their effect on surface roughness, and subsequently the effect of surface roughness on impact behavior.

Table 8. AWJ Experimental Conditions for TiGr Specimens

Parameter	Description
Abrasive	Garnet, mesh 80
Abrasive flow rate	6.05 gram/s
Impact angle	90°
Standoff distance	2.8 mm

Nozzle	Tungsten carbide length 101.6 mm diameter 0.889 mm
Orifice	Ruby diameter 0.33 mm

All specimens were trimmed solely using AWJ except for specimens t11 and t12. For these specimens one side was trimmed using conventional milling techniques, and the other side was trimmed using AWJ with 350 MPa pressure and 21.17 mm/s traverse rate. Conventional techniques used a four-fluted, uncoated carbide end mill with a 30° helix angle. For specimen t11 the feed rate was 10.6 mm/s and spindle speed was 6000 rpm; for specimen t12 the feed rate was 0.85 mm/s and the spindle speed was 6000 rpm. Prior to impact the surface roughness was measured using a Keyence VR3100 3D measurement system optical profilometer with resolutions of 7.39 μm in the x and y directions and 100 nm in the z direction. The results of these roughness measurements are presented in the next chapter.

4.2 Experimental Analysis of Impact Panels

4.2.1 Industry Standard Data Collection

The apparatus for data collection used during a typical impact test is described in ASTM D7136/D7136M-15, and is summarized here in relation to these experiments. The test specification outlines the specimen geometry, tooling necessary for properly securing the specimen during testing, and the appropriate instrumentation for data collection. Properly following the method outlined in this specification ensures repeatability and reliability of test results. Again, data collected for this research varied from the prescribed methods in the ASTM specification. For each cited body of work and for the experimental work done in this research the specific test setup will be outlined.

Specimens of the geometry presented in section 3.1 are constrained in a square fixture with a rectangular hole, as shown in Figure 3.5.

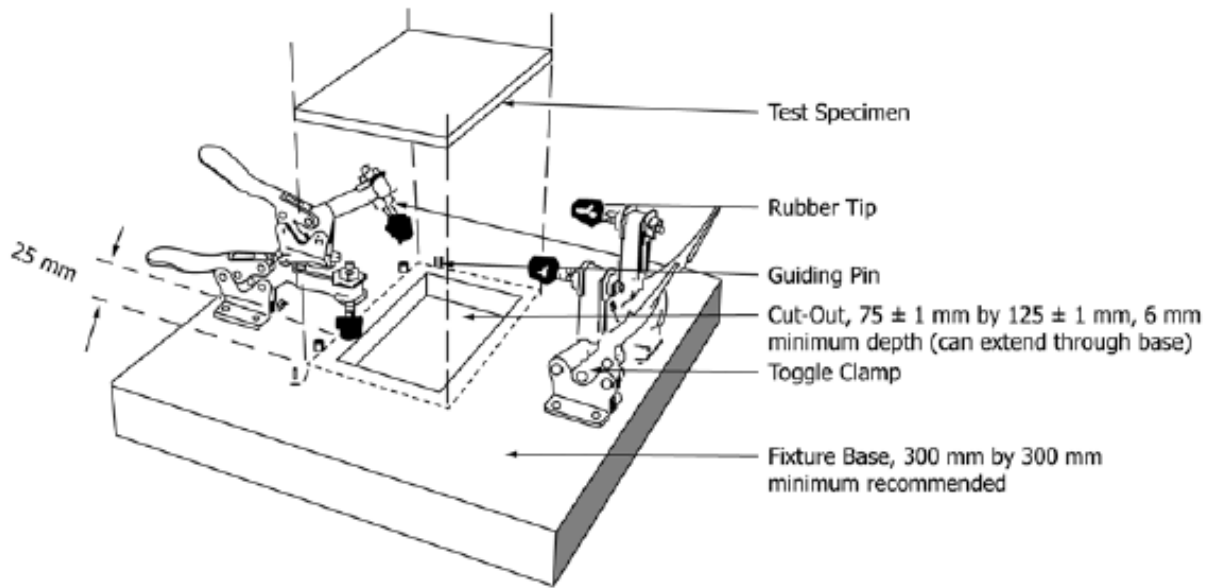


Figure 34. Test Fixture for Impact Testing

Installed in this fixture, the specimens will experience a constrained edge with an unsupported center measuring 75 x 125 millimeters. The impact will be centered in this unsupported region. The construction of this support fixture, the rigidity of its construction, and the clamping force applied at the edge of the specimen may impact the test results, therefore the following guidelines should be followed in its construction. The fixture base should be aluminum or steel, and should be at least 20 mm thick. The cut-out shall be 75 ± 1 mm by 125 ± 1 mm. The part of the base fixture top face that contacts the specimen should have a flatness tolerance of 0.1 mm. Four clamps should be used, applying a clamp force of at least 1100 N, and shall have tips made of neoprene rubber with durometer of 70-80.

This square fixture is typically constrained within a larger impact test stand, as shown in Figure 3.6.

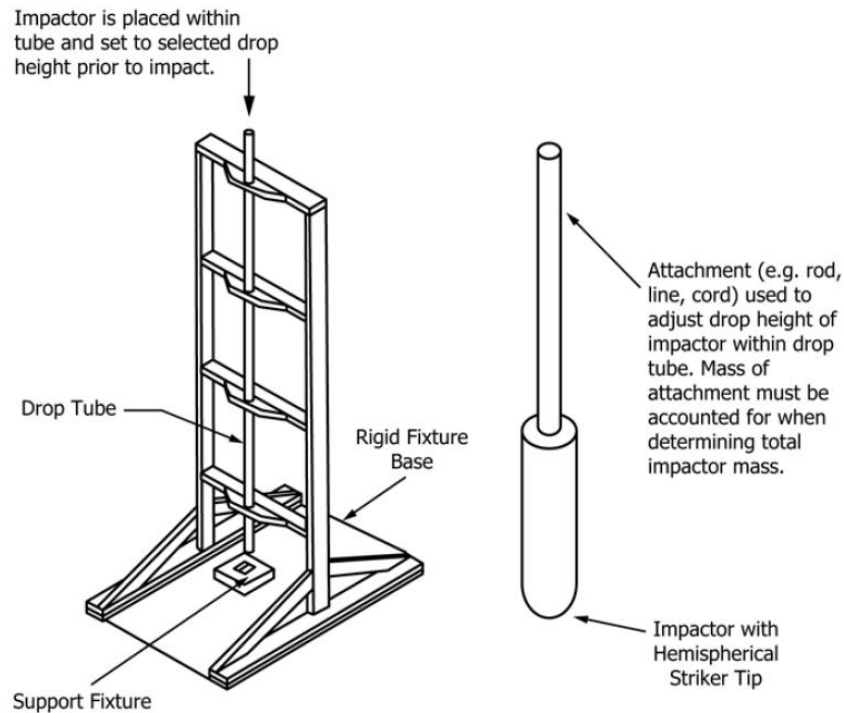


Figure 35. Impact Test Stand and Hemispherical Impactor Geometry

The impactor should have a mass of 5.5 ± 0.25 kg with a hemispherical tip with a diameter of 16 ± 0.1 mm. and a hardness of 60 – 62 HRC. This mass may have to be tailored to the laminate being tested, however, to ensure the specified impact energy is obtained while maintaining a minimum drop height of 305 mm. Other characteristics of the impact test fixture should include guide rails to insure that the impact is repeatable and targeted, and an automatic rebound catcher designed to arrest movement of the impactor after the initial contact.

Instrumentation necessary for impact testing includes force gauges, velocity indicators, and dent gauges as appropriate. The purpose of the force gauges is to measure force imparted to the specimen during impact, therefore the load cell should be positioned so that at least 95% of the impactor mass is above the cell to minimize error. Velocity indicators are only needed if it is determined that guide rail friction plays a measureable part in impact energy. If guide rail friction is not negligible, impact energy is calculated using measured velocity. This data is recorded using a data acquisition unit with an 8-bit analog-to-digital convertor and a minimum sampling rate of 200 kHz. Dent gauges are used after impact as a quantitative measure of plastic metal deformation and composite damage. Other ancillary equipment may be necessary

to facilitate accuracy of data collection. This equipment may include scales for measuring the impactor mass to within 0.5%, micrometers or calipers for verifying sample dimension, and environmental chambers for controlling conditioning of composite samples.

4.2.2 Industry Standard Experimental Approach

For each specimen, data recorded shall include any deviations or anomalous test conditions that could affect data quality. These notes shall be included with the test report.

After the specimens have been fabricated, and before they are impacted in the test rig, each specimen must be inspected to detect any flaws that exist prior to impact. This inspection shall include both a visual component and a NDI (non-destructive inspection) component such as thru-transmission ultrasonic (TTU) or x-ray. The visual inspection will identify any surface defects, while the ultrasonic or x-ray inspection will identify internal delaminations, cracks, voids, or fiber fracture. It is important that the specimens are inspected prior to impact to avoid inadvertently attributing pre-existing defects to the test condition. Any defects shall be recorded in the test notes with the defect type, location, and size identified.

Specimen length, width, and thickness shall be recorded for each specimen prior to impact. Length and width measurements shall be taken in two locations on the specimen using calipers, and thickness shall be measured in four locations on each specimen using micrometers. These measurements may be recorded as the average of the individual values, and shall be recorded to three significant figures in units of millimeters.

Because specimen conditioning is not within the scope of this work there are no specific conditioning requirements, however the environment during testing should be the same as the environment during specimen storage and manufacture, to prevent environmental factors from influencing data quality.

After the specimen has been inspected and measured, the impact test fixture can be prepared. The hemispherical striker tip can be installed and the added mass can be weighed using a laboratory scale. The sum total of the impact striker tip and any added mass (including any instrumentation or load cell) shall be recorded for each drop event, measured to a 0.5% precision.

When the test rig is ready, the specimen can be installed. The specimen shall be positioned so it is centered over the rectangular hole. For non-symmetric layups, it is important to verify that the specimen is oriented with the correct side facing up, as specified in the test matrix. The clamps shall be secured so clamping force is applied roughly 25 mm from the specimen edges.

The drop height can now be calculated from the desired impact energy. This calculation is based on the potential energy of the impact mass, which is given by

$$E = C_E h$$

where E is the potential energy of the impactor in Joules, C_E is the ratio of impact energy to specimen thickness (6.7 J/mm), and h is the nominal thickness of the specimen, as recorded previously. The drop height can then be calculated as:

$$H = \frac{E}{m_d g}$$

where H is the drop height in meters, E is the potential energy, m_d is the mass of the impactor in kg, and g is the gravitational constant, 9.81 m/s².

Once the drop height is calculated, the impactor can be raised to this position. Once the height has been checked, the impactor can be dropped so it impacts the specimen with a single blow. Rebound impact can be prevented using a rebound “catch” mechanism or by sliding a piece of rigid material such as wood or metal between the impactor and the specimen after rebound and before the impactor strikes a second time.

During this impact event, the data system shall record at a rate of at least 100 kHz, with at least 100 data points being recorded during the impact event. If velocity measurements are taken, this data shall be recorded as well to validate the impact energy calculations above. The force vs time curves should clearly show impact initiation as the first non-zero force measurement, followed by an increasing load with a single overall maximum, denoting a single strike. Smaller, localized peaks may be evident, indicating damage in the laminate as local stiffness is degraded.

Finally, once the data has been saved and the system is at rest, the specimen can be removed from the test rig. A visual inspection will then be conducted to note damage modes and locations. Some general notes on the specimen condition will be made, with a more complete evaluation described in the next section. It shall be noted if significant damage occurs in a location other than the impact, as this may indicate support system effects. If a number of specimens exhibit such damage, the support apparatus will be examined to ensure proper alignment and positioning of the impactor and specimen.

4.2.3 Industry Standard Data Reduction

A number of different variables are important to properly describe the impact. The method by which raw data is collected and processed has a significant effect on the quality of the measurements, and to whether the damage is accurately characterized. Therefore the ASTM 7136 standard for impact data collection shall be followed exactly. Plots will be generated showing impactor velocity vs time, impactor displacement vs. time, and absorbed energy vs. time.

The impact velocity is measured just prior to impact commonly using a double-prong flag system. Many of these systems calculate velocity directly, however the value can be obtained manually by:

$$v_i = \frac{(W_{12})}{(t_2 - t_1)} + g \left(t_i - \frac{(t_1 + t_2)}{2} \right)$$

In this equation, v_i is the impact velocity, W_{12} is the distance between the two prongs on the detector, t_1 is the time the first (lower) flag prong passes the detector, t_2 is the time the second (upper) flag prong passes the detector, and t_i is the time the impactor makes first contact with the specimen, as indicated by the first non-zero value on the force vs. time curve. The actual impact energy is then calculated simply from:

$$E_i = \frac{mv_i^2}{2}$$

where E_i is the initial impact energy, m is the mass of the impactor in kilograms, and v_i is the impact velocity as calculated above.

For each series of test samples, that is, for each set of samples with duplicate specimen geometry and prescribed impact energy in the test plan, the average value, standard deviation, and coefficient of

variation shall be calculated as follows to characterize the data distribution. This statistical analysis shall be done for each measured variable.

Sample mean is given by

$$\bar{x} = \frac{(\sum_{i=1}^n x_i)}{n}$$

Sample standard deviation by

$$S_{n-1} = \sqrt{\frac{(\sum_{i=1}^n x_i^2 - n\bar{x}^2)}{n-1}}$$

Sample coefficient of variation by

$$CV = \frac{100 \times S_{n-1}}{\bar{x}}$$

In all of these formulae, n denotes the number of samples, and x_i the measured or derived property being represented.

To generate the plot of impact velocity vs. time, the force data recorded during impact is numerically integrated. The time step of this integration is set equal to the time step of the data sampling rate.

$$v(t) = v_i + gt - \int_0^t \frac{F(t)}{m} dt$$

In this equation, v is the impactor velocity at time t measured in meters/second, t is the time with $t=0$ at the instant when the impactor first makes contact with the specimen, m is the mass of the impactor, and F is the measured impactor contact force at time t , measured in newtons.

To generate the plot of impactor displacement vs. time, the force vs. time data is numerically integrated according to the following equation:

$$\delta(t) = \delta_i + v_i t + \frac{gt^2}{2} - \int_0^t \left(\int_0^t \frac{F(t)}{m} dt \right) dt$$

where δ is the impactor displacement at time t measured in meters with $t=0$ at the instant the impactor first touches the specimen, and δ_i is the initial displacement from a reference location at time $t=0$.

To generate the plot of absorbed energy vs time, the displacement data is used along with the previous calculated data.

$$E_a(t) = \frac{m(v_i^2 - v(t)^2)}{2} + mg\delta(t)$$

In this equation, E_a represents the absorbed energy at time t , measured in Joules.

These three plots form the basis of quantification of the impact event. However, there are other elements of the data reporting that must be included in the test write-up as well. Items to be included in the test report are listed in ASTM 7136, and are duplicated below with some annotation:

- The revision level or date of issue of this test method (ASTM D7136/D7136M-15)
- The name of the test operator(s)
- Any variations to the test method or anomalous events or equipment problems
- Identification of all the applicable specimen information, including material specification, material type, manufacturer's material designation, manufacturer's batch or lot number, source (if not from manufacturer), date of certification, expiration of certification, filament diameter, tow or yarn filament count and twist, sizing, form or weave, fiber areal weight, matrix content, and volatiles content.
- Description of the fabrication steps used to prepare the parent laminate including: fabrication start date, fabrication end date, process specification, cure cycle, consolidation method, and a description of the equipment used.
- Ply orientation and stacking sequence of the laminate, relative to the longitudinal (long) dimension.
- Density, volume percent reinforcement, and void content test methods, specimen sampling method and geometries, test parameters, and test results.
- Method of preparing the test specimen, including specimen labeling scheme and method, specimen geometry, sampling method, and specimen cutting method.
- Calibration dates and methods for all measurements and test equipment.
- Type and configuration of test machine, data acquisition equipment, data sampling rate.

- If applicable, type of velocity detector and key parameters (for example, height of detector above test specimen, distance between leading edges of flag prongs), velocity measurement accuracy and method for verifying the measurement accuracy, type of force detector.
- Measured length, width and thickness for each specimen (prior to and after damage and conditioning, if appropriate).
- Weight of specimen, type of balance or weighing scale, and measurement accuracy.
- Conditioning parameters and results.
- Relative humidity and temperature of the testing laboratory.
- Environment of the test machine environmental chamber (if used) and soak time at environment.
- Number of specimens tested.
- Diameter of hemispherical impactor striker tip.
- Total mass of impactor.
- Nominal impact energy and drop height.
- Results of nondestructive evaluation tests, including method, specification, inspection parameters and operator, both before and after impact.
- Damage geometry, including positions of the eight specified measurement points described below, damage width, damage length, maximum damage diameter, damage area, and through-thickness location.

The following graphic shows the location of the eight points of measured damage, as well as the length, width, and maximum diameter measurements.

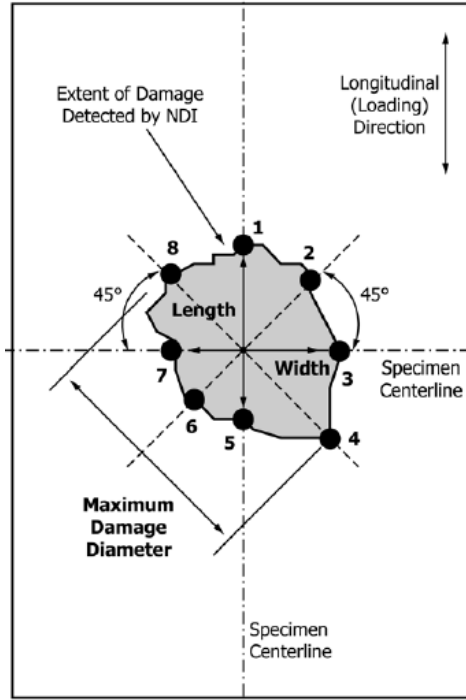


Figure 36. Specimen Damage Measurement Locations

Damage shall be measured using non-destructive methods. Thru-transmission ultrasonic (TTU) is the preferred method for visualization of internal damage. The damage measurements will be taken at each ply through the thickness of the laminate, allowing construction of a 3-dimensional perspective of through-thickness damage propagation.

- Damage modes and locations observed for each specimen.
- Individual dent depths, along with average value, standard deviation, and coefficient of variation (in percent) for the population.
- If dent relaxation is evaluated, individual dent depths after relaxation, along with the time duration after impacting and the environmental conditions prior to measurement.
- Individual values of $F1$, $Fmax$, $E1$ and $Emax$, if these parameters were measured, along with average value, standard deviation, and coefficient of variation (in percent) for the population.
- Contact force vs. time history for each specimen, as recorded by the data acquisition system.
- Actual impact velocity and impact energy for each specimen as calculated above, along with the average value, standard deviation, and coefficient of variation percentage for the population.

- Contact duration for each specimen, along with average value, standard deviation, and coefficient of variation percentage for the population.
- Velocity vs. time, impactor displacement vs. time, and absorbed energy vs. time histories for each specimen, calculated according to the instruction above.

[ASTM D7136/D7136M-15]

4.2.4 Experimental Approach

The experimental work used in this research adapted the ASTM industry standard to use a 3-point-bend configuration. This was done primarily to investigate edge finishing effects on impact fracture performance, and to allow easy visualization of composite-metal debonding (delamination) and other thru-thickness damage mechanisms. Although the specimen geometry is different from the industry standards for impact testing, the theory and processing steps remain analogous.

Bernhardt used a testing configuration with a hemicylindrical impactor that applied a line load across the specimen. His impactor was 5.59 mm in diameter, and the mass of the falling weight and sensors was 2.013 kg. Specimens measured 76.2 x 12.7 mm, and were cut parallel to the zero-degree ply orientation [2]. This apparatus is shown below:

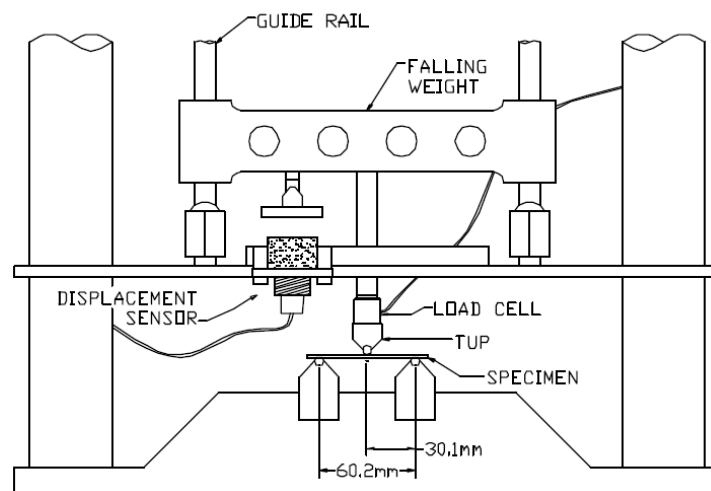


Figure 37. Drop Test Apparatus

During Bernhardt's experiments, both force and position were monitored directly using sensors attached to the drop-test apparatus. A PCB Piezotronics, Inc. model 208C04 force transducer powered by a

Piezotronics, Inc model 484B power supply was used to measure force during impact at the location shown in the above schematic. Meanwhile, a Kaman KD2300-8C eddy-current position sensor monitored tup position at a rate of 30,000 Hz and recorded this data through a National Instruments data-acquisition system and a LabView interface to a computer [2].

For V. Isvonelda's quasi-static specimens, flexural testing was performed using a 3-point bend fixture with a span of 40 mm and a crosshead feed-rate of 1.0 mm/min, in accordance with ASTM D3039 and ASTM D790. A maximum deflection of 15 mm was reached before specimens were unloaded. Figure 1 shows the test fixture with one of the specimens under load.

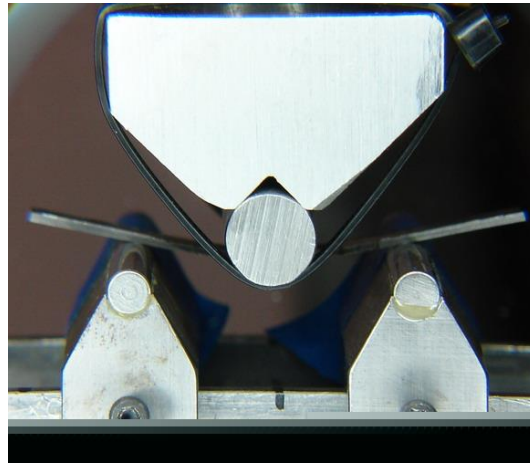


Figure 38. 3-Point Bend Fixture with TiGr Specimen Under Load

During loading a load cell on the crosshead measured applied load and crosshead displacement, then during post-processing results were reported in terms of stress-strain relation, flexural failure load, maximum stress at the outer fibers, and flexural modulus for each specimen. Optical micrographs were obtained before and after loading using a Nikon SMZ1000 and LV1450, and surface profile measurements were taken to illustrate trimmed surface roughness using a MarSurf XR20 surface profilometer.

For the experimental work conducted during the course of this research, specimens were impacted in a 3-point-bend configuration, using a cylindrical impactor and cylindrical supports. The fixture was mounted in an Instron drop-weight testing fixture with a 15 kN load capacity. The impactor had a diameter of 6.35 mm, and was made from shock resistant steel, while the supports were slotted and screwed to the

impact fixture walls, which were welded to a steel base plate. The supports were positioned 50 mm apart, which left 10 mm of overhang on each side of the specimens.

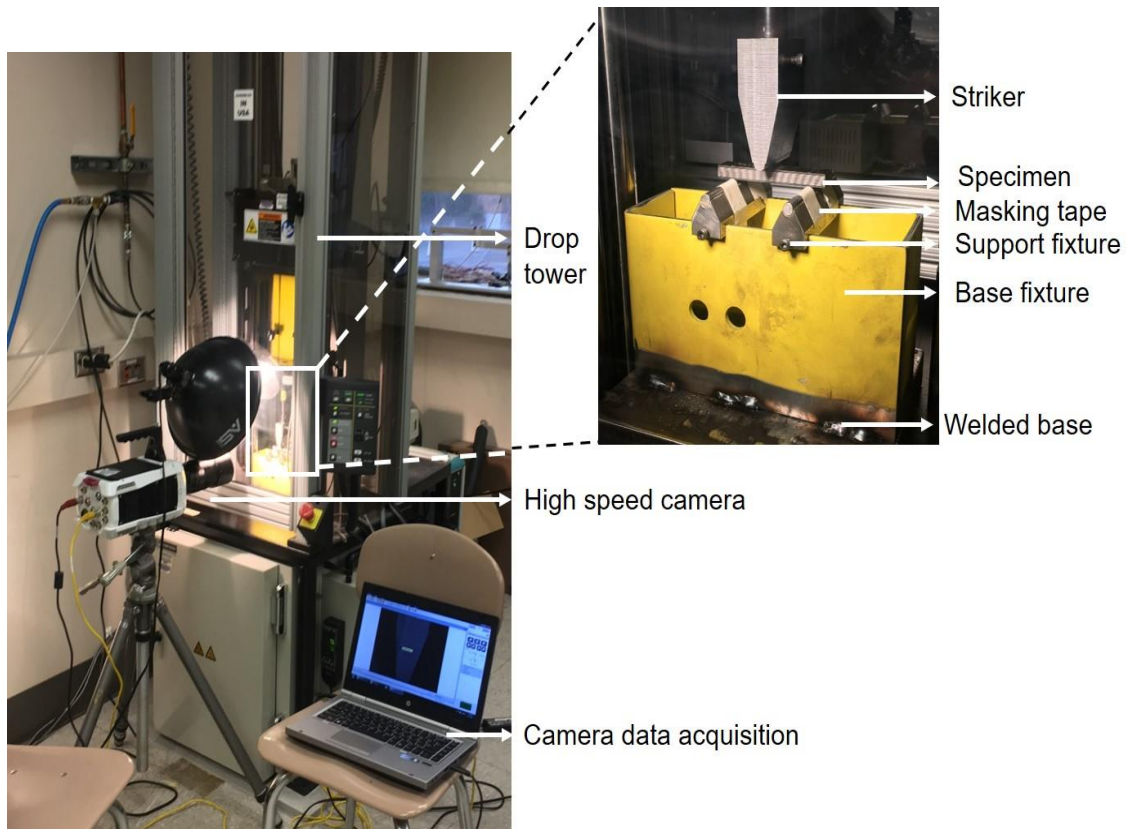


Figure 39. Experimental Setup For Low-Velocity Impact Experiments

The following table shows the label of each specimen, along with the AWJ trimming parameters as well as the impact conditions.

Table 9. Low Velocity Impact in Flexure and AWJ Process Variables for TiGr Specimens

Nomenclature	Process	Pressure (MPa)	Speed (mm/s)	Mass (kg)	Velocity (m/s)	Impact energy (J)
t1	AWJ	350	2.12	7.41	2.5	23.16
t2	AWJ	350	21.17	7.41	2.5	23.16
t3	AWJ	200	10.58	7.41	2.5	23.16
t4	AWJ	200	2.12	7.41	2.5	23.16
t5	AWJ	350	21.17	7.41	2.5	23.16
t6	AWJ	350	2.12	7.41	2.5	23.16

t7	AWJ	350	2.12	7.41	4	59.28
t8	AWJ	350	21.17	7.41	4	59.28
t9	AWJ	200	10.58	7.41	4	59.28
t10	AWJ	200	2.12	7.41	4	59.28
t11	AWJ/CNC	-	-	7.41	4	59.28
t12	CNC	-	-	7.41	4	59.28
t13	AWJ	350	2.12	7.41	5.5	112.12
t14	AWJ	350	21.17	7.41	5.5	112.12
t15	AWJ	200	2.12	7.41	5.5	112.12

Results from these impacts as well as those of other cited experimental work are described in the following chapter.

4.3 Numerical Modeling of Low Velocity Impact

4.3.1 Typical Model Geometry

The model is constructed using the ABAQUS graphical user interface such that each ply is defined by an identical 2-dimensional sketch, then extruded to the specified thickness. Although dimensions vary, the basic model for Bernhardt, Vara, and experimental work done for this research is similar. The impactor dimension is also detailed in section 4.3, and is represented here by a single hemisphere of zero thickness.

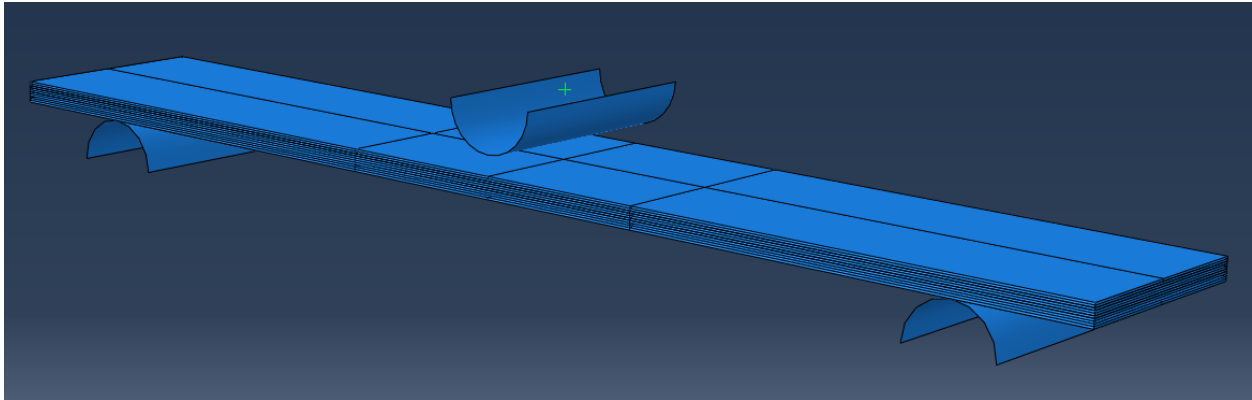


Figure 4.15 – Impact Model Geometry

Each lamina is given identical specification for mesh density, and is partitioned such that the zone representing supported material can be independently selected to assign appropriate boundary conditions.

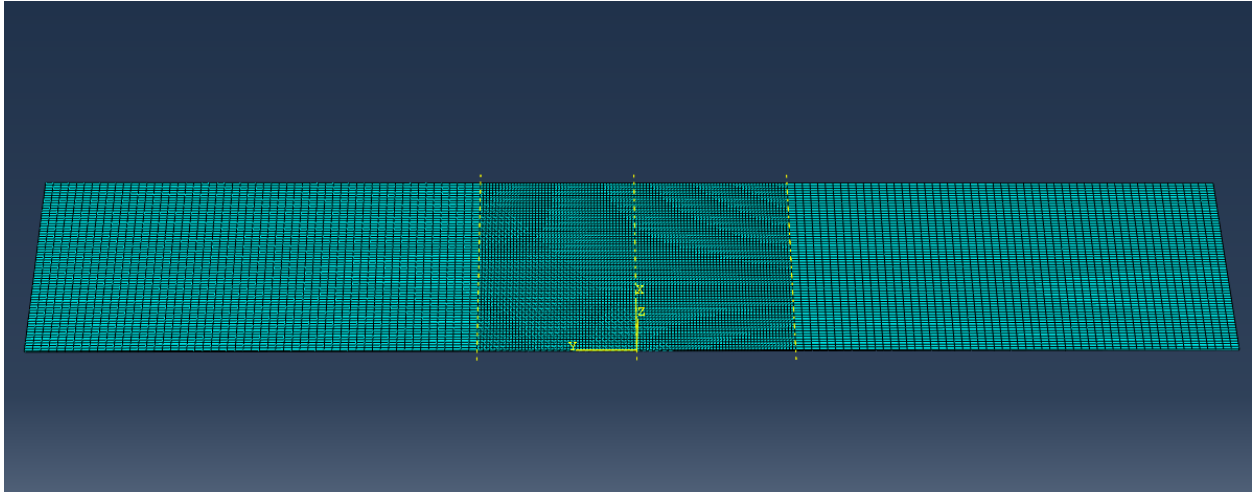


Figure 4.16 – Lamina Mesh and Partitioning

For the case of the Bernhardt model, thicknesses of each layer are approximately 125-130 μm , and this value is assigned to each layer, along with the material properties, mesh, and element type.

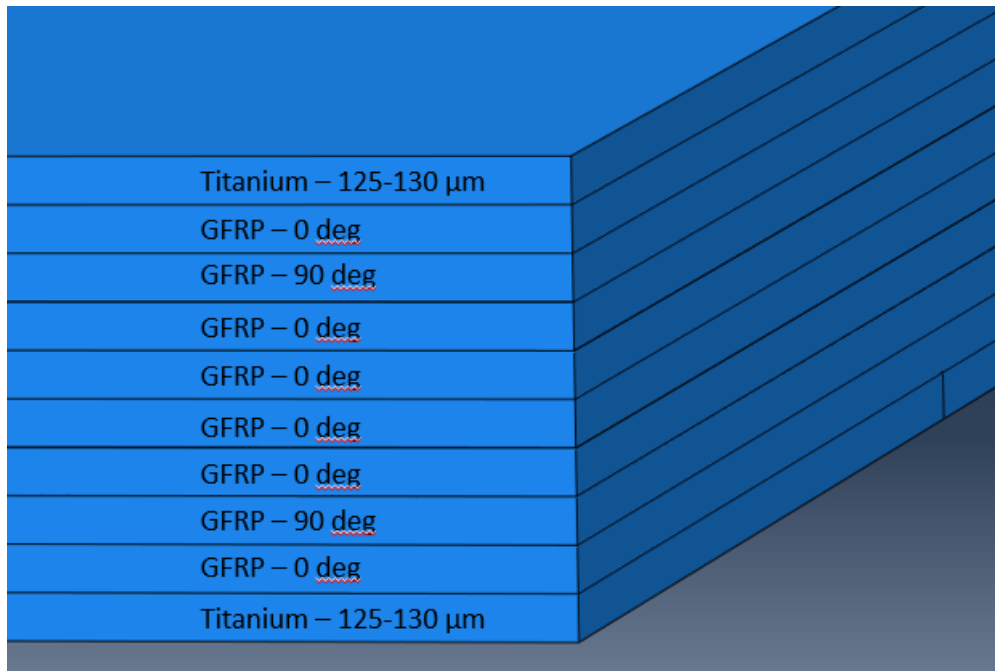


Figure 4.16 – Test Laminate Lay-Up Specification

Material properties are defined from the literature as described in Chapter 2. The material cards are more compactly represented below.

Table 10. Titanium 15-3-3-3 Material Properties

Titanium 15-3-3-3						SOURCE
Density						
4.43E3 kg/m ³						[6]
Elastic						
Young's Modulus				Poisson's Ratio		
85.9 GPa				0.38		[6]
Johnson-Cook Plasticity						
A	B	n	m	Melting Temp	Transition Temp	
984 Mpa	380 Mpa	0.3	1.1	1669 C	882 C	[88]
Johnson-Cook Damage						
d1	d2	d3	d4	d5	Melting Temp	Transition Temp
-0.09	0.25	-0.5	0.014	3.87	1669 C	882 C
						Reference Strain Rate [10]
						2.33E-05
Damage Evolution						
Fracture Energy, Linear Softening						
17.5 kJ/m ²						[93,94]

Table 11. GFRP/PEEK Material Properties

GFRP/PEEK						SOURCE
Density						
1578 kg/m ³						[89]
Elastic						
E1	E2	Nu12	G12	G13	G23	
139 GPa	10 GPa	0.28	3.9 GPa	3.9 GPa	3.9 GPa	[89]
Hashin Damage						
Longitudinal Tensile Strength	Longitudinal Compressive Strength	Transverse Tensile Strength	Transverse Compressive Strength	Longitudinal Shear Strength	Transverse Shear Strength	
1710 MPa	938 MPa	60 MPa	182 MPa	72.4 MPa	72.4 MPa	[89]

Damage Evolution			
Longitudinal Tensile Fracture Energy	Longitudinal Compressive Fracture Energy	Transverse Tensile Fracture Energy	Transverse Compressive Fracture Energy
128 kJ/m ²	128 kJ/m ²	5.6 kJ/m ²	5.9 kJ/m ²

[90]

Table 12. Cohesive Surface Properties

Ti/CFRP Cohesive Property			SOURCE
Elastic			
Knn	Kss	Ktt	
1E13 Pa	1E13 Pa	1E13 Pa	[77]
Maxs (Maximum Stress) Damage Criterion			
Nominal Stress Normal-Only Mode	Nominal Stress First Direction	Nominal Stress Second Direction	
0.1713 MPa	18.91 MPa	18.91 MPa	[95]
Benzeggagh-Kenane (BK) Damage Evolution			
BK Exponent	Normal Mode Fracture Energy	Shear Mode Fracture Energy First Direction	Shear Mode Fracture Energy Second Direction
2.284	969 J/m ²	1719 J/m ²	1719 J/m ²

Table 13. Interlaminar Cohesive Properties

Gr/PEEK Interlaminar Property			SOURCE
Elastic			
Knn	Kss	Ktt	
1E13 Pa	1E13 Pa	1E13 Pa	[77]
Maxs (Maximum Stress) Damage Criterion			
Nominal Stress Normal-Only Mode	Nominal Stress First Direction	Nominal Stress Second Direction	
75.4 MPa	96.3 MPa	96.3 MPa	[91]

Benzeggagh-Kenane (BK) Damage Evolution			
BK Exponent	Normal Mode Fracture Energy	Shear Mode Fracture Energy First Direction	Shear Mode Fracture Energy Second Direction
2.3	980 J/m ²	1625 J/m ²	1625 J/m ²

[91]

Finally, elements are assigned and a mesh is generated for each lamina. For the titanium plies the C3D8I element is used. This three dimensional solid element represents an 8-node linear brick element with incompatible modes, as discussed in Chapter 1. The GFRP layers use a SC8R element, which is a continuum shell element. This element is also represented by an 8-node quadrilateral, using reduced integration with hourglass control and finite membrane strains. The impactor mesh is a simple 4-node shell element, however it is given a rigid property which assumes infinite rigidity and thus zero deformation. A single node is defined for the point mass of the impactor, and this node is tied to the rest of the impactor surface, simulating the total weight of the impacting assembly. The cohesive surface property is not given an element or mesh per se, but is applied as an interaction between the coplanar surfaces of adjacent GFRP plies. Thus the cohesive layer has zero thickness, but governs the conditions by which delamination of the GFRP plies can occur. The impactor is then positioned above the center of the laminate, and the loads and boundary conditions are applied to generate the test condition.

4.3.2 Applied Loads and Boundary Conditions

Boundary conditions are applied to the model to constrain part movement to degrees of freedom representing the physical experiment. The supports are rigid elements, and are restricted from any movement. The impactor is restricted to only translate in the “z” direction, similar to the drop test fixture. A general contact constraint is used to define parts in space and to prevent penetration of parts. Finally, the individual contact properties are applied at the interfaces between laminate plies. A point mass is defined representing the weight of the impactor, and is set at the center of area of the impactor.

The only load applied is the predefined condition of the impactor’s velocity at the instant before it impacts the specimen. This velocity is defined to give the requested impact energy. The point-mass of the impactor is 2 kg, and the kinetic energy is defined by:

$$KE = \frac{1}{2}mv^2$$

so if a 4.7 Joule impact is desired, the velocity entered in the predefined field is 2.168 m/s.

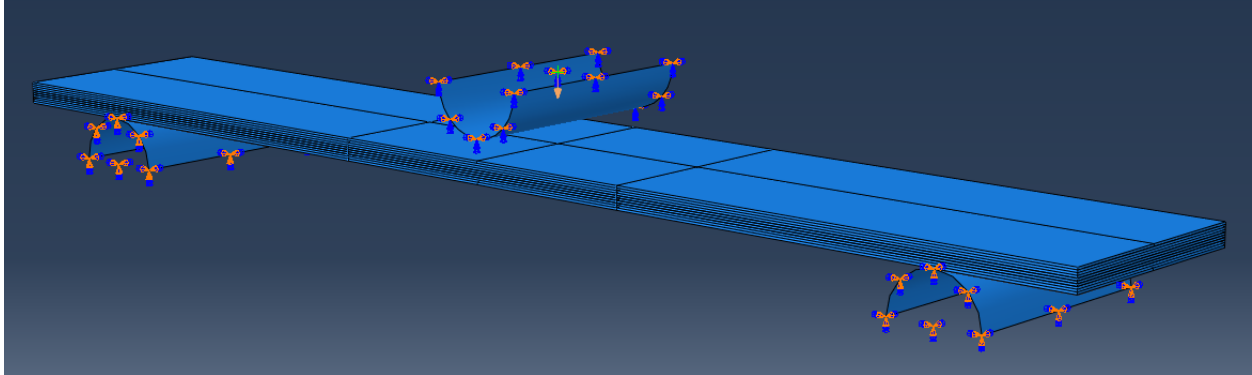


Figure 40. Finite Element Applied Boundary Conditions

4.3.3 Post Processing

After the impact analysis has completed, plots can be generated representing the same quantities requested from the experimentation. Plots of contact force, velocity, displacement, and absorbed energy vs. time can be constructed as outlined in the ANSI specification. Representative figures are included below as an example:

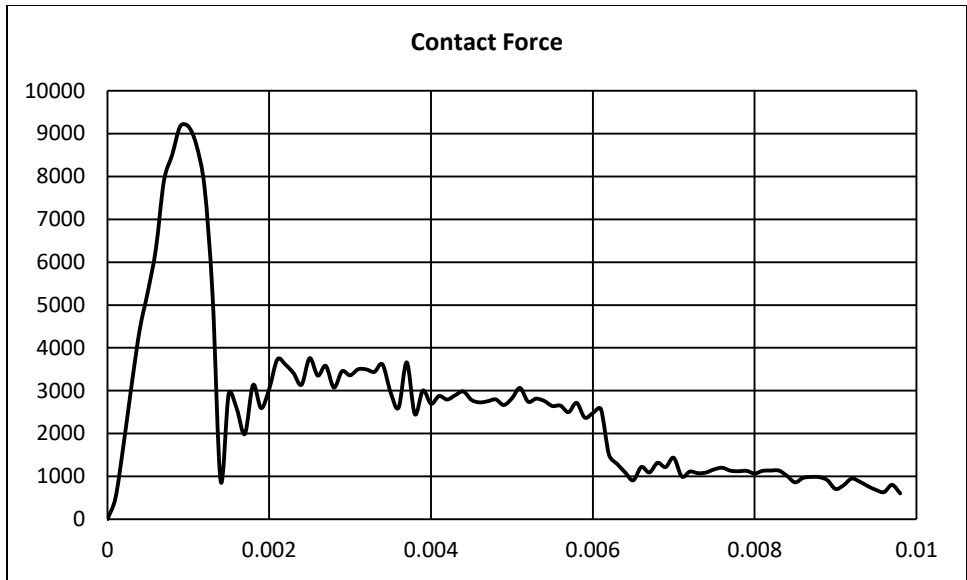


Figure 41. Contact Force Time History

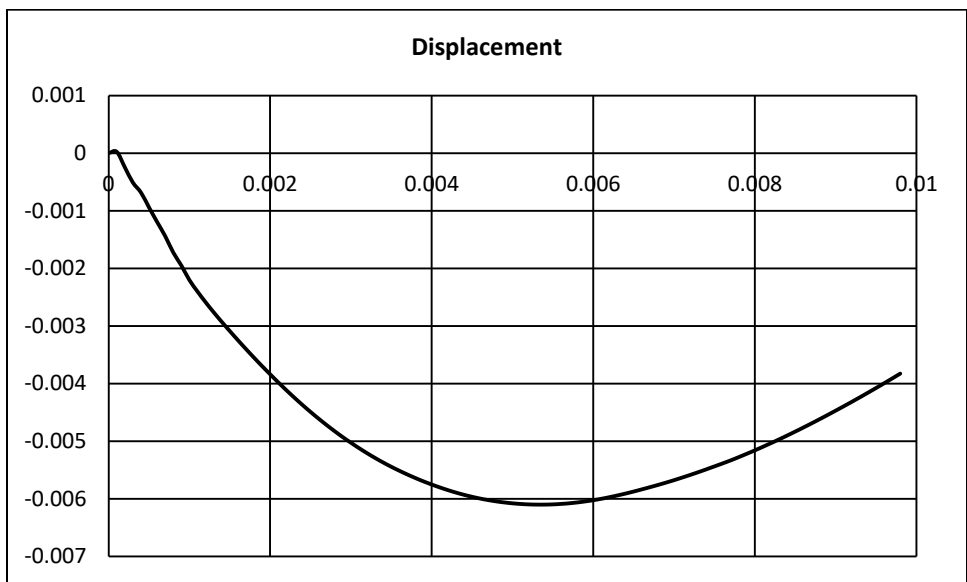


Figure 42. Impactor Displacement Time History

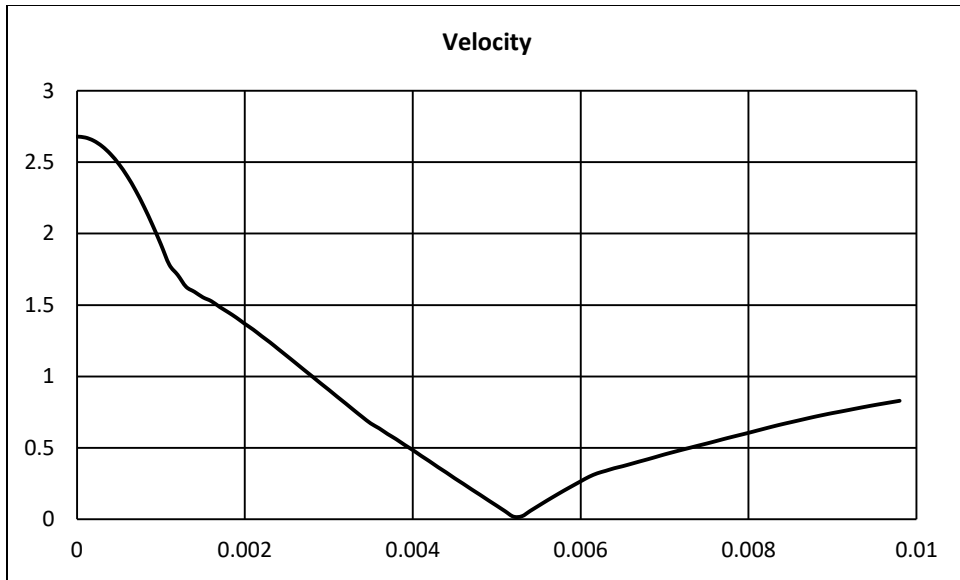


Figure 43. Impactor Velocity Time History

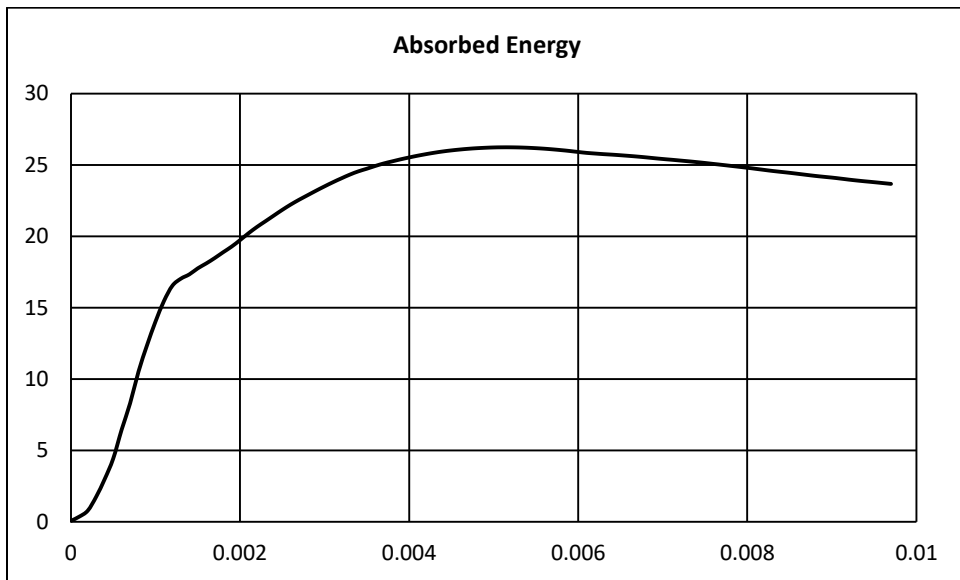


Figure 44. Laminate Absorbed Energy Time History

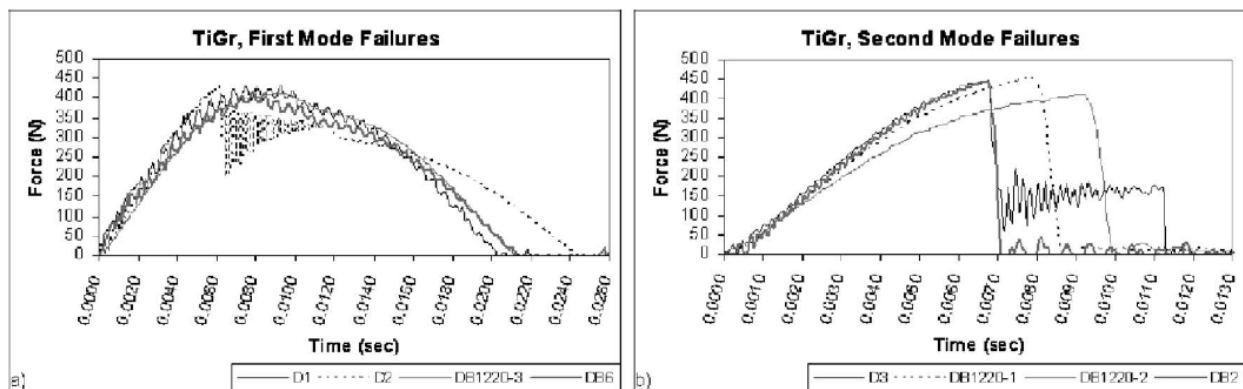
In addition, graphics showing the individual failure mechanisms can be generated by selecting the associated damage variable in the graphical user interface. Images are generated over the course of the impact to show damage progression, and are included in the appendices.

CHAPTER 5: RESULTS

An ordered approach was adopted to characterize damage of different titanium laminates. This approach considered laminates of different thicknesses as well as metal volume fraction (MVF). As summarized in Chapter 2, Bernhardt and Ramulu did low-velocity impact experiments with TiGr laminates with titanium face sheets. These experiments constitute only metal face sheet and the lowest MVF, at 0.197. Next, thin laminates were investigated using static test data obtained by Vara and simulated using the numerical modeling techniques outlined previously. These laminates increased the number of titanium plies to 4, more than doubling the MVF to 0.46. Finally, specimens tested during the course of this research had 15 plies and were much thicker. The MVF of these specimens was 0.279, and provided a contrast in fracture damage evolution to the thinner laminates. Both static and dynamic impact testing were conducted on these specimens, illustrating the effect of impact energy and dynamic effects on the propagation of damage.

5.1 TiGr Laminates with Titanium Face Sheets

Results showed two primary failure modes, dependent on whether the bottom titanium ply fractured or not. Mode 1 represents an impact where the bottom ply didn't fracture, and the laminate experienced elastic rebound. Mode 2 represents an impact where the bottom ply failed, causing subsequent ply failure and no elastic rebound. Absorbed energy can then alternatively be calculated as the area contained under the force-displacement curves.



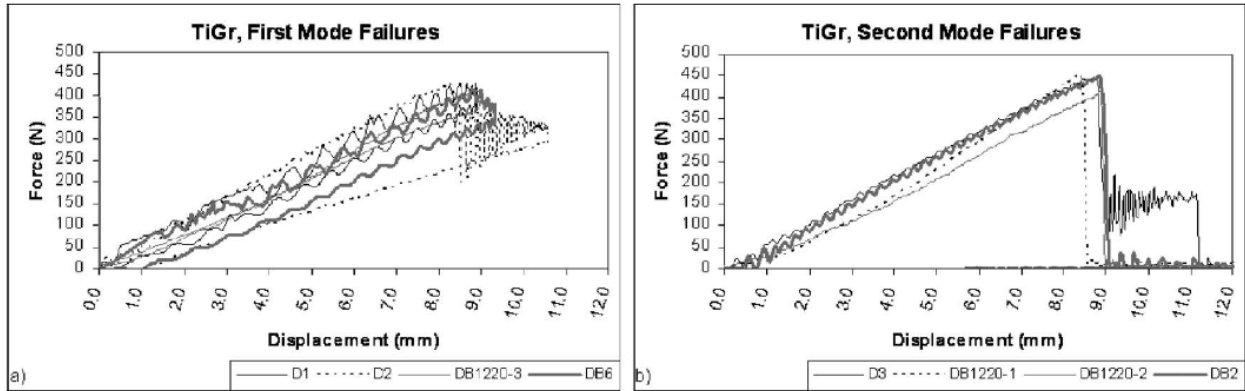


Figure 45. Bernhardt Drop Test Data [X]

As noted above, Bernhardt noted two primary failure modes of his TiGr laminate; one mode when the bottom ply fractured, and one mode when it remained intact. This event has a big effect on how damage propagates through the rest of the laminate, and was controlled using the Maximum Degradation parameter in Abaqus. For Mode 1 fracture, the maximum degradation of the top ply was set slightly below that of the bottom, thus ensuring that the top ply would buckle before the bottom ply fractured. For Mode 2, the parameters were reversed, causing the bottom ply to fail first. The figure below shows Mises stress after a Mode 1 fracture. Additional images of the various failure modes are shown in Appendix I.

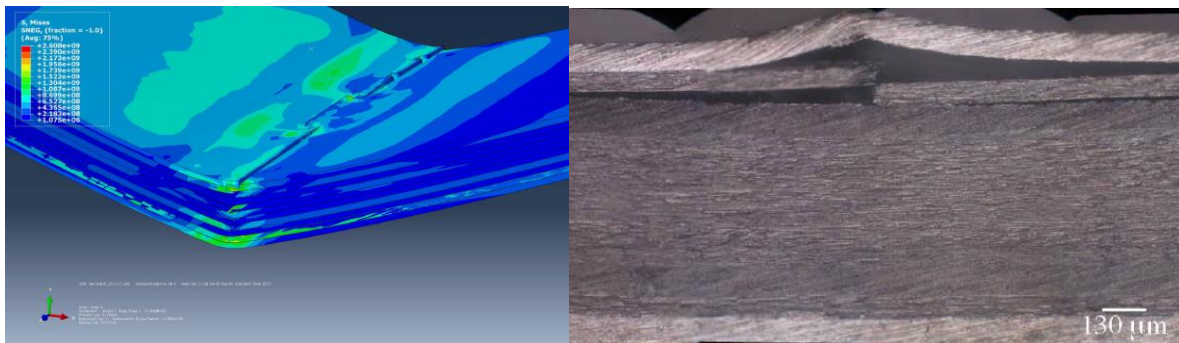


Figure 46. Mode 1 Failure Comparison

Mode 2 failure is described by complete fracture of the bottom titanium layer, followed by progressive fiber fracture of the 0-degree plies upward from the bottom of the laminate. The following plot shows a Mode 1 failure just after initial fracture. The bottom titanium ply has fractured, as well as the first, third, and fourth 0-degree plies. The second ply from the bottom is oriented at 90 degrees, and would realistically be failed as well, but still shows attachment due to the higher ductility of the matrix material.

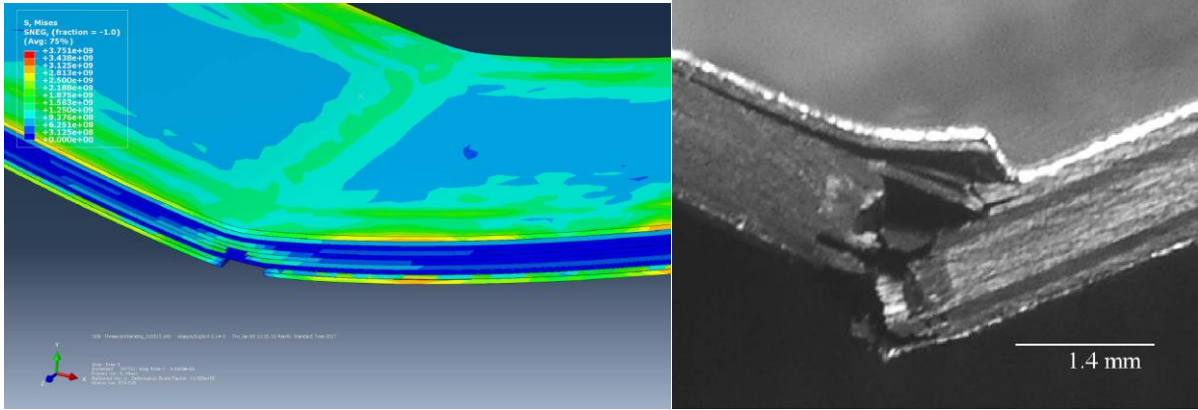


Figure 47. Mode 2 Failure Comparison

This plot can be compared to Bernhardt’s micrograph for a Mode 2 fracture. This plot was taken after complete fracture, and thus shows the further progression of damage. Additional plots showing damage propagation during impact simulation can be found in Appendix I.

Looking beyond comparisons of general fracture morphology, plots were generated showing impact force as a function of time and impactor displacement, mirroring data taken during Bernhardt’s experiments. The first of these shows force as a function of time for a Mode 1 failure, with the red line representing numerical data. In general, force increases until it reaches a maximum point, at which there is a drop in force brought about by the delamination of the uppermost 0-degree ply from the adjacent 90-degree ply. This is close-coupled with buckling of the upper titanium layer, causing a drop in force and followed by elastic rebound of the laminate. Though the Abaqus simulation does not extend through the entire time period, relatively good correlation exists with Bernhardt’s experimental data.

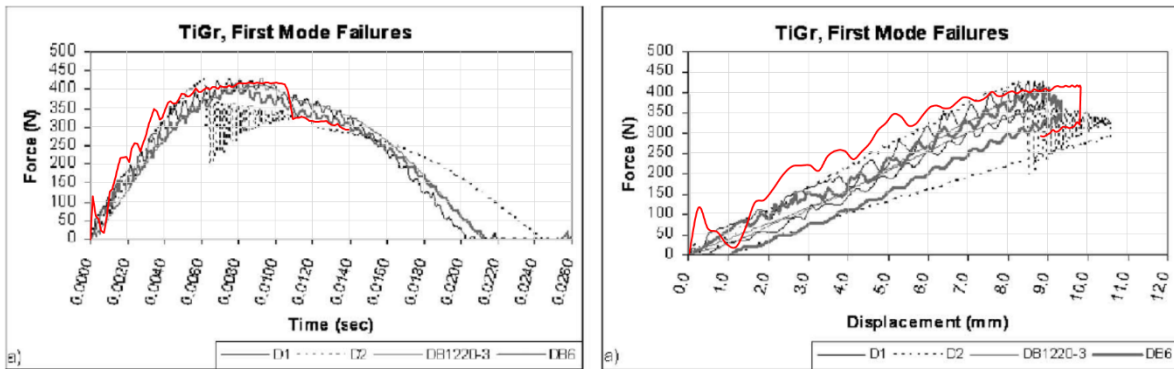


Figure 48. Mode 1 Failure Comparison

Force-displacement plots correlate strains in the laminates through a generalization about overall laminate displacement. Also, the area contained within the force-displacement boundary is representative of the energy absorbed during impact through metal plasticity, damage, and delamination. Numerical results fall in the same range of overall laminate displacement, indicating good representation of flexural rigidity and absorbed energy, if the trend is extrapolated.

Bernhardt's second mode fracture is represented below by a force vs time plot. Because this fracture mode results in complete fracture of the laminate, no elastic rebound exists, and the force drops to zero following fracture of the bottom titanium ply. The spurious peaks following this fracture are due to the applied gravity field causing repeated impacts after the initial catastrophic failure. No "brake" was applied to the numerical model, therefore repeated impacts are seen as jittery propagation of delamination causes vibration of the laminate against the impactor.

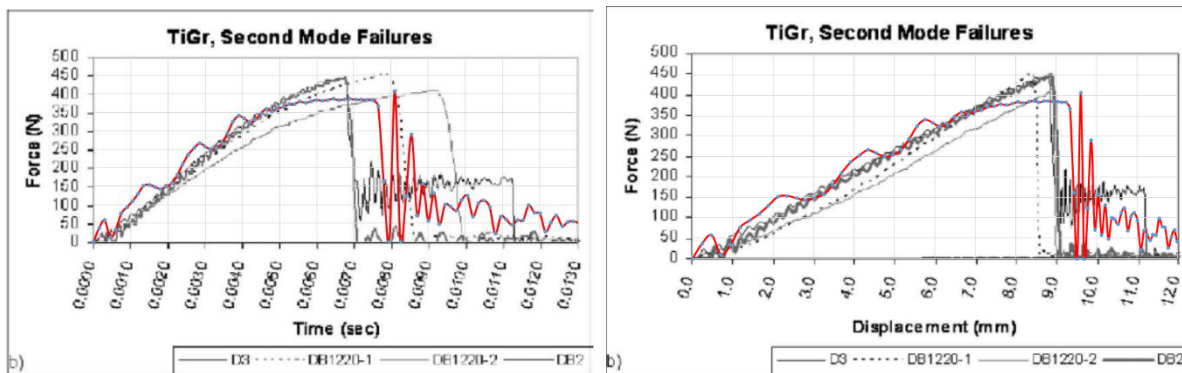


Figure 49. Mode 2 Failure Comparison

As with the Mode 1 impact, the force/displacement plot shows a similar initial trajectory indicating a fairly good approximation of flexural rigidity. The area contained under the curve is also similar, indicating that a similar amount of energy was absorbed by the laminate during the impact. The numerical model over-predicts the displacement at catastrophic fracture by about 14%, and under-predicts the maximum force seen by the impactor by about 13%. This could be indicative of slightly differing fracture energy values at the ply interfaces, and is not surprising considering numerical values were taken from different previous test data.

Next, it is interesting to look at the total delamination area in order to make inferences and comparisons about absorbed energy during impact. Bernhardt did not measure delamination area, so there is no experimental data with which to compare, but the numerical models can be compared for the two failure cases. The following graphic shows areas where the traction-separation law has reached a value of 1.0, indicating that the stiffness of cohesion between the two surfaces is zero, and the ply has delaminated. For illustration, partial transparency has been activated to allow visualization of the interface between the top titanium ply and the adjacent 0-degree ply.

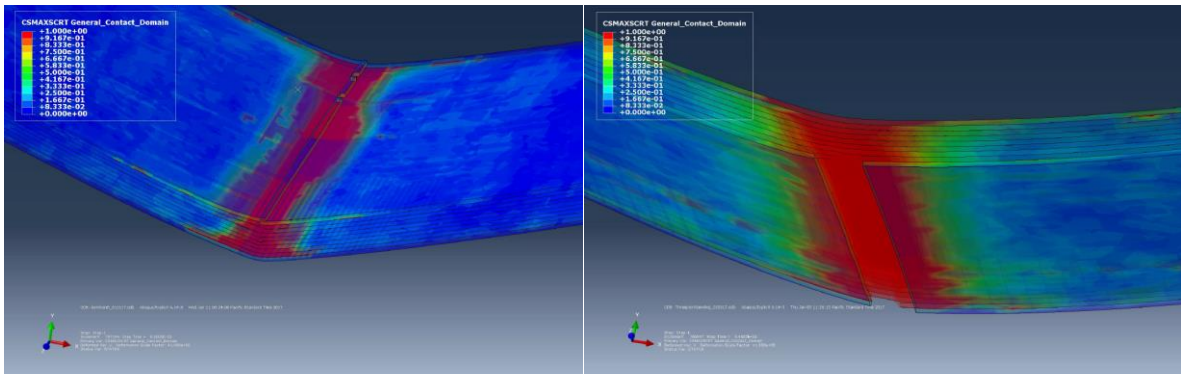


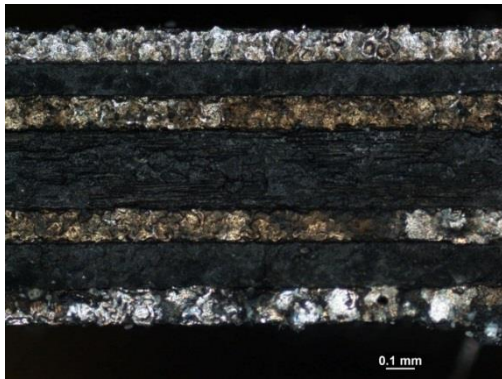
Figure 50. Interlaminar Delamination

For Mode 2 fracture, the bottom titanium ply fails first, and this results in delamination propagating through the thickness from the bottom up. From the numerical model, it appears that Mode 2 fracture results in a larger delamination area at the titanium-CFRP interfaces localized at the fracture zone, while Mode 1 fracture results in more widespread delamination of the top CFRP plies at the edges of the laminate.

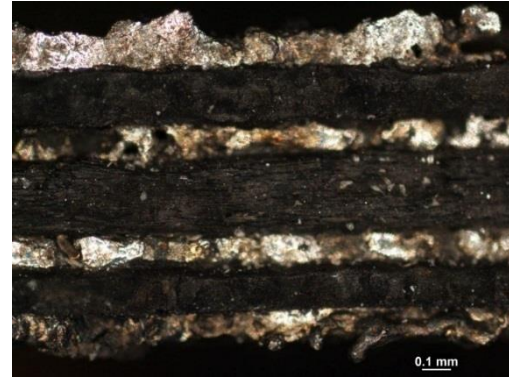
In both cases, delamination area between plies follows the expected stress distribution for a beam in bending; extreme fibers exhibit larger delamination areas and the neutral axis interface presents the smallest delamination area.

5.2 Quasi-Static Loading of Thin Laminates & Size Effects

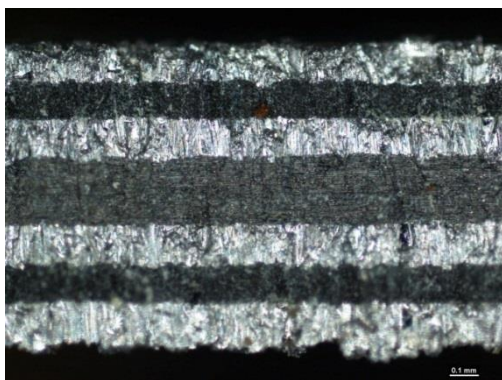
Specimens studied by Vara were prepared using both AWJ and EDM, which yielded different surface qualities. It is hypothesized that the differences in surface quality contribute to variation in damage behavior under flexural loading.



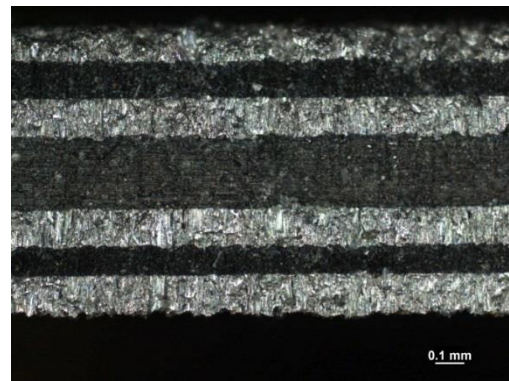
(a)



(b)



(c)



(d)

Figure 51. Trimmed Surfaces (a) fine EDM, (b) rough EDM, (c) rough AWJ, and (d) fine AWJ

In general, the “fine” trimming parameters yielded smoother surfaces compared to the “rough” parameters. For EDM trimming, thermal damage and ply separation was observed in all specimens, and was much more prevalent in the rough EDM specimens. In these specimens titanium melting and matrix cracking was observed prior to flexural loading. For the AWJ specimens, no delamination or matrix cracking was observed, although specimens trimmed at high speed and with low abrasive flow rate yielded a rougher surface. In general, the profilometer measurements supported observations made using optical microscopy.

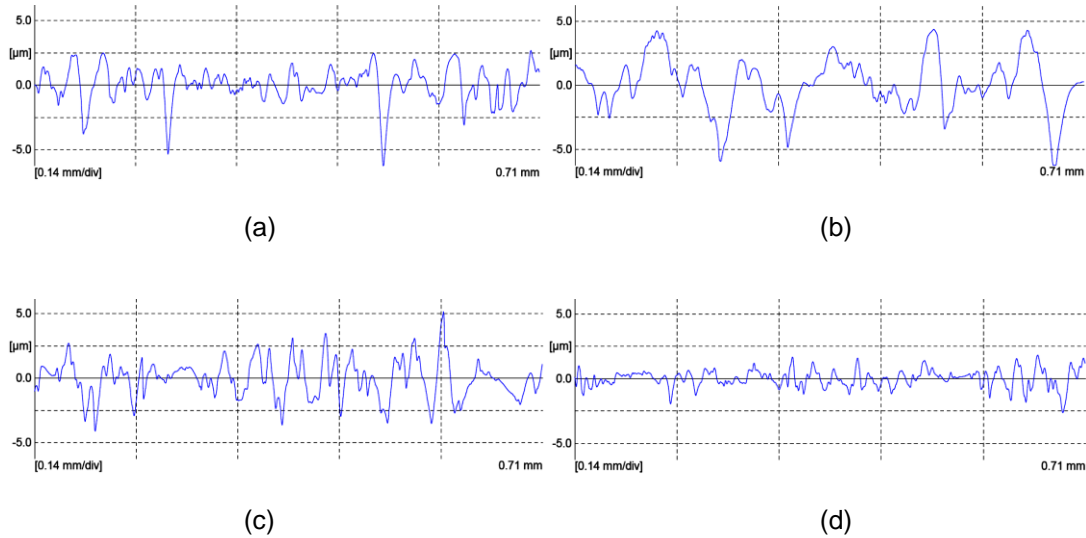


Figure 52. Profile Along Thickness Direction of Machined Surfaces (a) fine EDM, (b) rough EDM, (c) rough AWJ, and (d) fine AWJ

All 12 specimens underwent 3-point bend tests according to ASTM D3039 and ASTM D790. Stress-strain plots were generated from load-displacement data as shown in Figure 6. During initial loading the response was linear, then began to diverge from the flexural modulus as the bottom titanium ply yielded. Yielding of the bottom titanium ply followed the same general curve for all specimens; the only difference between specimens was the failure strain at which the bottom titanium ply fractured.

Table 14. Experimental Results from Quasi-Static 3-Point-Bend Testing

	Conditions	Failure Load (N)		Deflection at Failure (mm)		Max Stress at Failure (GPa)		Strain at Max Stress (mm/mm)		Flexural Modulus (GPa)	
		Avg	SD	Avg	SD	Avg	SD	AVG	SD	Avg	SD
Specimen 4-6	Fine EDM	187.0	15.7	11.85	1.89	1.26	0.044	0.044	0.007	83.43	6.24
Specimen 13-15	Rough EDM	208.7	7.1	7.48	0.62	1.39	0.015	0.028	0.002	83.52	3.97
Specimen 7-9	Rough AWJ	208.1	15.2	9.16	1.37	1.43	0.039	0.034	0.005	86.65	7.05
Specimen 10-12	Fine AWJ	204.3	7.4	9.01	0.28	1.43	0.013	0.034	0.001	79.87	3.3

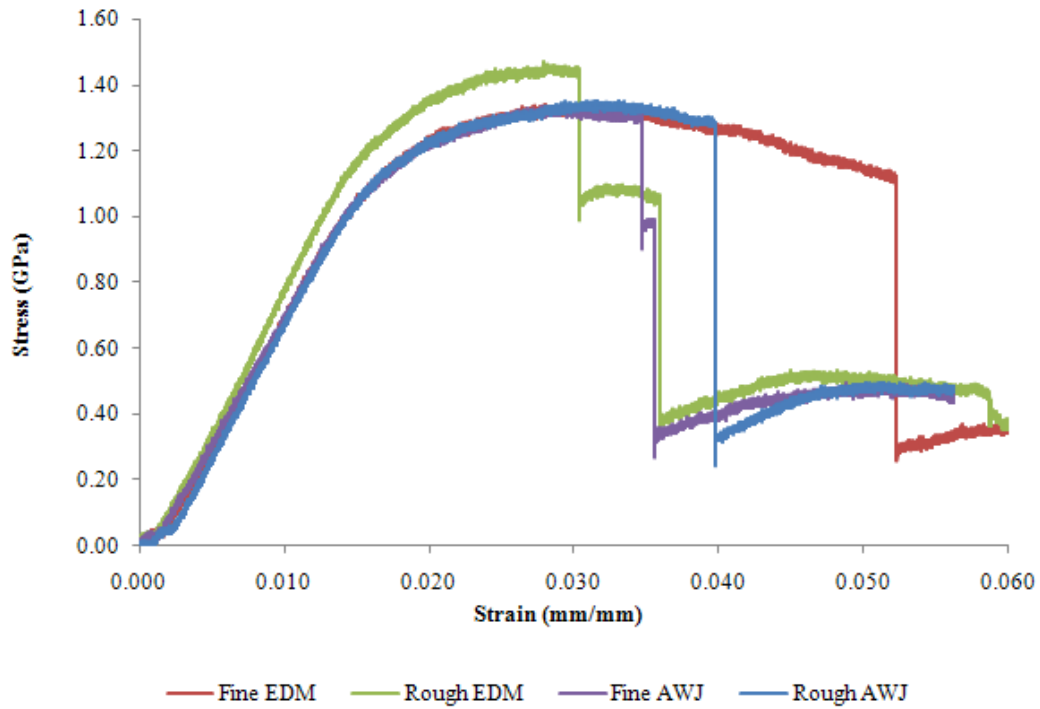


Figure 53. Stress-Strain Curves for Static TiGr Samples

Results of the flexural tests indicated two primary failure modes. The first mode occurred when the bottom four plies (Ti, 90, Ti, 0) failed simultaneously, resulting in a large drop in the stress-strain curve. The other failure mode occurred when the bottom two plies (Ti, 90) failed simultaneously, followed by the next two plies (Ti,0). This is seen as two drops in the stress-strain curve, illustrated by rough EDM and fine AWJ specimens.



(a)



(b)

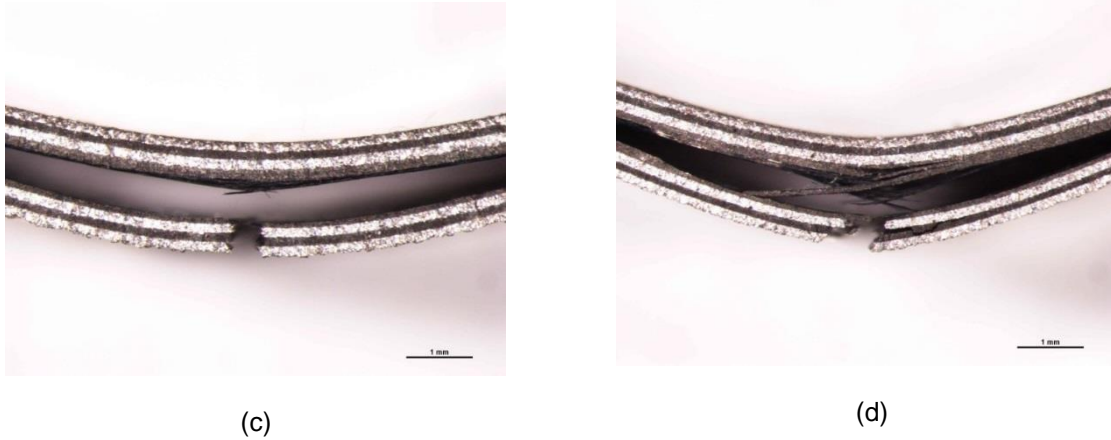


Figure 54. Sample of Specimens after 3-Point Bend Test (a) EDM 4A 25 μ s, (b) EDM 11A 200 μ s, (c) AWJ 720mm/min 3.53g/s, and (d) AWJ 60mm/min 9.78g/s

Using optical microscopy, shear planes at 45 degree angles were observed in the fractured bottom titanium ply, suggesting ductile tensile fracture. Specimens trimmed using the EDM method exhibited severe debonding between the metallic and composite plies, where this phenomenon was not observed with the AWJ specimens. In all specimens there was observed interlaminar delamination between the center two 0 deg plies, corresponding to the highest shear stresses developing at the neutral axis of bending, as well as from stress redistribution after the failure of the bottom plies.

5.2.1 Numerical Modeling Data

Results of the experimental testing indicated that titanium fracture was the primary predictor of flexural displacement at failure. Because of the macro scale of the finite element model, a universal failure strain was assigned as a material parameter, and used to “calibrate” the model to fail within the range of Fine EDM specimens. Other failure criteria were similarly adjusted to reflect nonlinear behavior prior to ply failure shown by experimental specimens #4-6.

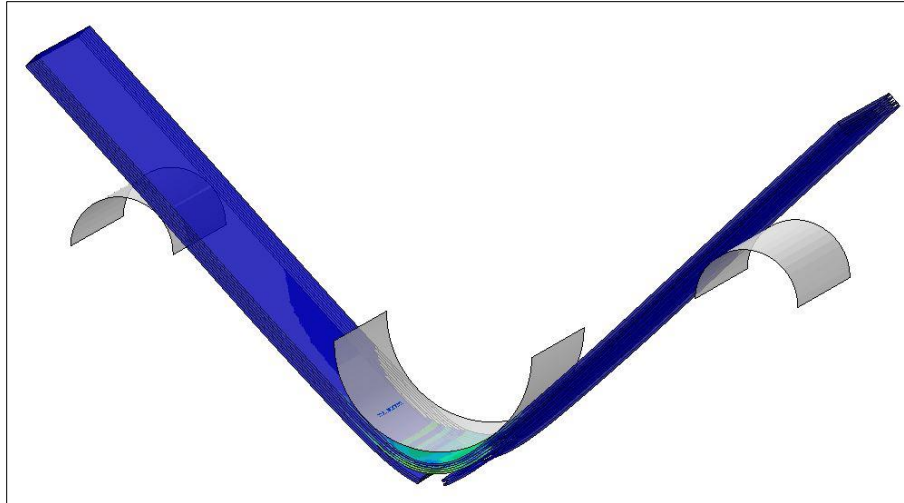


Figure 55. Numerical Modelling of TiGr Specimen

Given literature values for strength and stiffness of the constituent materials, the finite element laminate failed in the same way as the experimental specimens; with sudden fracture of the bottom four plies (Ti, 90, Ti, 0). A stress-strain curve could then be assembled, extracting values from the normal force exerted on the virtual crosshead as well as its vertical extension.

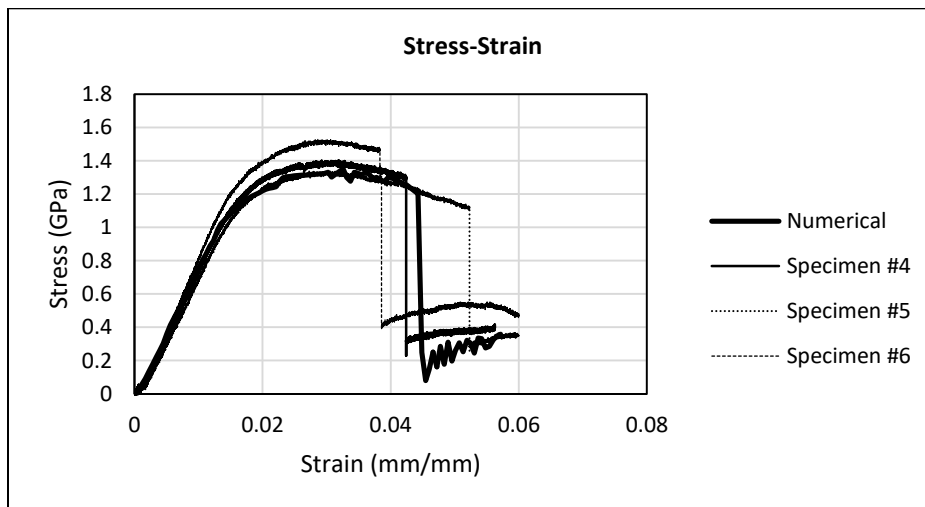


Figure 56. Stress-Strain Plot of Numerical and Experimental Data

To compare flexural energy as a function of crosshead extension, energy is first calculated at each data point as $\frac{\text{average incremental load}}{\text{incremental extension}}$. The running sum is then plotted for each specimen as well as the simulation. Prior to bottom ply fracture there is good correlation with the experimental data, indicating good

agreement with the pre-fracture damage progression. After fracture there is an inflection in the running sum, indicative of the stiffness reduction. There is some scatter in the experimental data, and the numerical model shows a post-fracture energy slope very similar to Specimen #5, with a normalized energy value very similar to Specimen #4.

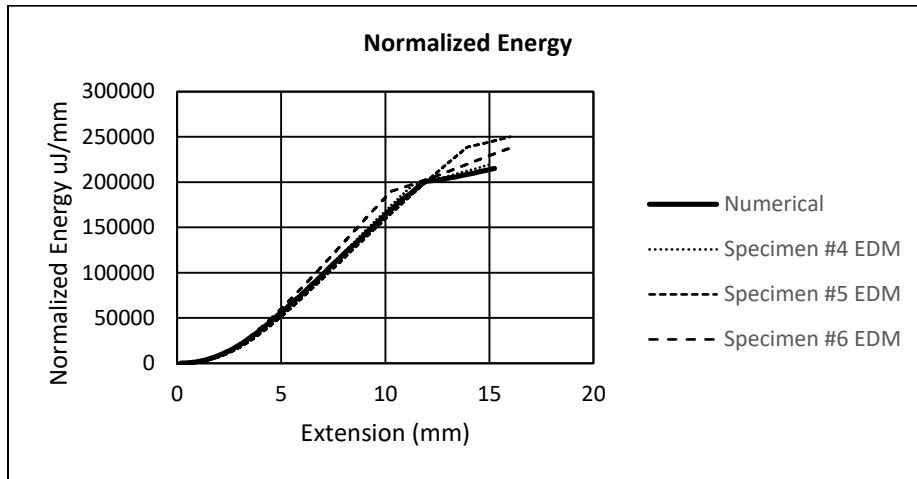


Figure 57. Normalized Energy Plot of Numerical and Experimental Data

To further highlight the rate of energy change, the differential derivative of the above data is plotted below. Again, there is good agreement with the experimental data, especially with the rate of specimen #5 prior to ply fracture. Good agreement of energy absorption rate would indicate the fracture energy (strain energy release rate) for the affected damage mechanisms is appropriately selected for the given materials.

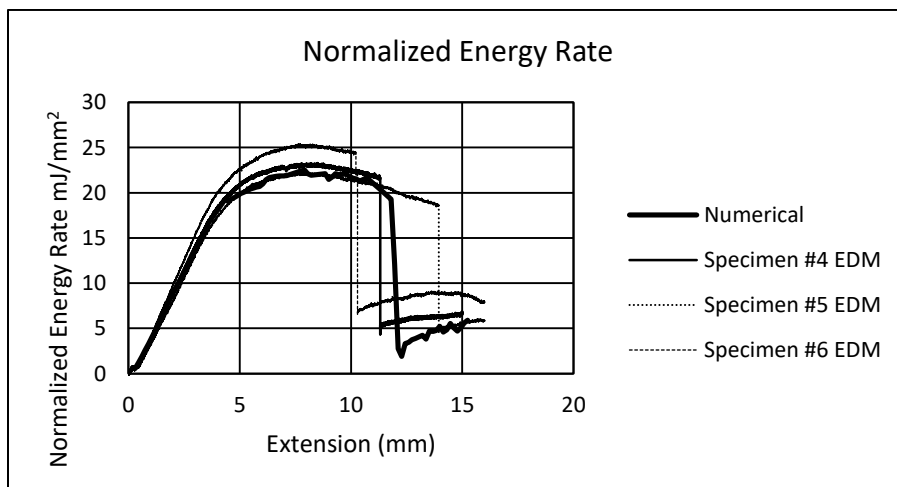
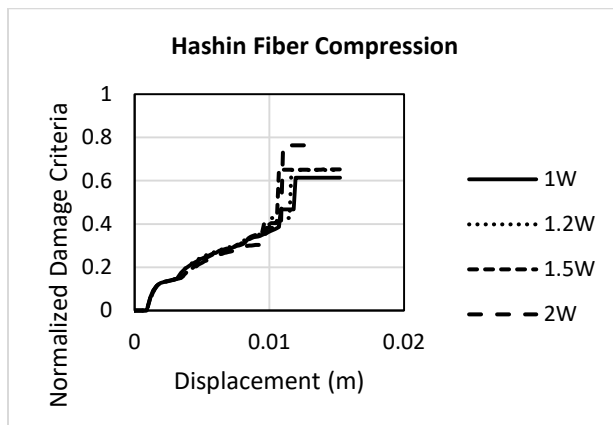


Figure 58. Normalized Energy Rate of Numerical and Experimental Data

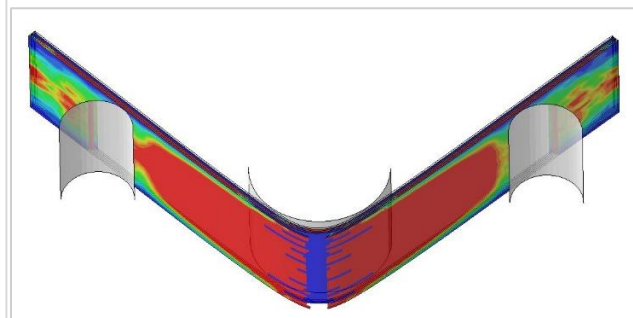
5.2.2 Width Effects

A benefit of the finite element model is the ability to interrogate contributions of different damage modes prior to laminate failure. With an experimental specimen this isn't possible, as laminate behavior is seen as a single amalgam of different interconnected material properties. With a fiber metal laminate the individual contributions are of particular interest, as these damage models drive pre-fracture nonlinearity and determine the maximum flexural strength of the laminate.

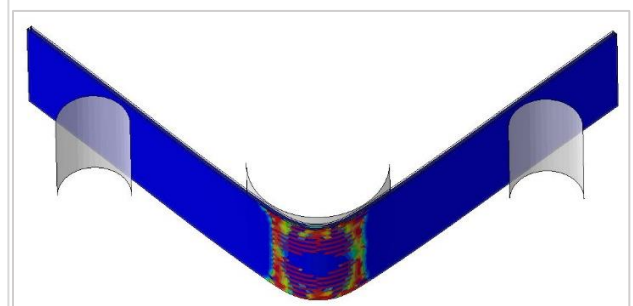
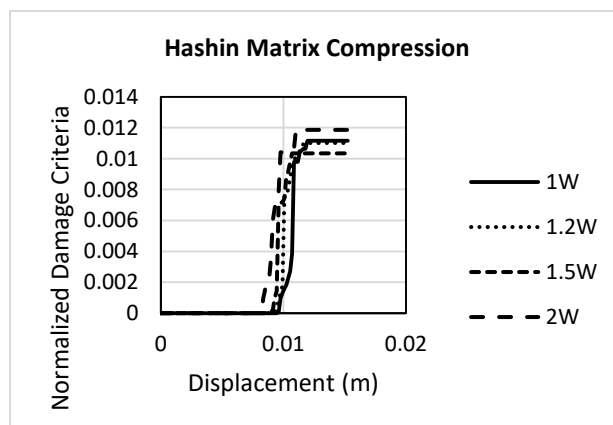
Another advantage of the simulation is the ability to quickly investigate how changes in part geometry can affect damage mechanisms. In this study, the finite element model was used to illustrate how damage progression can vary based on specimen width. Data was normalized based on number of elements (for Hashin & Johnson-Cook criteria) or interface nodes (for traction-separation law). Additional damage mechanisms are illustrated for all laminates in Appendix I.



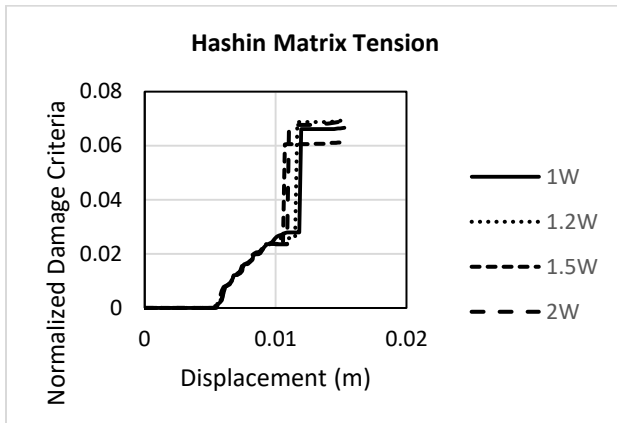
(a)



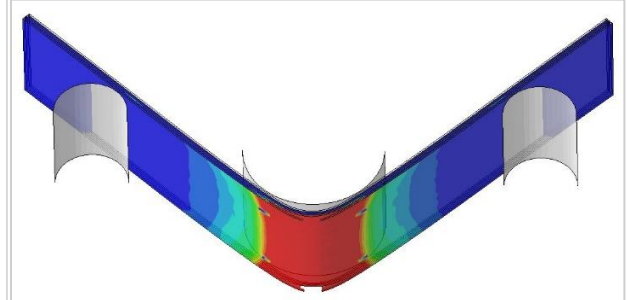
(b)



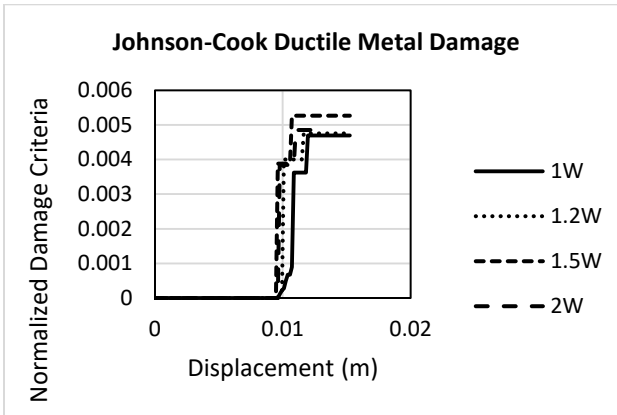
(c)



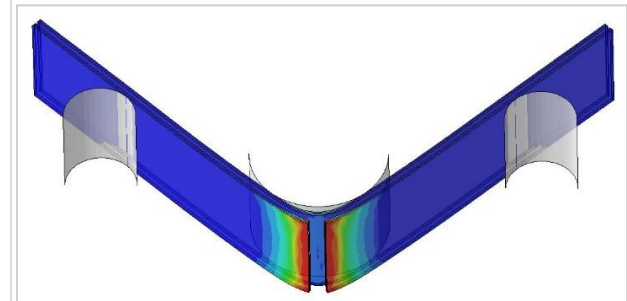
(d)



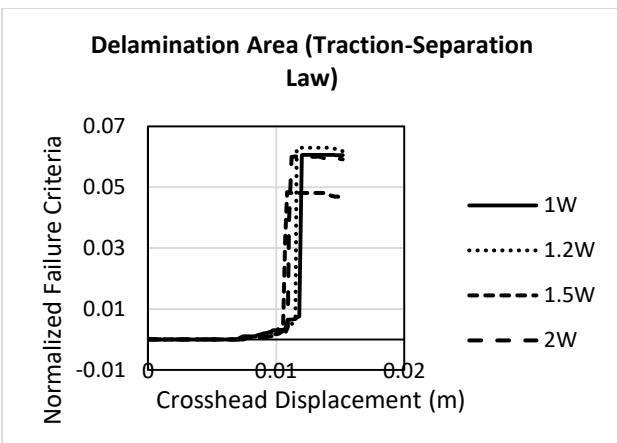
(e)



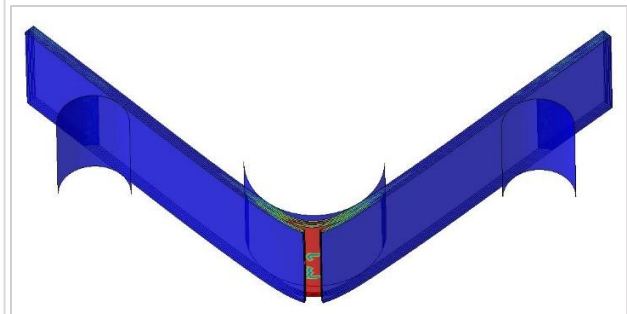
(f)



(g)



(h)



(i)

(j)

Figure 59. Width Effect on Fracture Mechanisms of FMLs

As shown in figures 59(a) and (b) and Appendix I, fiber compression damage occurs early in the loading, and progresses to the point of ply fracture. As the width of the specimen increases, the displacement at which fracture occurs decreases, while the percentage of fiber damage increases. Significant compression damage occurs in the lowest 90 degree ply, extending through most of the span.

Matrix compression damage is far more localized, as shown in figures 59(c) and (d) and Appendix I, and accounts for less of the total damage to the laminate. Due to the orthotropic nature of the material constitutive model, matrix compression is only shown to occur in the zero degree plies as the bottom plies fracture and the bending neutral axis is shifting. Again, with increased width the displacement at which matrix compression damage begins decreases, while its overall damage contribution stays nominally the same.

Matrix tension damage begins earlier in the loading and affects both zero and 90 degree plies, as illustrated in 59(e) and (f) and Appendix I. Simulations didn't show a difference in normalized damage as width was increased, however the amount of damage at ply fracture decreased with increasing width. Matrix tension damage primarily affected the lower 90 and zero degree plies, and was mostly localized at the point of load application.

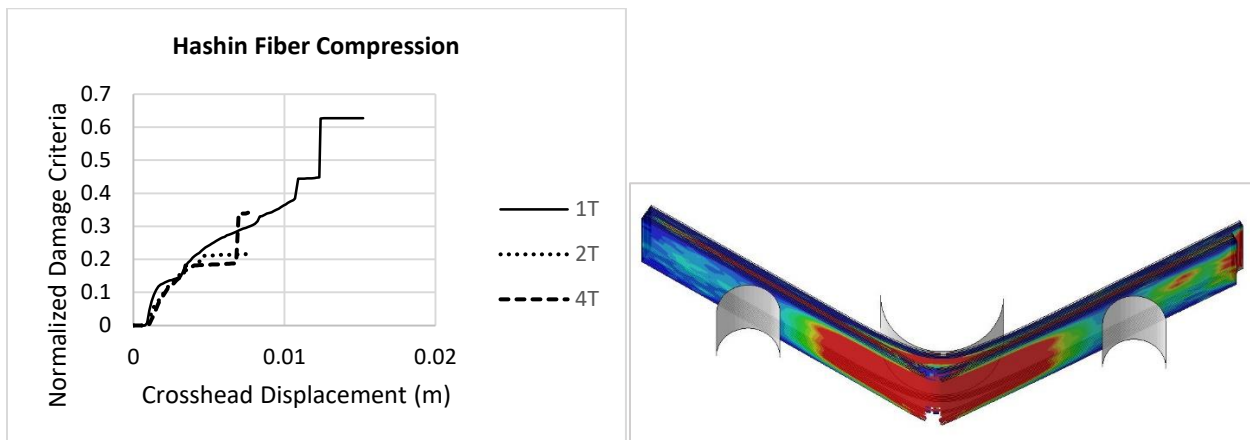
Johnson-Cook damage initiation criteria was met for the bottom two titanium plies at the point of ply fracture, shown in Figure 59(h). The width effect study indicates that for narrower specimens there is damage that occurs prior to ply fracture, while as width increases the fracture is much more brittle. This is consistent with the necking observed in the experimental work after the laminates had fractured. Damage is localized at the fracture location with slight necking visible at the outer edges of the fractured plies.

Ply fracture initiates the most severe debonding between the titanium and composite interfaces, shown by the traction separation law in Figures 59(i) and (j) and Appendix I. Prior to fracture, debonding occurs due to laminate flexure, with damage highly localized under the load point. The width effect study indicates that debonding prior to fracture is reduced with increased specimen width.

5.2.3 Thickness Effects

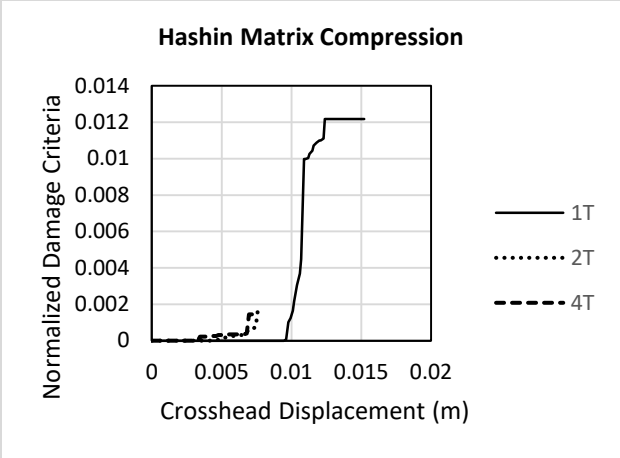
To assess the effect of metal volume fraction (MVF) on the behavior of a fiber metal laminate, additional titanium plies were added to the top and bottom, while retaining laminate symmetry. For the “2T” case the laminate simulated was [Ti, 90, Ti, 90, Ti, 0]s and for the “4T” case the laminate was [Ti, 90, Ti, 90, Ti, 90, Ti, 90, Ti, 0]s. Additional 90 degree plies were added to visualize the relative contribution of debonding at the Ti-graphite interface.

As shown below, the lower the thickness, the greater the degree of fiber compression damage. The amount of damage decreases significantly prior to first ply fracture with the addition of more plies. However, as shown in Figure 13i, the amount of delamination prior to ply fracture is significantly higher, suggesting that some damage energy shifts from fiber compression to delamination/debonding with thicker laminates.

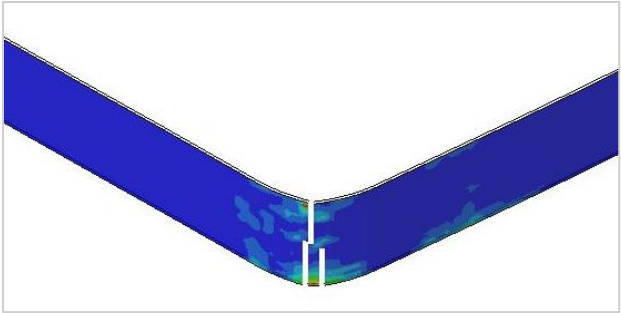


(a)

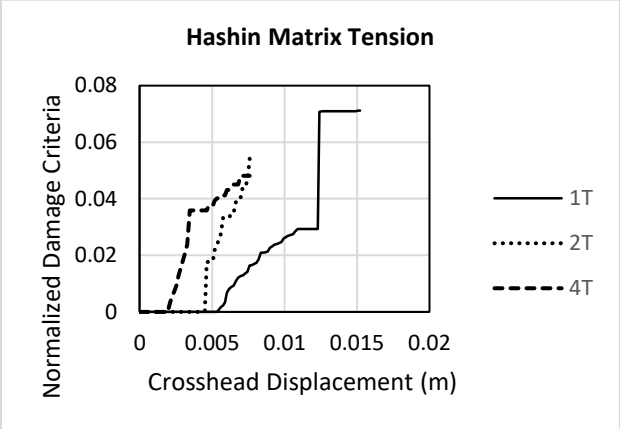
(b)



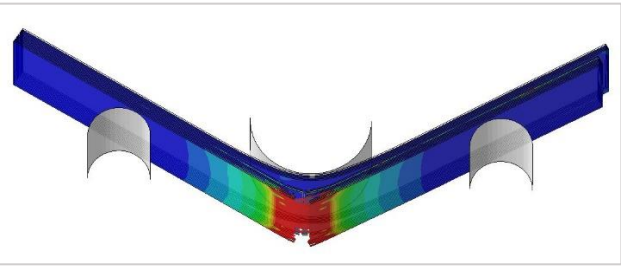
(c)



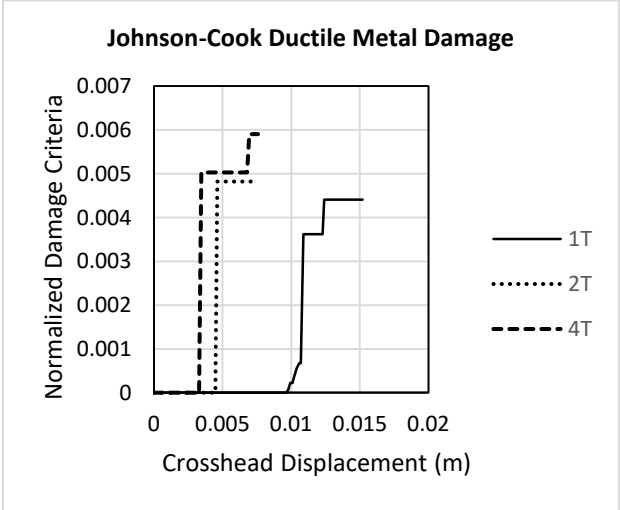
(d)



(e)



(f)



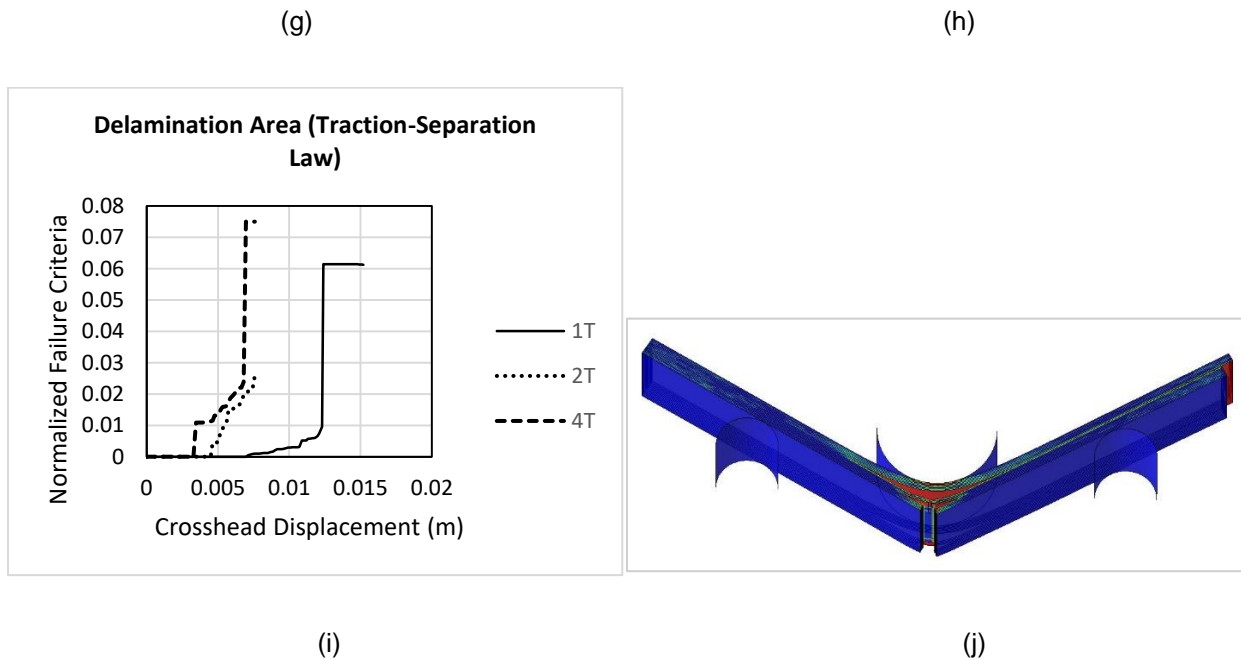


Figure 60. Thickness Effects on Damage Mechanisms of FMLs

Matrix compression damage was drastically reduced with the addition of titanium plies, as shown in Figure 13(c) and in Appendix I. More 90 degree plies were able to carry the transverse compressive load resulting from bending. Additionally, the transverse shear carried by the bonds with the added titanium plies resulted in more load transfer and lower matrix compression damage in the middle 0-degree plies.

As laminate thickness increases, matrix tension damage occurs faster and at lower crosshead displacement, illustrated by Figures 13(e) and 13(f) and in Appendix I. The tensile stresses in the bottom-most 90 degree plies increase much faster in the thicker laminates, and cause failure of these elements earlier in the loading. Once the bottom titanium face sheet fails, this 90 degree ply fails immediately. Subsequent 90 degree plies continue to experience tensile matrix failure as the next titanium ply fails, and so on. This effect results in a continued ramping of matrix failure after initial ply failure.

Johnson-Cook failure of ductile metal layers is driven by the failure strain of the bottom-most titanium ply in tension. Failure of this ply results in near-immediate failure of the next few 90 degree composite plies and titanium plies.

5.3 Static Loading of Thick Laminates

Quasi-static load-displacement data was collected for two specimens of the thick TiGr laminate. An Instron 5585H electro-mechanical test frame was used with a cylindrical cross-head, similar to the test setup for the impact tests. Support and crosshead diameters were the same as the impact setup as well. A crosshead rate of 1 mm/min was used, and total extension was 15 mm.

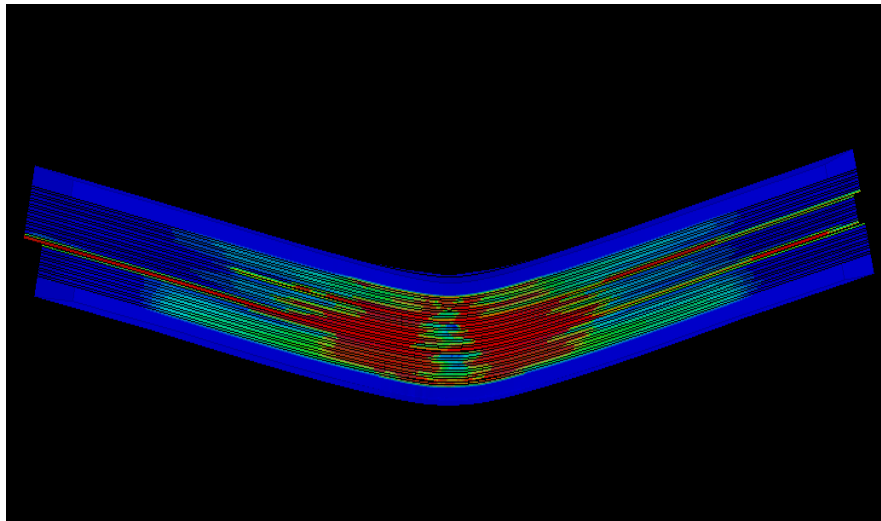


Figure 61. Numerical Model of Quas-Static Specimen

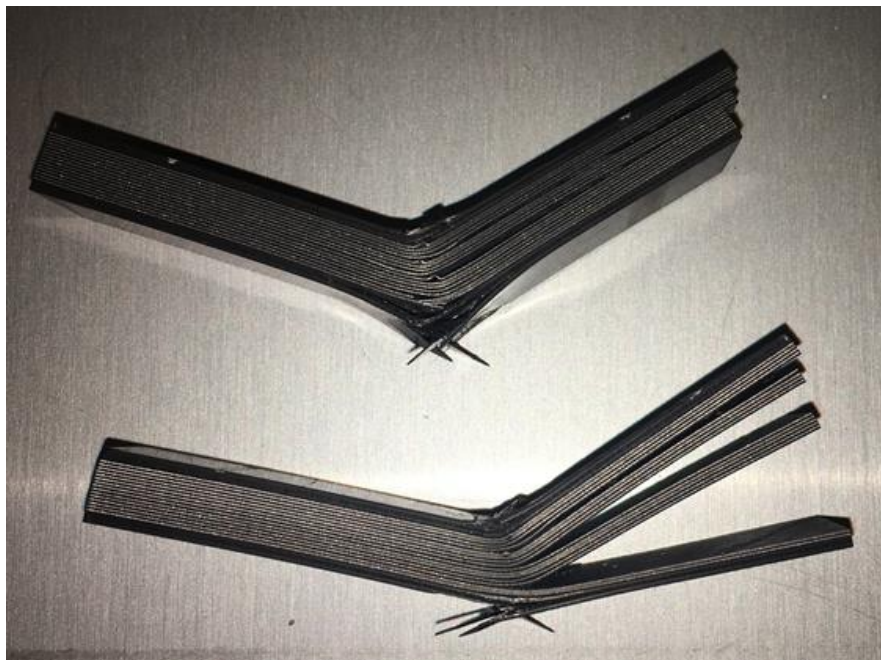


Figure 62. Quasi-Static Test Specimens after Loading

Progressive damage shows delamination advancing through the thickness of the laminate as the crosshead advances, remaining fairly localized in the region of highest curvature. At the same time, compressive buckling of the composite plies in the upper section of the laminate progresses, leading to half-span delamination at around 2.5 mm. Successive half-ply delaminations are indicated by step-wise drops in load shown in the following plots:

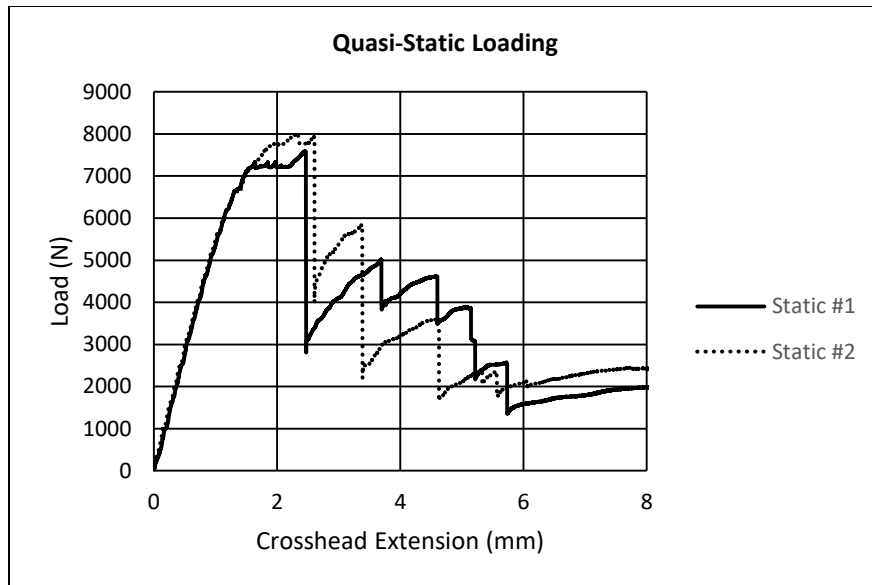


Figure 63. Load-Displacement of Quasi-Static Loading

Numerical modeling exhibits similar peak load and subsequent load drop as the first half-ply delamination advances to the free edge. The load then increases before another drop caused by another half-ply delamination. This is repeated several times until the laminate stiffness has decreased sufficiently to allow the remainder of the displacement. Figures illustrating all of the failure modes over the course of this loading can be found in Appendix I.

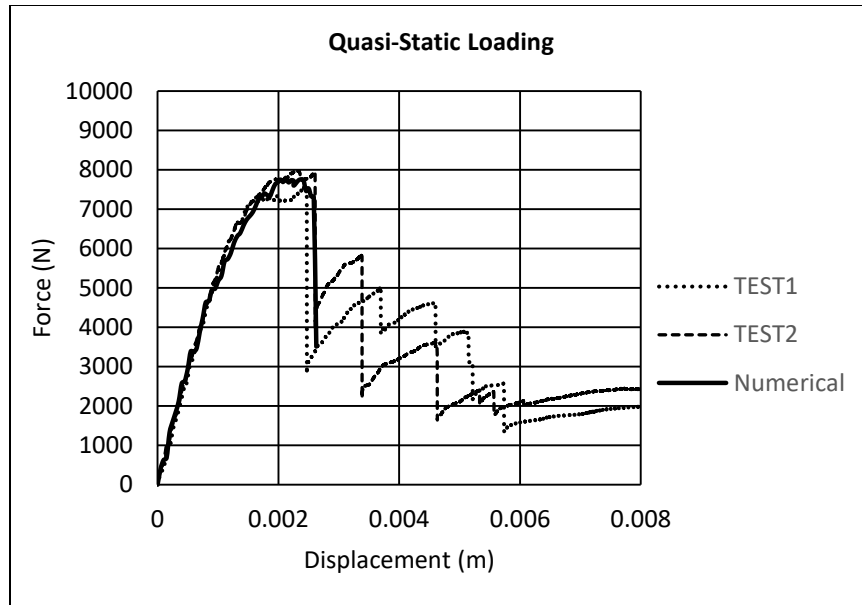


Figure 64. Load-Displacement Numerical Model Comparison

5.4 Low-Velocity Impact Loading of Thick Laminates

As described in Chapter 4, specimens were impacted at 2.5 m/s and 4 m/s. Plots of measured load vs. displacement are shown below. In general, the data repeatability prior to max load is good, while oscillatory load behavior after the first big load drop has similar amplitude and character. Additional load information is included in Table 15, showing that peak loads for 2.5 m/s impacts were around 9000 N, and around 10,400 N for 4 m/s impacts. Interestingly, impacts at 2.5 m/s indicate some elastic rebound toward the end of the contact interval, indicating residual flexural elasticity after dissipation of the impact energy, while impacts at 4 m/s do not rebound and exhibit more complete failure of the laminate. Some of the specimen data was determined to be unusable due to recording equipment anomalies, and this data was not included in the following plots.

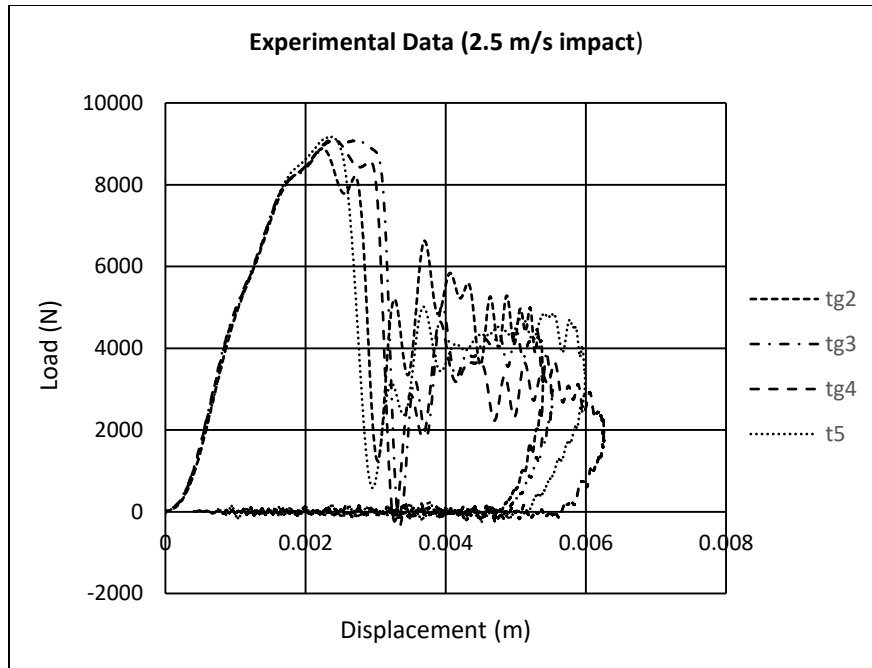


Figure 65. Load-Displacement of 2.5 m/s Impact Loading

Energy absorbed was calculated as area under the load-displacement curve via the relation:

$$E_a = \sum_{x=0}^n \left(\frac{P_n + P_{n-1}}{2} \right) (\delta_n - \delta_{n-1})$$

where P represents the load value at time-increment n , and δ represents the displacement. The value of absorbed energy at peak load was identified for each specimen, indicating the amount of energy the laminate was capable of absorbing at the point when initial major failure occurred. For the 2.5 m/s specimens there was some variation in this value between 10-15 J while for the 4 m/s group the spread was smaller with most specimens seeing about 12 J of energy absorption.

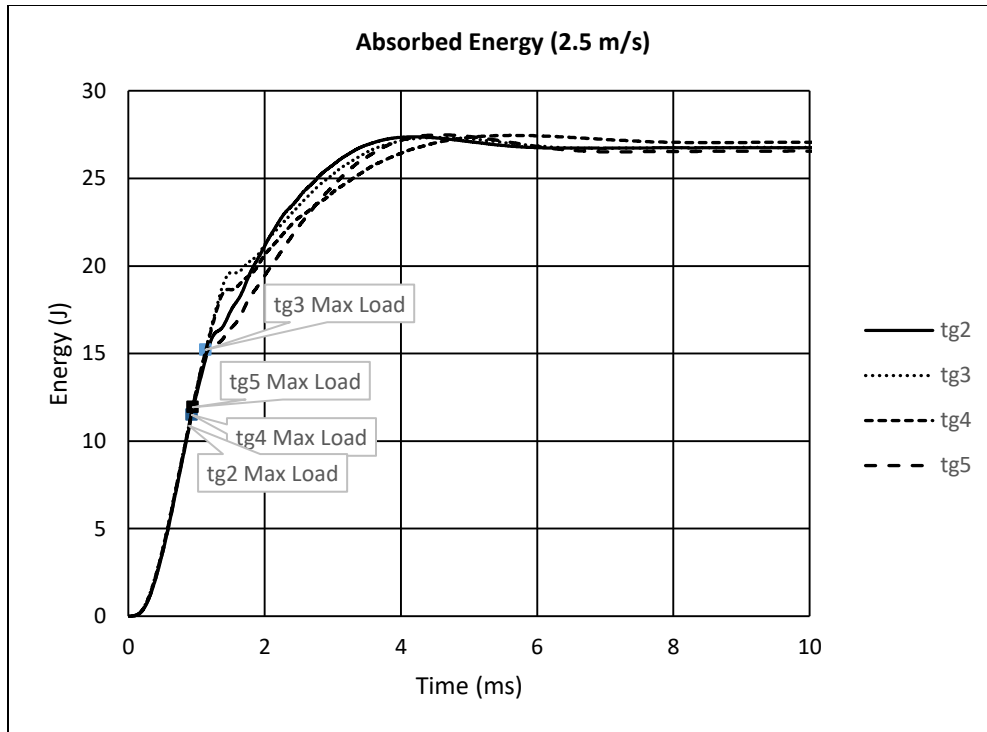


Figure 66. Absorbed Energy, 2.5 m/s Impact Loading

Numerical simulation data of the 2.5 m/s impact yielded good agreement with the load-displacement plots. Peak load was closely replicated, as was the magnitude of load drop and corresponding post-failure oscillation and rebound. Maximum displacement was matched closely, indicating the numerical specimen saw similar deflection characteristics, and thus would likely see similar

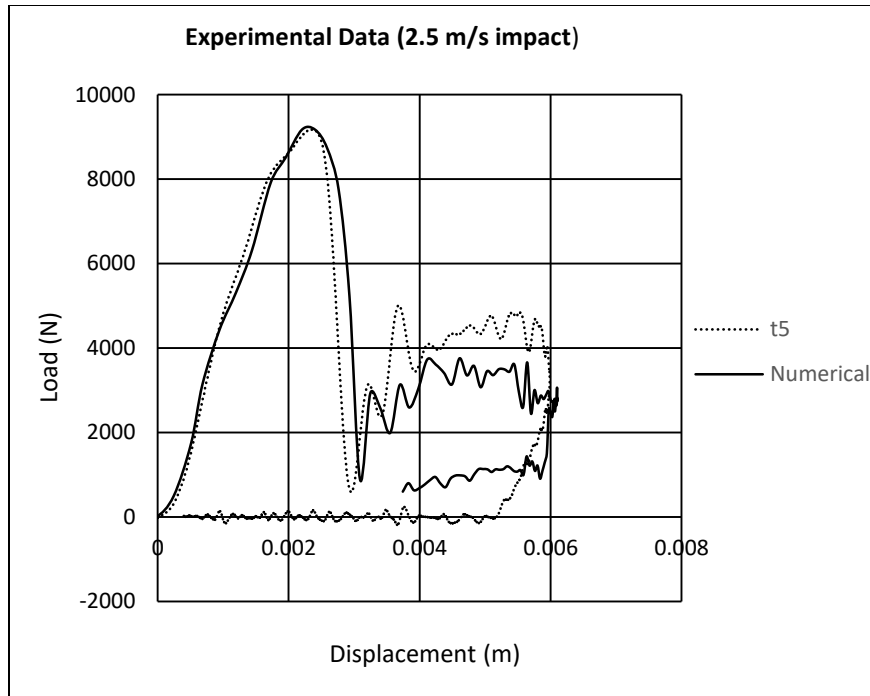


Figure 67. Numerical Comparison, 2.5 m/s Impact Loading

post-impact damage characteristics. High-speed video of the experimental impacts was recorded, and is presented below along with the corresponding numerical simulation frame. Additional frames depicting all damage variables during this timeframe are shown in the appendix.

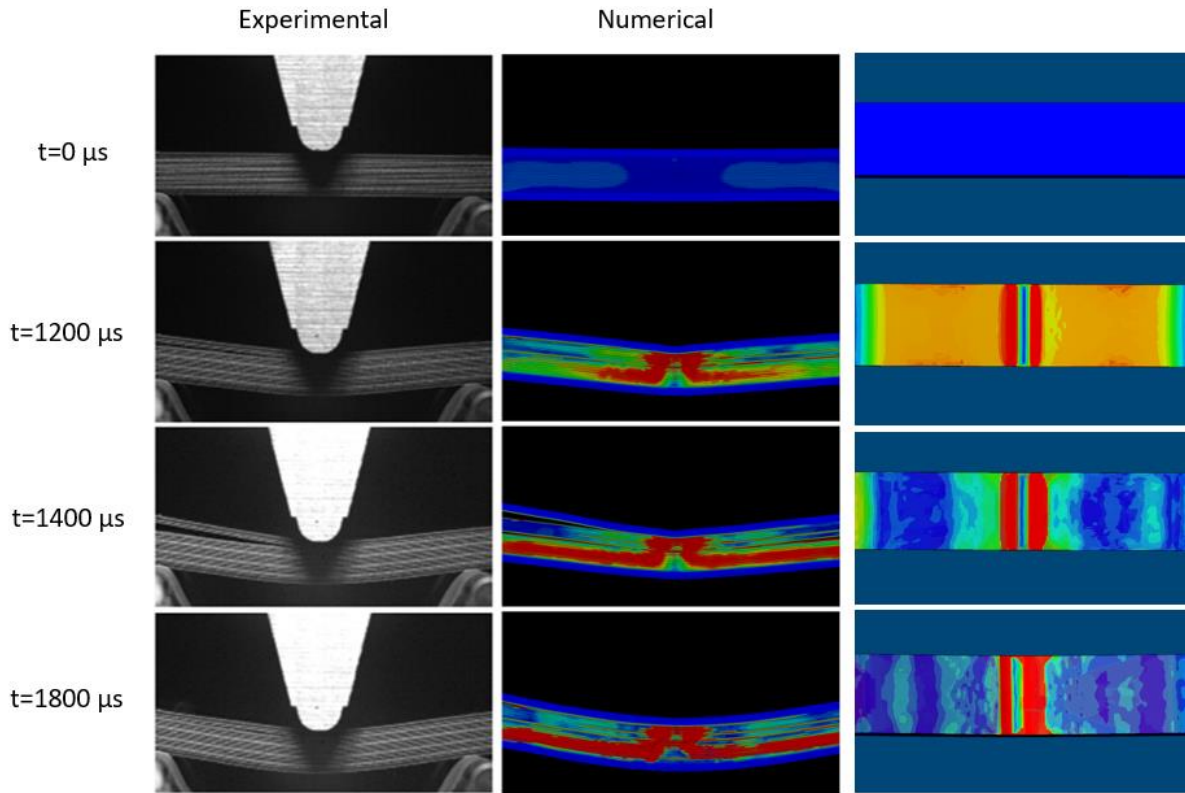


Figure 68. Delamination Damage Progression, 2.5 m/s Impact Loading

For both of the specimens illustrated first failure occurs at $t=1200\mu s$, when delamination becomes visible between the uppermost titanium layer and the adjacent composite ply. The delamination becomes more visible as the localized crushing action under the crosshead propagates mode-1 failure, prying the sections of laminate apart. At $1400\mu s$ the second failure becomes visible; the bottom composite plies can be seen fracturing. As the bottom ply is 45 deg, this fracture can be assumed to be driven by longitudinal shear in the bottom-most layer, leading to tensile fiber fracture of the bottom 45, 0, and -45 degree plies. At $1800\mu s$ the effects of load re-distribution can be seen, as the delaminated plies are pushed back into contact with the rest of the laminate, overall deflection increases, and tensile load shifts upward to the undamaged lower plies. As the numerical model of the traction-separation law damage variable shows, crushing under the crosshead causes localized delamination through the upper half of the laminate, which then spreads longitudinally along the load path toward each of the supports. Interlaminar shear causes delamination at the extreme lateral fibers, visible as red in the figures above. This delamination then propagates transversely inward as well as along the longitudinal front as laminate deflection increases.

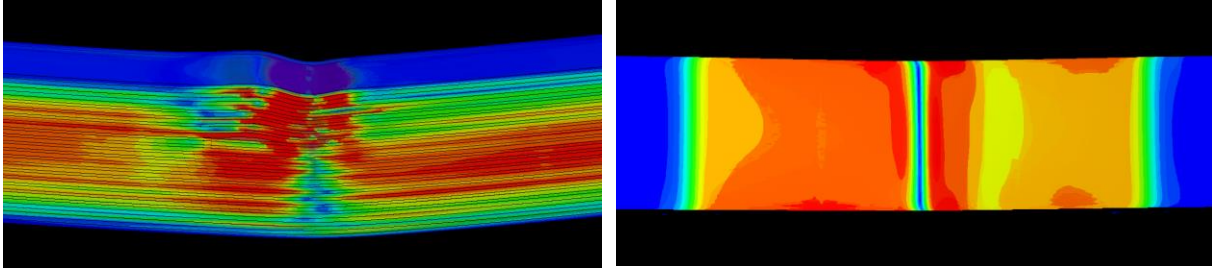


Figure 69. Delamination Damage Progression, Crosshead Indentation

With this laminate in particular it is the crushing action immediately underneath the crosshead that causes the highest deflection gradient in the uppermost plies, resulting in a localized delamination front at the uppermost titanium layer. Since the composite plies crush rather than absorbing energy into the transverse plane (as observed with face-sheet laminates) the deflection gradient is higher, forcing energy to be absorbed as delamination rather than plastic deformation. As stiffness degrades the delamination front accelerates through a half-span of the laminate. This is both a function of laminate thickness and associated higher shear stress in the outer upper and lower fibers, as well as a function of layup.

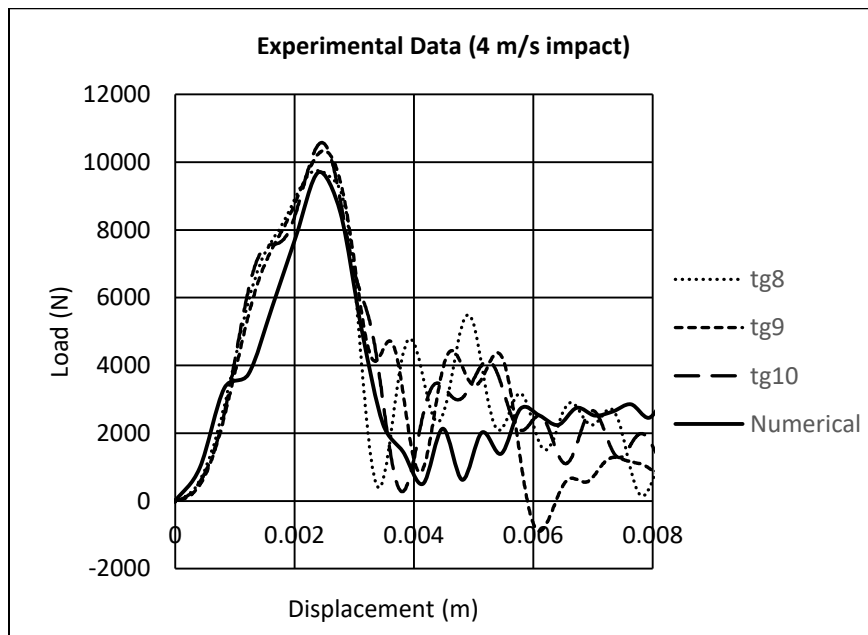


Figure 70. Load-Displacement of 4 m/s Impact Loading

Specimens impacted at 4 m/s exhibited higher peak loads, nominally around 10 kN. While there was some variance between acceptable specimens, the load-displacement behavior prior to peak loads is

again well repeated. After the initial load drop oscillation associated with continued damage propagation is similar in character, showing no elastic rebound.

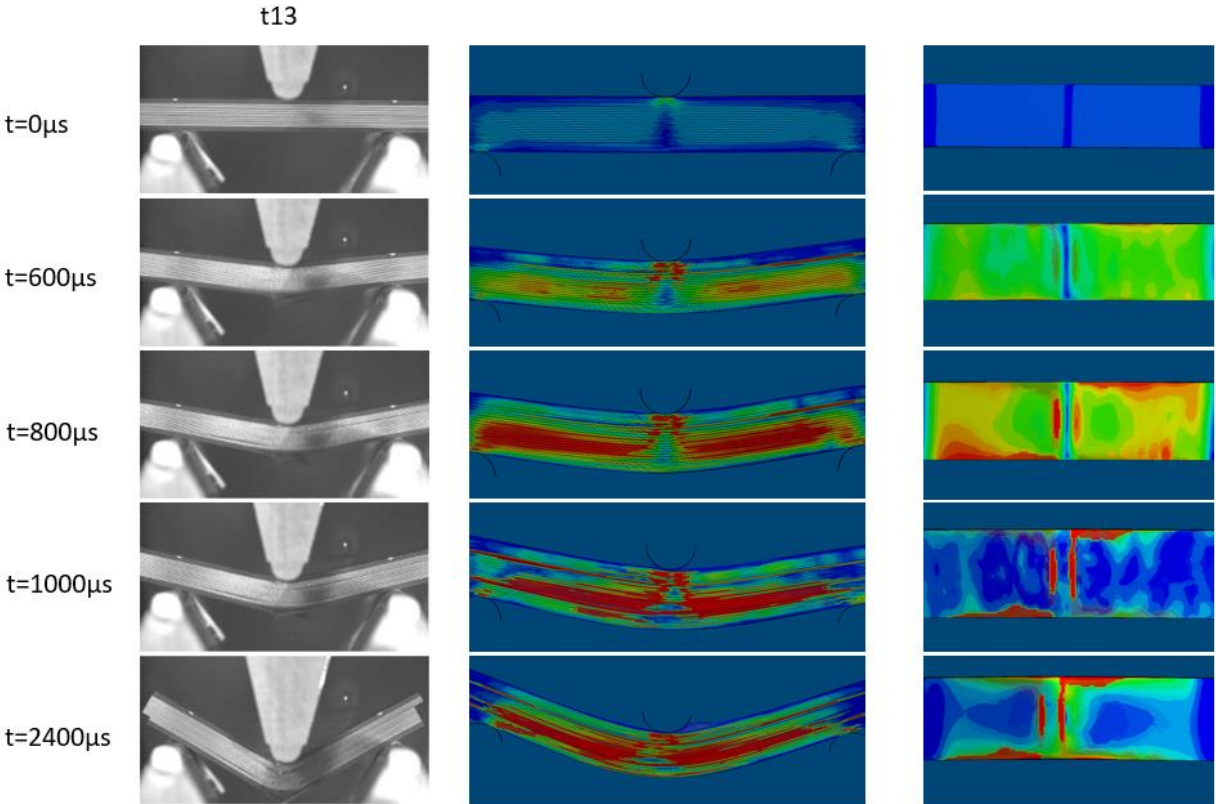


Figure 71. Delamination Damage Progression, 4 m/s Impact Loading

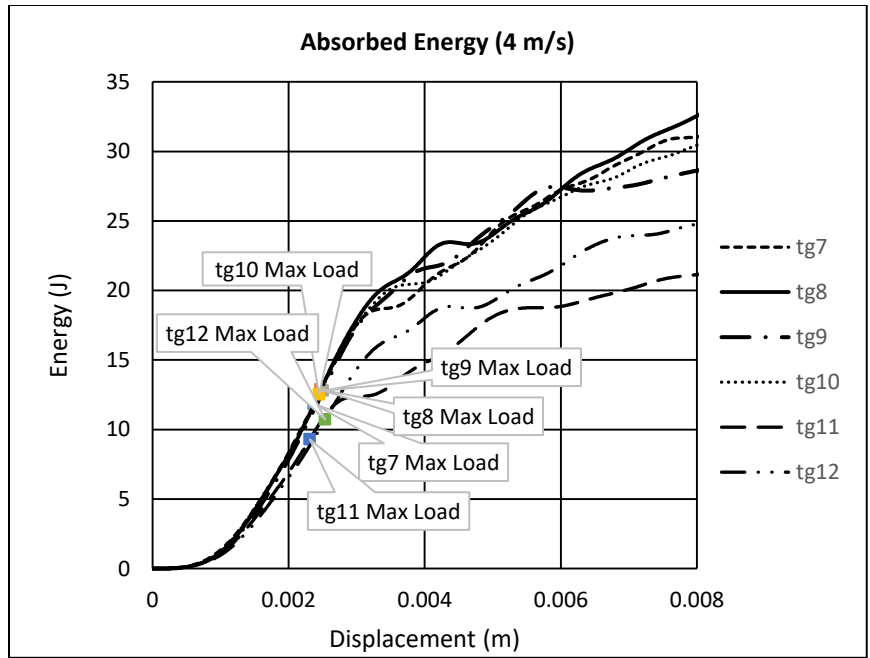


Figure 71. Absorbed Energy, 4 m/s Impact Loading

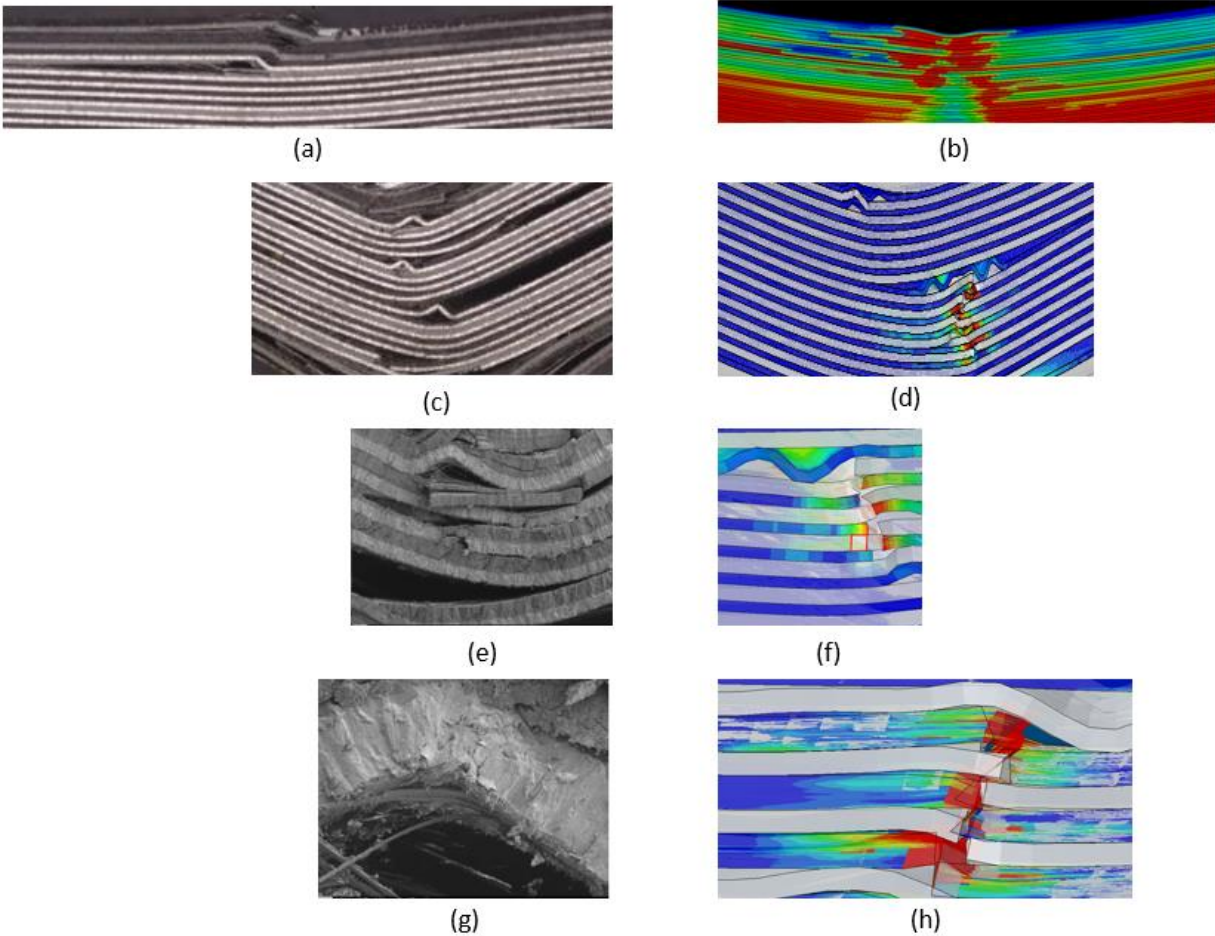


Figure 72. TiGr Laminate Damage Types indicating crushing and increased deflection gradient under crosshead (a), (b), titanium compressive buckling (c), (d), titanium buckling and tensile fracture transition (e), (f), and fiber fracture near regions of titanium buckling (g), (h).

The images again show progression of damage from initial delamination to final fiber fracture through buckling and tensile failure, as well as metal buckling and tensile failure. In the initial stages the initial delamination is again instigated by crushing and local deformation gradients under the crosshead, and this is almost immediately proceeded by delamination in the lower half of the laminate, as well as fiber and matrix fracture at the bottom exit plies. Looking at the numerical model the reason for this is clear; the load path extends downward through the laminate thickness from the crosshead, then splits out longitudinally toward the supports. As impact velocity increases the load path is increasingly pushed downward through the thickness then out to the supports through the lower plies. Thus the higher velocity impacts see more initial half-span delamination at the lower plies, compared to static and 2.5 m/s load cases.

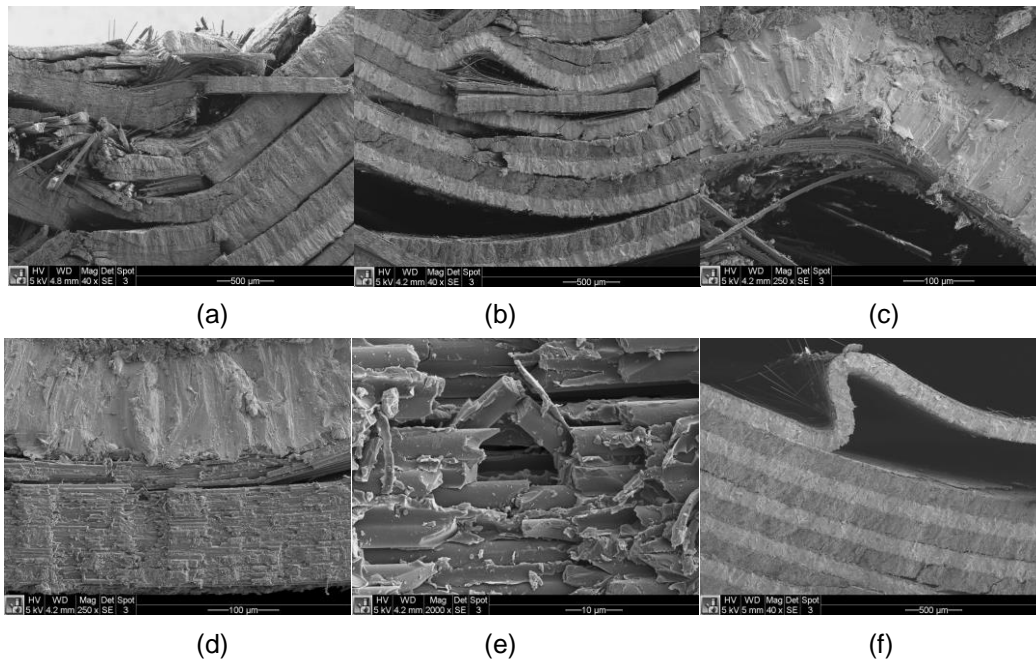


Figure 73. SEM micrograph for t7 (AWJ machined, $R_z=11.83 \mu\text{m}$) depicting (a) Top ply crushing, (b) Ti first ply buckling, (c) magnified view of Ti buckling, (d) Abrasive wear track, (e) magnified view of wear track and crack initiation site and (f) Ti buckling near the neutral axis of TiGr specimen

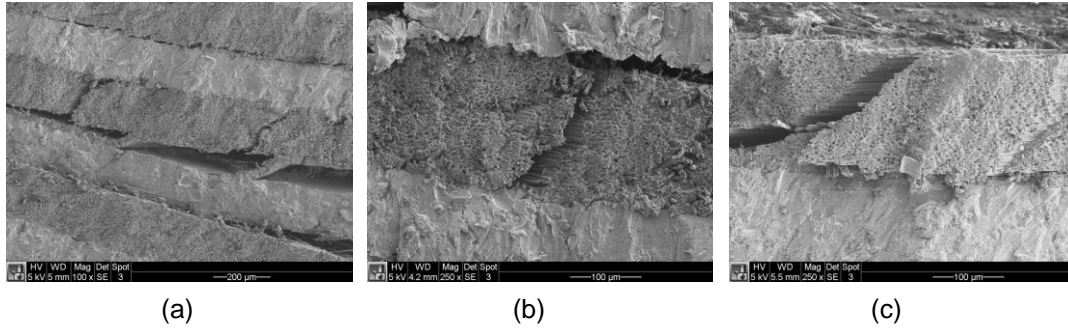


Figure 74. SEM micrograph for t7 (AWJ machined, $R_z=11.83 \mu\text{m}$) depicting (a) lateral cracking (b) lateral crack in striated channel and (c) lateral crack path

The SEM micrographs show some of the differences between machining methods of the specimens. Because interlaminar shear in the deflected specimen means that delamination stresses are highest at the edges of the specimens, the surface quality of the manufactured edge is hypothesized to affect bending performance.

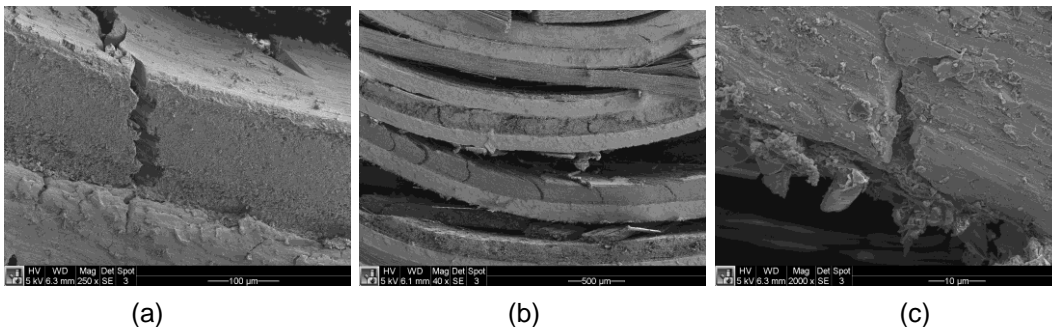


Figure 75. SEM micrograph for t12 (CNC trimmed, $R_z=31.5 \mu\text{m}$) depicting (a) lateral cracking (b) lateral crack in striated channel and (c) lateral crack path

CHAPTER 6: DISCUSSION

6.1 Laminates with Titanium Face Sheets

In laminates where titanium is used as a face sheet on the bottom and top layers, damage of the laminate is governed by plastic deformation and tensile failure of the titanium face sheets. Two principle modes have been identified for this case. The first mode when the bottom titanium ply remains intact is described by top titanium ply buckling and damage to the uppermost GFRP ply, accompanied by significant delamination of the GFRP plies. The second mode when the bottom titanium ply fails in tension is described by buckling of the top titanium ply, significant fiber breakage and matrix cracking through the GFRP layers, and delamination. In this failure mode final fracture is governed by fiber breakage. The second conclusion drawn is that the sequence of damage for TiGr laminates typically begins with buckling of the uppermost GFRP ply, immediately followed by buckling of the upper titanium surface. Damage propagation continues as a mix of intra and inter-laminar delamination through the thickness of the GFRP plies, until local deflection causes tensile failure of the lower titanium surface. Once the titanium surface has failed, the remaining GFRP fibers fail in tension, instigating final failure through the thickness. Because failure of the lowest titanium surface directly results in failure of the remaining composite, the damage resistance of the laminate is directly tied to the ability of the composite to absorb energy through delamination rather than directing the energy through the zone of localized plasticity. Finally, because the first indication of damage is the buckling failure of the uppermost GFRP ply and the uppermost titanium layer, visual inspection for impact damage is much easier with TiGr than with a traditional GFRP composite.

6.2 Thin Laminates and Size Effects

In the experimental data the edge trimming method didn't have an appreciable effect on failure strain or peak stress. Two distinct failure modes were observed; either the bottom four plies fracturing simultaneously, or the bottom two plies fracturing, followed by the next two in quick succession. The biggest difference was between fine and rough EDM methods, with fine EDM seeing similar peak stress but much greater strain at failure. When developing the numerical model assumptions were made about material properties based on previously published empirical data. While differences in modulus and ultimate stress exist based on processing and material pedigree, for a given material it is assumed that these differences are relatively small. However, when determining parameters for the traction-separation damage law it can

be assumed that these differences are much more layup-specific. Details such as titanium bonding surface pre-treatment, autoclave parameters, and metal-CFRP bonding agent can have a much larger effect on ultimate bond strength and fracture energy. Estimation of fracture energy values is currently done based on DCB and ENF data, using experimental compliance calibration to calculate G_c .

In both experimental and numerical cases the driver for laminate failure was the ductile failure of the titanium layers in tension. It can be seen that for thin laminates noticeable necking occurs at the bottom titanium ply prior to fracture. This necking is reduced in thicker layups with more titanium layers, as the greater number of 90 degree CFRP plies constrain transverse movement. Pre-fracture metal damage is also reduced in wider specimens, as is the presence of necking.

As laminate thickness increases, there is a general trend from more compressive damage in the CFRP plies to delamination damage through the traction-separation law. Although failure of the first metal ply remains the instigator for catastrophic failure, the amount of delamination damage prior to the big drop in energy is significantly higher in thicker laminates. This compressive damage, both in fibers and matrix, begins almost immediately with crushing damage under the crosshead, followed by fiber and matrix compressive damage in the upper plies. In the original laminate the delamination damage remains localized under the crosshead, while the thicker plies experience more disperse damage, followed by complete delamination.

Delamination increased with the addition of plies, and a greater percentage of the bonded area delaminated prior to ply fracture. The decrease in compressive fiber and matrix damage along with increased delamination suggests that with thicker laminates delamination plays a greater role in pre-fracture damage than material strength. Also of note is that with the thin laminate the mode of delamination damage accompanying ply fracture was mode I, whereas with the thicker laminate the traction-separation law wasn't as sensitive to ply fracture, but experienced a later large mode II fracture at the lower interface between the titanium and 0-degree plies. This would suggest that there is a thickness at which the mode of delamination damage shifts from primarily mode I fracture at the failed plies to the more global mode-II fracture at the area of maximum interfacial shear stress. One explanation of this effect is that when the bottom plies fracture, the load they were carrying in tension is re-distributed through the remaining intact plies via the

traction-separation law. The primary mode of delamination fracture switches when the load re-distribution exceeds the imposed maximum shear value of the traction-separation law. This yielding is preceded by linear softening and fracture, as described earlier.

6.3 Static & Low-Velocity Impact Loading of Thick Laminates

A fundamental difference between laminates with titanium face sheets and thick laminates with intermediate titanium plies was illustrated by these experimental and numerical tests. Laminates with face sheets have failure modes that are dominated by the tensile or buckling behavior of the outermost titanium plies, which means the failure of the laminate is tied closely to the properties of titanium. In these thicker laminates the primary failure modes were driven by the composite layers and the interfacial bonds between composite and titanium layers. The numerical simulations clearly illustrated how localized crushing of composite plies under the impactor resulted in a locally increased deformation gradient at the interface between composite and upper-most titanium layer. This deformation gradient caused a local delamination at this interface which then propagated outward toward the free edge. Continued laminate displacement caused the complete half-span delamination and the subsequent buckling of the adjacent titanium ply at or near the point of load application. Load transfer occurs within the remaining bonded lamina, and a new delamination front forms between an intermediate titanium ply and adjacent composite ply. The process is then repeated, resulting in another drop in the load/displacement curve. It should be noted that in addition to compressive crushing under the crosshead the uppermost composite plies experience fiber buckling and extensive fiber/matrix debonding, while the lowermost composite plies experience corresponding tensile

fiber fracture, matrix cracking, and fiber/matrix debonding as these lamina fail in tension/bending.

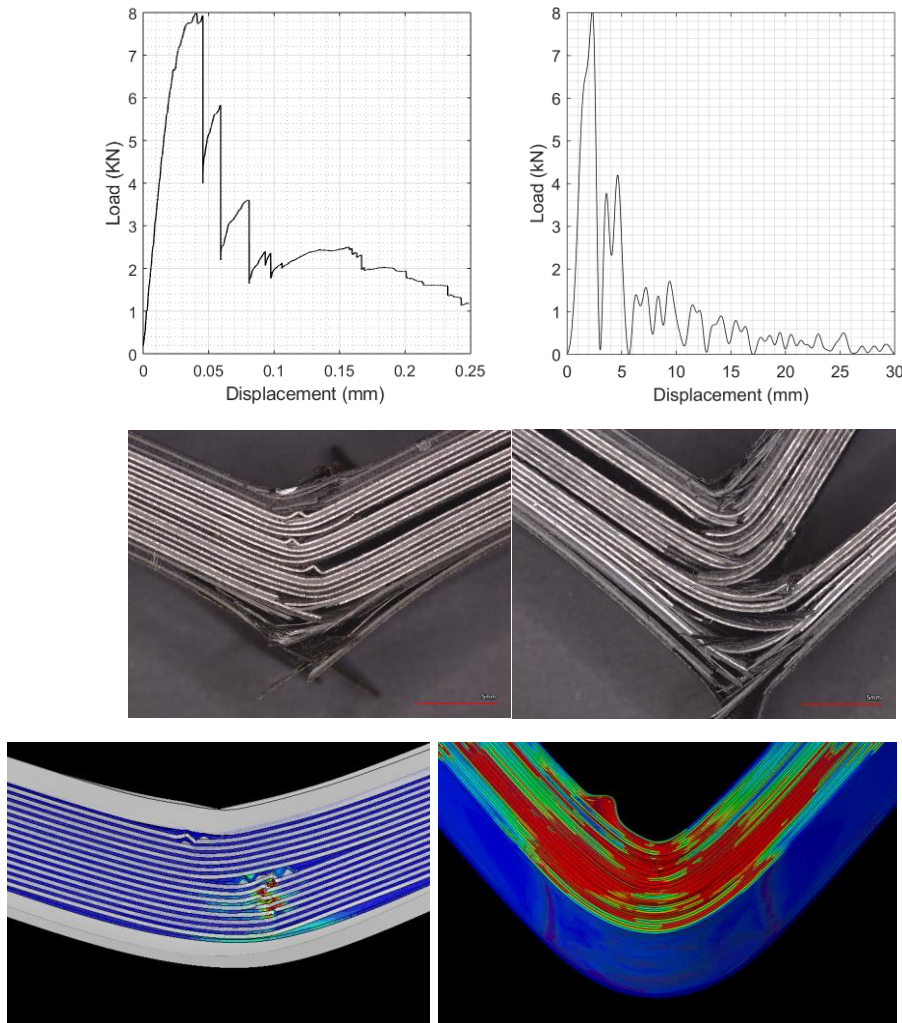


Figure 77. Differences between Quasi-Static and Low-Velocity Impact Loading

Differences between static and dynamic loads were subtle; static loading illustrated by abrupt drops in the load/displacement curve coincident with half-span delaminations at several thru-thickness intervals, while dynamic loads demonstrated a smooth drop in load coincident with a general drop in stiffness associated with impact damage. Damage in the metallic layers also exhibited differences between quasi-static and impact loading. Quasi-static specimens exhibited buckling behavior evident by “rippling” of the metallic layers after a half-span delamination had occurred. As load is re-distributed after the delamination, the metallic ply that suddenly finds itself on the upper surface of a section of bonded laminate thickness experiences a sudden rise in compressive stress. This causes the rippling effect as the ply buckles. During

dynamic loading the time interval was much shorter, and this resulted in more evident tensile failure of titanium plies, as tensile failures occurred in sequential plies concurrently.

For impacts of different magnitudes the numerical simulations allow visualization of the relative effect of metal plasticity on overall impact energy absorption. The following plot shows total internal energy during the 2.5 m/s and 4 m/s impacts, as well as the energy dissipated by plastic deformation of the metal layers. The kink in the curve corresponds to the major load drop in both cases, occurring during the half-span delamination.

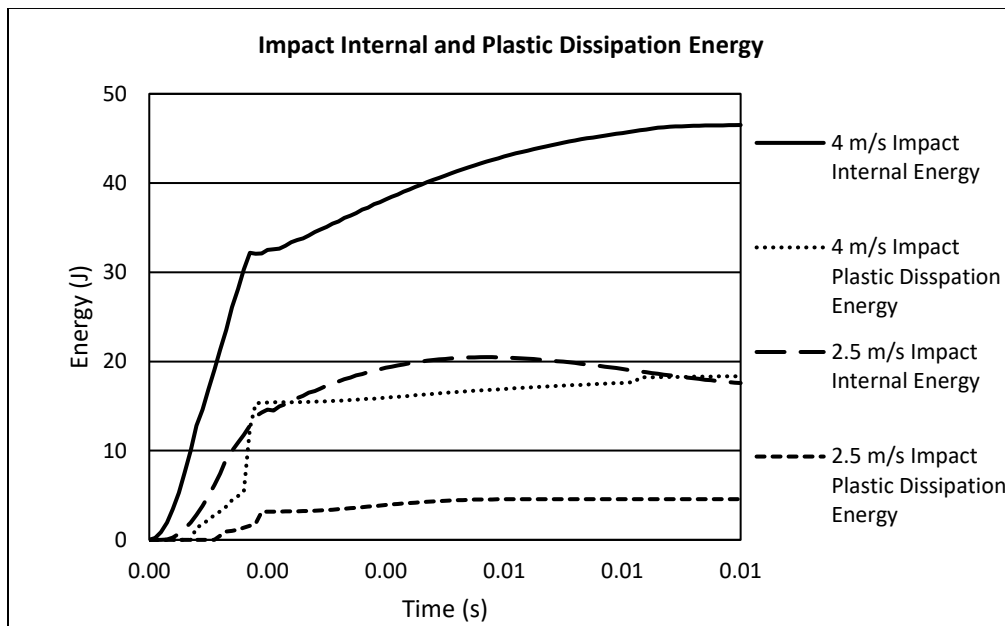


Figure 78. Internal and Plastic Dissipation Energies for 2.5 and 4 m/s Impact Simulations

During the 4 m/s impact the plastic dissipation energy level is roughly half the total internal energy of the specimen, while during the 2.5 m/s impact the plastic dissipation energy level is much lower. This reinforces the hypothesized role of metallic layers in fiber metal laminates: during impact the metal layers absorb a greater percentage of the overall impact energy through plastic dissipation leading to greater energy absorption capability. This effect increases with increasing impact velocity.

6.4 Classical Laminate Theory

The formulation of thru-thickness stresses in composite laminates using classical laminate theory is well documented. Using stiffness components for individual unidirectional composite lamina with

appropriately applied transformations to resolve properties into a global coordinate system, a stiffness matrix can be constructed for an entire laminate. Considering titanium as an isotropic material, a similar matrix can be constructed for TiGr laminates. The result is a constitutive equation describing the laminate stress-strain relationship. Classical laminate theory is subject to linear elastic behavior, is only valid for small displacements, and is subject to the following additional assumptions:

- Perfect bonding is assumed between lamina; that is, no delamination damage or softening, and no slippage between layers. Displacement must be continuous through the thickness.
- Properties of each lamina are assumed to be constant through the lamina thickness. Because each lamina is described by its own stiffness matrix, the in-plane elastic constants are assumed to be homogenous.
- A state of plane stress is assumed for each lamina.
- Lamina elastic constants may describe isotropic, orthotropic, or transversely isotropic properties.
- Deformation according to Kirchoff-Love assumptions for thin plates:
 - Lamina normals to the laminate midplane remain straight and normal to the midplane after deformation.
 - These normals do not change length.

Formulation of the A (extensional) and D (flexural) matrices is described in Appendix II. The moment equation describing the 3-point-bending load case is then used to calculate lamina stresses.

The moment equation is given by:

$$M = \begin{bmatrix} \frac{-PL}{4} & & \\ & 0 & \\ & & 0 \end{bmatrix}^T$$

where P is an arbitrary load, L is the span, and w is the width. Lamina middle-surface curvatures can then be found from:

$$k = D^{-1}M$$

Finally, flexural stresses can be calculated by:

$$\sigma_{lamina} = Q_{lamina}k$$

where Q is the transformed reduced stiffness matrix for each lamina. The stress in each specific lamina must finally be multiplied by the distance from the laminate midplane to the *lamina* midplane, given the stress distribution through the thickness of the laminate as shown below:

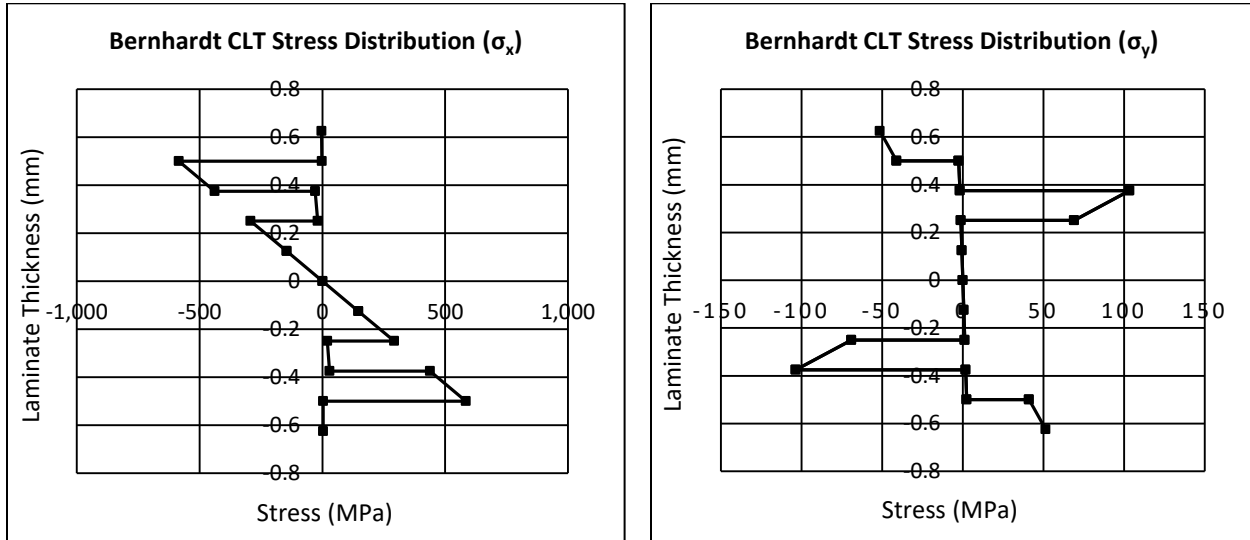


Figure 76. Bernhardt Laminate CLT Stress Distributions

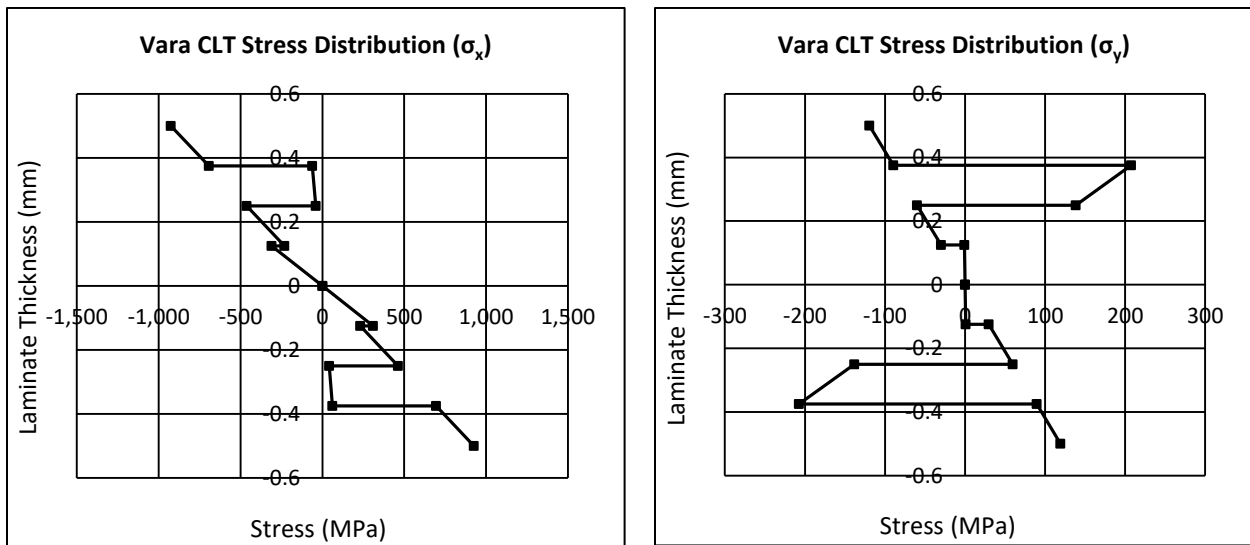


Figure 80. Vara Laminate CLT Stress Distributions

Comparing the distributions through the Bernhardt and Vara laminates, classical laminate theory can help to explain the fracture behavior observed during experimental testing. The Bernhardt laminate had relatively stiff 0-degree plies immediately underneath the titanium face-sheets, and these stiffer plies

carry the majority of the longitudinal load. Thus it is the buckling of the uppermost 0-degree composite ply (for mode-1 failure) or the lowermost 0-degree composite ply (for mode-2 failure) that governs catastrophic failure. The titanium ply carries much less of the load until the composite fails, then abruptly fails either in buckling or tension. As shown in the numerical model, delamination in thin laminates is mostly localized prior to ply fracture meaning there is little load re-distribution through the thickness. The Vara laminate had 90 degree plies under the titanium face sheets, followed by another layer of titanium. Thus the longitudinal load is primarily carried by the titanium layers. In this case fracture was governed by tensile titanium failure at the lower plies, immediately proceeded by failure of the 90 degree ply. Then either the next titanium ply failed as well, or soon thereafter.

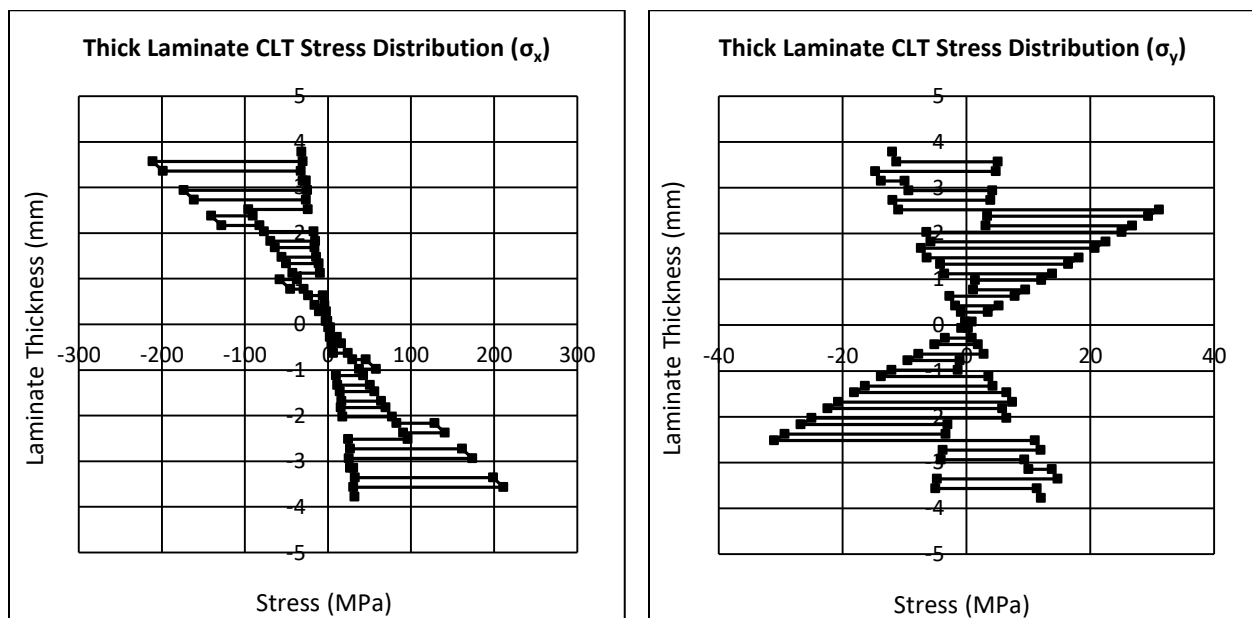


Figure 81. Thick Laminate CLT Stress Distributions

Classical laminate theory provides an interesting picture of the thick laminate, demonstrating how titanium layers act as an intermediary longitudinal load bearing layers between 45/-45 layers and 0 degree layers. Since the failure progression of these laminates was more global, and significant localized indentation damage likely instigated initial delamination, this representation is only representative of initial loading state, and doesn't represent most of the load history. For cases with complex damage mechanisms extending through the time-history of the laminate numerical modeling with associated damage remains the optimal tool for damage characterization.

6.5 Metal Volume Fraction

To investigate the effect of metal volume fraction on fracture performance it was necessary to propose a common framework for evaluating different laminates. Because different layups typically produce different peak loads under impact loading, it is difficult to make a like comparison. The numerical model provided a good framework for such a comparison, as laminates with identical dimensions and load conditions could be constructed with different metal-volume-fractions. Because it was desirable to emulate similar metal-composite bonding conditions the “4T” Vara laminate was chosen for the MVF comparison. Two additional laminates were formulated with metal volume fractions of 0.18 and 0.59, but with the same thickness dimension as the 4T laminate. The layups for these laminates were as follows: for the 0.18 MVF laminate the titanium layer was .189 mm thick and the layup was $[Ti, 0, 90, 90, 0, 0, 0]_{sym}$ and for the 0.59 MVF laminate the titanium layers were .203 mm thick and the layup was $[Ti, 90, Ti, 90, Ti, 0]_{sym}$. In all cases the modeled specimens had a total laminate thickness of 2.056 mm.

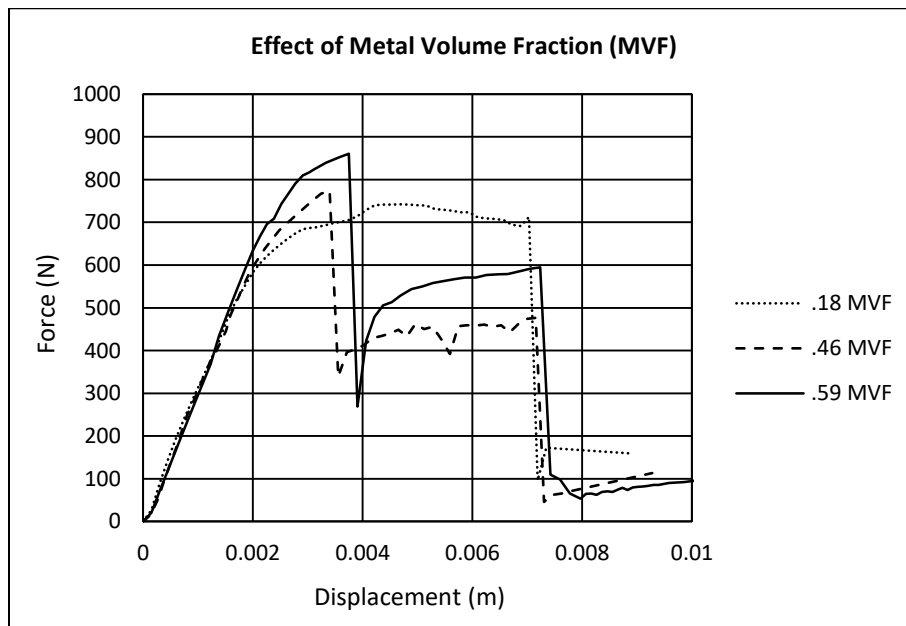


Figure 82. Force-Displacement of MVF-comparison Models

As shown in the above figure, the laminate with the lowest MVF shows a distinctly different failure mode than the other two specimens. This laminate has titanium face sheets only, and exhibits significant internal composite ply damage prior to upper titanium ply buckling (see Appendix I), which instigates the large drop in force. This failure mode is similar to the Mode 2 failures observed by Bernhardt, but with more

extensive compression damage to the composite layers. Because this test was run as a quasi-static load case there is no rebound in displacement. The two specimens with higher MVFs show similar failure modes; tensile failure of one or more of the titanium layers is followed by increasing delamination and load transfer to the upper plies as the load increases again, followed by half-span delamination coupled with additional tensile metal fracture resulting in the second major load drop. The peak load of the laminate increases with greater MVF as does the first failure displacement, however the second load drop occurs at roughly the same laminate displacement regardless of MVF. The damage progression of the .18 MVF laminate shows extensive compressive damage in the transverse fibers of the composite layers, beginning in the upper half of the laminate due to the Poisson effect (in ply adjacent to titanium) and orthotropic nature of unidirectional composites (in plies adjacent to longitudinally oriented composite). Associated compressive matrix damage is localized to either side of the crosshead, then converges in the upper half of the thickness. Delamination begins between the upper titanium ply and adjacent composite in the region of the crosshead, leading to compressive buckling failure of the upper titanium followed by overall buckling failure of the laminate.

The effect of increased MVF shifts the failure mode location from the upper to the lower surface, although both modes are driven by compressive failure of transversely-oriented adjacent composite layers. In laminates with face sheets (lower MVF) the progression of damage under quasi-static loading begins at the upper surface, while in laminates with higher MVF the failure begins at the lower surface with final failure depending on tensile fracture of titanium.

Comparison of these numerical results with experimental data is complicated by the fact that different specimens had different layups, thicknesses, geometries, and load types. To construct a notional comparison these variables would have to be normalized to show the effect of MVF. The method proposed for such a comparison follows, that peak load and energy absorbed at the point of peak load will nominally vary with flexural rigidity. Flexural rigidity is the product of longitudinal flexural modulus and moment of inertia, and therefore considers both the laminate stiffness (derived using classical laminate theory) as well as the individual specimen geometry. Derived values for all of the specimens detailed in this body of work are listed below. Derivations are detailed in the appendix.

Table 15. Specimen Flexural Rigidity Comparison Data

Specimen	MVF	Max Load (N)	Absorbed Energy at Max Load(J)	Flexural Modulus (Gpa)	Flexural Rigidity (N*m ²)	Normalized Max Load	Normalized Energy at Max
Bernhardt 1st Mode	0.197	400.000	1.700	103.203	0.251	1592.295	6.767
Bernhardt 2nd Mode	0.197	450.000	2.025	103.203	0.251	1791.331	8.061
Vara #4	0.455	195.520	1.206	74.359	0.056	3495.517	21.563
Vara #5	0.455	168.934	1.093	74.359	0.052	3258.459	21.086
Vara #6	0.455	196.538	1.120	74.359	0.058	3378.958	19.259
Vara #13	0.455	216.640	1.034	74.359	0.057	3771.435	17.994
Vara #14	0.455	206.255	0.886	74.359	0.055	3762.465	16.164
Vara #15	0.455	203.125	0.824	74.359	0.055	3699.792	15.018
Vara #3	0.455	223.538	1.317	74.359	0.056	3962.768	23.354
Vara #7	0.455	210.144	1.050	74.359	0.055	3801.893	19.002
Vara #8	0.455	191.939	1.194	74.359	0.051	3783.588	23.544
Vara #9	0.455	222.204	1.091	74.359	0.056	3974.043	19.505
Vara #10	0.455	210.194	1.107	74.359	0.054	3879.636	20.423
Vara #11	0.455	206.729	1.199	74.359	0.054	3809.871	22.097
Vara #12	0.455	195.952	1.059	74.359	0.051	3840.800	20.756
TG1	0.279	9912.100	11.605	66.523	29.562	335.296	0.393
TG2	0.279	8886.700	10.823	66.523	30.722	289.261	0.352
TG3	0.279	9085.600	15.413	66.523	30.438	298.495	0.506
TG4	0.279	9105.100	12.329	66.523	29.823	305.308	0.413
TG5	0.279	9170.900	11.798	66.523	30.722	298.512	0.384
TG6	0.279	9150.500	13.747	66.523	29.562	309.533	0.465
TG7	0.279	9756.200	11.851	66.523	29.562	330.022	0.401
TG8	0.279	10743.500	12.679	66.523	30.722	349.700	0.413
TG9	0.279	10341.700	12.691	66.523	30.438	339.763	0.417
TG10	0.279	10584.100	12.622	66.523	29.823	354.902	0.423
TG11	0.279	8055.200	9.446	66.523	23.740	339.313	0.398
TG12	0.279	8345.300	10.713	66.523	26.036	320.534	0.411
Static-1	0.279	7586.558	12.850	66.523	31.550	240.458	0.407
Static-2	0.279	7982.210	12.107	66.523	31.550	252.998	0.384
Vara 1.5W (numerical)	0.455	330.093	1.800	74.359	0.089	3718.685	20.278
Vara 2W (numerical)	0.455	436.316	2.000	74.359	0.118	3686.511	16.898
Vara 2T (numerical)	0.455	418.776	1.210	67.000	0.196	2142.061	6.189
Vara 4T (numerical)	0.455	773.692	1.300	63.742	0.441	1754.894	2.949
Vara .18 MVF (numerical)	0.180	742.194	2.494	63.230	0.437	1697.082	5.703
Vara .59 MVF (numerical)	0.590	860.855	1.939	77.822	0.538	1599.323	3.602

Although the value obtained by normalizing peak load using flexural modulus has no physical significance, it provides a useful tool for comparison of laminates. Plots of normalized peak load and energy absorbed at peak load are shown below.

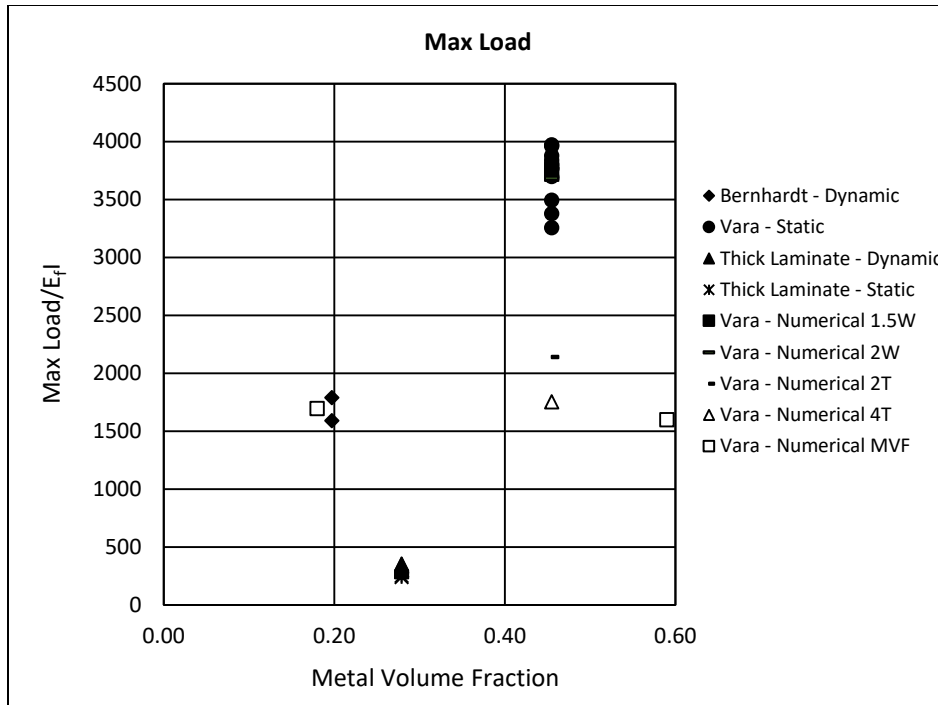


Figure 83. Laminate Max Load Normalized by Flexural Rigidity

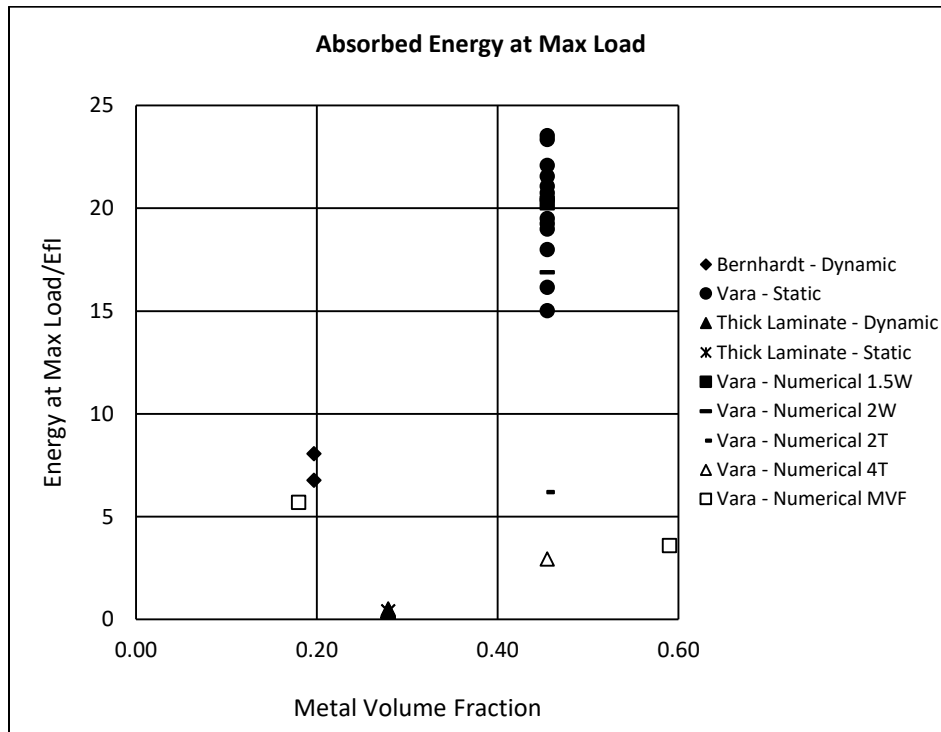


Figure 77. Laminate Absorbed Energy at Max Load Normalized by Flexural Rigidity

As shown, peak load increases significantly with metal volume fraction in thin laminates. The spread of normalized peak loads for Vara's specimens are roughly double that of Bernhardt's and the metal volume fraction is roughly double as well, indicating the viability of this method as a rough comparison tool between laminates. For the thick laminate the normalized max load and energy absorbed are significantly lower; this can be explained by examining the failure modes of each of these laminates. In both the Bernhardt and Vara laminates the peak load occurred just prior to tensile failure of titanium layers, whether this failure was propagated by microbuckling of the adjacent composite ply or titanium tensile fracture. In the thick laminate the primary failure mode (prior to the first major load drop) was delamination closely coupled with exit ply fiber breakage. The plot indicates that this failure mode is a significantly lower-energy failure mode than those experienced by the thin laminates. Presumably, the cause of the difference in failure modes could be related to specimen geometry. The thin laminates had thickness-to-span ratios of .022 for Bernhardt and .025 for Vara, while the thick laminate had a ratio of .151, roughly six times higher. It can be assumed that at some length-to-thickness ratio between .025 and .151 the primary failure mode changes from tensile/compressive fracture to delamination, and that this difference accounts for the varying degree of rigidity-specific peak load and energy absorption. The numerical Vara simulations added plies, but didn't significantly change the MVF. However peak loads and absorbed energy dropped significantly when related to flexural rigidity. This suggests that flexural rigidity itself, and not solely MVF may be a determining factor for peak load and energy absorption. This concept is reinforced by the numerical data of specimens with higher and lower MVF; for a given specimen geometry the flexural rigidity increases with MVF, however the ratio of peak load to flexural rigidity actually decreases.

Next, it was helpful to directly correlate the role of flexural rigidity to un-altered peak load and absorbed energy. Although flexural rigidity only considers the beginning of the load history, sufficient experimental data should eventually allow its use as a predictor for peak load capacity. With the limited dataset a power-curve adequately describes the relationship, however more data should be collected to validate this assumption.

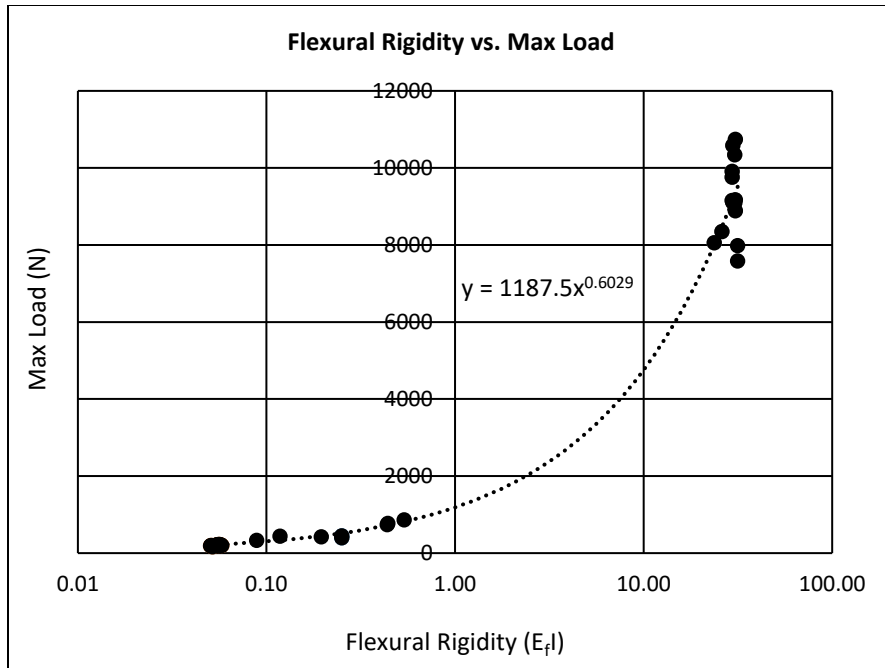


Figure 78. Flexural Rigidity vs. Max Load for All Specimens

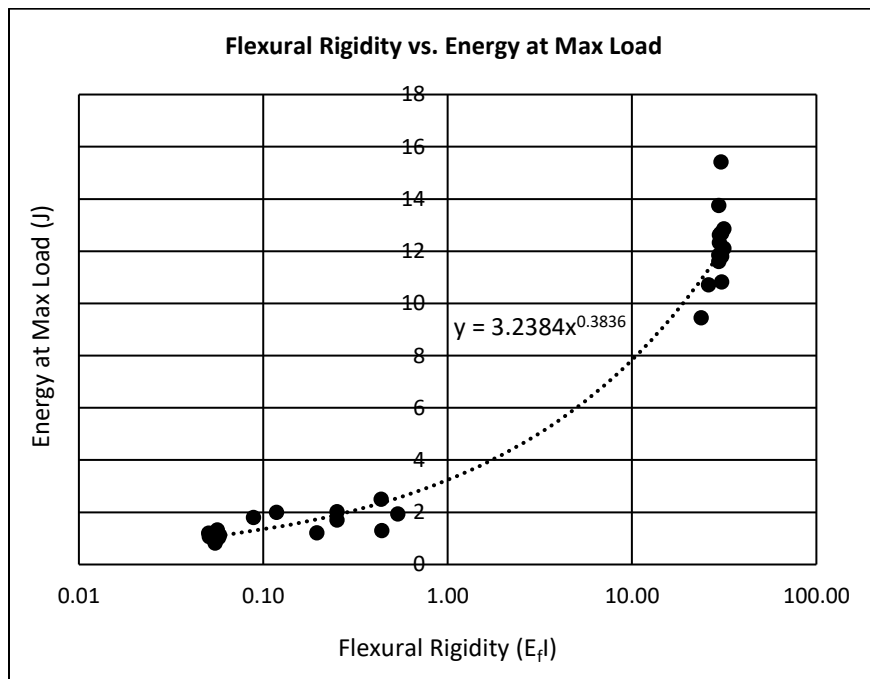


Figure 79. Flexural Rigidity vs. Absorbed Energy at Max Load

Although the tools of classical laminate theory as well as the analytical models for impact described in Chapter 2 provide some methods for rough prediction of load capacity in different TiGr laminates, the interactions of different failure mechanisms can only be truly illustrated using the numerical modeling

techniques described in this section. For instance, the interaction of composite buckling and titanium fracture for Mode 1 Bernhardt is clearly shown, as is the extent of delamination after ply fracture. Additionally, numerical modeling provides the framework for calculating *residual* strength of laminates after fracture, a critical design component for any commercial application.

CHAPTER 7: CONCLUSIONS AND FUTURE WORK RECOMMENDATIONS

7.1 Conclusions

This body of work describes methods for modeling and simulation of low-velocity impact events on fiber metal laminates, specifically TiGr. Several different TiGr laminates were reviewed and simulated in detail using the 3-point-bend specimen as a benchmark, and experimental impact data was taken for thick TiGr specimens to contrast previously acquired data.

- Models were generated using the finite element software ABAQUS. Models simulated composite layers as three-dimensional orthotropic solids, and metal layers as isotropic solids. The bonds between metal and composite layers were simulated using cohesive elements and a traction-separation law. Support structure and impactor geometry were simulated using rigid elements. Localized mesh refinement was applied near the field of interest. Material models were applied consistent with previously observed mechanical behavior of the constituent parts.
- Experimental data was taken using 3-point-bending configuration, with both quasi-static and dynamic loadcases. Numerous specimens were tested, employing a variety of different layups and edge trimming methods. Force and displacement data were recorded and observations were made about visible fracture mechanisms.
- Two unique failure modes were observed both in numerical simulations and physical experiments. The first mode was that of thin laminates, characterized by tensile fiber fracture and compressive buckling, closely coupled with titanium fracture and/or buckling. Delamination in these laminates remains relatively localized around the point of fiber or titanium fracture. The second failure mode is that of thicker laminates, and is characterized by localized crushing under the crosshead resulting in localized compressive fiber damage, leading to deformation gradients that cause formation of a delamination front advancing from the crosshead out toward one of the free ends. This delamination quickly advances through the half-span, and causes the first major drop in load through the contact history. Subsequent half-span delamination fronts form as load is re-distributed through the weakened laminate.
- Differences between static and dynamic loading of thick laminates were evident in both experimental specimens and numerical models. The load/displacement curves for static

specimens show nonlinear behavior indicating damage propagation and metal yielding with increasing displacement, followed by abrupt drops in load as half-span delaminations occur. These drops are followed by increasing load, albeit at a new compliance slope, followed by secondary and tertiary delamination load drops. Dynamic load-displacement curves exhibit less abrupt load drops; catastrophic damage and subsequent load drop occurs almost simultaneously and is followed by oscillatory load behavior as stress waves propagate through the specimen.

- For macro-scale static and dynamic analysis, the Hashin criteria for composites and the Johnson-Cook model for metal fracture are adequate material models. Composite fracture mechanisms were simulated representing experimental results, and provided force-deflection and energy curves that closely matched experimental data. Although numerical analysis is computationally expensive, it is the only documented technique that can adequately model fracture behavior, including residual stiffness during progressive fracture. Without this granularity predictions are constrained to the linear regime and small-deflection assumptions, as noted in the section on analytical modeling in Chapter 2.

7.2 Future Work Recommendations

The concepts relating flexural rigidity to peak loads and energy absorption should be investigated experimentally with laminates using different MVF. Specifically, the thickness and layup configurations that bracket the transition from tensile/compressive failure modes to shear/delamination dominant failure modes should be understood. This was modeled numerically but should be verified experimentally.

Formulation of good numerical models requires material-specific strength and fracture data that is not readily available. While properties for titanium grades are published and stabilized in the literature, properties for the interfacial bonds formed during different curing/consolidation processes are not standardized for TiGr laminates. Therefore a degree of variability can exist from laminate to laminate depending on which process was followed. More work needs to be done to define and control processes for TiGr manufacturing, including titanium pre-treatment, sol-gel application, and laminate consolidation and autoclave parameters. As noted above, thicker laminates' impact behavior is closely tied to the

interfacial properties since interlaminar delamination is the primary failure mode. Therefore variability in laminates leads to uncertainty in numerical modeling predictions.

Impact loading of 3-point-bend specimens results in complex failure of fiber-metal laminates, and the propagation of interlaminar damage occurs via both mode 1 and mode 2 mechanisms. The properties governing the traction-separation law are taken from double-cantilever-beam (DCB) and end-notch-flexure (ENF) test data, however more mixed-mode testing needs to be conducted to validate the Benzeggagh-Kenane relationship.

The laminates modeled in this work all used titanium sheet that was roughly comparable to composite lamina thickness. There is an advantage to this philosophy, as titanium can selectively replace composite plies in a given laminate, allowing tailoring of properties base on expected loads. However, the effect of titanium sheet thickness should be studied to map the relationship between increased energy absorption in thicker sheets and associated delamination with adjacent composite plies.

There are many subtle factors involved with dynamic finite element simulation that are useful for getting solutions to converge. Appropriate use of viscous damping in the material models should be investigated, as should the effects of mass scaling and single versus double point precision. These factors are part of the “art” of finite element analysis, and can greatly increase the performance of a model with little impact to the final solution, if applied correctly. In particular these factors are useful for models experiencing fracture, and their effect on fracture solutions should be understood.

REFERENCES

1. Alderliesten, R. C. (2015). Designing for damage tolerance in aerospace: A hybrid material technology. *Materials & Design*, 66, 421-428.
2. Bernhardt, S., Ramulu, M., & Kobayashi, A. S. (2007). Low-velocity impact response characterization of a hybrid titanium composite laminate. *Journal of engineering materials and technology*, 129(2), 220-226.
3. Bernhardt S, Ramulu M, Briggs T, Kobayashi AS. Effects of edge finishing on the impact behavior of a hybrid titanium composite laminate. Department of Mechanical Engineering, University of Washington.
4. Gray, G. T., Chen, S. R., Wright, W., & Lopez, M. F. (1994). Constitutive equations for annealed metals under compression at high strain rates and high temperatures. *Los Alamos National Laboratory, Los Alamos*.
5. El Moufari, M., & El Bakkali, L. (2015, December). Effect of combination of thermal and mechanical loading on delamination onset and growth of unidirectional composite materials. In *Xème Conférence Internationale: Conception et Production Intégrées*.
6. Nakatani, H., et al. "Damage evaluation of Ti/GFRP laminates under low-energy impact loading." *Proceedings of the international committee on composite material ICCM-17, Edinburgh, Scotland* (2009).
7. Ramulu, M., Stickler, P. B., McDevitt, N. S., Datar, I. P., Kim, D., & Jenkins, M. G. (2004). Influence of processing methods on the tensile and flexure properties of high temperature composites. *Composites science and technology*, 64(12), 1763-1772.
8. Handbook-Mil-HDBK, M. (2003). 5H: Metallic Materials and Elements for Aerospace Vehicle Structures (Knovel Interactive Edition). *US Department of Defense*.
9. Meyer, H. W., & Kleponis, D. S. (2001). Modeling the high strain rate behavior of titanium undergoing ballistic impact and penetration. *International Journal of Impact Engineering*, 26(1), 509-521.
10. Kay, G. (2002). Failure modeling of titanium-61-4V and 2024-T3 aluminum with the Johnson-Cook material model. *Technical Rep., Lawrence Livermore National Laboratory, Livermore, CA*.
11. Meyer Jr, H. W., & Kleponis, D. S. (2001). *An analysis of parameters for the Johnson-Cook strength model for 2-in-thick rolled homogeneous armor* (No. ARL-TR-2528). Army Research Lab Aberdeen Proving Ground MD.
12. Hashin, Z. (1980). Failure criteria for unidirectional fiber composites. *Journal of applied mechanics*, 47(2), 329-334.
13. Lapczyk, I., and J. A. Hurtado, "Progressive Damage Modeling in Fiber-Reinforced Materials," *Composites Part A: Applied Science and Manufacturing*, vol. 38, no.11, pp. 2333–2341, 2007
14. Vlot, Ad. "The birth of Arall (1945–1981)." *Glare: history of the development of a new aircraft material* (2001): 17-50.
15. Vlot, Ad, and Jan Willem Gunnink, eds. *Fibre metal laminates: an introduction*. Springer Science & Business Media, 2011.

16. Rans, C. D. "Bolted joints in glass reinforced aluminium (Glare) and other hybrid fibre metal laminates (FML)." *Composite Joints and Connections*. Woodhead Publishing, 2011. 35-76.
17. Li, Edward. "Residual tension strength study of fatigued open-hole titanium-graphite hybrid composite laminates." *39th AIAA/ASME/ASCE/AHS/ASC Structures, Structural Dynamics, and Materials Conference and Exhibit*. 1998.
18. Airplanes, Boeing Commercial. *High-speed civil transport study*. Langley Research Center, 1989.
19. Kim, D., and M. Ramulu. "Study on the drilling of titanium/graphite hybrid composites." *Journal of Engineering Materials and Technology* 129.3 (2007): 390-396.
20. Ramulu, M., and Mathew Spaulding. "Drilling of hybrid titanium composite laminate (HTCL) with electrical discharge machining." *Materials* 9.9 (2016): 746.
21. Ramulu, M., et al. "Abrasive waterjet machining effects on kerf quality in thin fiber metal laminate." *Proceedings of*. 2015.
22. Burianek, Dennis, and S. Spearing. "Fatigue damage in titanium-graphite hybrid laminates." *39th AIAA/ASME/ASCE/AHS/ASC Structures, Structural Dynamics, and Materials Conference and Exhibit*. 1998.
23. Burianek, Dennis A., and S. Mark Spearing. "Delamination growth from face sheet seams in cross-ply titanium/graphite hybrid laminates." *Composites Science and Technology* 61.2 (2001): 261-269.
24. Shim, D. J., et al. "Fatigue crack growth prediction in GLARE hybrid laminates." *Composites Science and Technology* 63.12 (2003): 1759-1767.
25. Hundley, Jacob M., et al. "Multi-scale modeling of metal-composite interfaces in titanium-graphite fiber metal laminates part i: molecular scale." *Open Journal of Composite Materials* 1.01 (2011): 19.
26. Hundley, Jacob M., et al. "Multiscale modeling of metal-composite interfaces in titanium-graphite fiber metal laminates part II: Continuum scale." *Journal of Composite Materials* 46.10 (2012): 1235-1249.
27. Hundley, Jacob M., et al. "Three-dimensional progressive failure analysis of bolted titanium-graphite fiber metal laminate joints." *Journal of composite materials* 45.7 (2011): 751-769.
28. Hundley, Jacob M., et al. "Bearing strength analysis of hybrid titanium composite laminates." *AIAA journal* 46.8 (2008): 2074-2085.
29. Bernhardt, S., M. Ramulu, and A. S. Kobayashi. "Low-velocity impact response characterization of a hybrid titanium composite laminate." *Journal of Engineering Materials and Technology* 129.2 (2007): 220-226.
30. Nakatani, Hayato, et al. "Damage characterization of titanium/GFRP hybrid laminates subjected to low-velocity impact." *Composites Part A: Applied Science and Manufacturing* 42.7 (2011): 772-781.
31. Nakatani, H., et al. "Facesheet effects on the low velocity impact damages in titanium/GFRP hybrid laminates." *18th Conference on Composite Materials (ICCM), Jeju, South Korea, Aug. 2011*.

32. Reiner, Johannes, et al. "Experimental and numerical analysis of drop-weight low-velocity impact tests on hybrid titanium composite laminates." *Journal of Composite Materials* 50.26 (2016): 3605-3617.
33. Dauskardt, Reinhold H., et al. *Interphase Thermomechanical Reliability and Optimization for High-Performance Ti Metal Laminates*. Stanford Univ. CA Dept of Materials Science and Engineering, 2011.
34. Paul, S., Hoogstrate, A.M., Van Praag, R., 2002. Abrasive water jet machining of glass fibre metal laminates. *J. Eng. Manuf. Part B* 216, 1459–1469.
35. Chai, Gin Boay, and Periyasamy Manikandan. "Low velocity impact response of fibre-metal laminates—A review." *Composite Structures* 107 (2014): 363-381.
36. Abatan, Ayo, Hurang Hu, and David Olowokere. "Impact resistance modeling of hybrid laminated composites." *Journal of Thermoplastic Composite Materials* 11.3 (1998): 249-260.
37. Vlot, A. "Impact properties of fibre metal laminates." *Composites Engineering* 3.10 (1993): 911-927.
38. Vlot, A. "Impact loading on fibre metal laminates." *International Journal of Impact Engineering* 18.3 (1996): 291-307.
39. Shivakumar, K. N., W. Elber, and W. Illg. "Prediction of low-velocity impact damage in thin circular laminates." *AIAA journal* 23.3 (1985): 442-449.
40. Setoodeh, AliReza, P. Malekzadeh, and K. Nikbin. "Low velocity impact analysis of laminated composite plates using a 3D elasticity based layerwise FEM." *Materials & Design* 30.9 (2009): 3795-3801.
41. Olsson, Robin. "Mass criterion for wave controlled impact response of composite plates." *Composites Part A: Applied Science and Manufacturing* 31.8 (2000): 879-887.
42. Tan, T. M., and C. T. Sun. "Wave propagation in graphite/epoxy laminates due to impact." (1982).
43. Sankar, B. V., and C. T. Sun. "An efficient numerical algorithm for transverse impact problems." *Computers & structures* 20.6 (1985): 1009-1012.
44. Malekzadeh, K., M. R. Khalili, and R. K. Mittal. "Analytical prediction of low-velocity impact response of composite sandwich panels using new TDOF spring–mass–damper model." *Journal of composite materials* 40.18 (2006): 1671-1689.
45. Tsamasphyros, George J., and George S. Bikakis. "Analytical modeling to predict the low velocity impact response of circular GLARE fiber–metal laminates." *Aerospace Science and Technology* 29.1 (2013): 28-36.
46. Goldsmith, W. "Impact: the theory and physical behaviour of colliding solids. 1960." *Edward Arnold, London*.
47. Vlot, Arie. "Low-velocity impact loading on fibre-reinforced aluminium laminates (ARALL) and other aircraft sheet materials." (1993): 0554-0554.
48. Tsamasphyros, George J., and George S. Bikakis. "Dynamic response of circular GLARE fiber—metal laminates subjected to low velocity impact." *Journal of Reinforced Plastics and Composites* 30.11 (2011): 978-987.

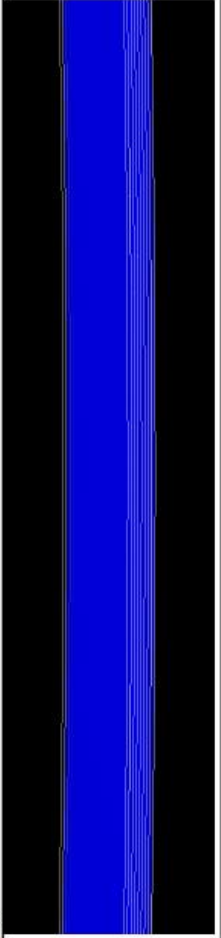
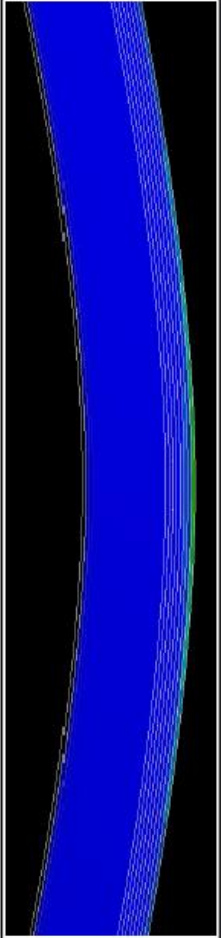
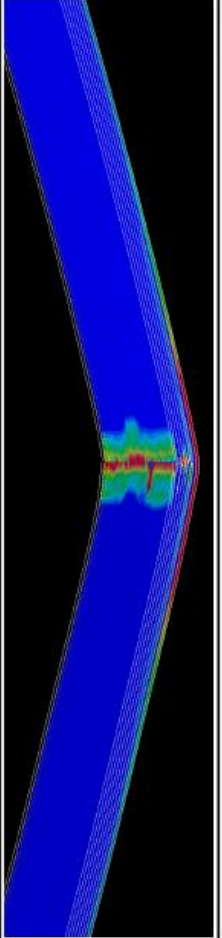
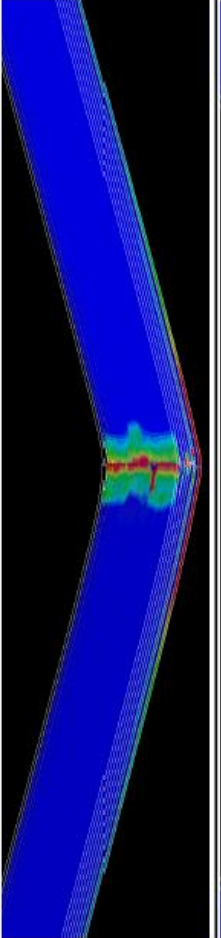
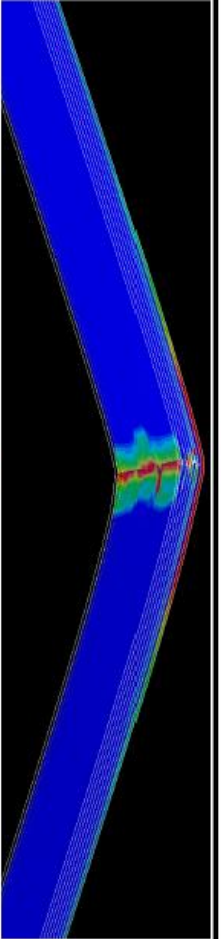
49. Tsamasphyros, George J., and George S. Bikakis. "Analytical modeling of circular GLARE laminated plates under lateral indentation." *Advanced Composites Letters* 18.1 (2009): 096369350901800102.
50. Khalili, MOHAMMAD REZA, K. Malekzadeh, and R. K. Mittal. "A new approach to static and dynamic analysis of composite plates with different boundary conditions." *Composite Structures* 69.2 (2005): 149-155.
51. Khalili, S. M. R., et al. "Low-velocity impact response of active thin-walled hybrid composite structures embedded with SMA wires." *Thin-walled structures* 45.9 (2007): 799-808.
52. Shokuhfar, A., et al. "Analysis and optimization of smart hybrid composite plates subjected to low-velocity impact using the response surface methodology (RSM)." *Thin-Walled Structures* 46.11 (2008): 1204-1212.
53. Choi, Ik Hyeon, and Cheol Ho Lim. "Low-velocity impact analysis of composite laminates using linearized contact law." *Composite structures* 66.1-4 (2004): 125-132.
54. Abatan, Ayo, Hurang Hu, and David Olowokere. "Impact resistance modeling of hybrid laminated composites." *Journal of Thermoplastic Composite Materials* 11.3 (1998): 249-260.
55. Nakatani, Hayato, et al. "Damage characterization of titanium/GFRP hybrid laminates subjected to low-velocity impact." *Composites Part A: Applied Science and Manufacturing* 42.7 (2011): 772-781.
56. Sadighi, M., et al. "Experimental and numerical investigation of metal type and thickness effects on the impact resistance of fiber metal laminates." *Applied Composite Materials* 19.3-4 (2012): 545-559.
57. Zhu, Shengqing, and Gin Boay Chai. "Low-velocity impact response of fibre-metal laminates—Experimental and finite element analysis." *Composites Science and Technology* 72.15 (2012): 1793-1802.
58. Fan, J., Z. W. Guan, and W. J. Cantwell. "Numerical modelling of perforation failure in fibre metal laminates subjected to low velocity impact loading." *Composite structures* 93.9 (2011): 2430-2436.
59. Song, S. H., et al. "Experimental and numerical investigation on impact performance of carbon reinforced aluminum laminates." *Journal of Materials Science & Technology* 26.4 (2010): 327-332.
60. Tsartsaris, Nikolaos, et al. "Low-velocity impact behavior of fiber metal laminates." *Journal of Composite Materials* 45.7 (2011): 803-814.
61. Laliberte, Jeremy, Cheung Poon, and Paul V. Straznicky. "Numerical modelling of low-velocity impact damage in fibre-metal-laminates." *ICAS 2002 Congress (The International Council of the Aeronautical Sciences Congress), Toronto, Canada*. 2002.
62. Guan, Z. W., W. J. Cantwell, and R. Abdullah. "Numerical modeling of the impact response of fiber-metal laminates." *Polymer Composites* 30.5 (2009): 603-611.
63. Camanho, P. P. , and F. L. Matthews. "A progressive damage model for mechanically fastened joints in composite laminates." *Journal of composite materials* 33.24 (1999): 2248-2280.

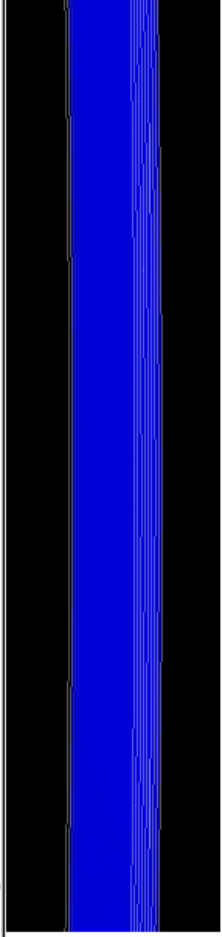
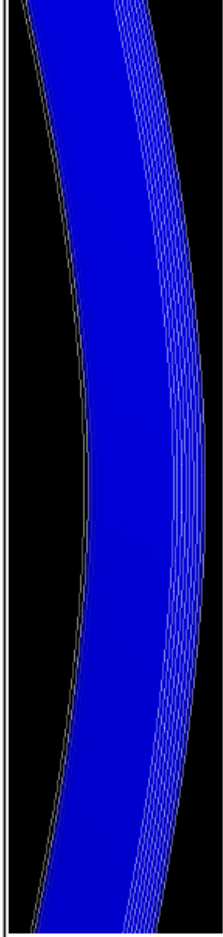
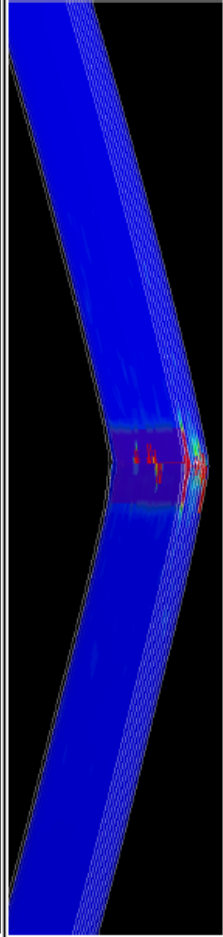
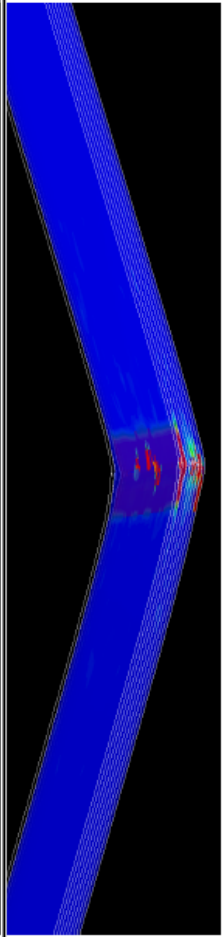
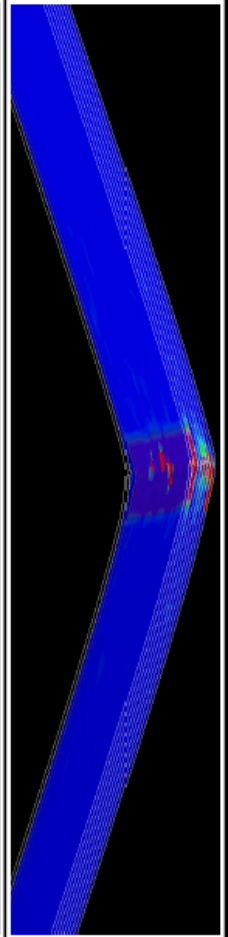
64. Johnson, Gordon R., and William H. Cook. "Fracture characteristics of three metals subjected to various strains, strain rates, temperatures and pressures." *Engineering fracture mechanics* 21.1 (1985): 31-48.
65. Hashagen, F., et al. "Finite element procedure for modelling fibre metal laminates." *Composite Structures* 32.1-4 (1995): 255-264.
66. Benzeggagh, M. L., and M. J. C. S. Kenane. "Measurement of mixed-mode delamination fracture toughness of unidirectional glass/epoxy composites with mixed-mode bending apparatus." *Composites science and technology* 56.4 (1996): 439-449.
67. Song, Kyongchan, Carlos G. Dávila, and Cheryl A. Rose. "Guidelines and parameter selection for the simulation of progressive delamination." (2008).
68. Morinière, F. D., et al. "An integrated study on the low-velocity impact response of the GLARE fibre-metal laminate." *Composite Structures* 100 (2013): 89-103.
69. Guo YJ, Wu XR. A theoretical model for predicting fatigue crack growth rates in fibre-reinforced Metal Laminates. *Fatigue Fract Eng Mater Struct* 1998;21:1133–45.
70. Wilson GS. Fatigue crack growth prediction for generalized fiber metal laminates and hybrid materials, PhD dissertation, Delft University of Technology, <<http://repository.tudelft.nl/assets/uuid:8925fc2a-47e8-457a-960c-f86b5065fa60/upload.wilson.thesis.pdf>>; 2013 [accessed 26.06.14].
71. Alderliesten RC. Analytical prediction model for fatigue crack propagation and delamination growth in Glare. *Int J Fatigue* 2007;29:628–46.
72. Olsson, Robin. "Mass criterion for wave controlled impact response of composite plates." *Composites Part A: Applied Science and Manufacturing* 31.8 (2000): 879-887.
73. Morinière, F. D. "Low-velocity impact on fibre-metal laminates." (2014).
74. Rhymer, Donald William, and W. Steven Johnson. "Fatigue damage mechanisms in advanced hybrid titanium composite laminates." *International Journal of Fatigue* 24.9 (2002): 995-1001.
75. Dandekar, Dattatraya P., and Stephen V. Spletzer. "Shock response of Ti-6Al-4V." *AIP Conference Proceedings*. Vol. 505. No. 1. AIP, 2000.
76. Hillerborg, A., M. Modeer, and P. E. Petersson, "Analysis of Crack Formation and Crack Growth in Concrete by Means of Fracture Mechanics and Finite Elements," *Cement and Concrete Research*, vol. 6, pp. 773–782, 1976
77. Systemes, Dassault. "Abaqus 2016 Documentation." *English. Version Version 6* (2018).
78. Tsai, Stephen W. *Strength Characteristics of Composite Materials*. Philco Corp Newport Beach CA, 1965.
79. Hill, Rodney. "A theory of the yielding and plastic flow of anisotropic metals." *Proceedings of the Royal Society of London. Series A. Mathematical and Physical Sciences* 193.1033 (1948): 281-297.
80. Hoffman, Oscar. "The brittle strength of orthotropic materials." *Journal of Composite Materials* 1.2 (1967): 200-206.

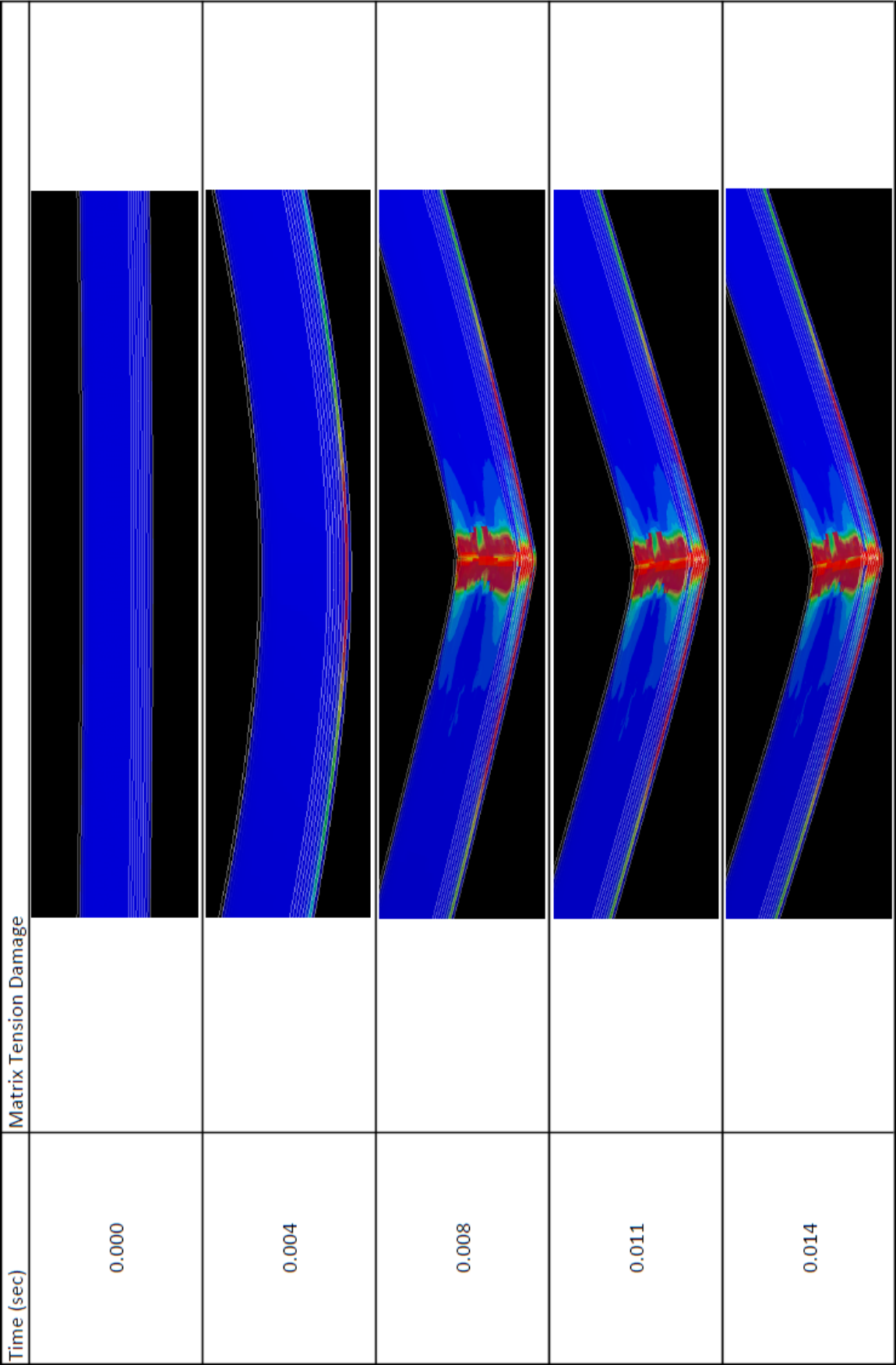
81. Seo, Hyoungseock, et al. "Numerical simulation of glass-fiber-reinforced aluminum laminates with diverse impact damage." *AIAA journal* 48.3 (2010): 676-687.
82. Hughes, Thomas JR, and James Winget. "Finite rotation effects in numerical integration of rate constitutive equations arising in large-deformation analysis." *International journal for numerical methods in engineering* 15.12 (1980): 1862-1867.
83. Abrate, Serge. "Modeling of impacts on composite structures." *Composite structures* 51.2 (2001): 129-138.
84. Sun, C. T., A. Dicken, and H. F. Wu. "Characterization of impact damage in ARALL laminates." *Composites Science and Technology* 49.2 (1993): 139-144.
85. Payeganeh, G. H., F. Ashenai Ghasemi, and K. Malekzadeh. "Dynamic response of fiber-metal laminates (FMLs) subjected to low-velocity impact." *Thin-Walled Structures* 48.1 (2010): 62-70.
86. Whitney, J. M., and N. J. Pagano. "Shear deformation in heterogeneous anisotropic plates." *Journal of applied mechanics* 37.4 (1970): 1031-1036.
87. Mindlin, R. D. "Influence of rotary inertia and shear deformation on the bending of elastic plates." *ASME J. Appl. Mech* 12 (1945): 69-76.
88. Hokka, Mikko, et al. "Dynamic behavior and numerical modeling of titanium 15-3-3-3 alloy." *Dynamic Behavior of Materials, Volume 1*. Springer, New York, NY, 2013. 235-242.
89. Demuts, E. "Low velocity impact in a graphite/PEEK." *34th Structures, Structural Dynamics and Materials Conference*. 1993.
90. Leach, D. C., and D. R. Moore. "Toughness of aromatic polymer composites reinforced with carbon fibres." *Composites Science and Technology* 23.2 (1985): 131-161.
91. Naghipour, P., et al. "Fracture simulation of CFRP laminates in mixed mode bending." *Engineering Fracture Mechanics* 76.18 (2009): 2821-2833.
92. Naghipour, Paria & Schneider, Janine & Bartsch, Marion & Hausmann, Joachim & Voggenreiter, Heinz. (2009). Fracture simulation of hybrid Titanium-CF/PEEK laminates.
93. Handbook, Structural Alloys, et al. "CINDAS/Purdue University." *West Lafayette, Ind, USA* (1996).
94. Welsch, Gerhard, Rodney Boyer, and E. W. Collings, eds. *Materials properties handbook: titanium alloys*. ASM international, 1993.
95. Du, Dandan, et al. "Open-hole tensile progressive damage and failure prediction of carbon fiber-reinforced PEEK-titanium laminates." *Composites Part B: Engineering* 91 (2016): 65-74.

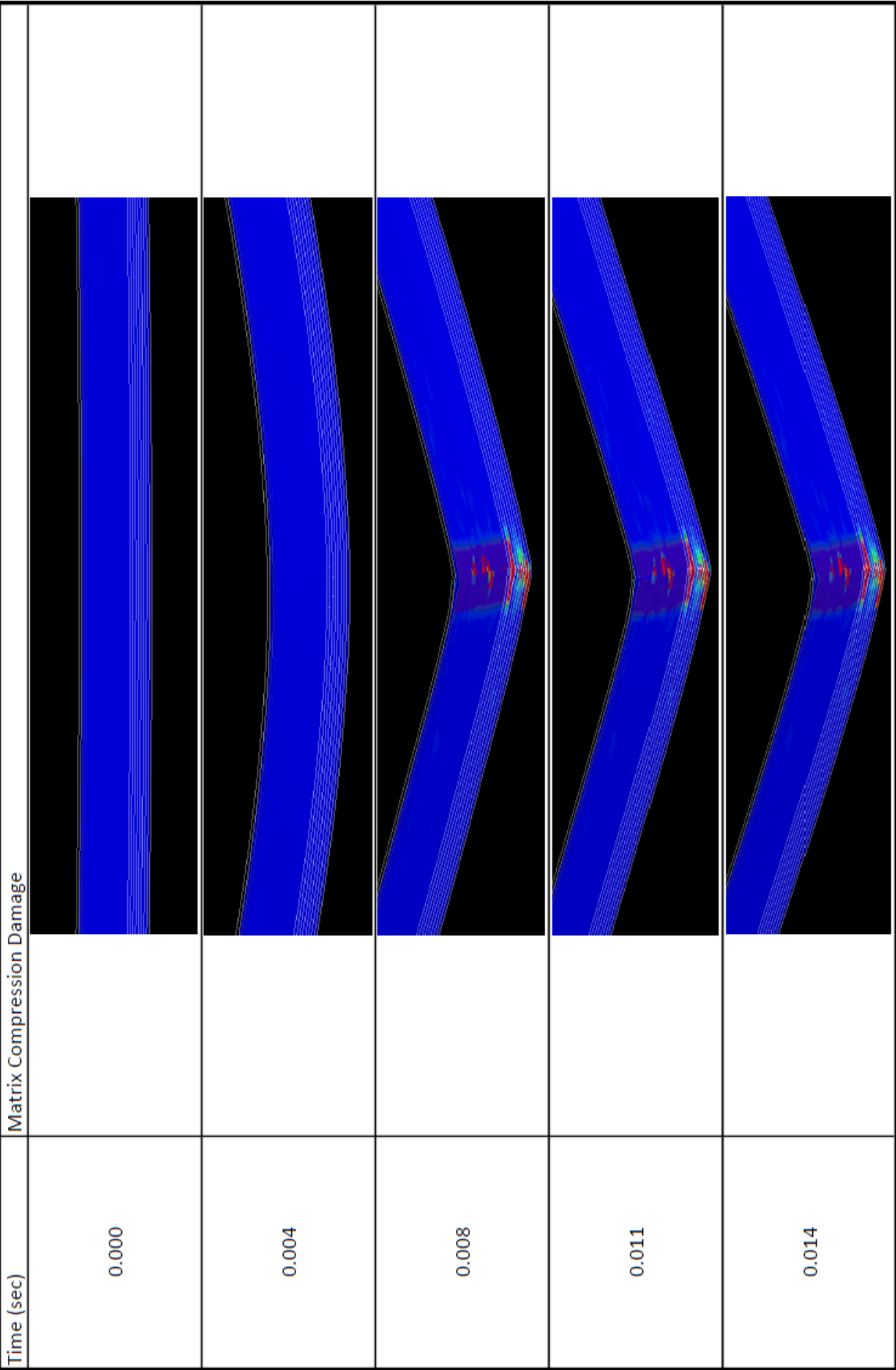
APPENDIX I: DAMAGE PROGRESSION IN NUMERICAL MODELS

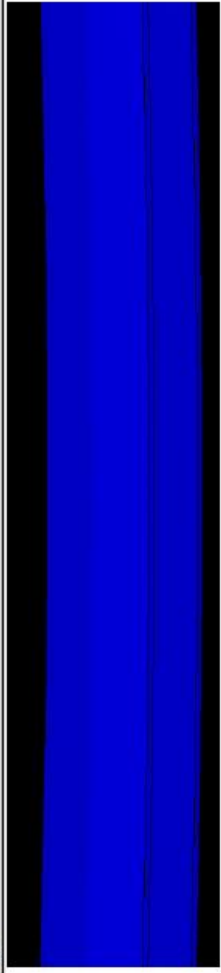
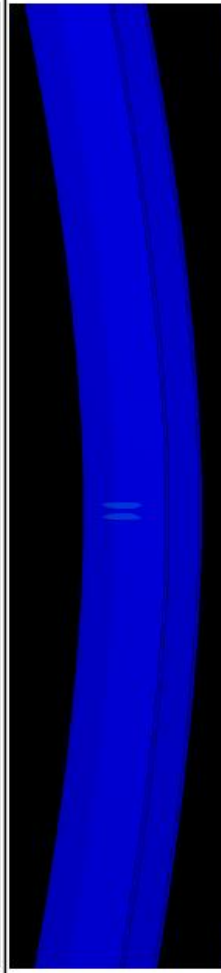
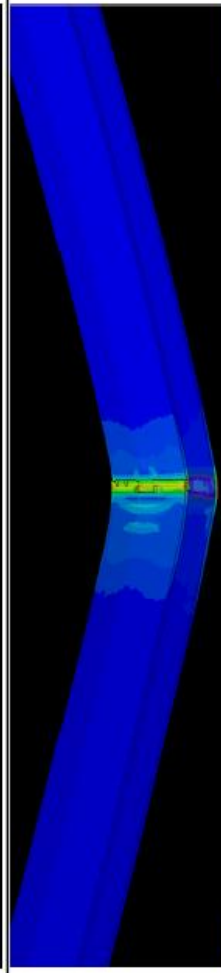
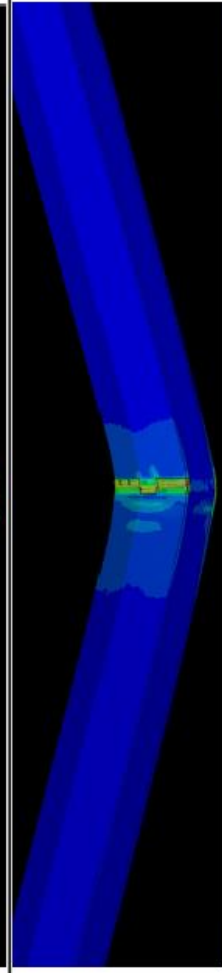
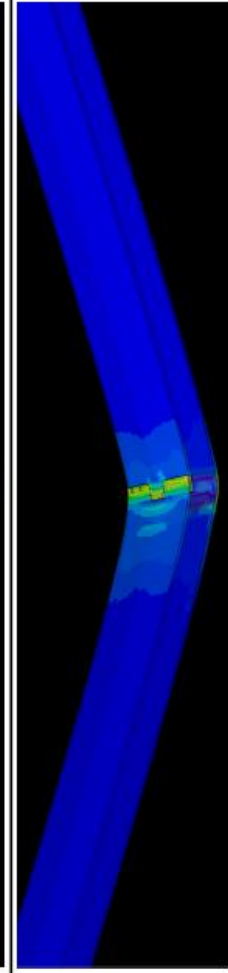
Bernhardt Model (First Mode Failures)

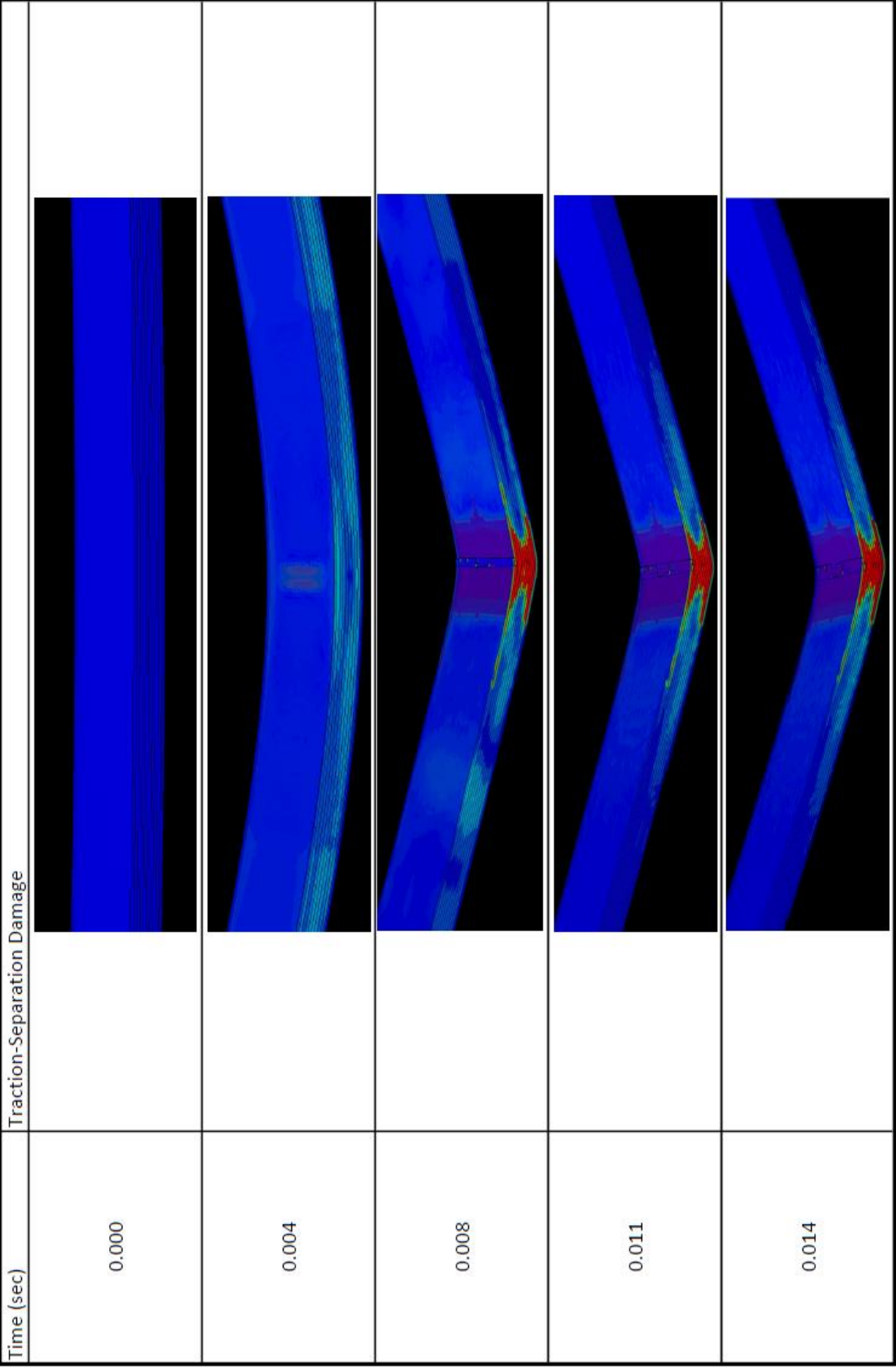
Time (sec)	Fiber Tension Damage
0.000	
0.004	
0.008	
0.011	
0.014	

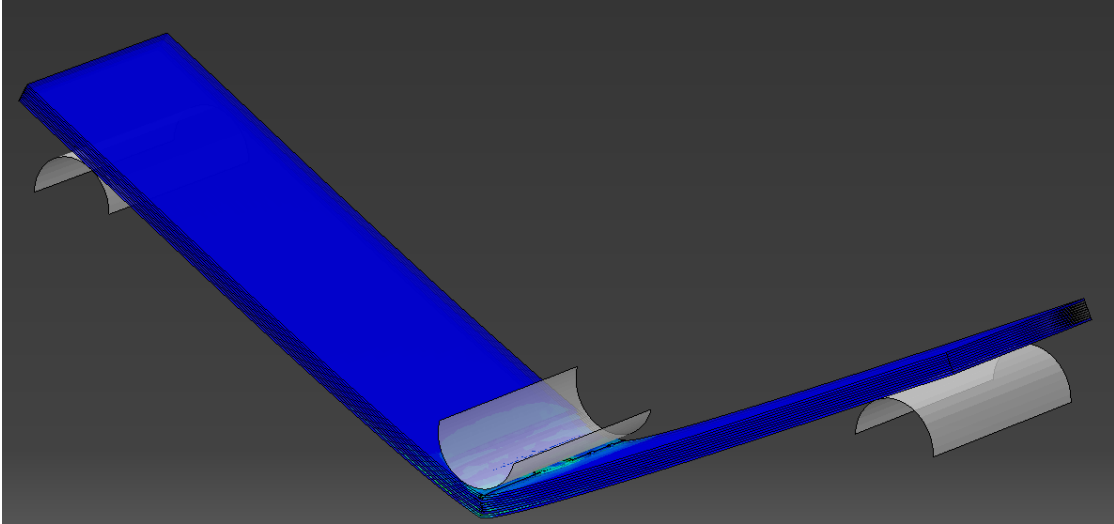
Time (sec)	Fiber Compression Damage
0.000	
0.004	
0.008	
0.011	
0.014	



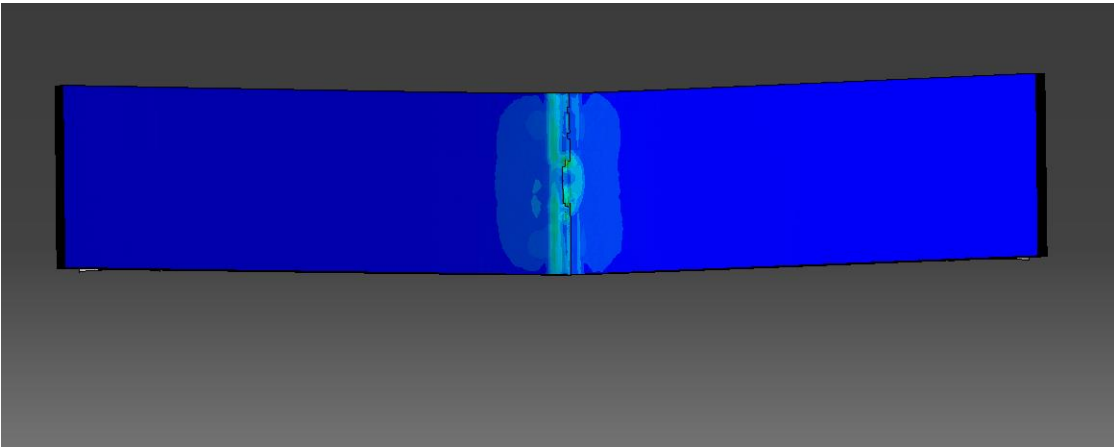


Time (sec)	Johnson-Cook Damage
0.000	
0.004	
0.008	
0.011	
0.014	

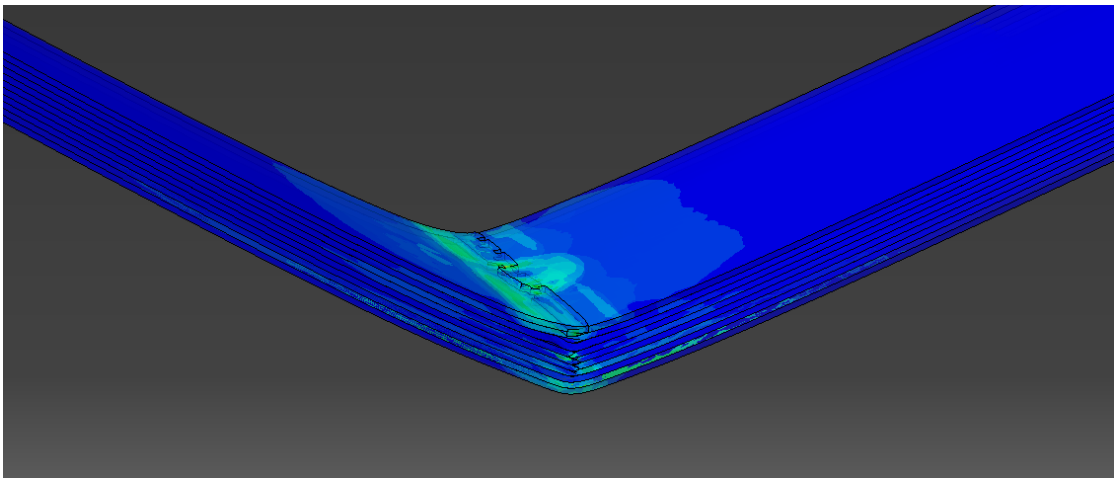




Bernhardt Mode 1 View

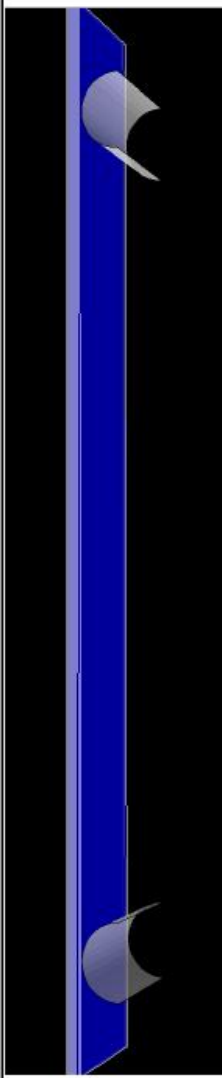
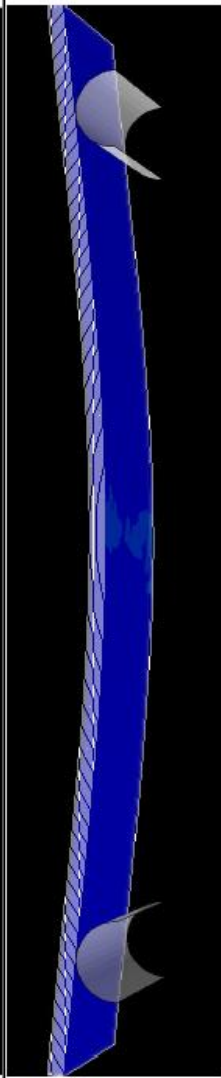
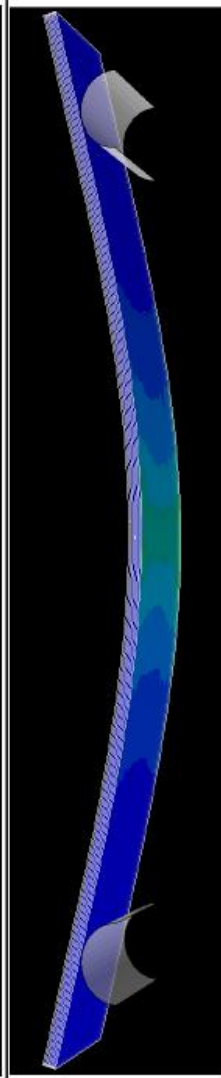
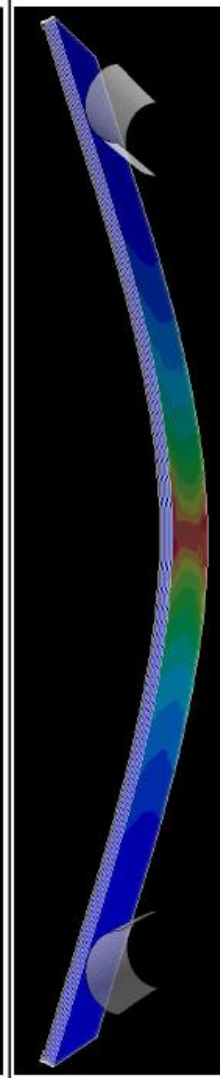
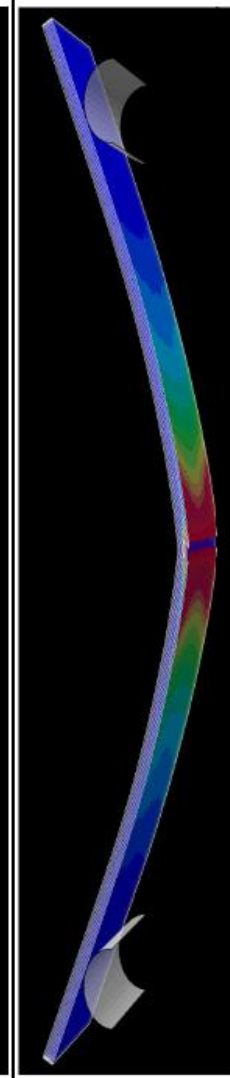


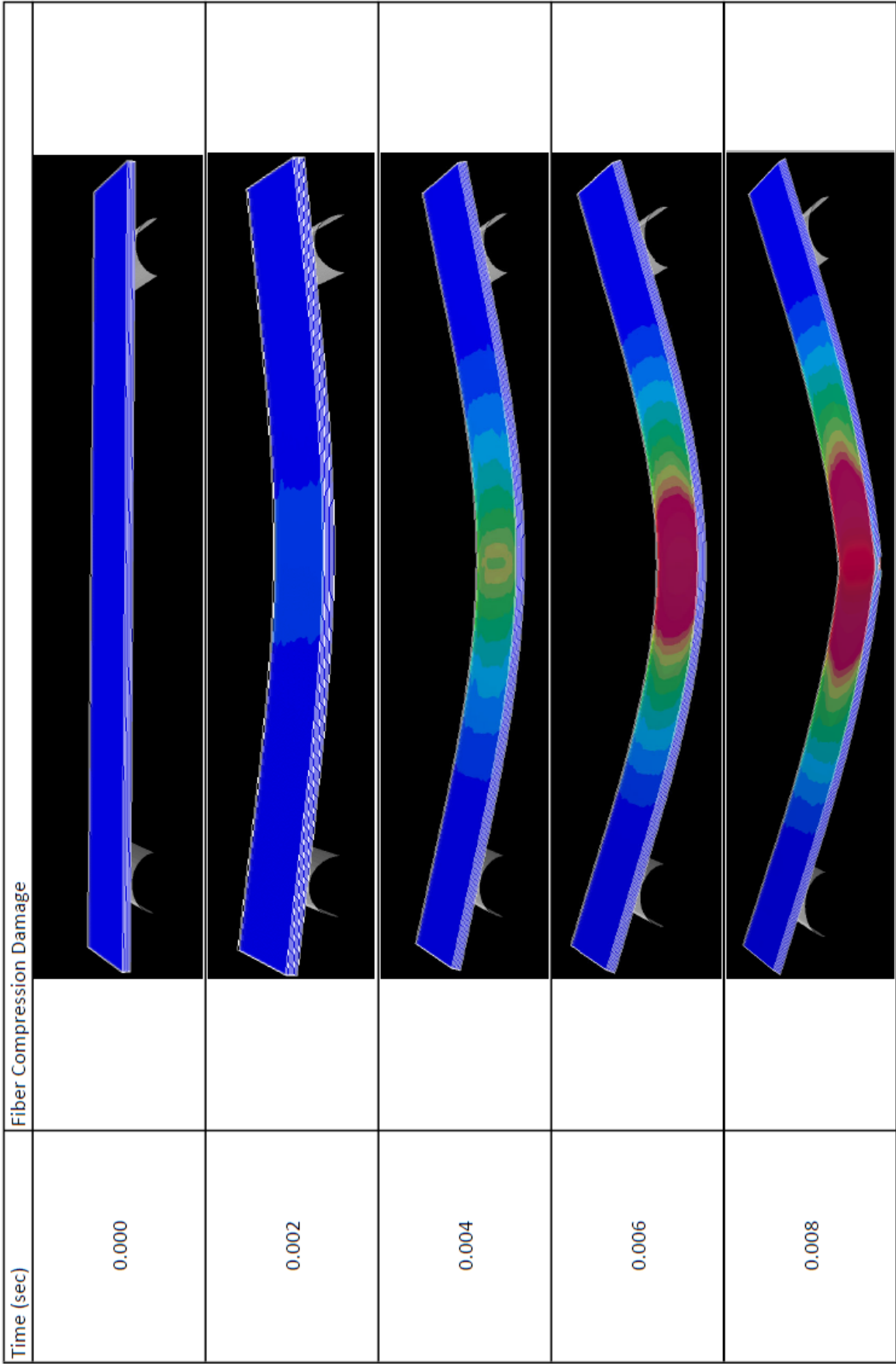
Bernhardt Mode 1 Top View with Impactor Hidden

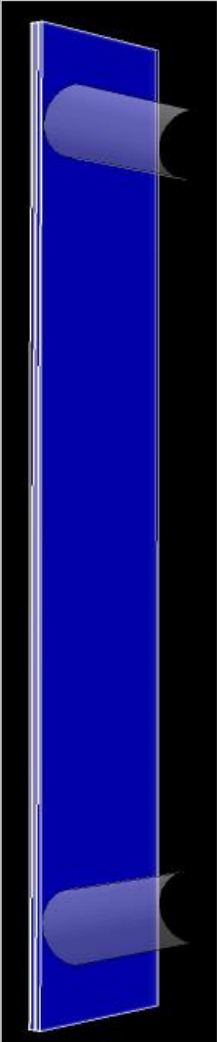
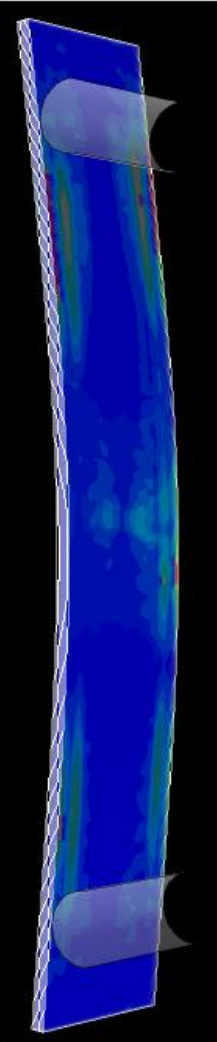
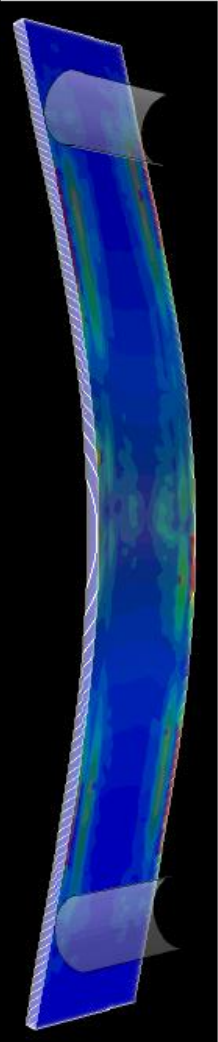
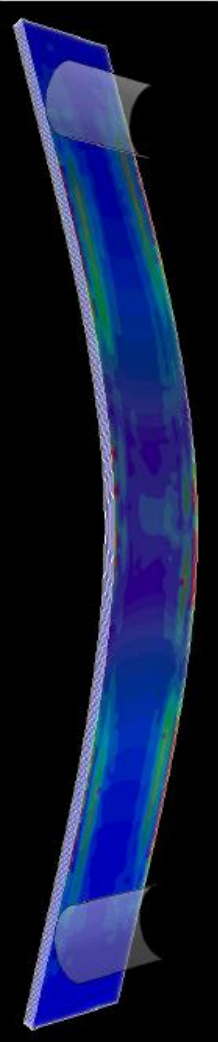
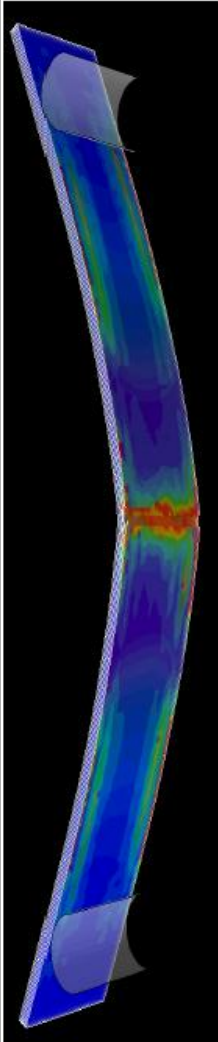


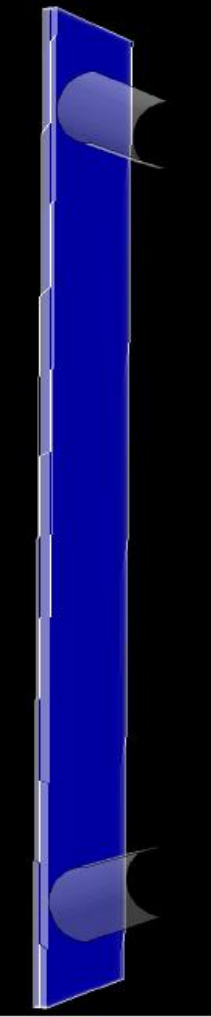



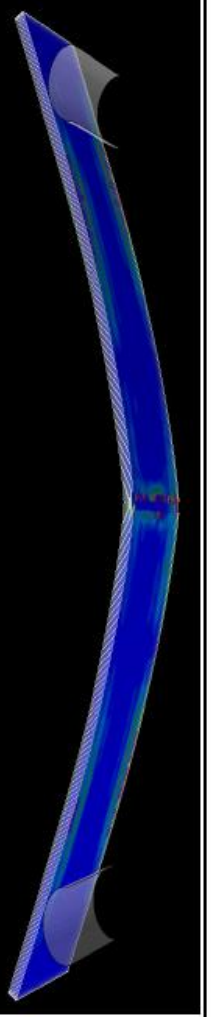
Bernhardt Mode 1 View with Impactor Hidden

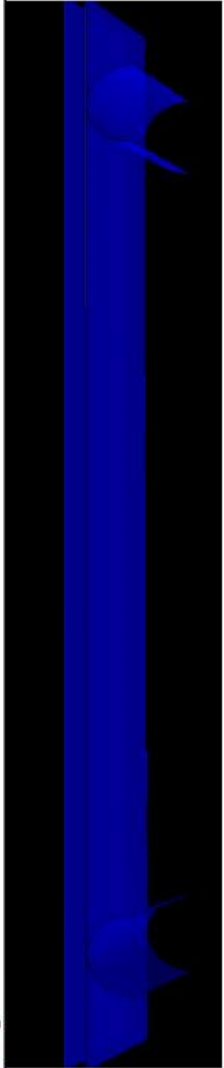
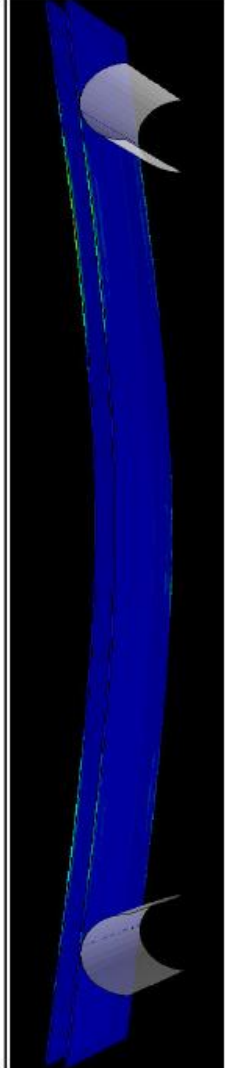
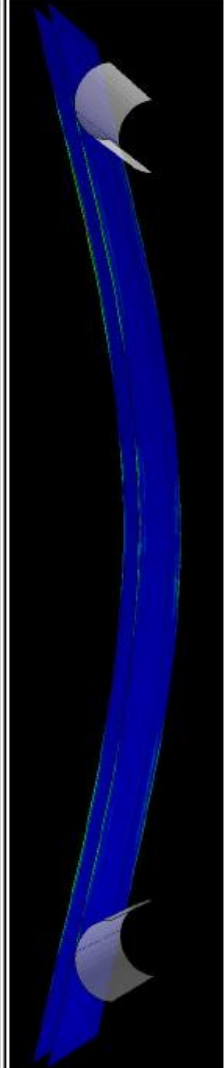
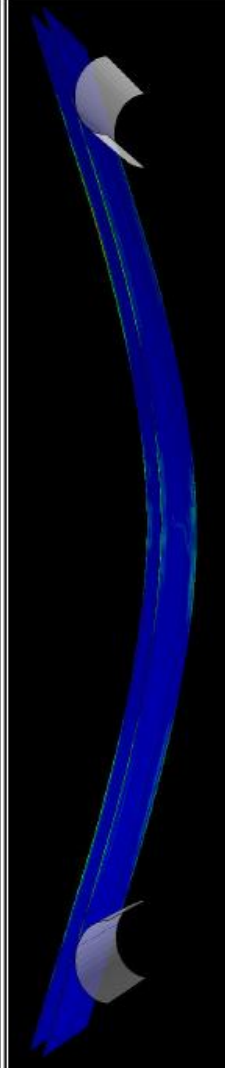
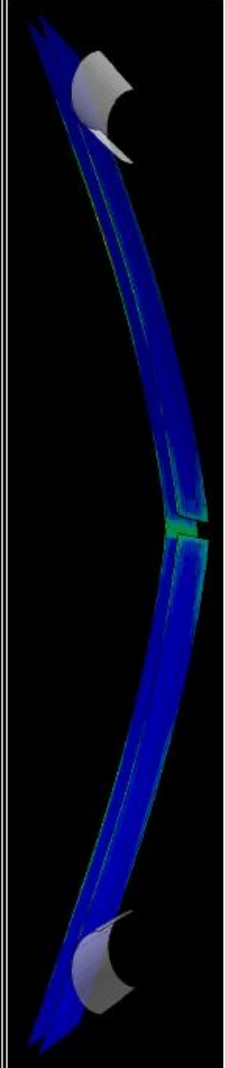
Bernhardt Model (Second Mode Failures)

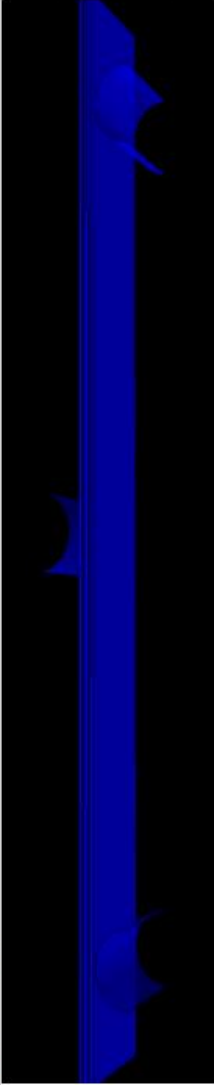
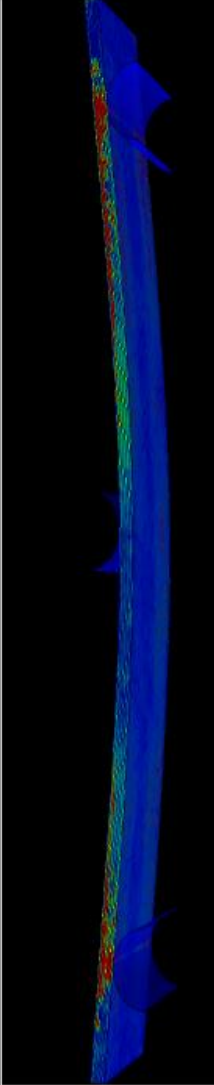
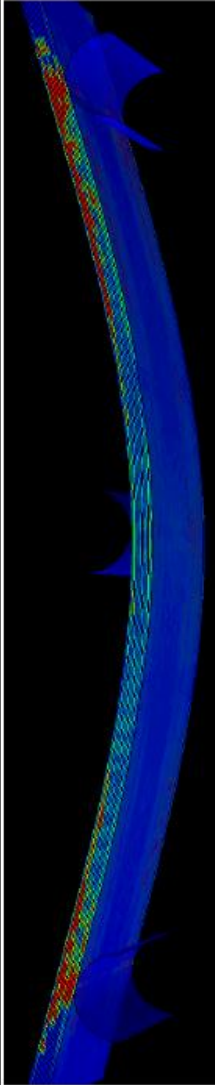
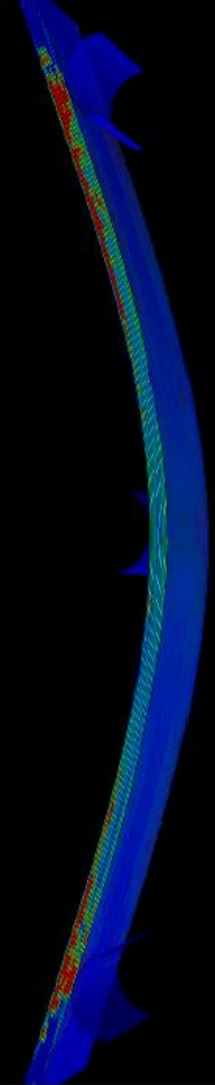
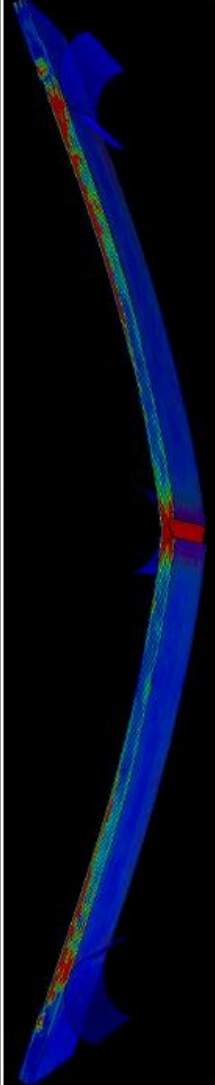
Time (sec)	Fiber Tension Damage
0.000	
0.002	
0.004	
0.006	
0.008	

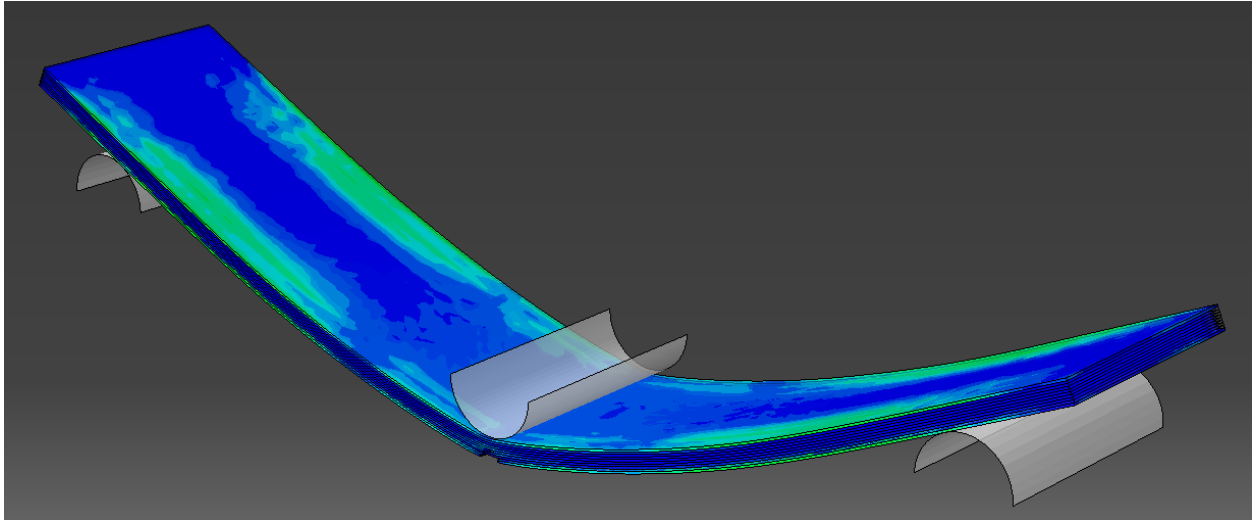


Time (sec)	Matrix Tension Damage
0.000	
0.002	
0.004	
0.006	
0.008	

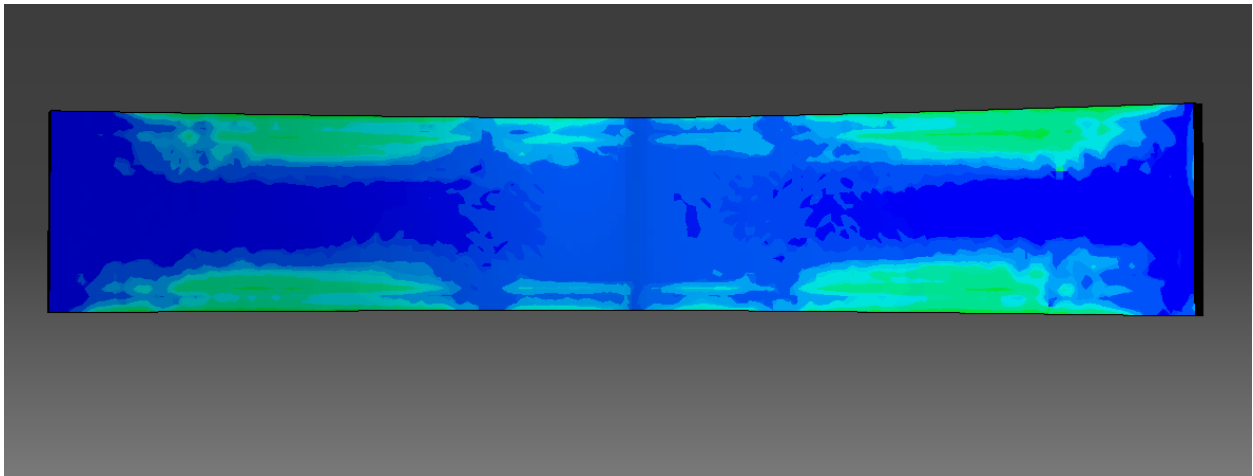
Time (sec)	Matrix Compression Damage
0.000	
0.002	
0.004	
0.006	
0.008	

Time (sec)	Johnson-Cook Damage
0.000	
0.002	
0.004	
0.006	
0.008	

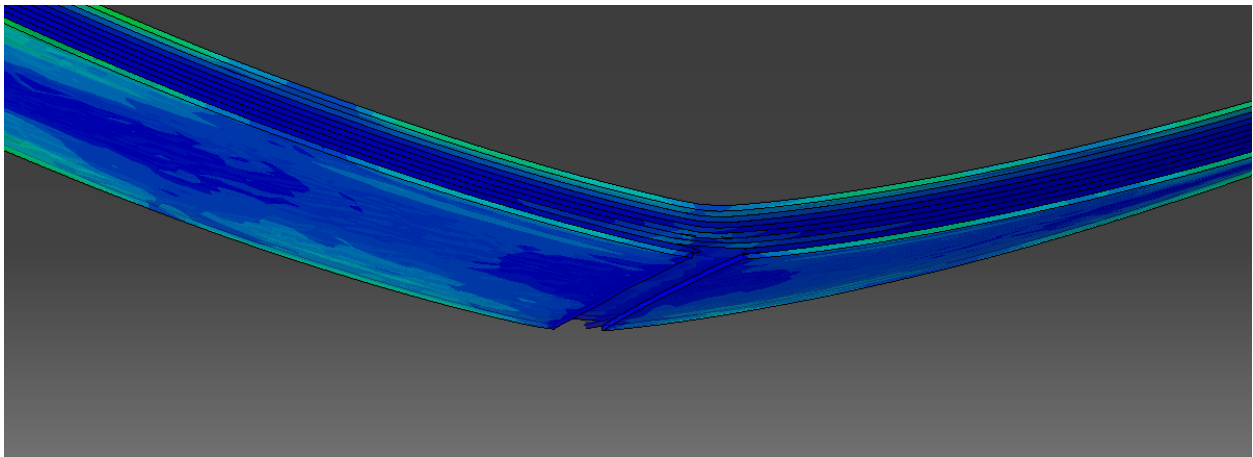
Time (sec)	Traction-Separation Damage
0.000	
0.002	
0.004	
0.006	
0.009	



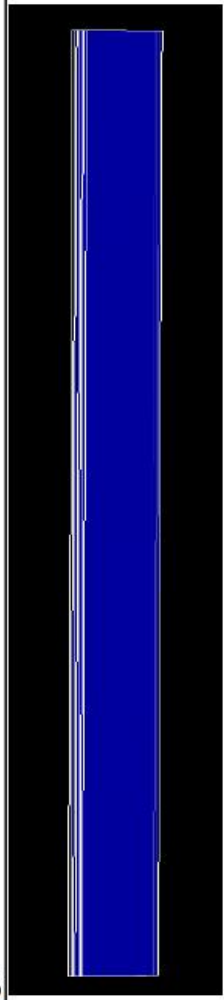
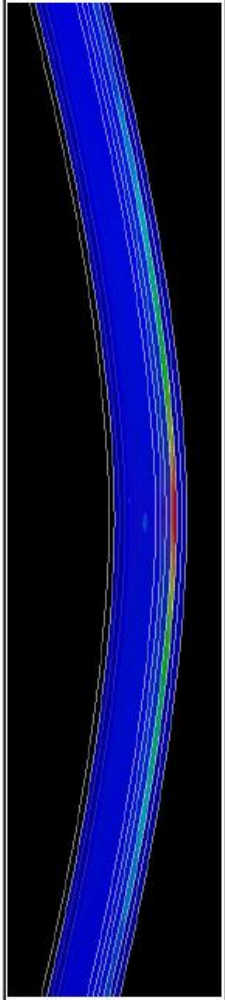
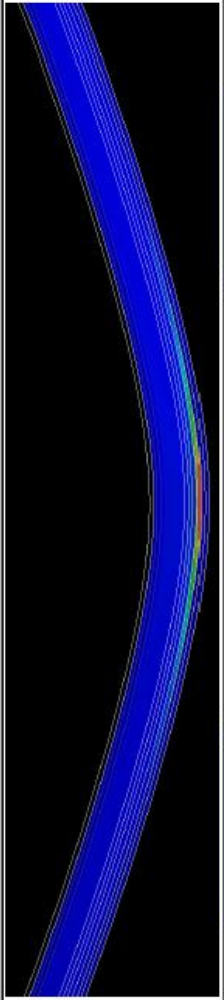
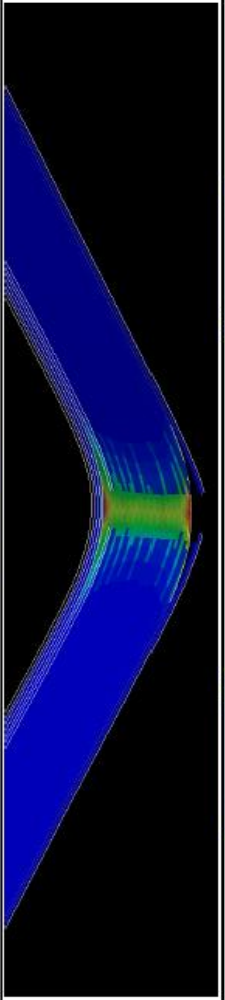
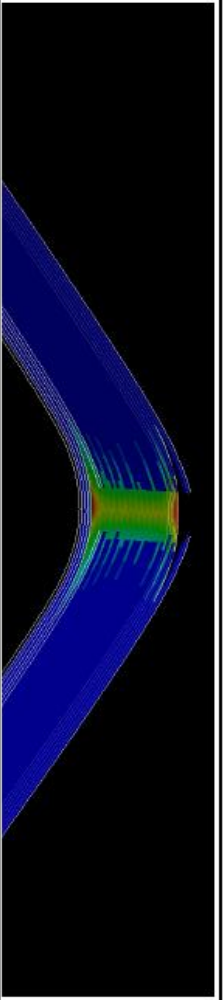
Bernhardt Mode 2 View

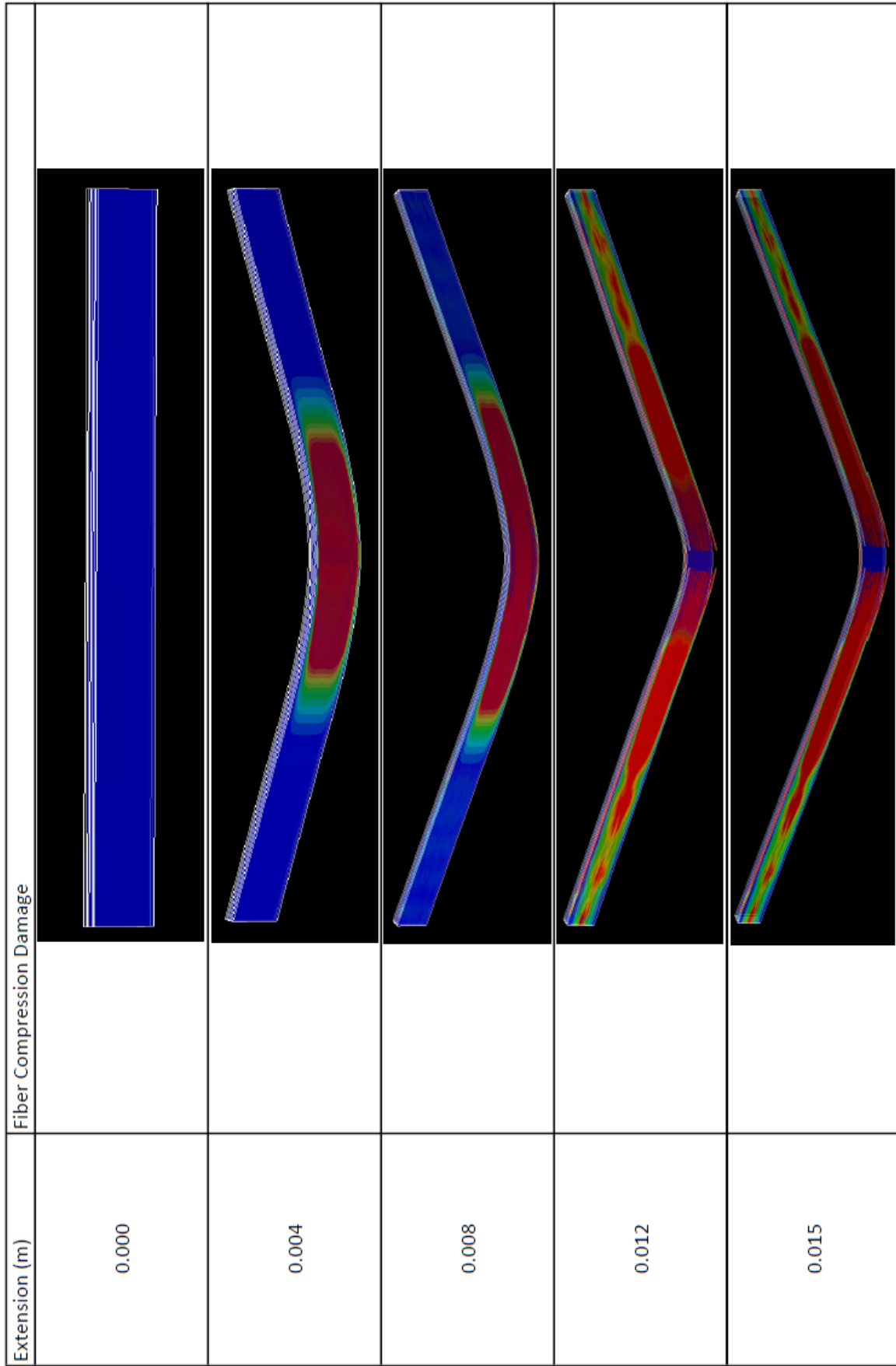


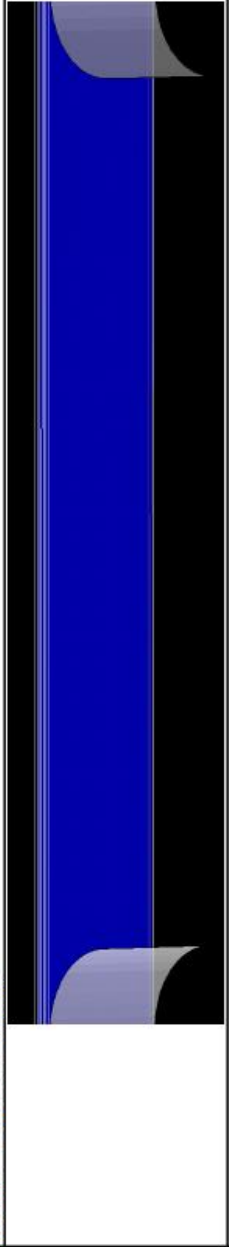
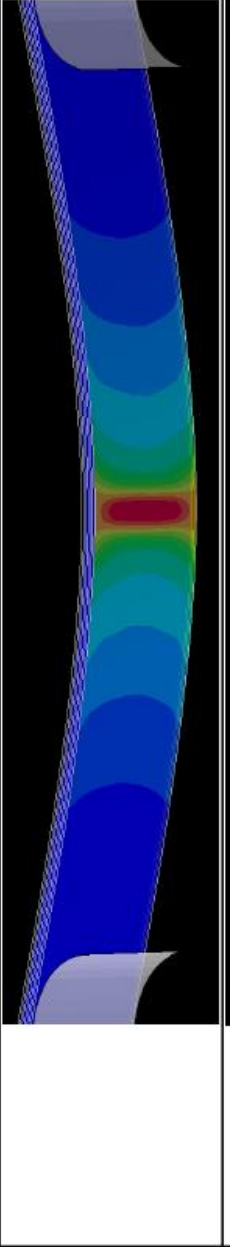
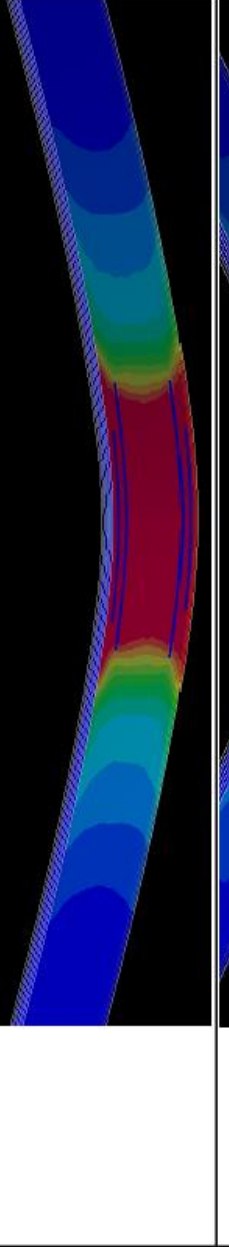
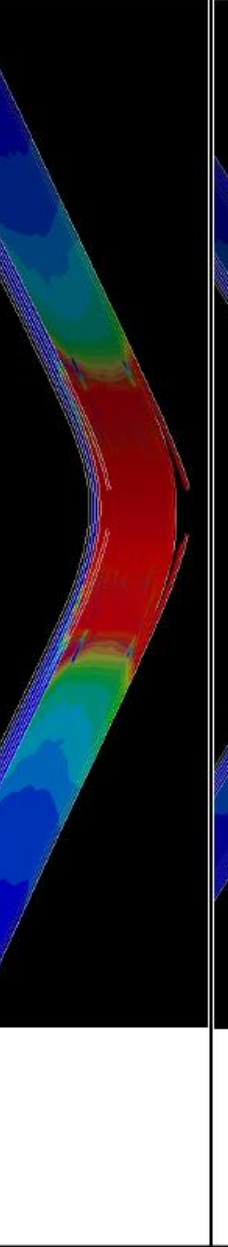
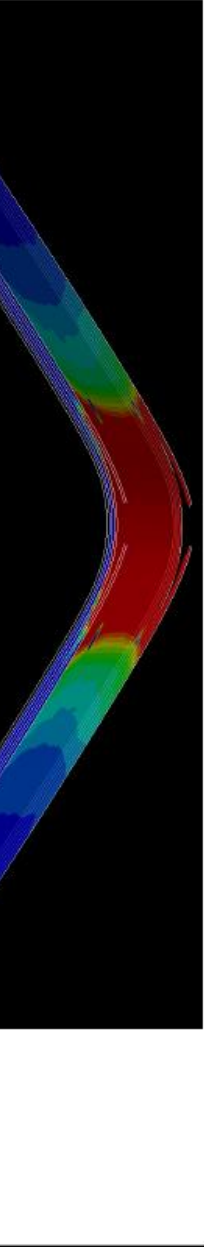
Bernhardt Mode 2 Top View with Impactor Hidden

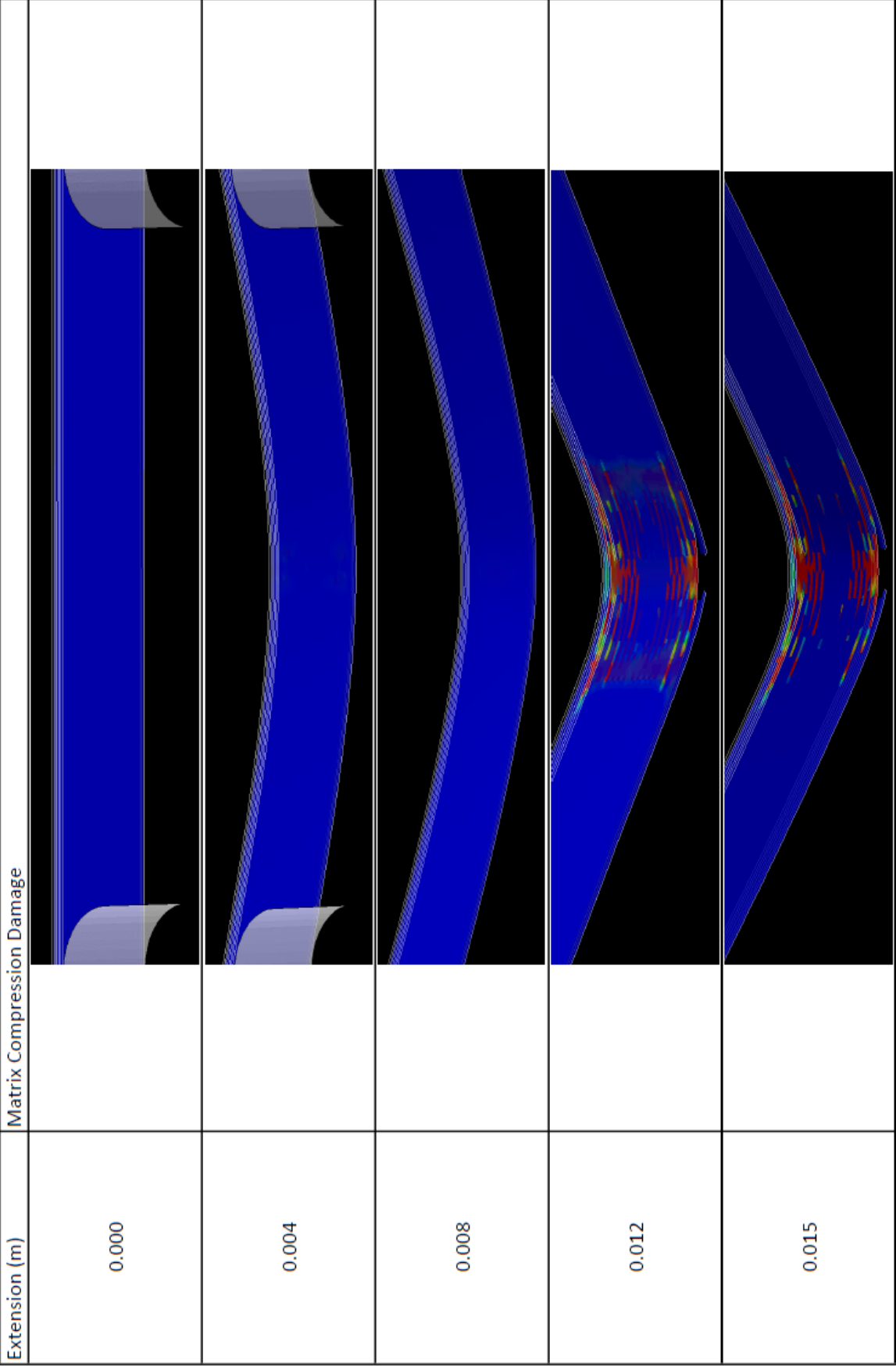


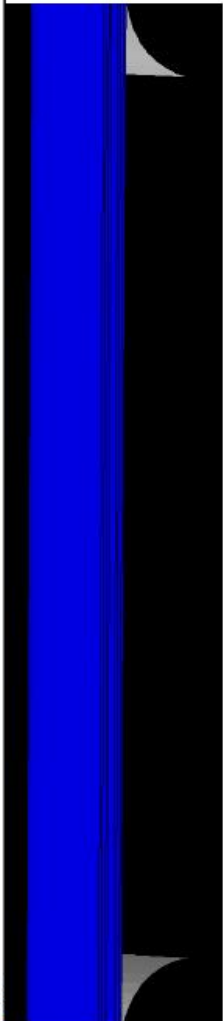
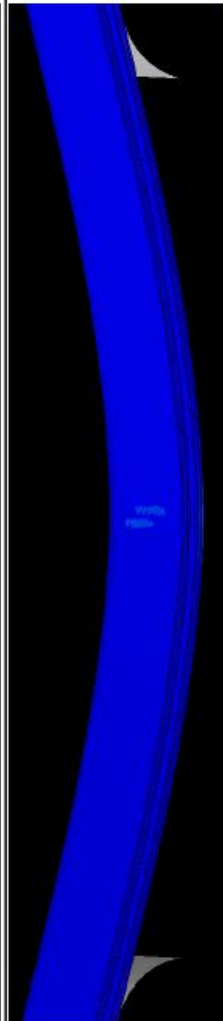
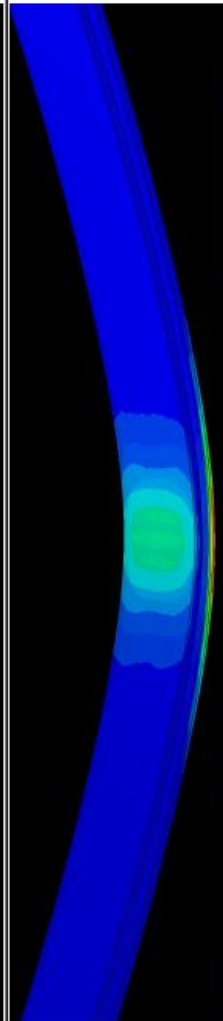
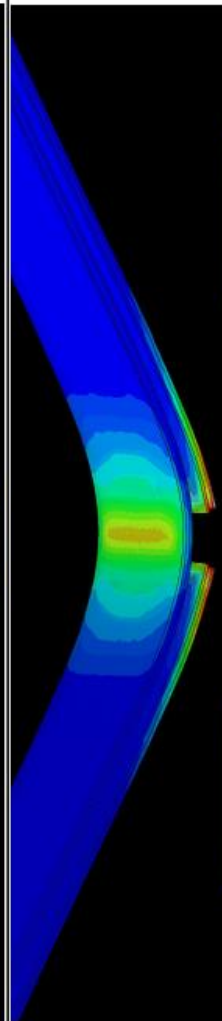
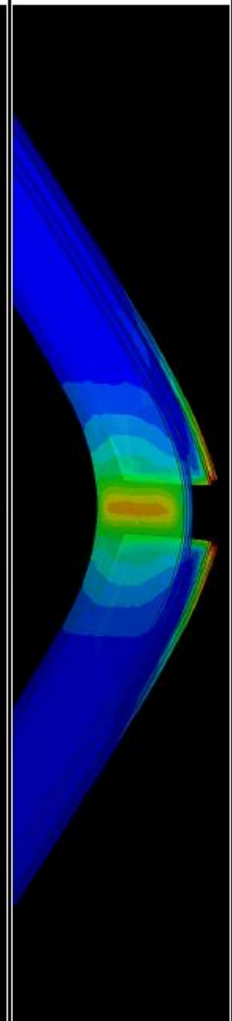
Bernhardt Mode 2 View with Impactor Hidden

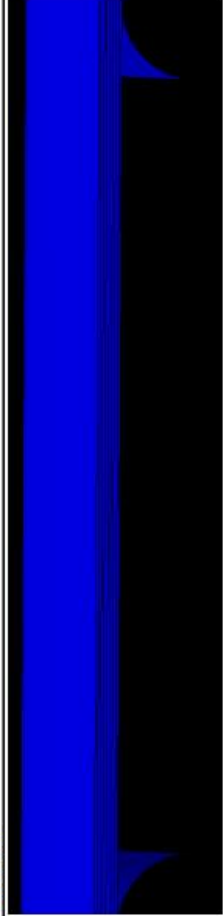
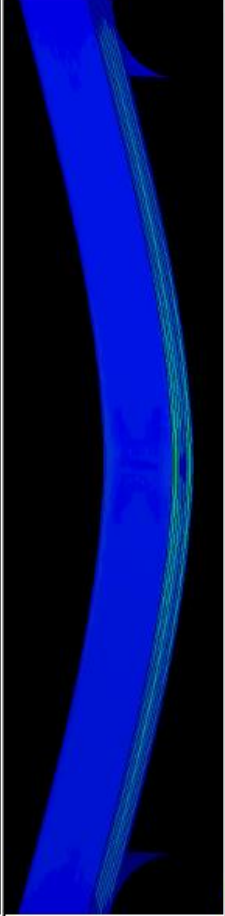
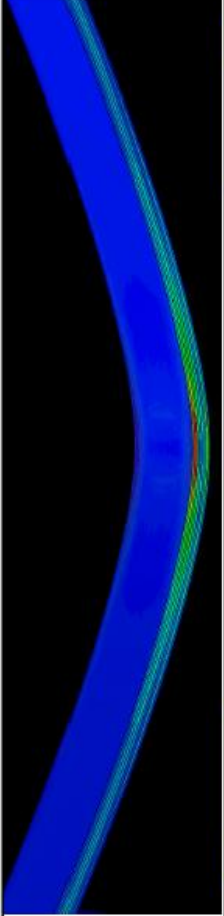
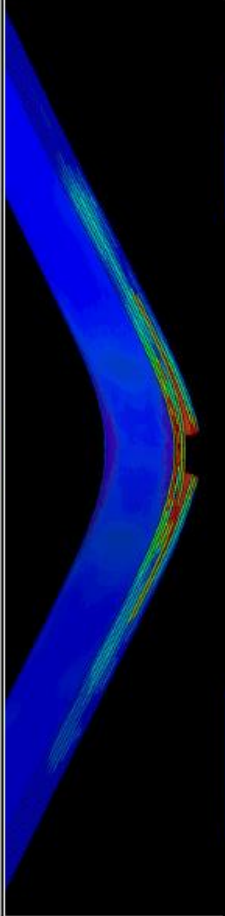
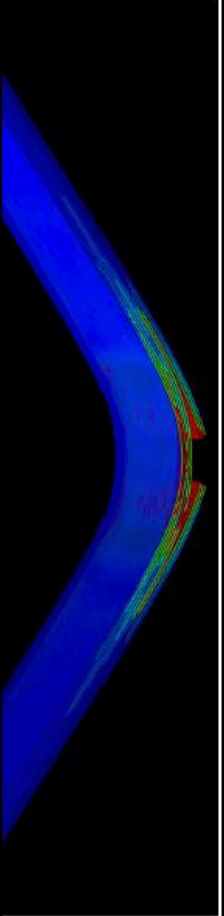
Vara Model Extension (m)	Fiber Tension Damage
0.000	
0.004	
0.008	
0.012	
0.015	

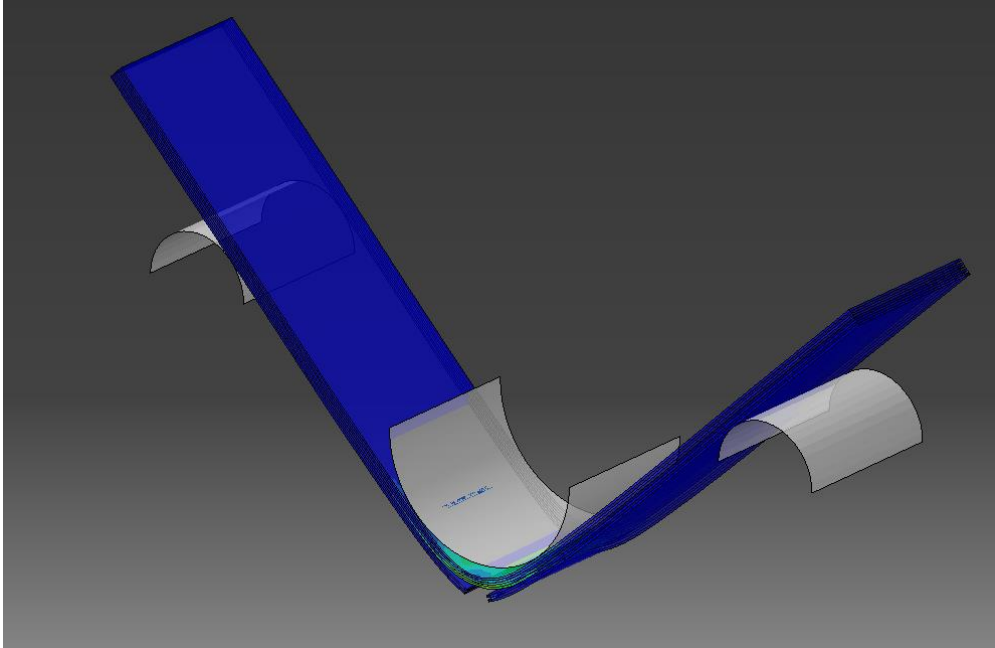


Extension (m)	Matrix Tension Damage
0.000	
0.004	
0.008	
0.012	
0.015	

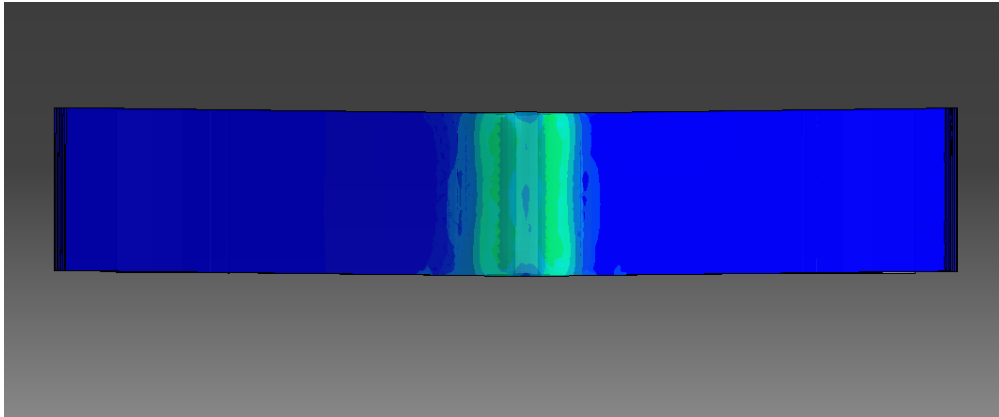


Extension (m)	Johnson-Cook Damage
0.000	
0.004	
0.008	
0.012	
0.015	

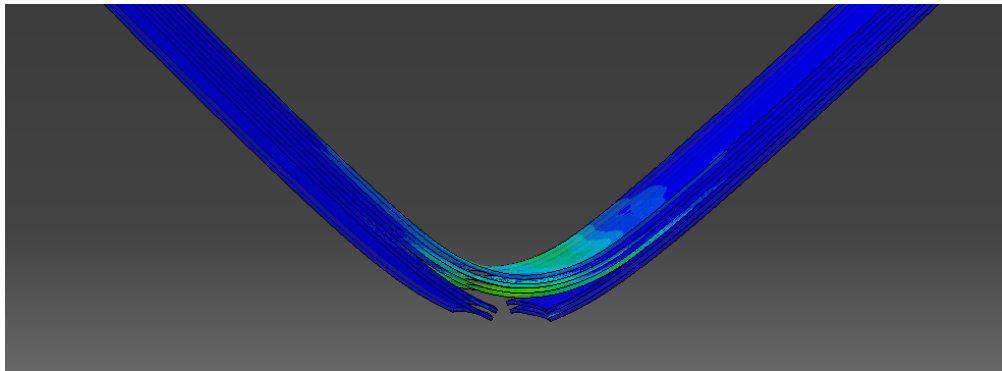
Extension (m)	Traction-Separation Damage
0.000	
0.004	
0.008	
0.012	
0.015	



Vara Model View

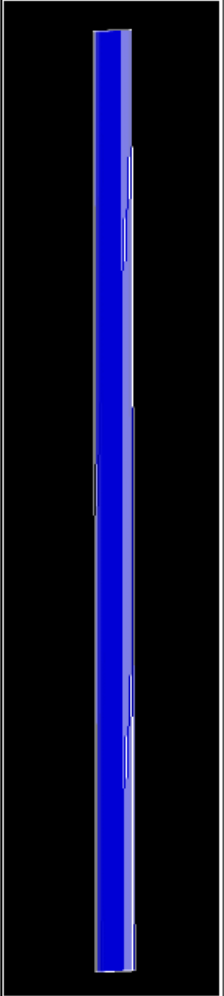
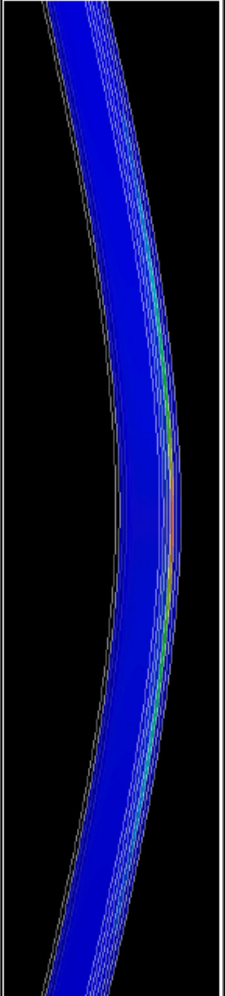
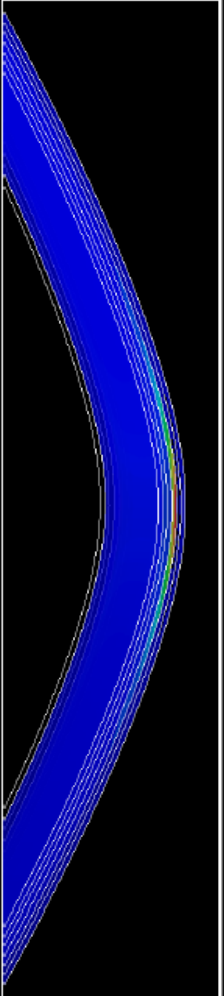
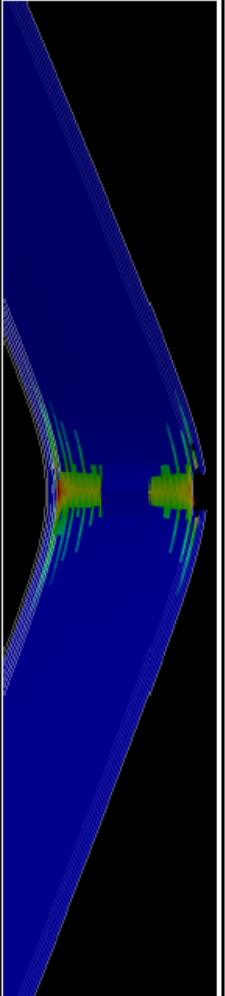
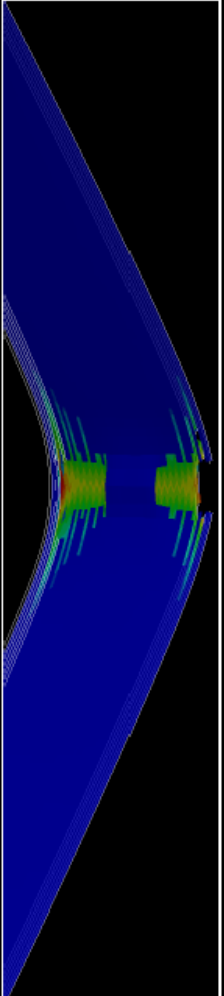


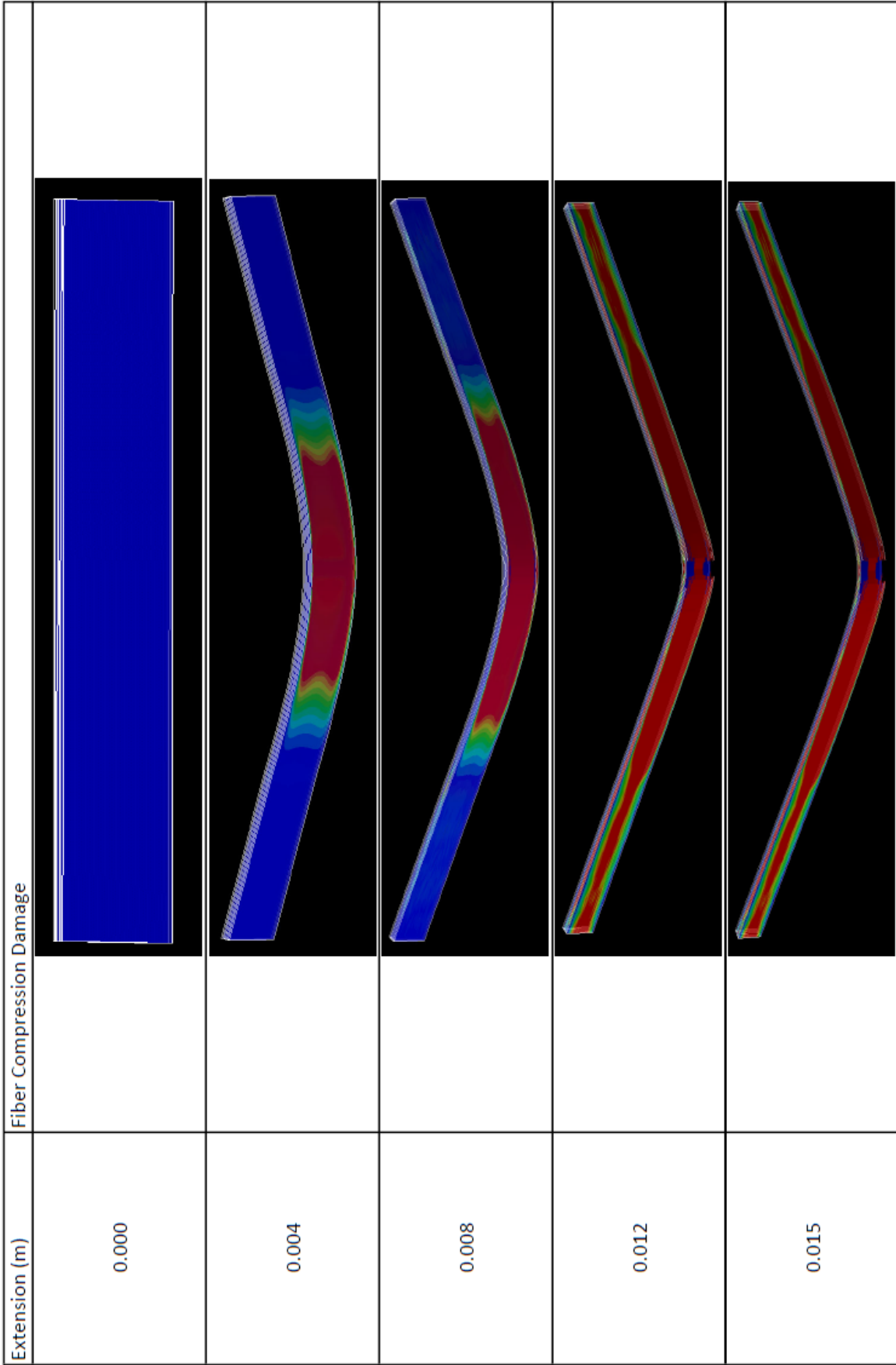
Vara Model Top View with Impactor Hidden

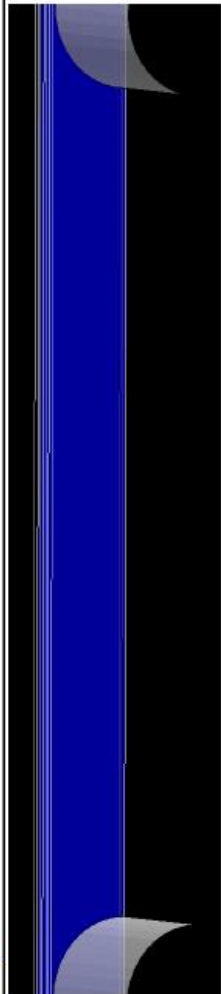
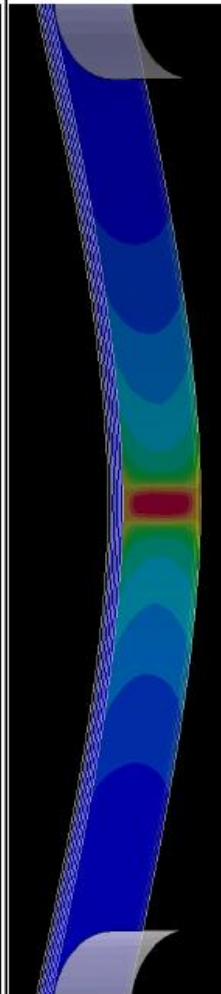
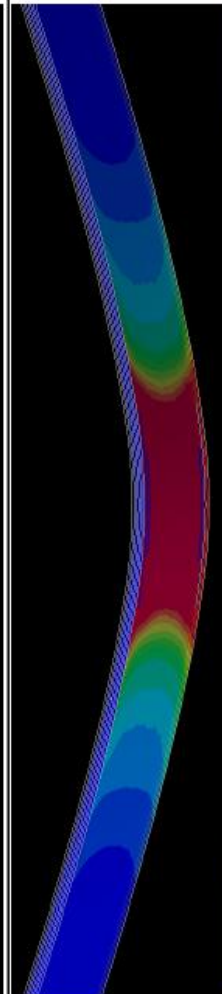
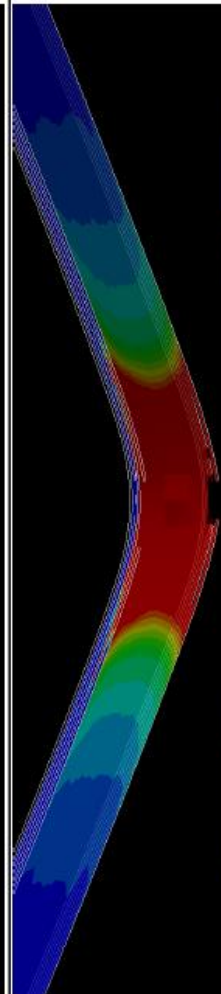
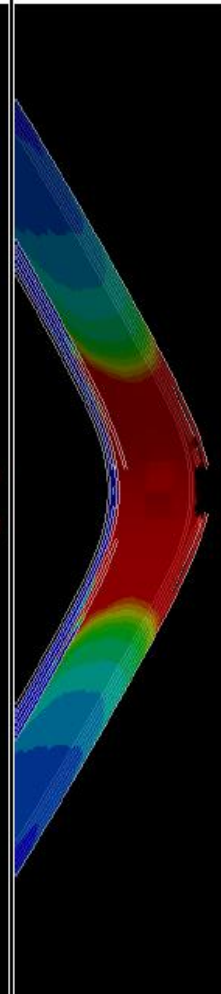


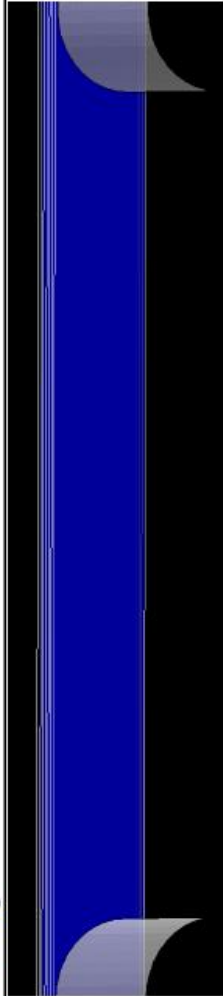
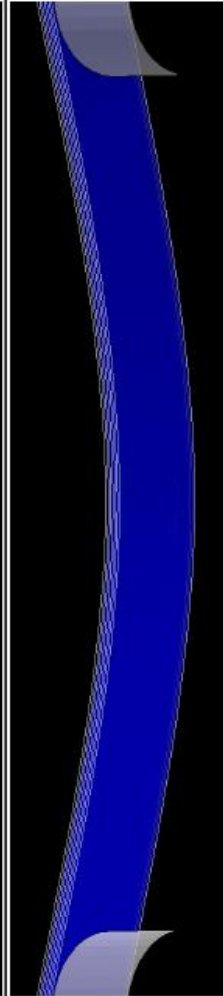
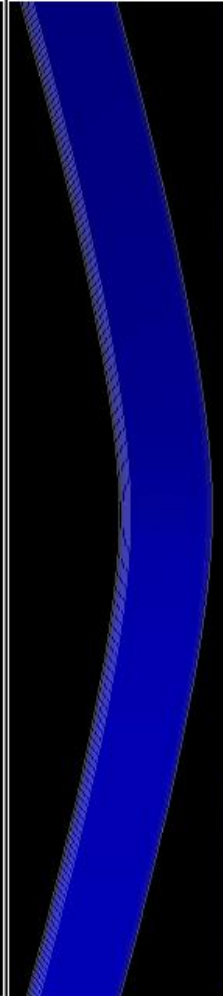
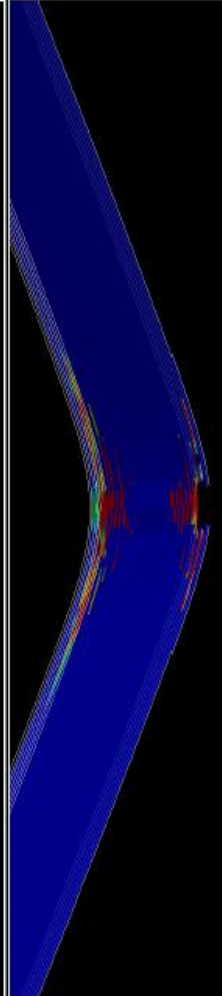
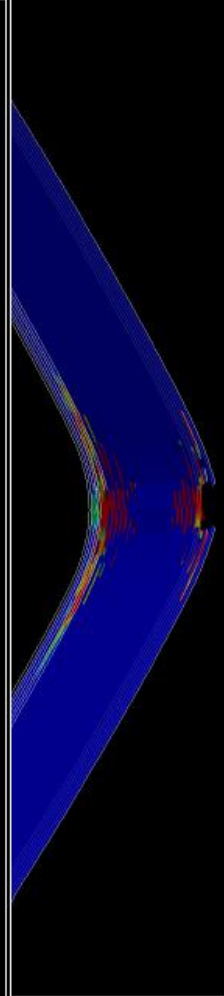
Vara Model View with Impactor Hidden

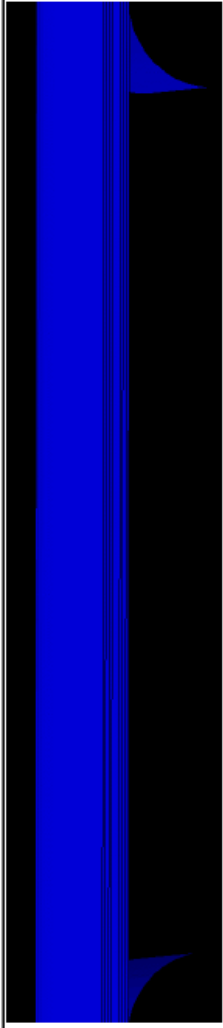
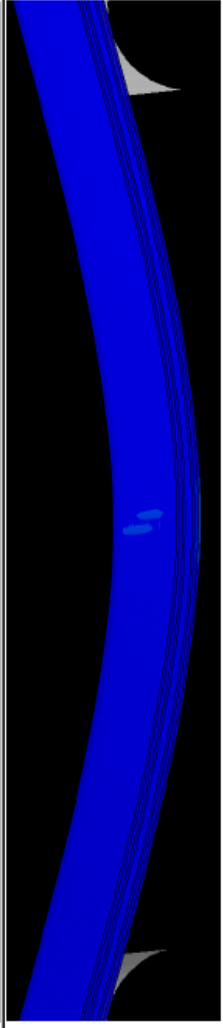
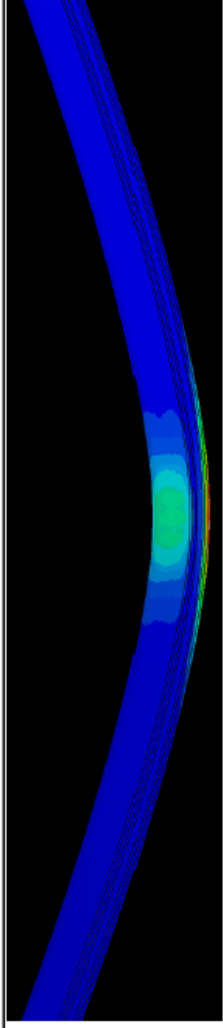
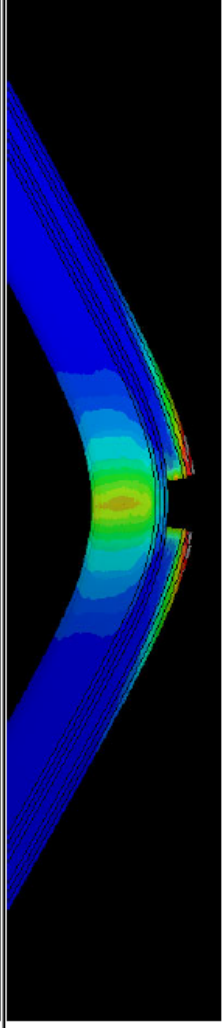
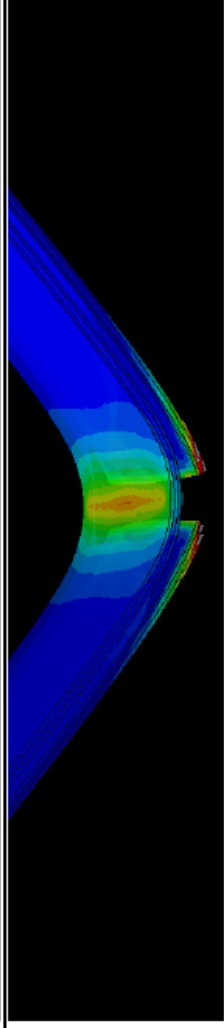
Vara Model 1.5X Width

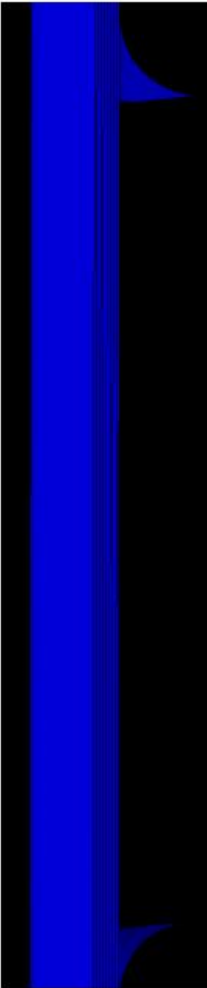
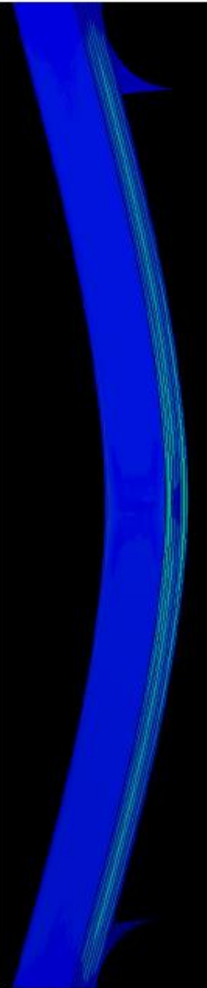
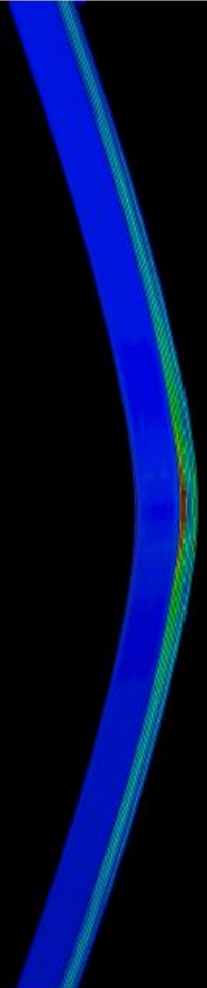
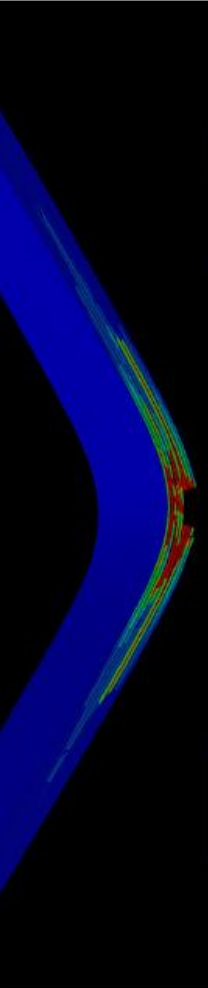
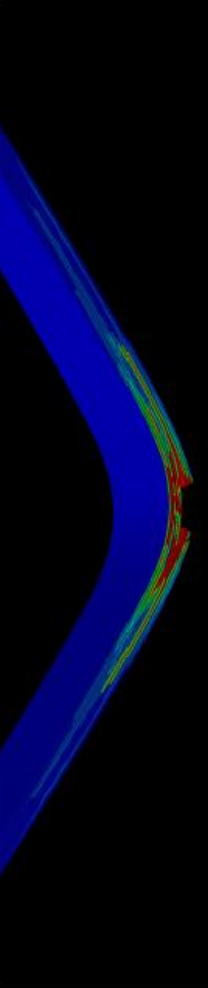
Extension (m)	Fiber Tension Damage
0.000	
0.004	
0.008	
0.012	
0.015	

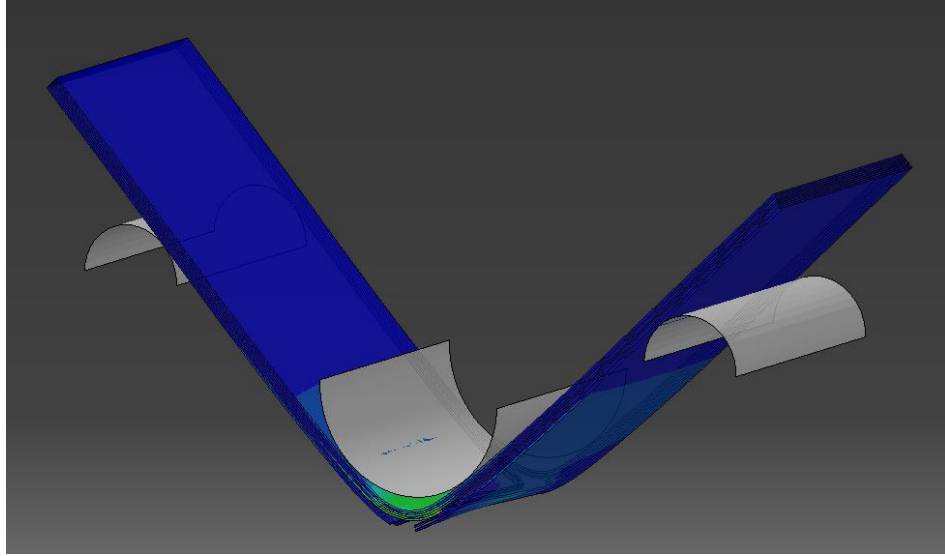


Extension (m)	Matrix Tension Damage
0.000	
0.004	
0.008	
0.012	
0.015	

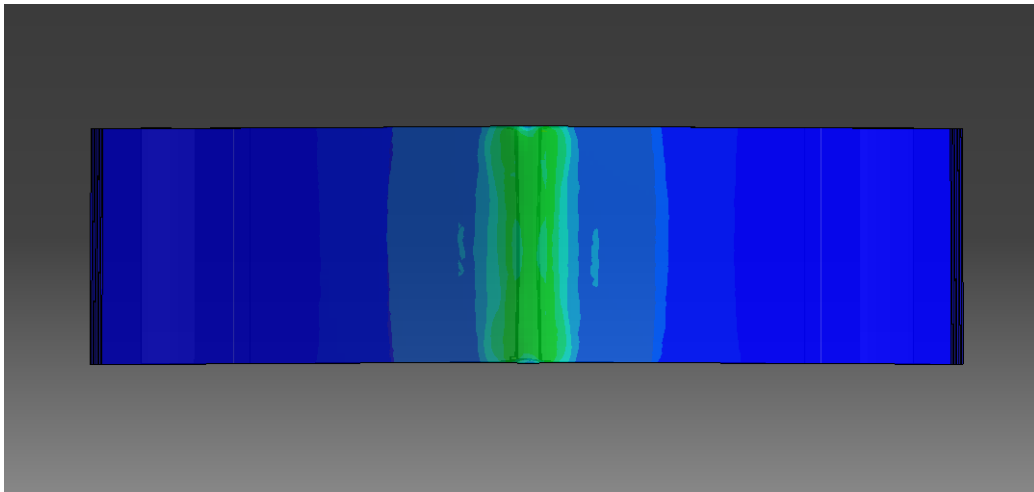
Extension (m)	Matrix Compression Damage
0.000	
0.004	
0.008	
0.012	
0.015	

Extension (m)	Johnson-Cook Damage
0.000	
0.004	
0.008	
0.012	
0.015	

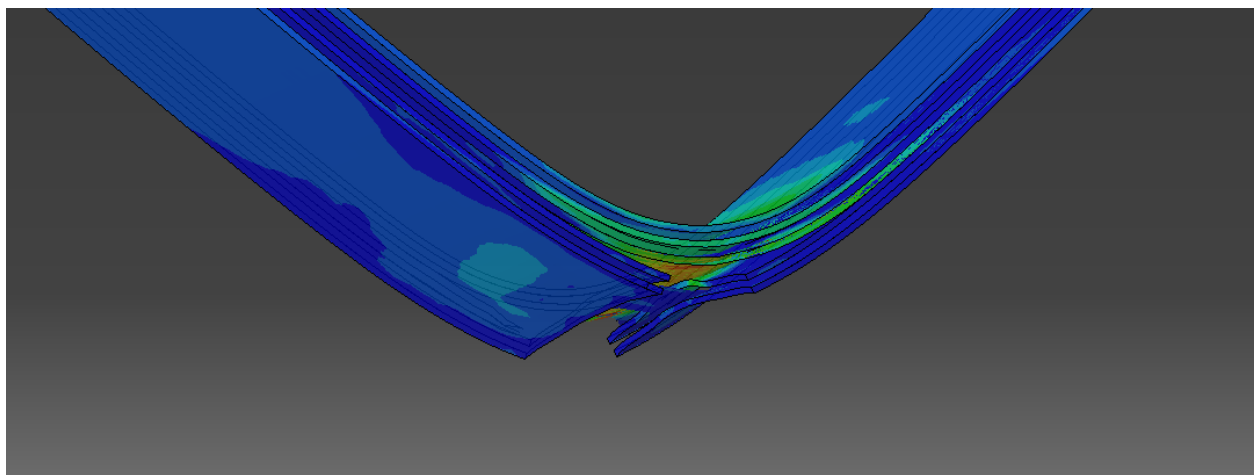
Extension (m)	Traction-Separation Damage
0.000	
0.004	
0.008	
0.012	
0.015	



Vara Model 1.5x Width View

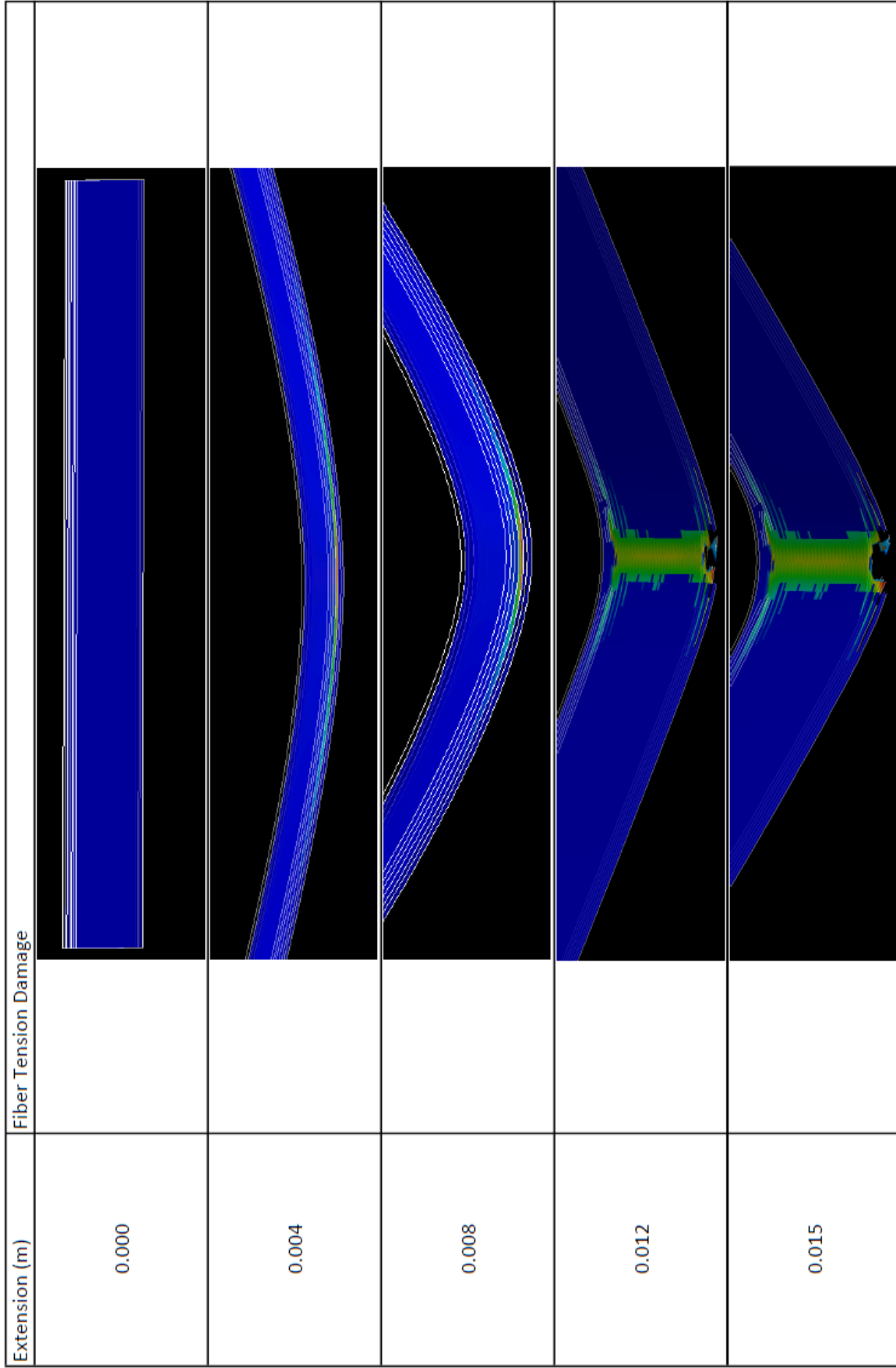


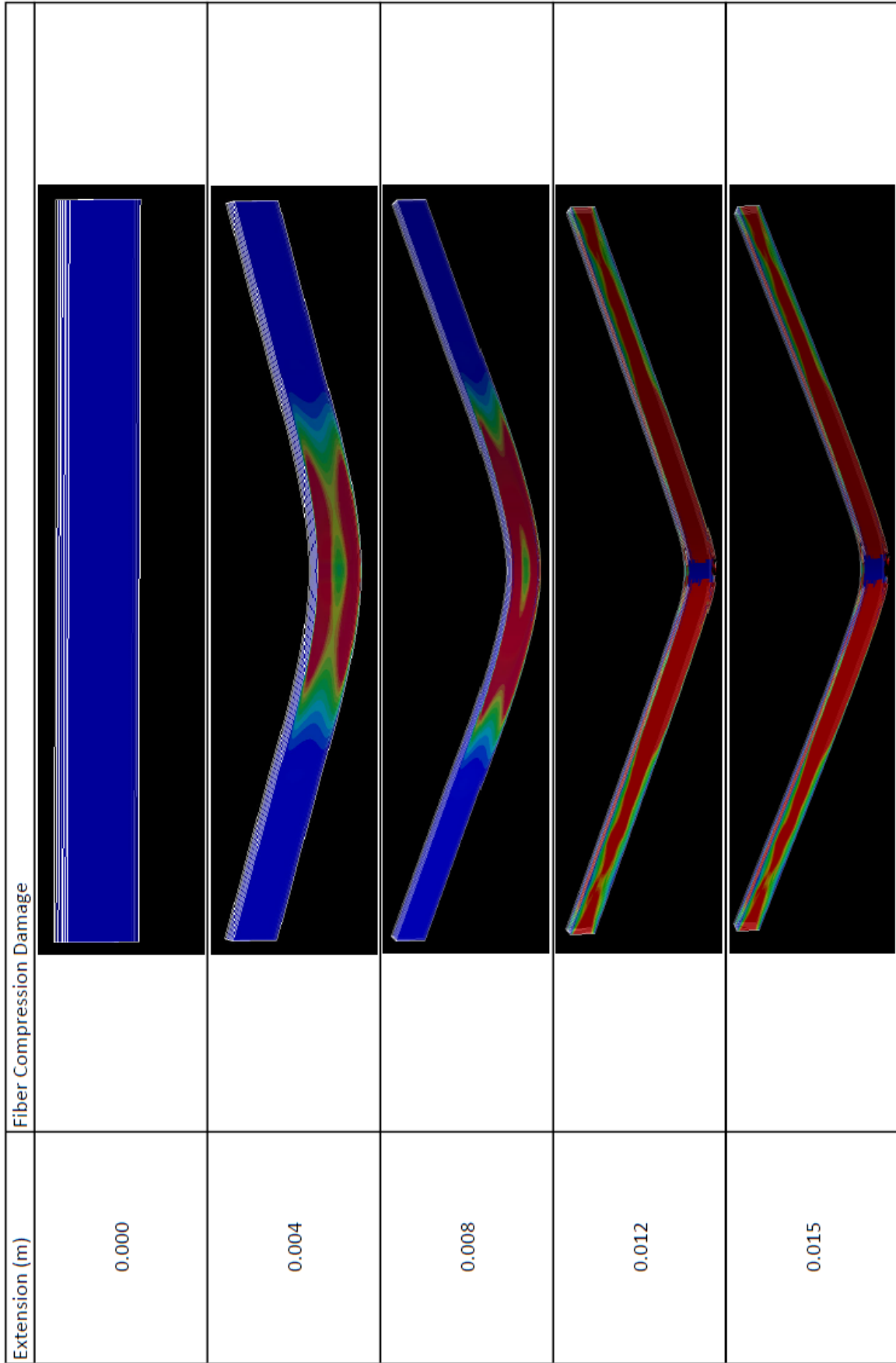
Vara Model 1.5x Width Top View with Impactor Hidden

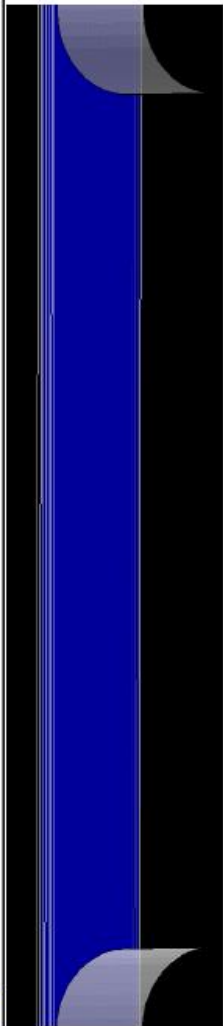
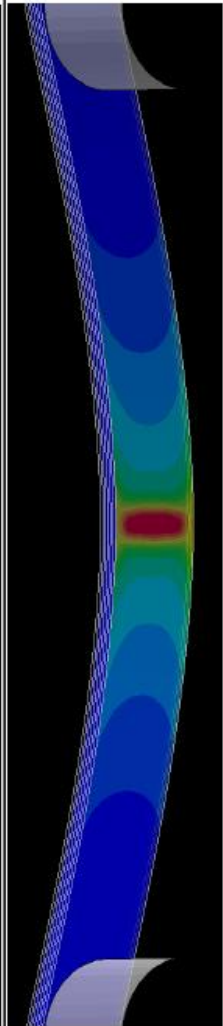
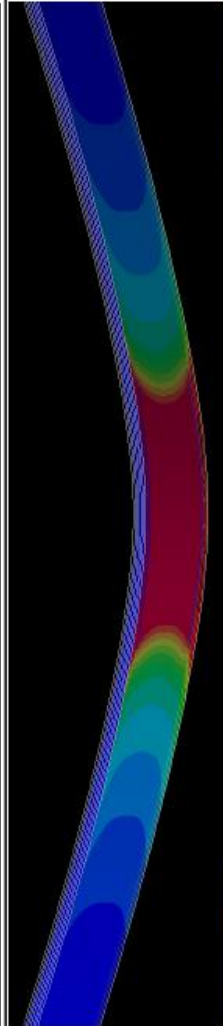
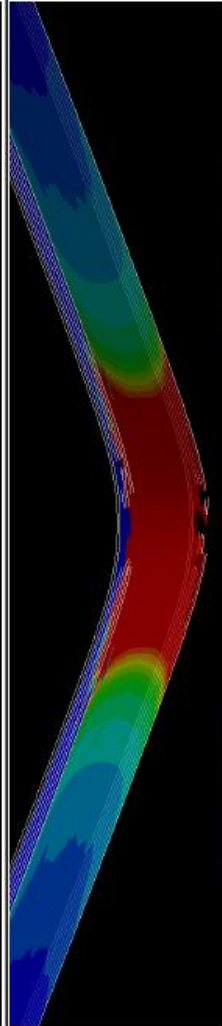
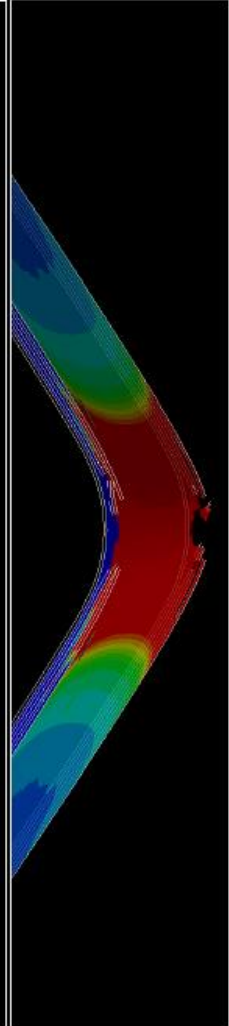


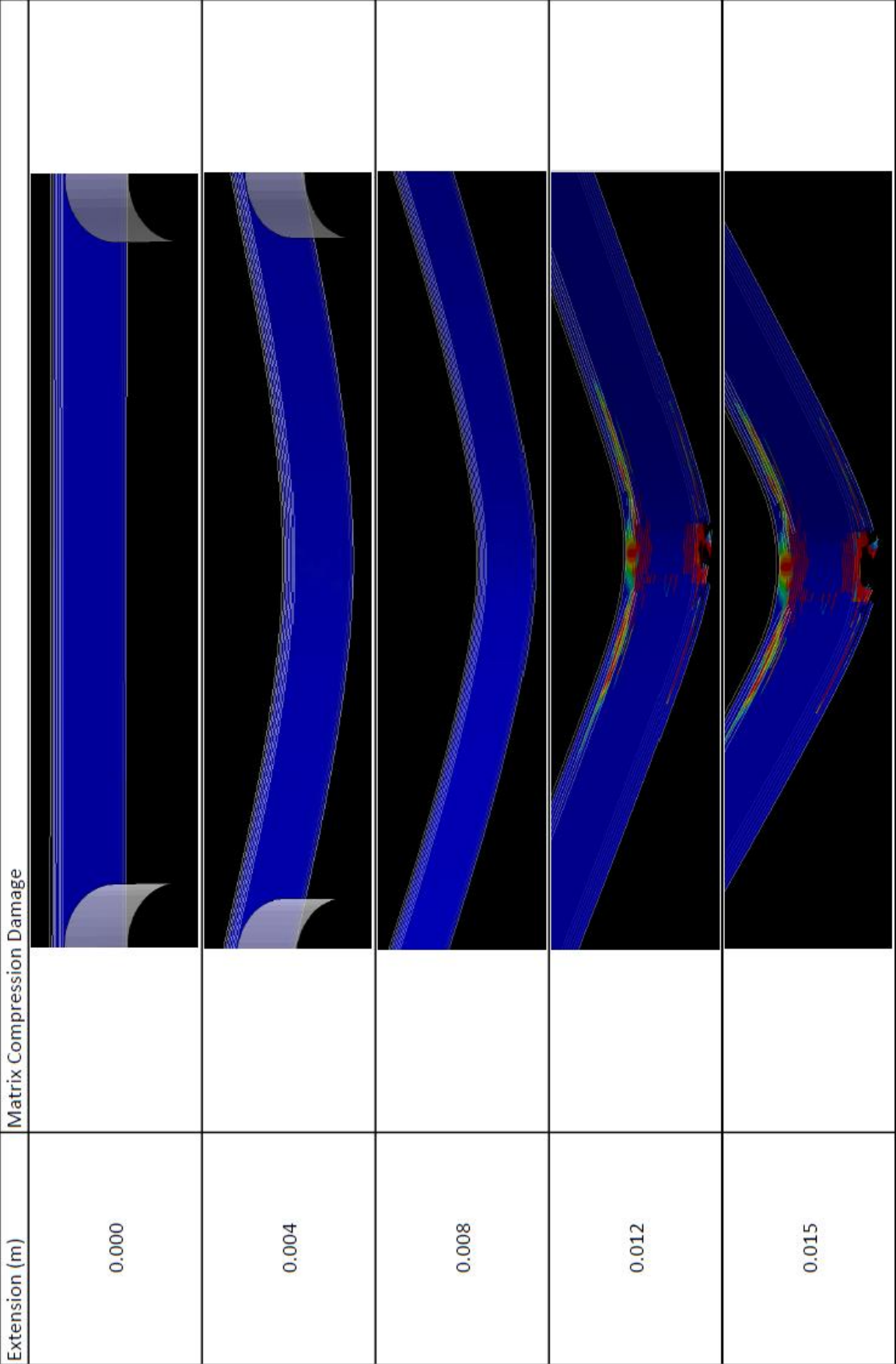
Vara Model 1.5x Width Top View with Impactor Hidden

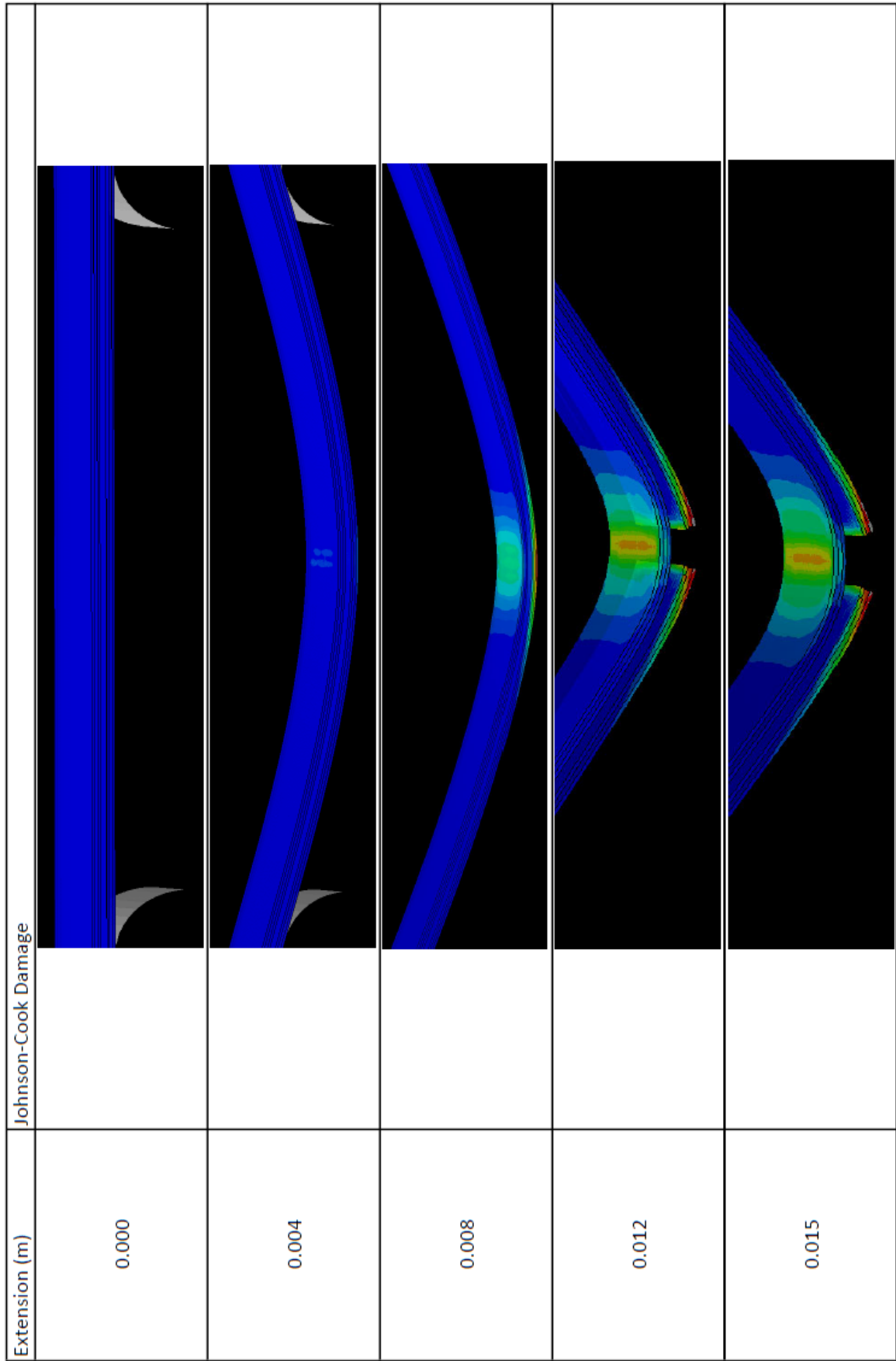
Vara Model 2X Width

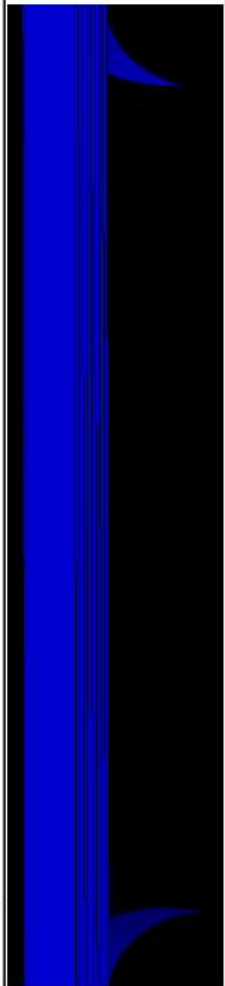
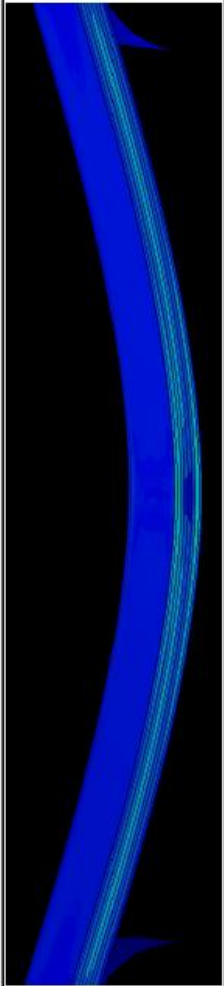
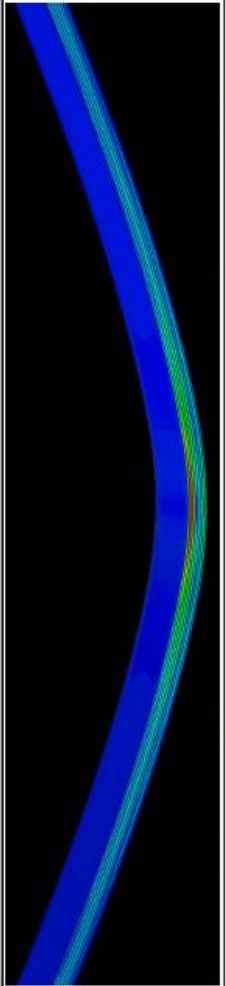
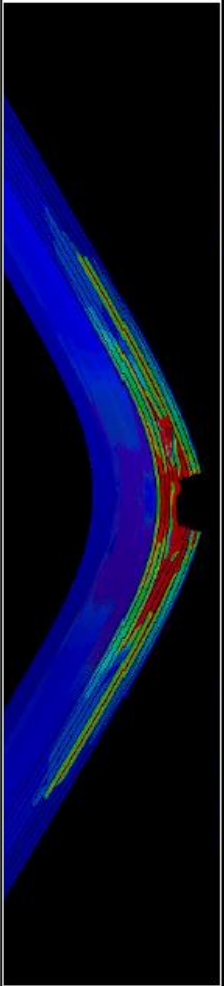
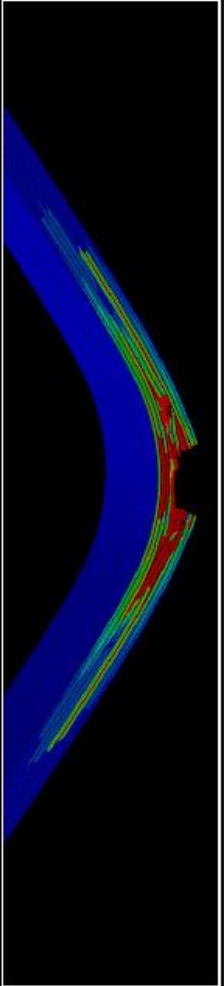


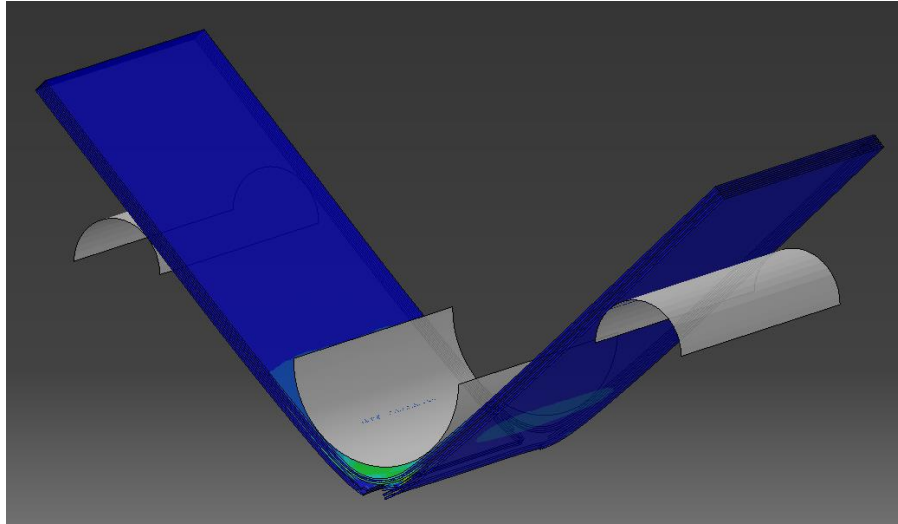


Extension (m)	Matrix Tension Damage
0.000	
0.004	
0.008	
0.012	
0.015	

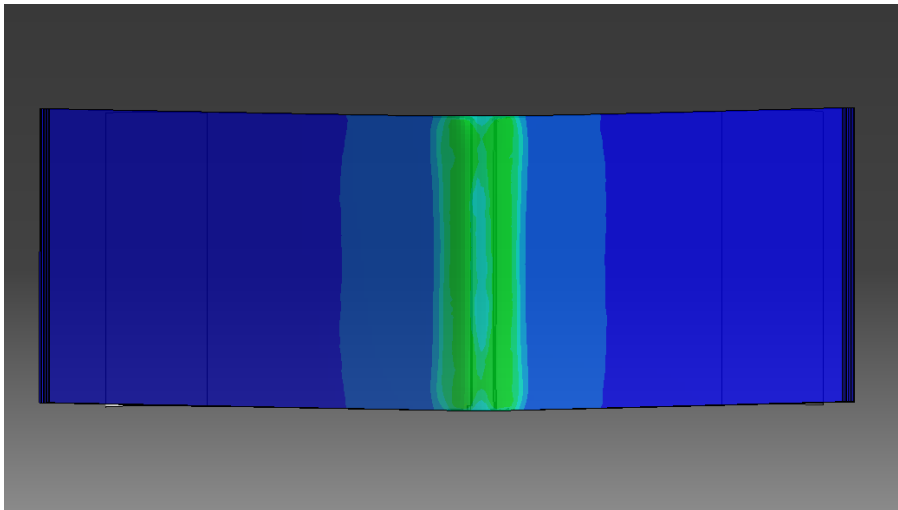




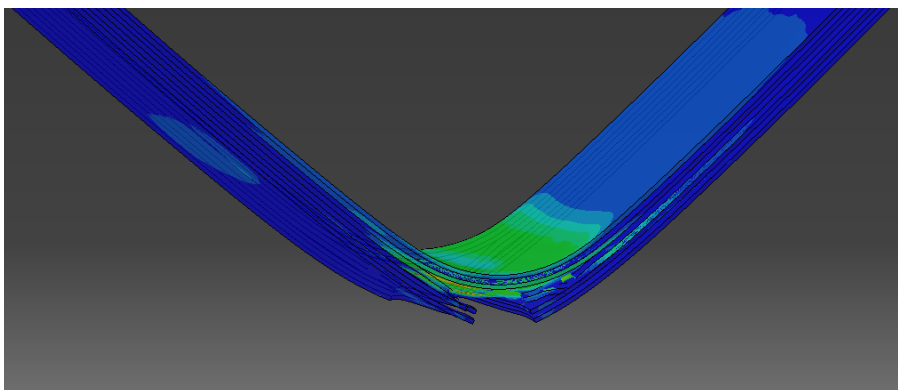
Extension (m)	Traction-Separation Damage
0.000	
0.004	
0.008	
0.012	
0.015	



Vara Model 2x Width View

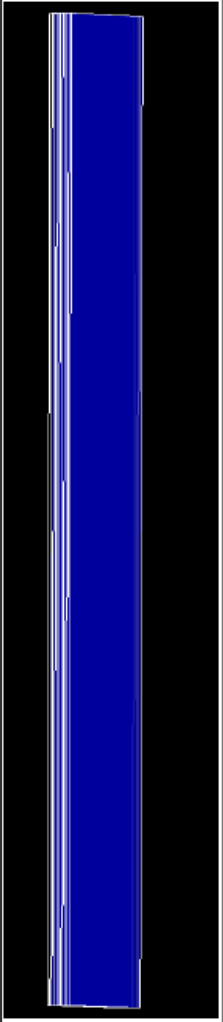
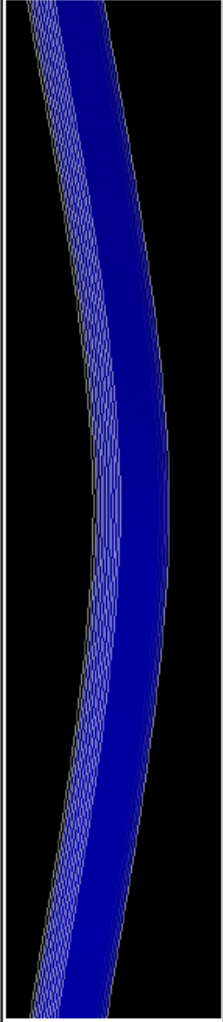
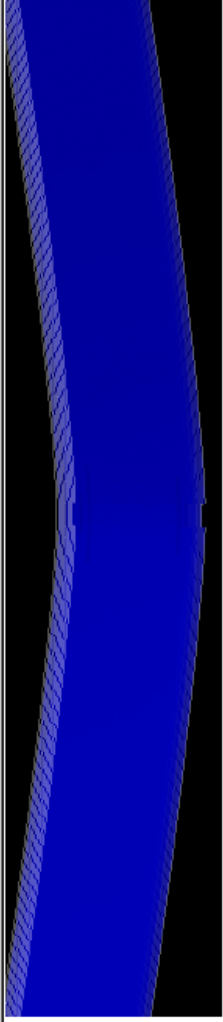
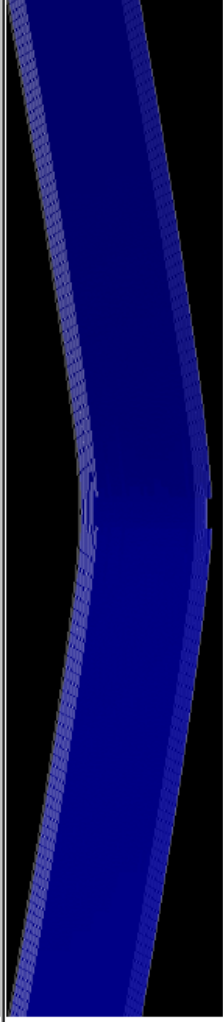
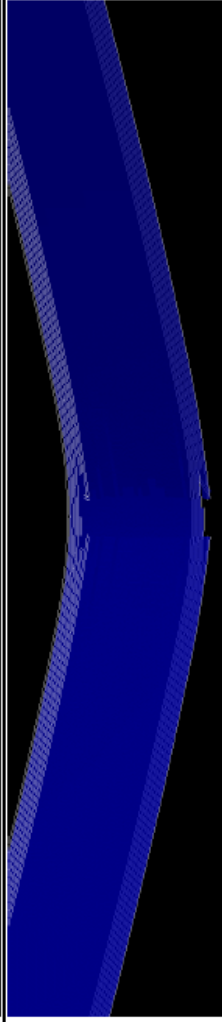


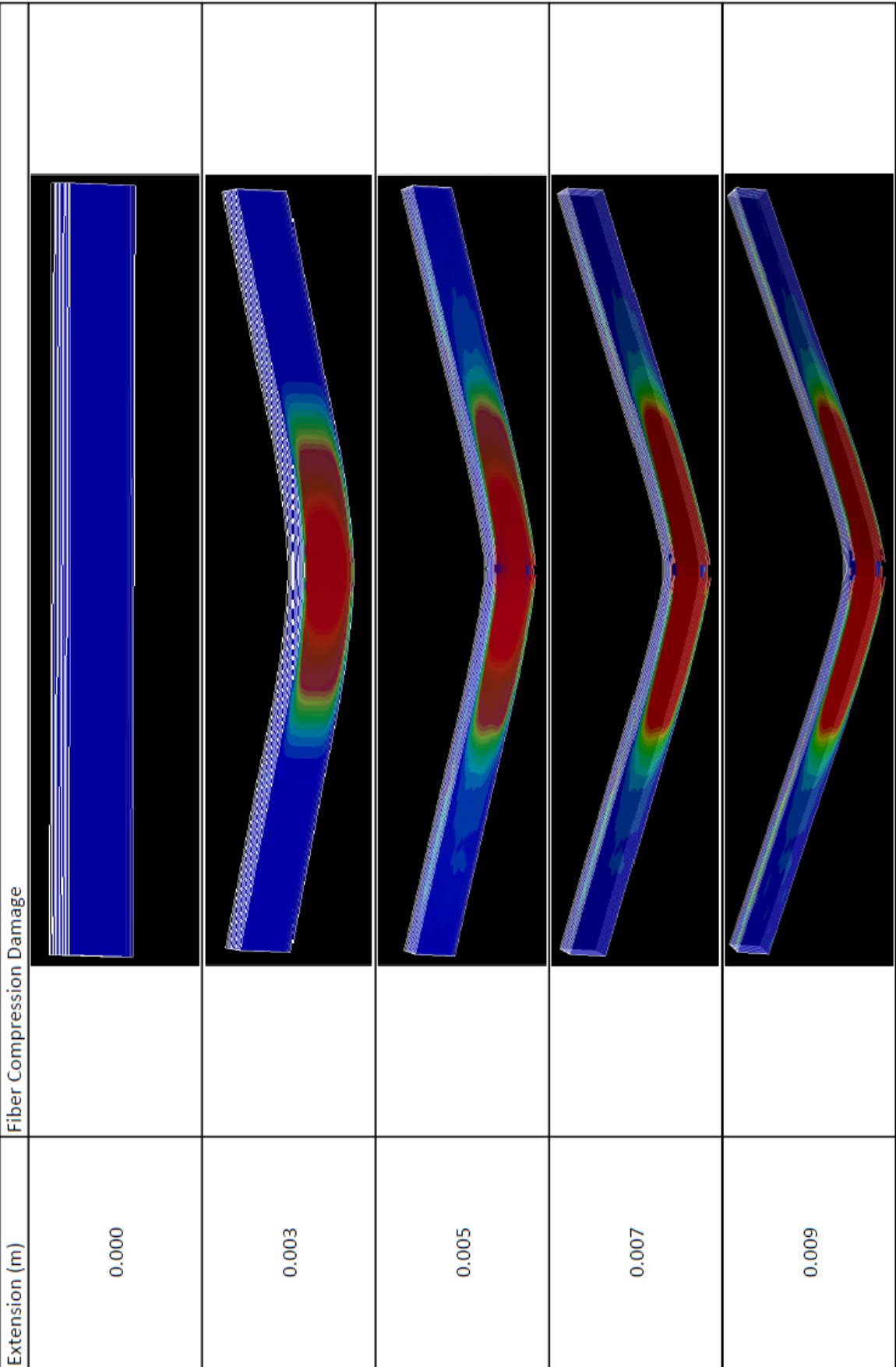
Vara Model 2x Width Top View with Impactor Hidden

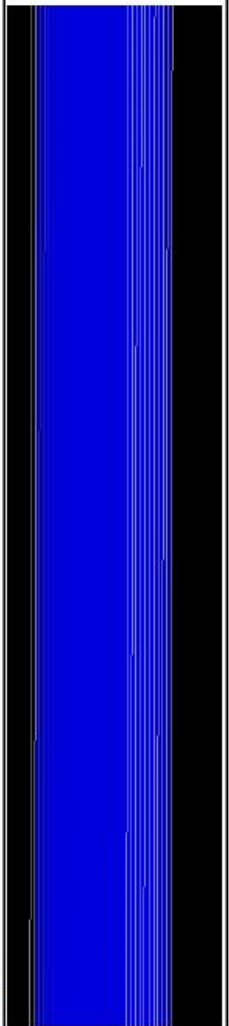
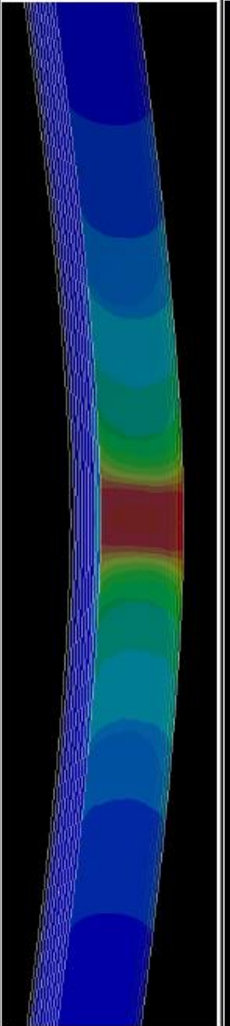
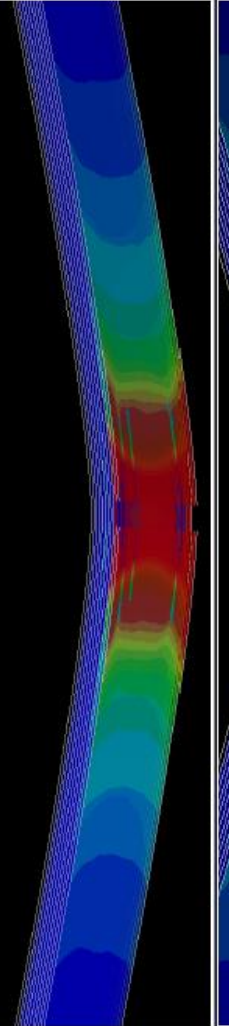
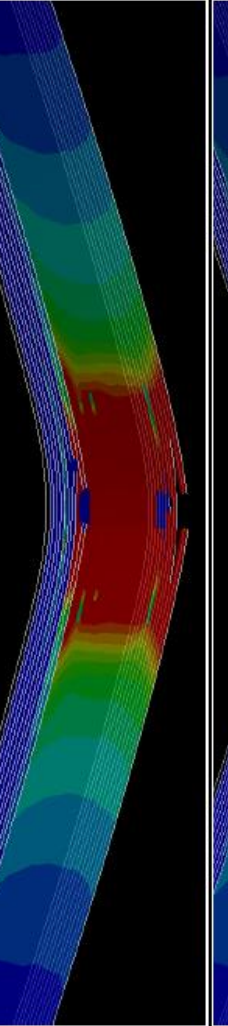
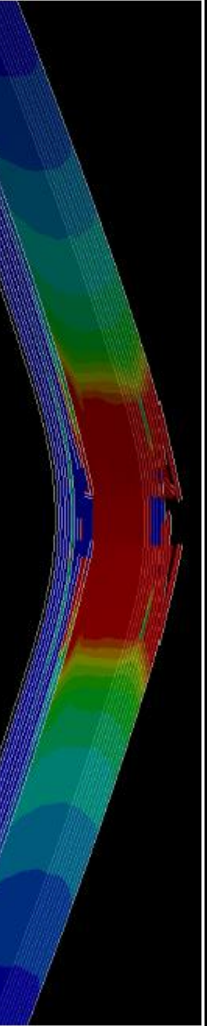


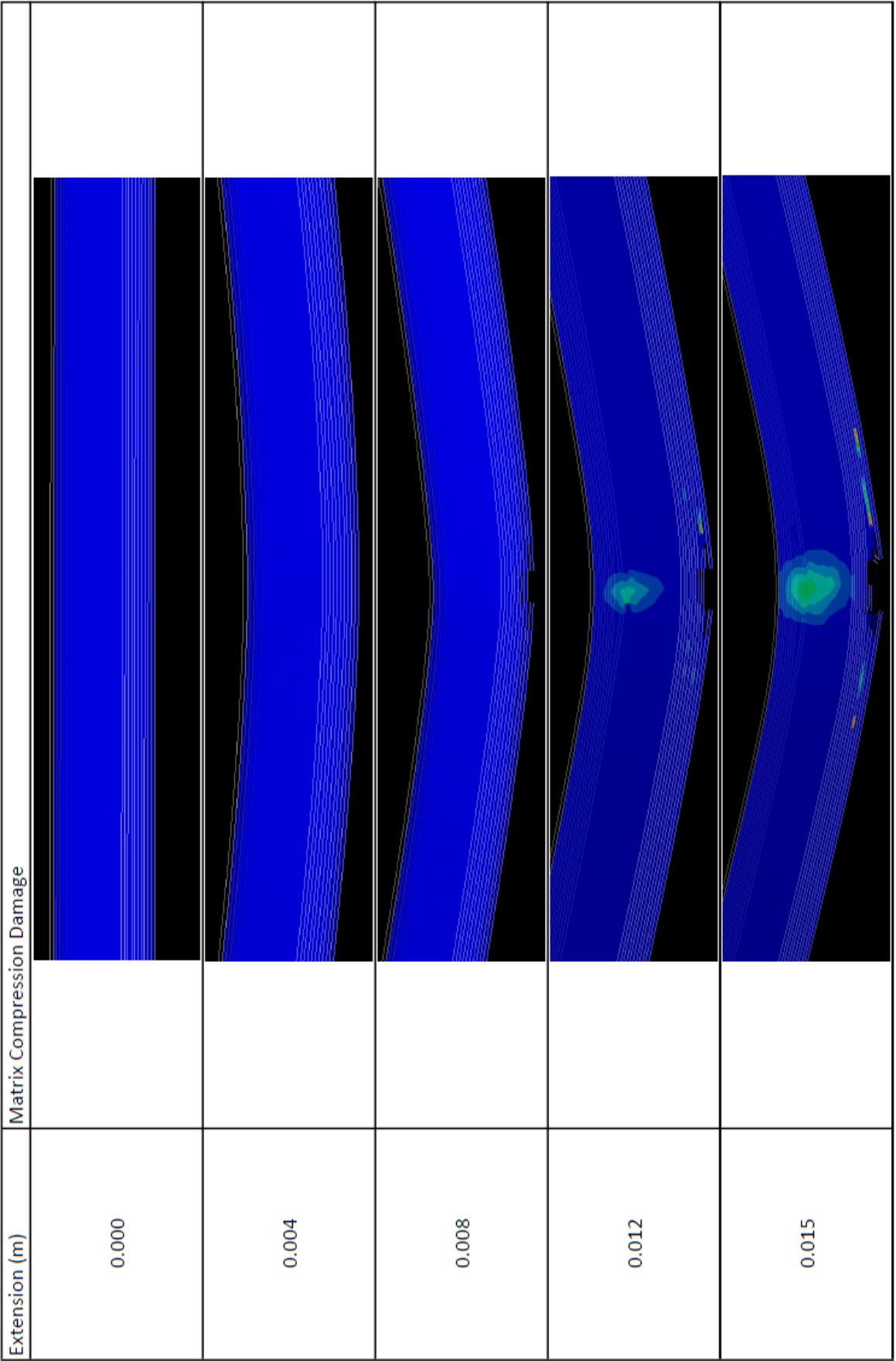
Vara Model 2x Width View with Impactor Hidden

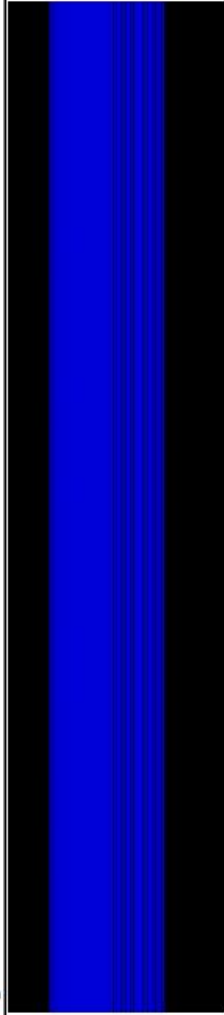
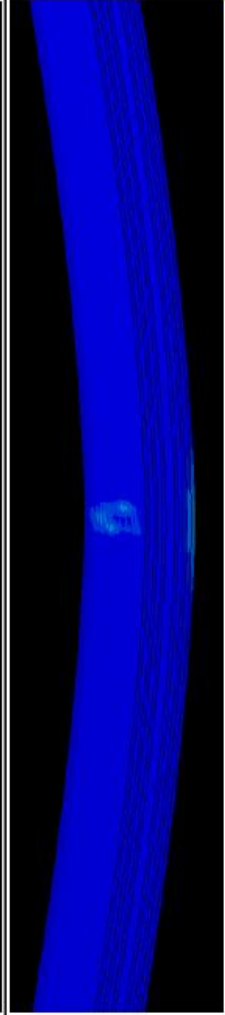
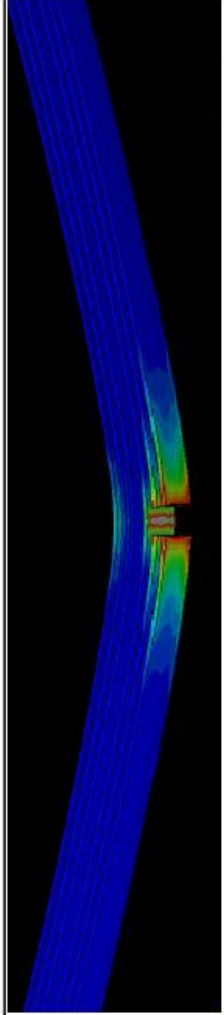
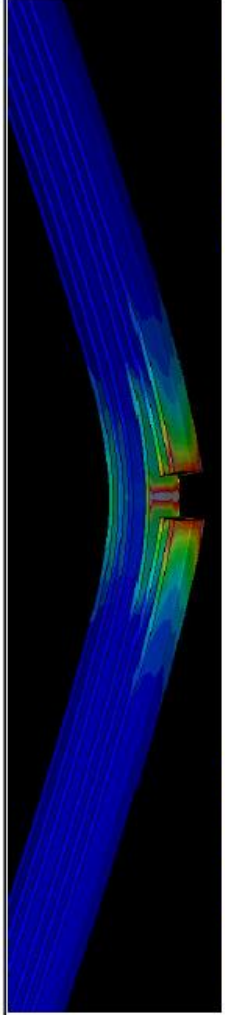
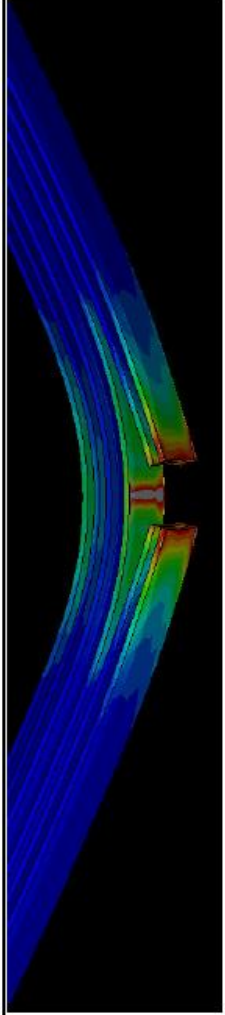
Vara Model 4 Added Plies

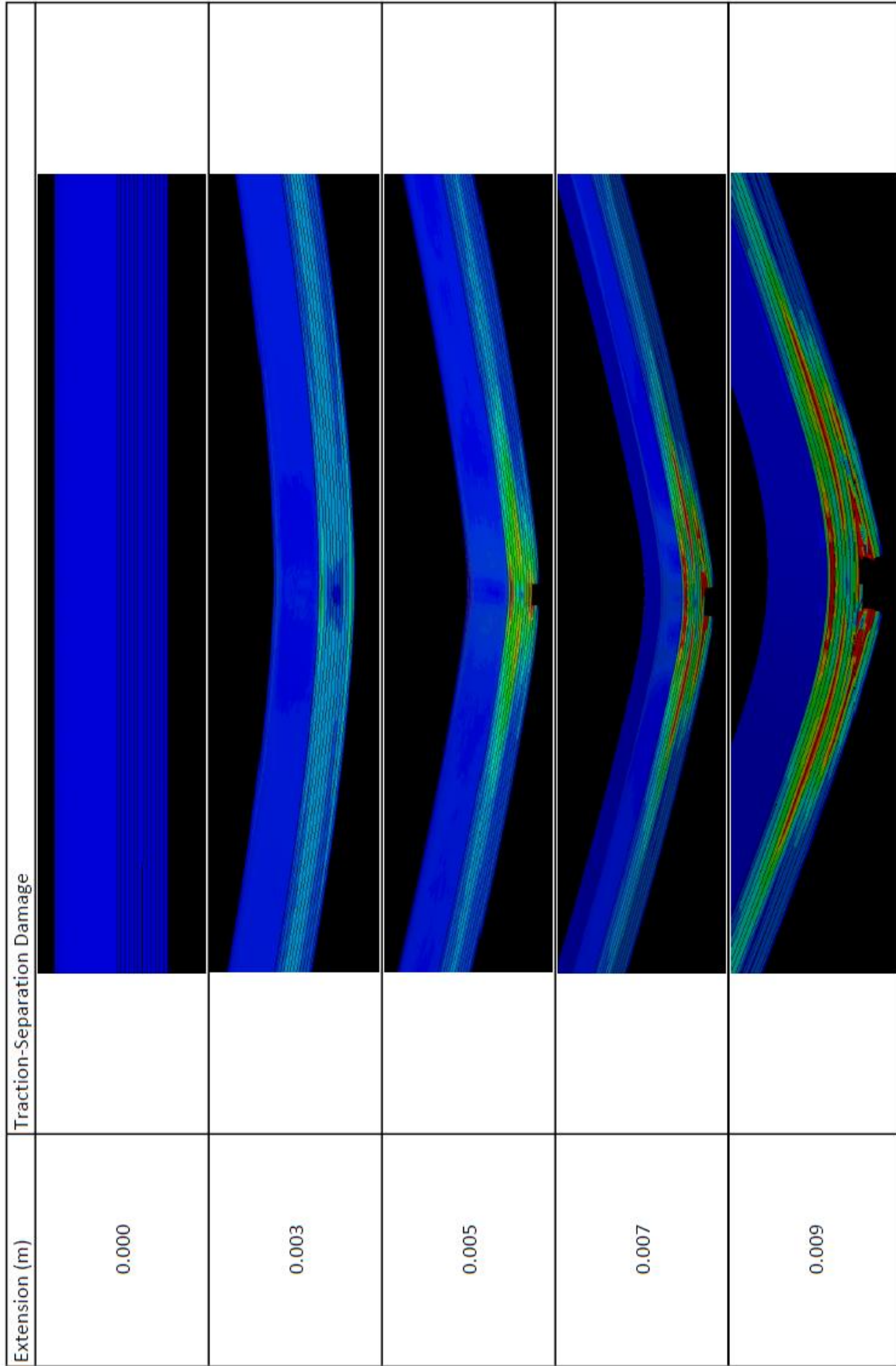
Extension (m)	Fiber Tension Damage
0.000	
0.003	
0.005	
0.007	
0.009	

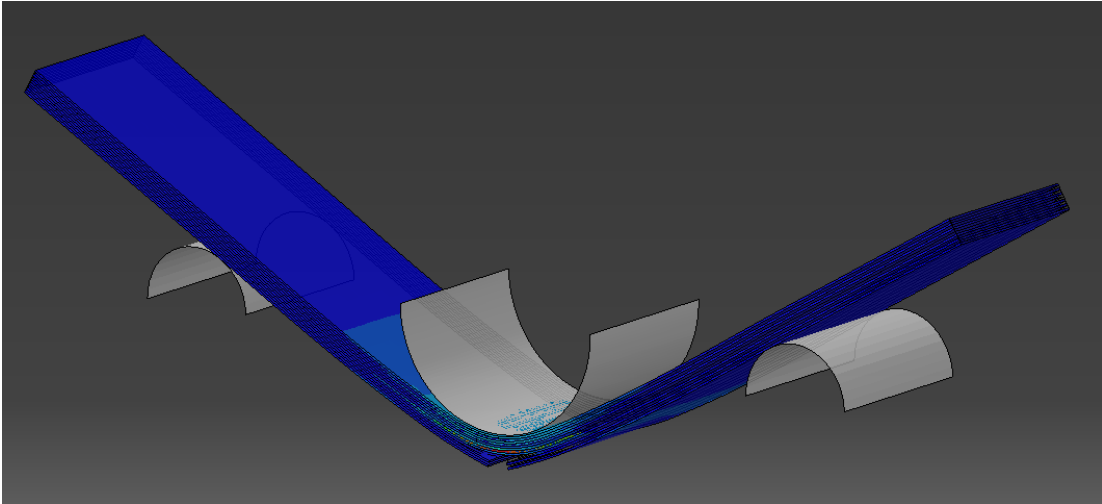


Extension (m)	Matrix Tension Damage
0.000	
0.003	
0.005	
0.007	
0.009	

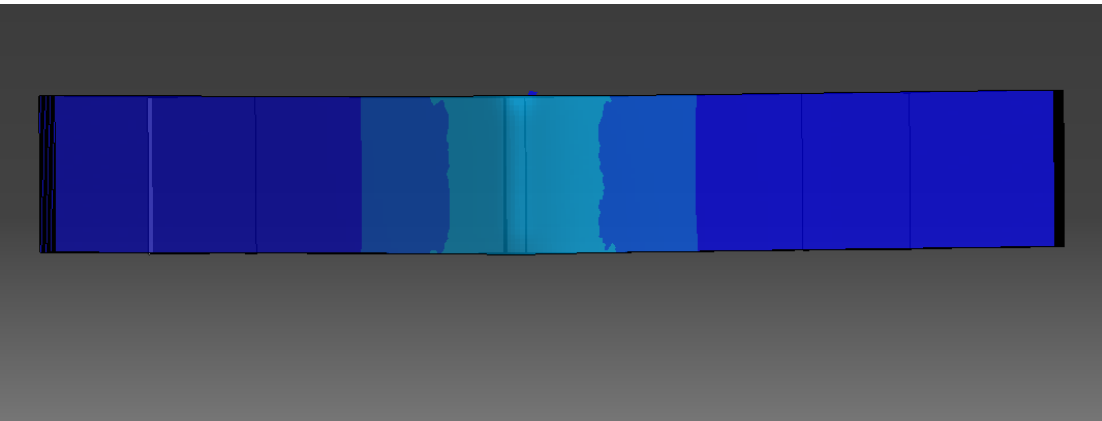


Extension (m)	Johnson-Cook Damage
0.000	
0.003	
0.005	
0.007	
0.009	

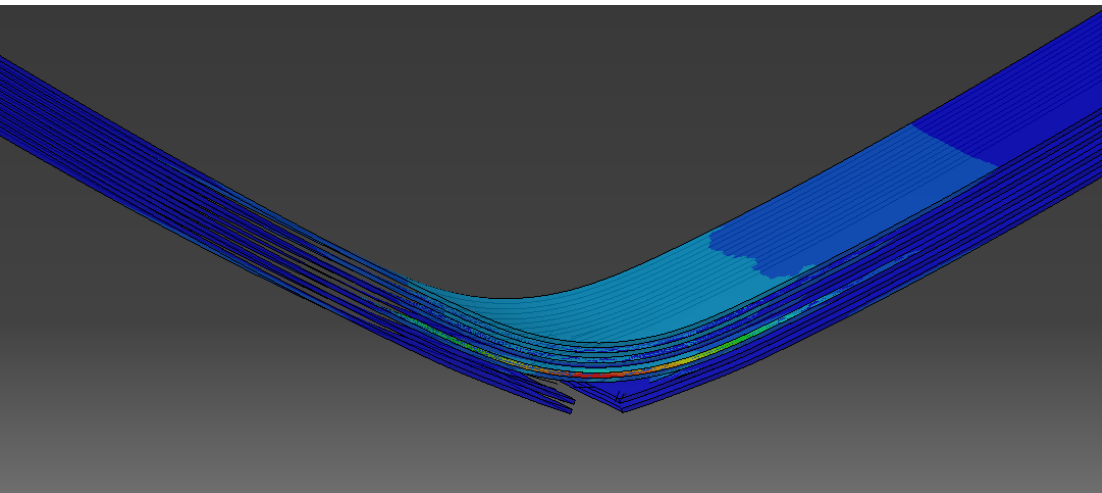




Vara Model +4 Plies View

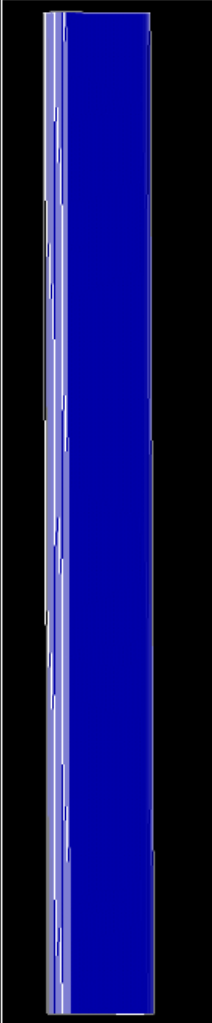
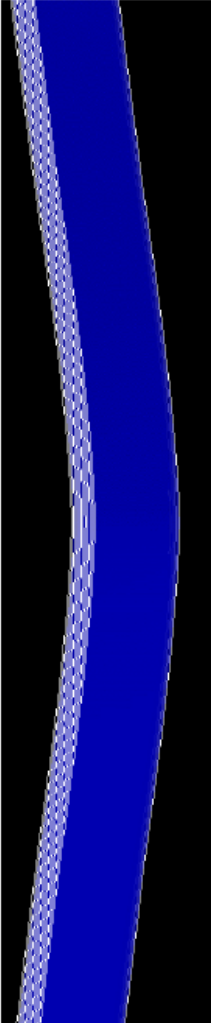
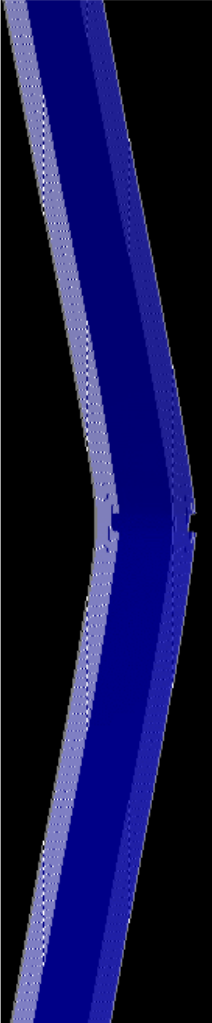
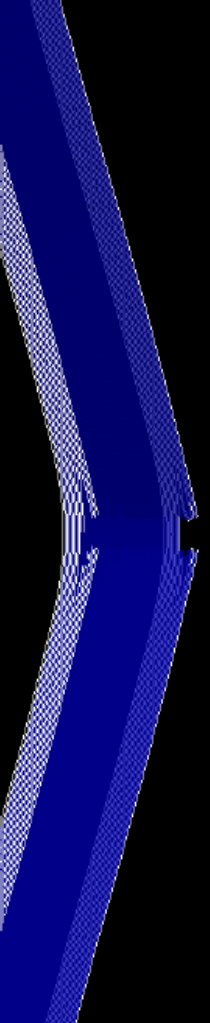
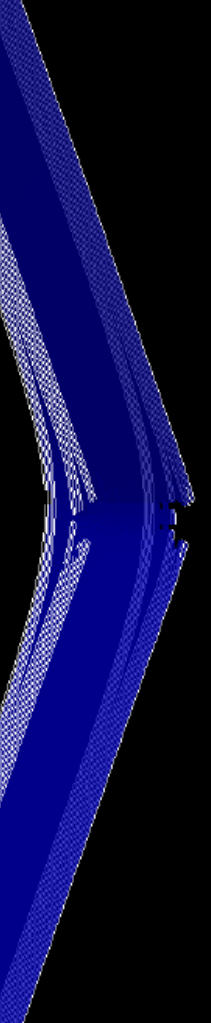


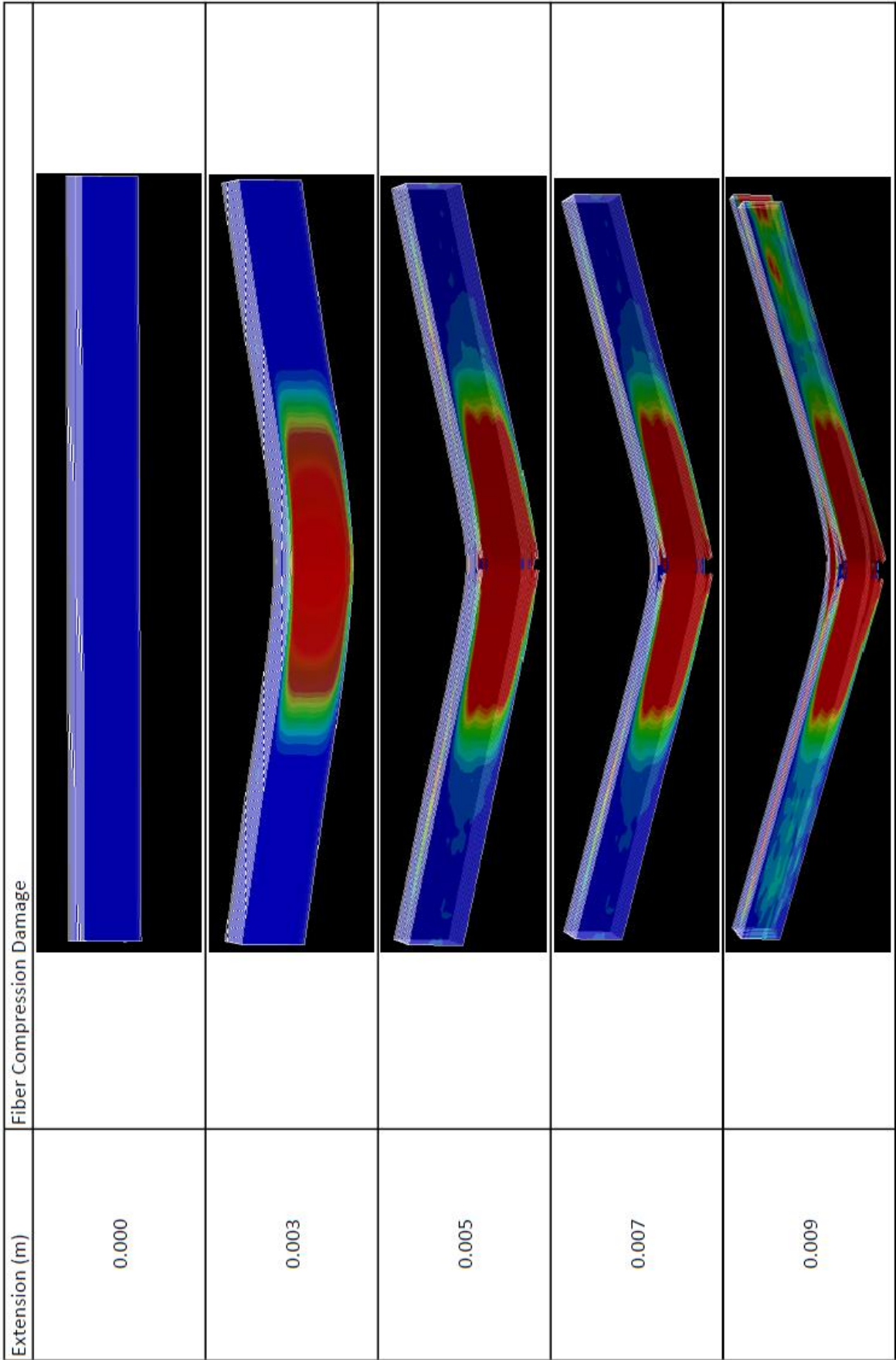
Vara Model +4 Plies Top View with Impactor Removed

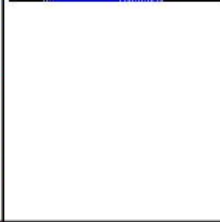

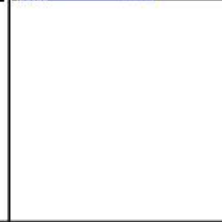

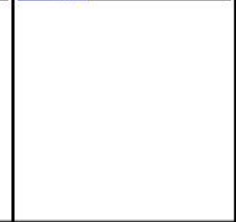


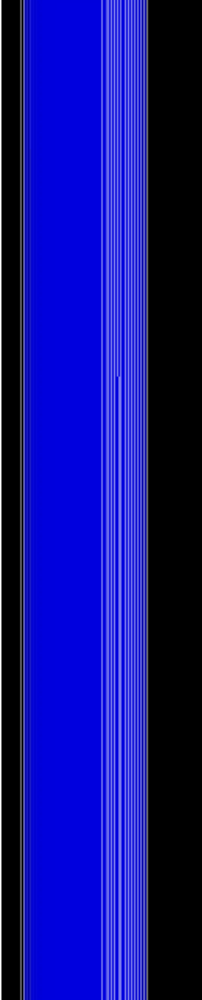
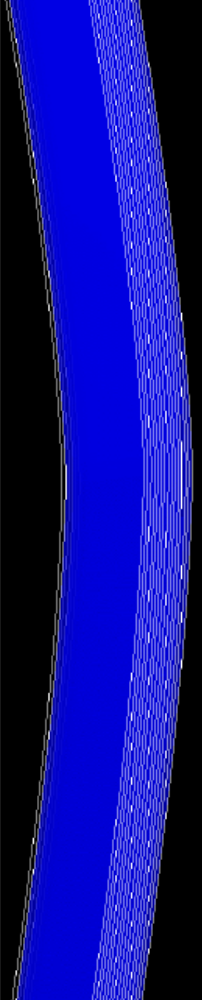
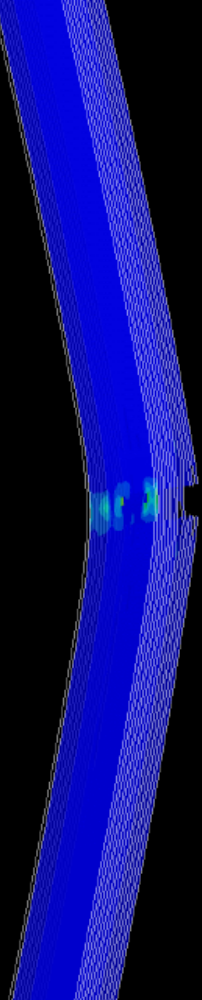
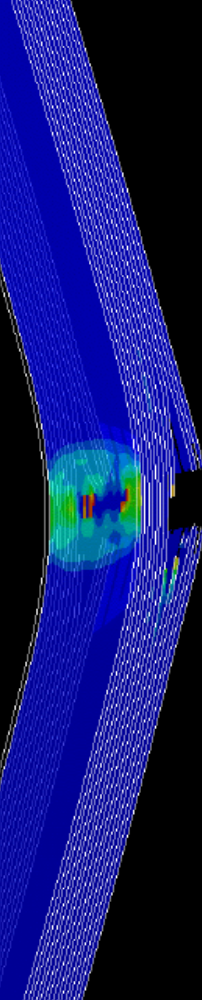
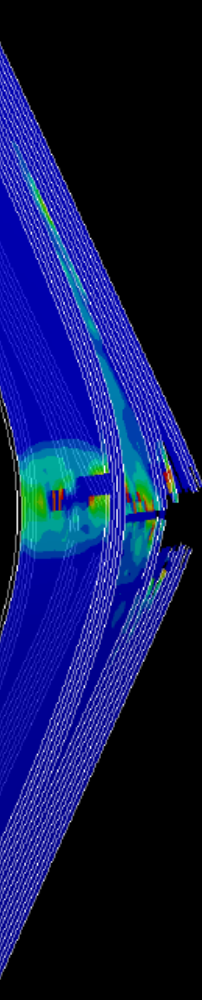
Vara Model +4 Plies View with Impactor Removed

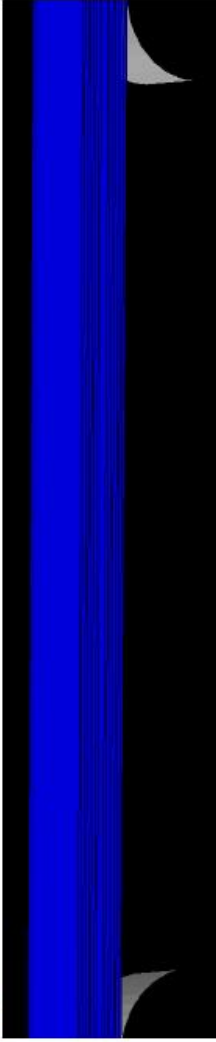
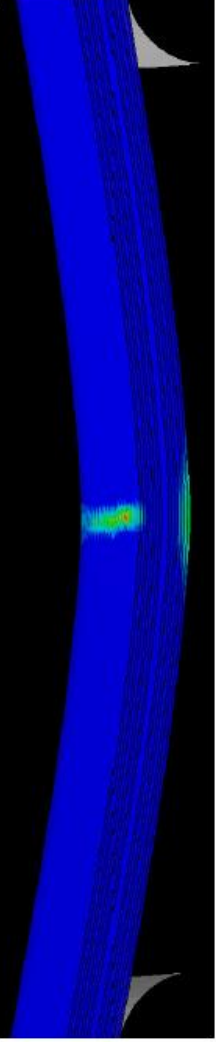
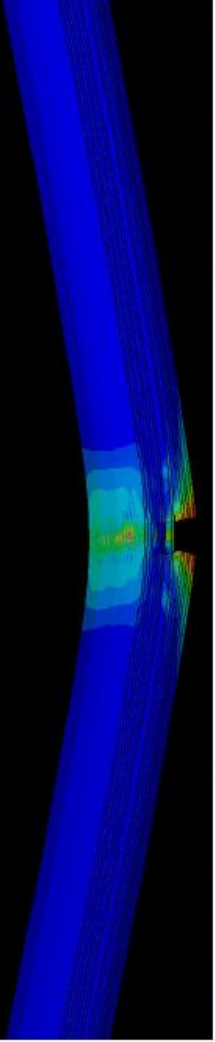
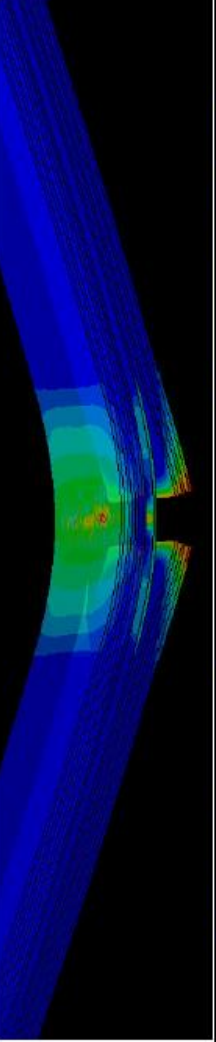
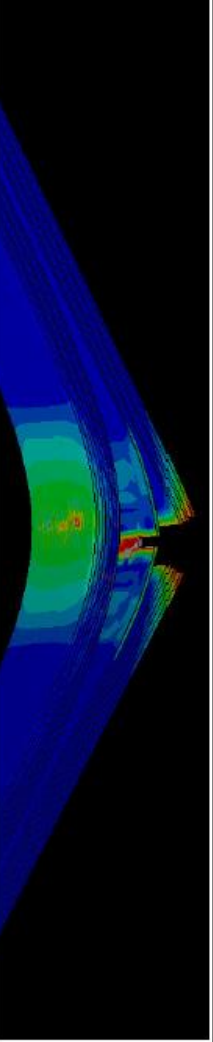
Vara Model 8 Added Plies

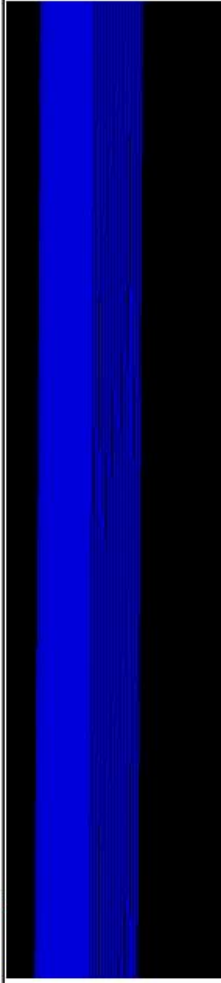
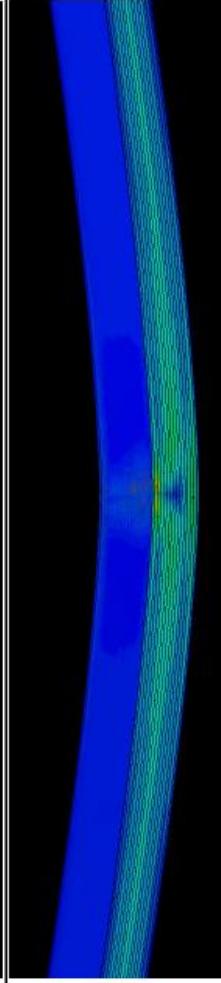
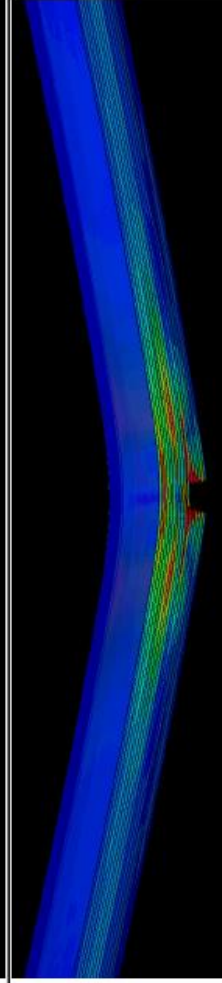
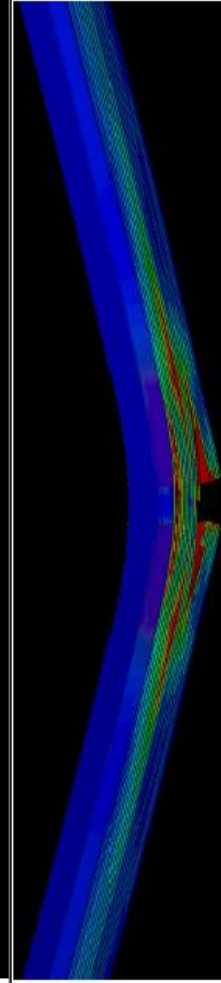
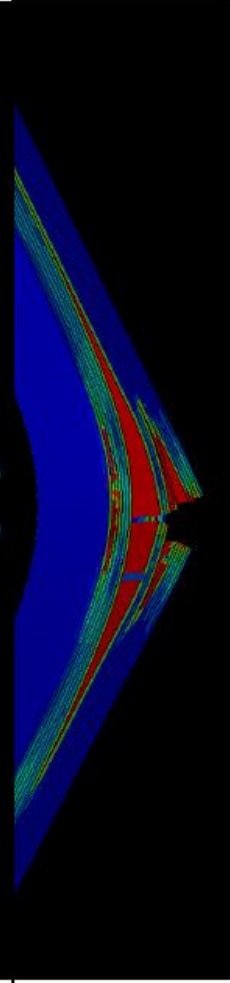
Extension (m)	Fiber Tension Damage
0.000	
0.003	
0.005	
0.007	
0.009	

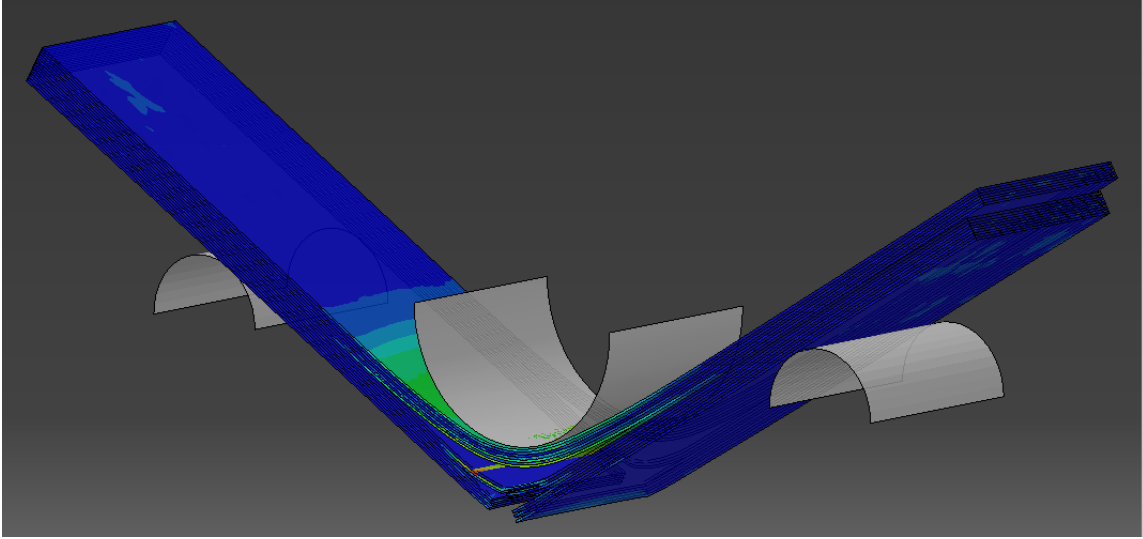


Extension (m)	Matrix Tension Damage
0.000	
0.003	
0.005	
0.007	
0.009	

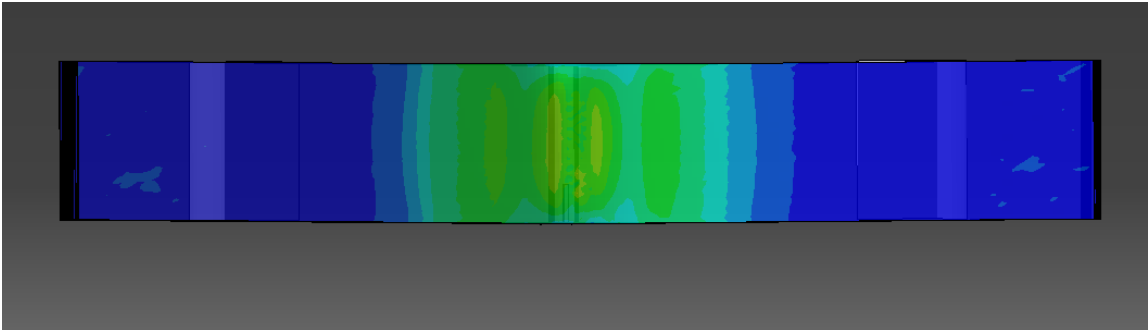
Extension (m)	Matrix Compression Damage
0.000	
0.003	
0.005	
0.007	
0.009	

Extension (m)	Johnson-Cook Damage
0.000	
0.003	
0.005	
0.007	
0.009	

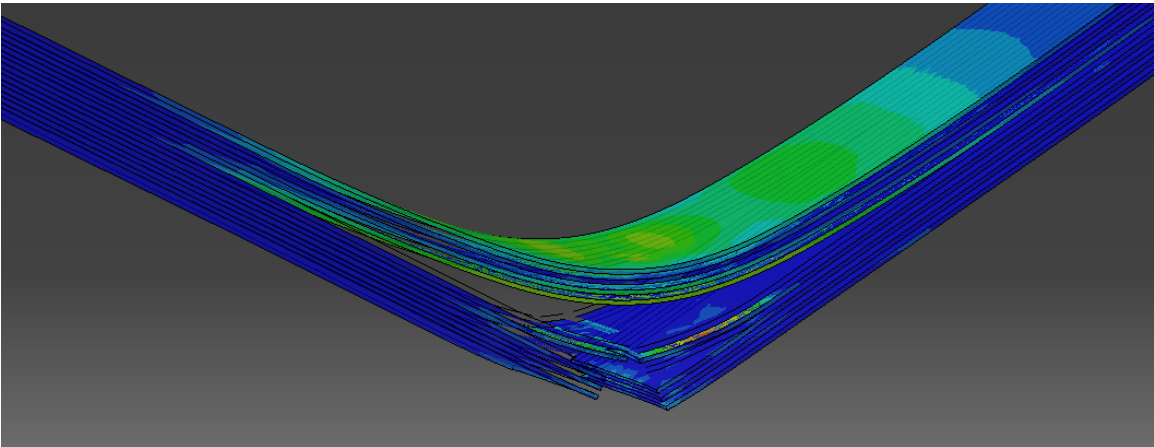
Extension (m)	Traction-Separation Damage
0.000	
0.003	
0.005	
0.007	
0.009	



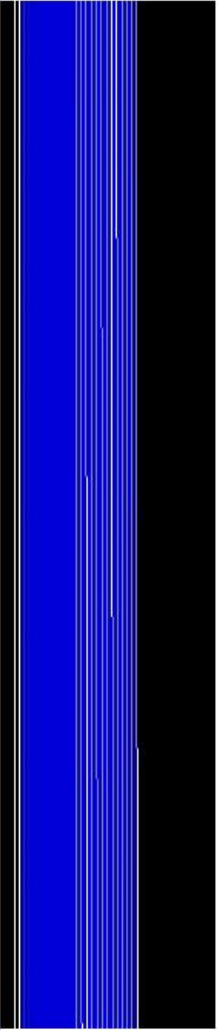
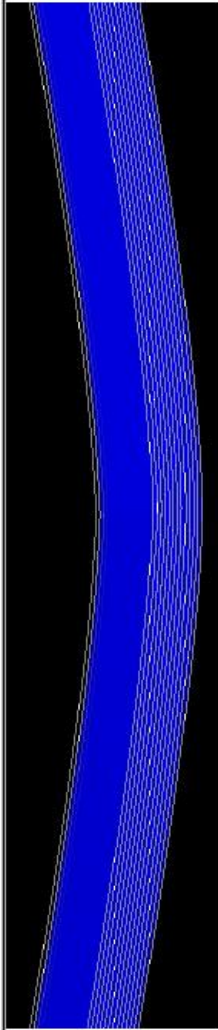
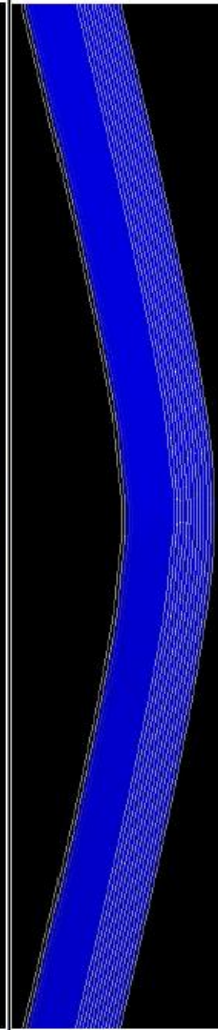
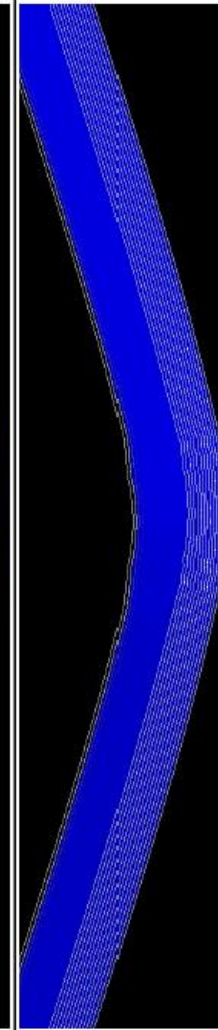
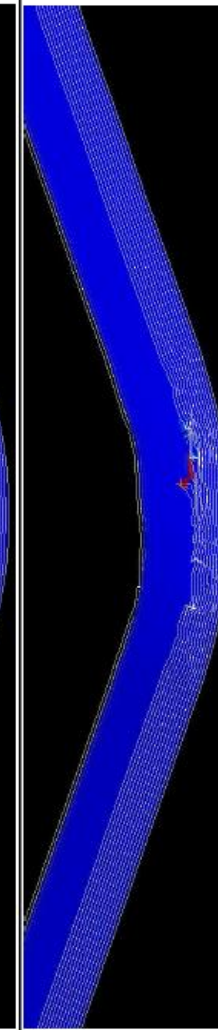
Vara Model +8 Plies View

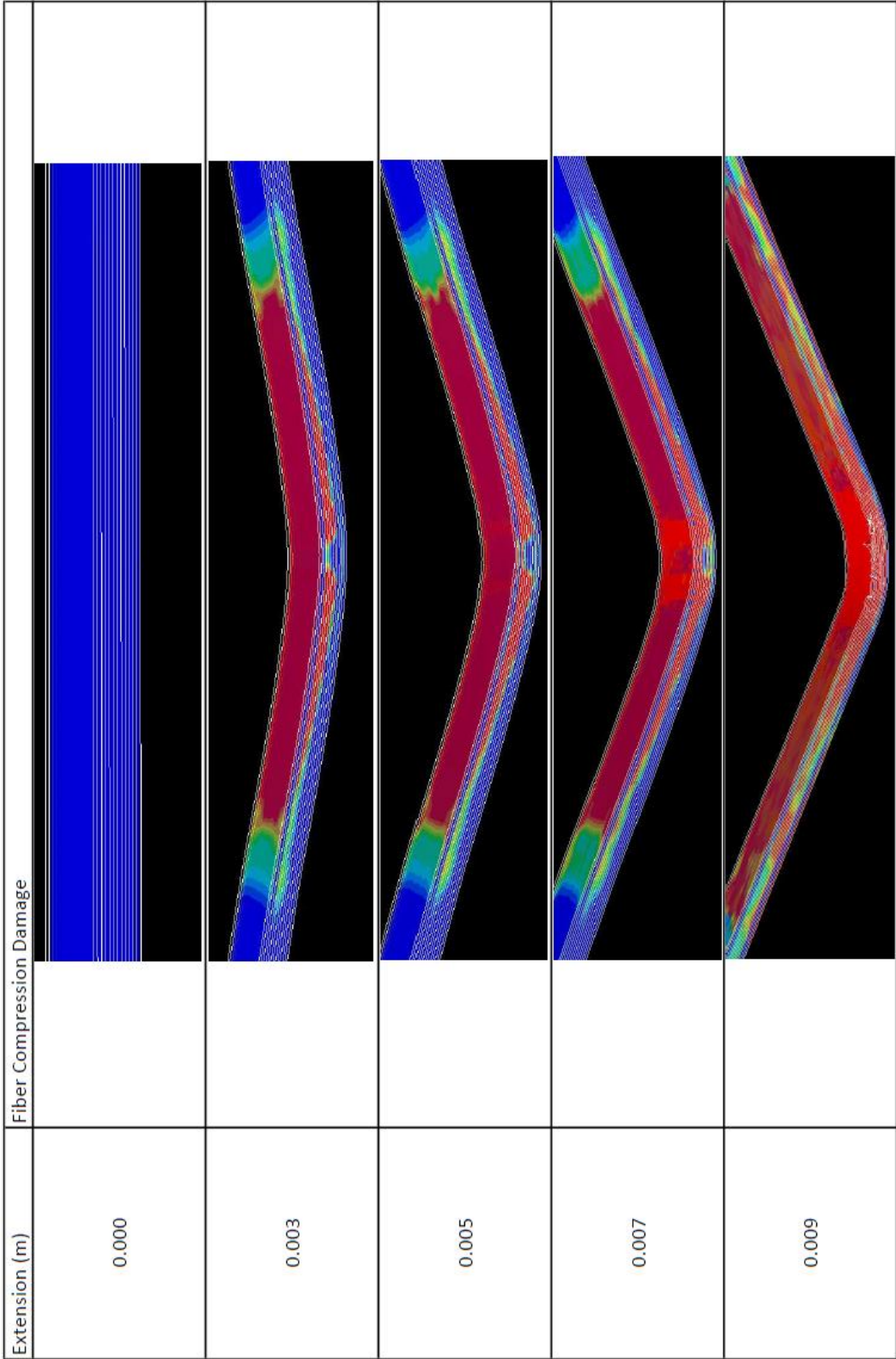


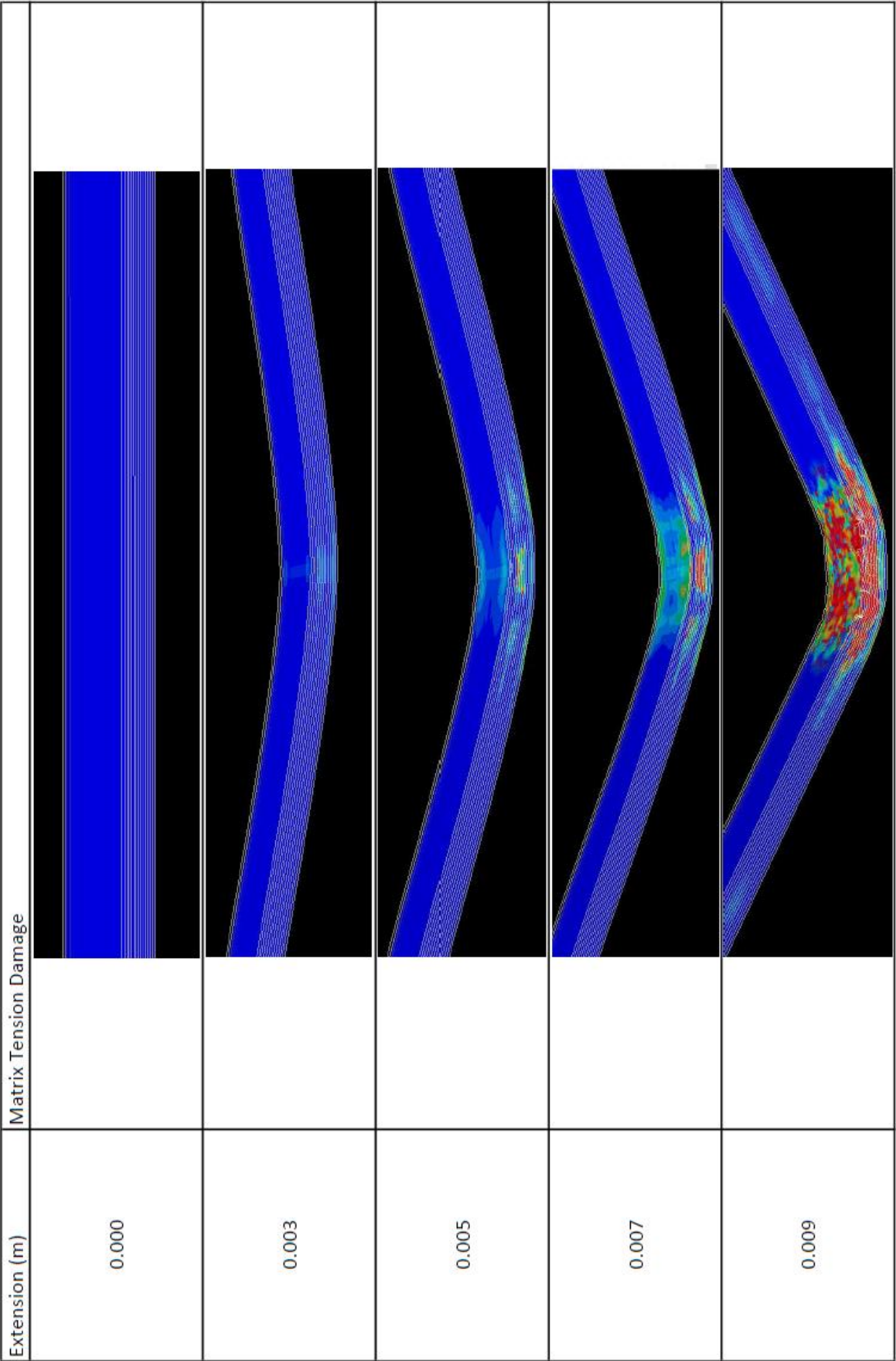
Vara Model +8 Plies Top View with Impactor Hidden

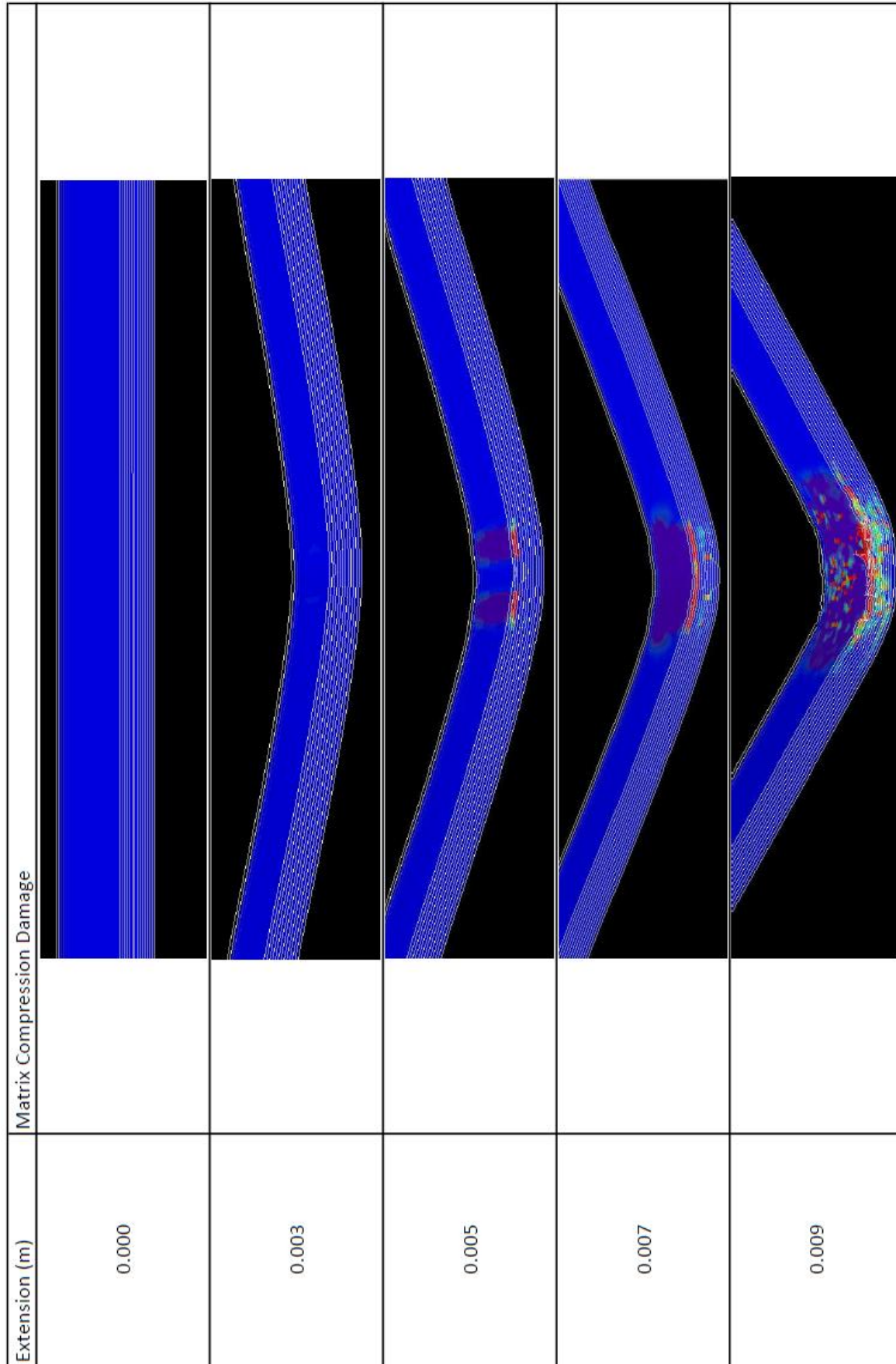


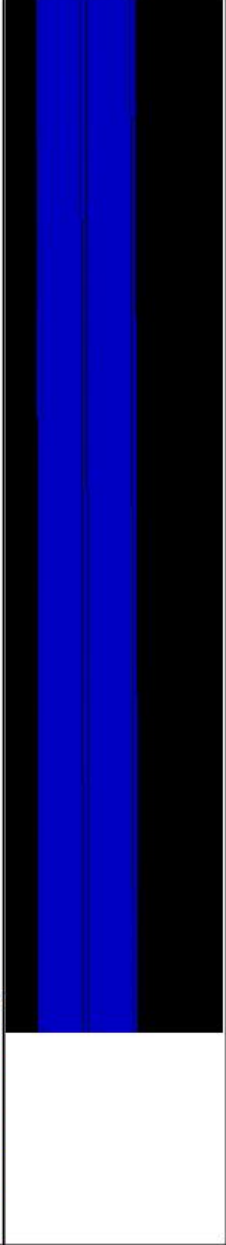
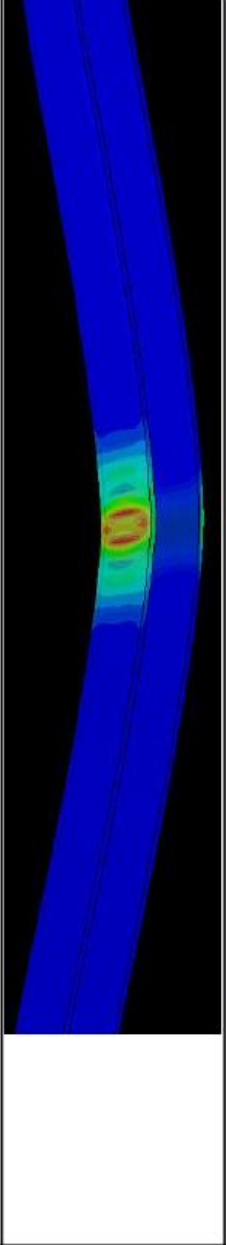
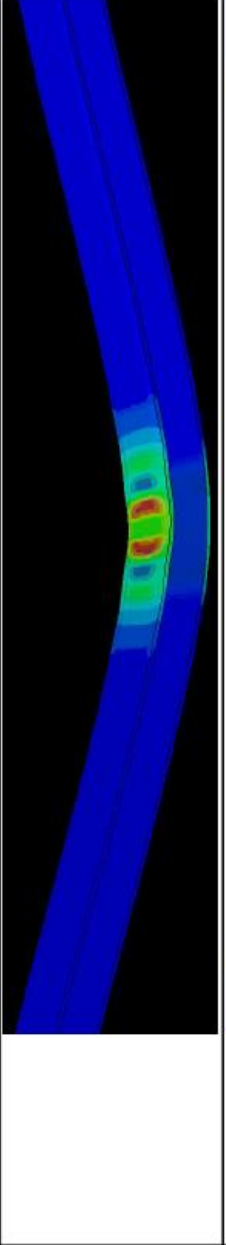
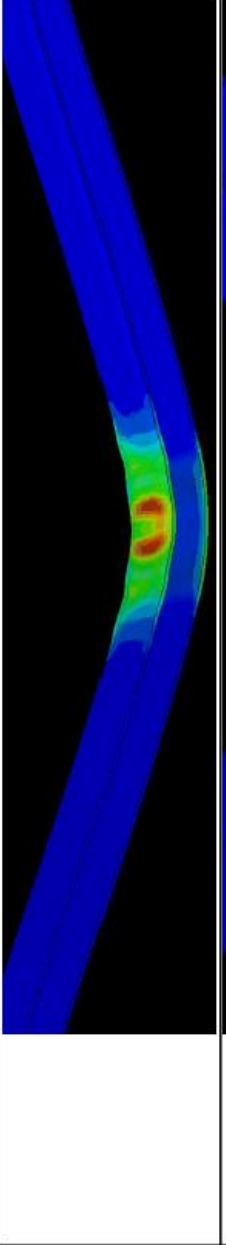
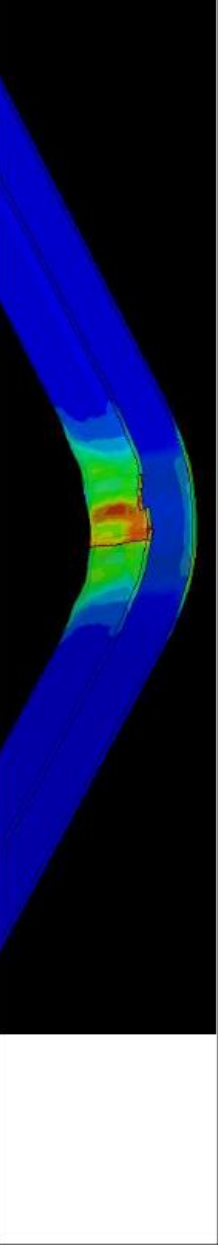
Vara Model +8 Plies View with Impactor Hidden

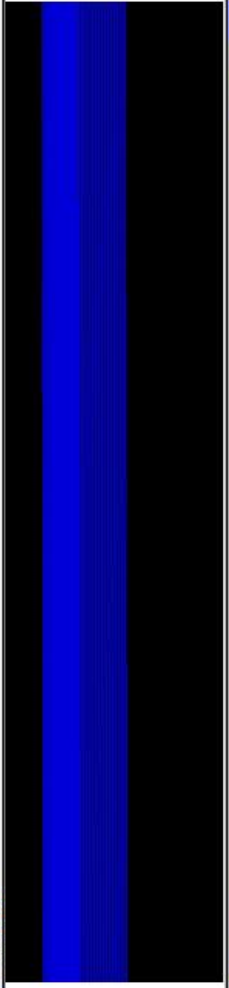
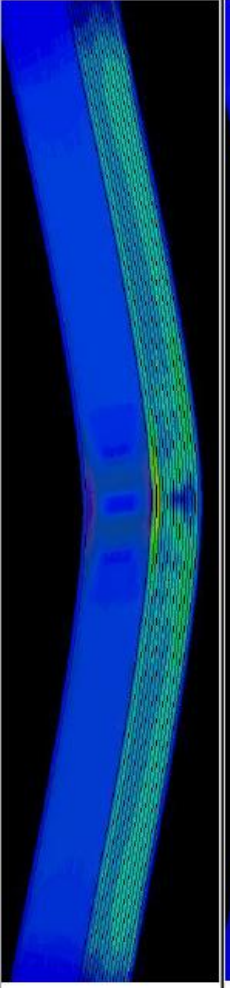
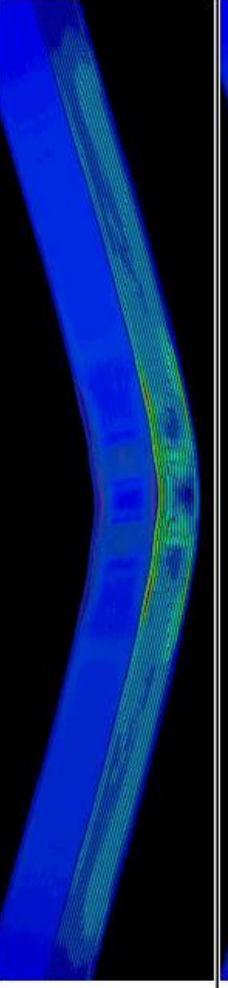
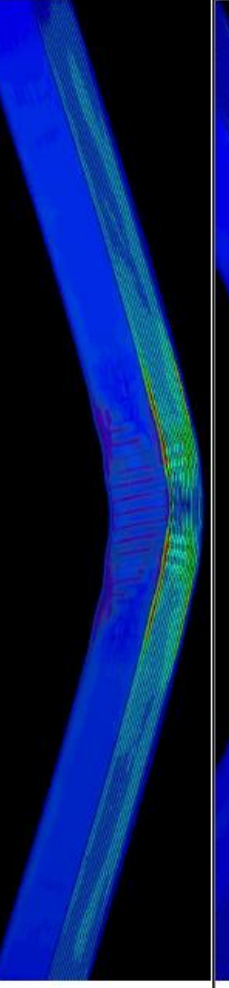
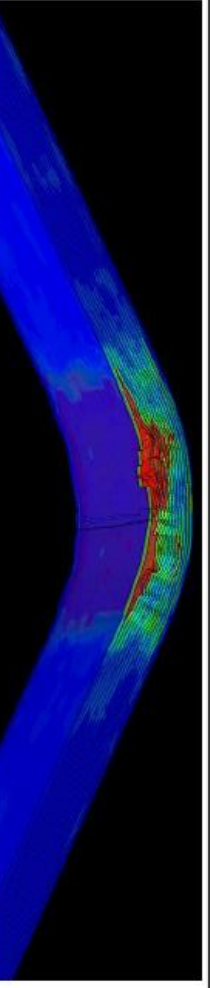
Vara Model .18 Metal Volume Fraction		Fiber Tension Damage
Extension (m)	0.000	
	0.003	
	0.005	
	0.007	
	0.009	

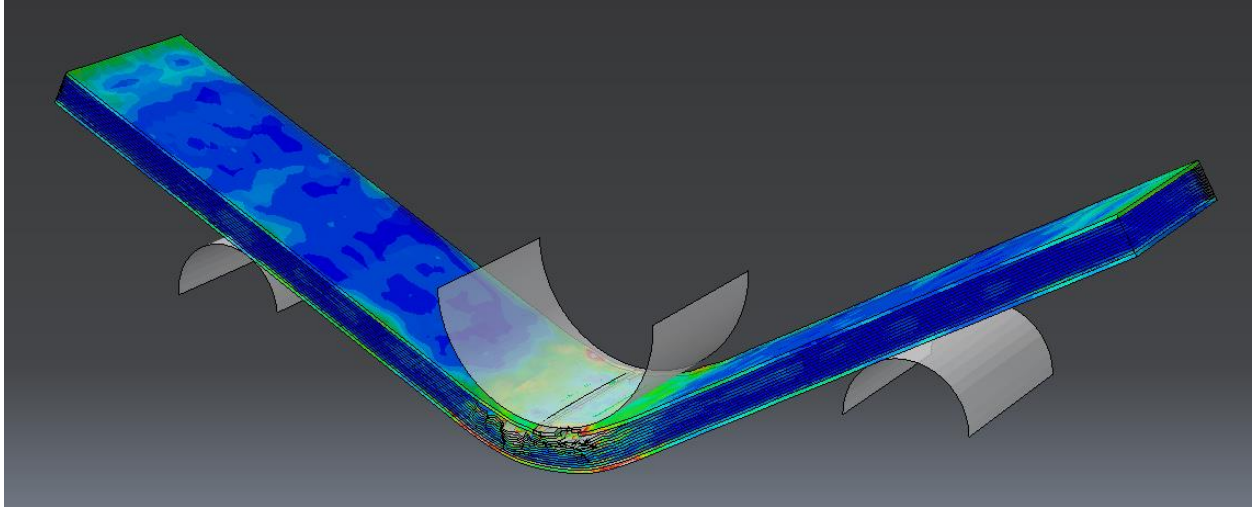




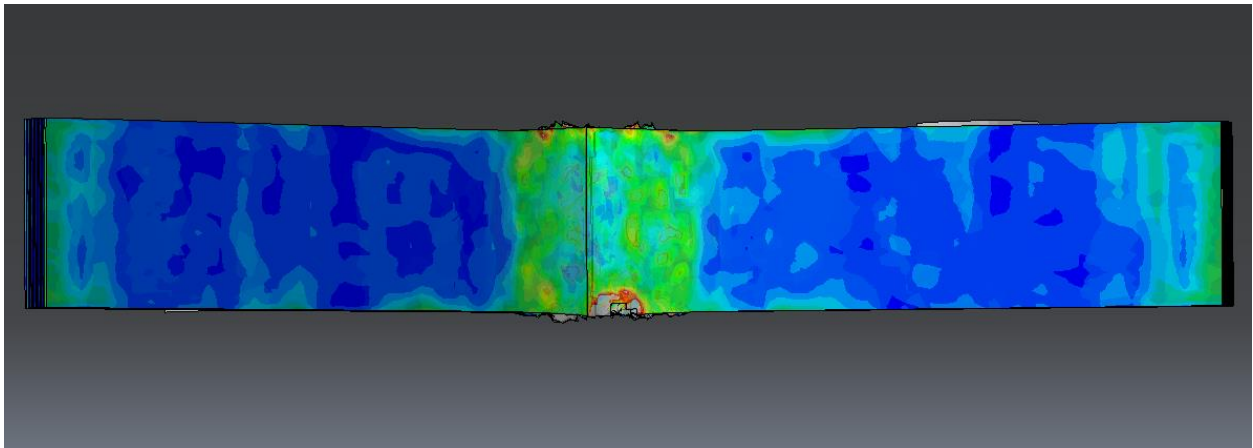


Extension (m)	Johnson-Cook Damage
0.000	
0.003	
0.005	
0.007	
0.009	

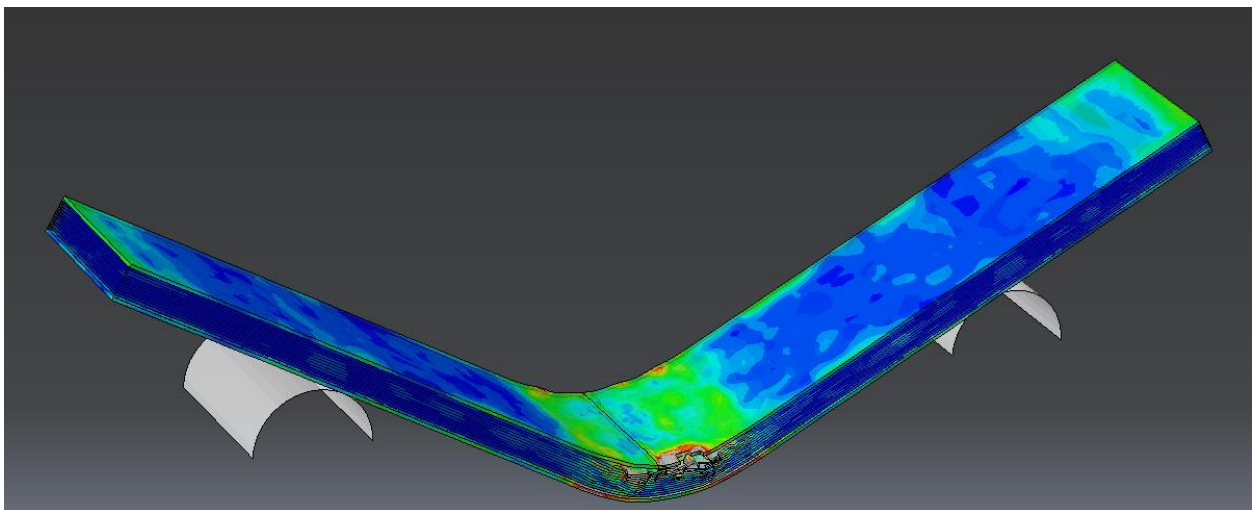
Extension (m)	Traction-Separation Damage
0.000	
0.003	
0.005	
0.007	
0.009	



0.18 MVF TiGr Laminate

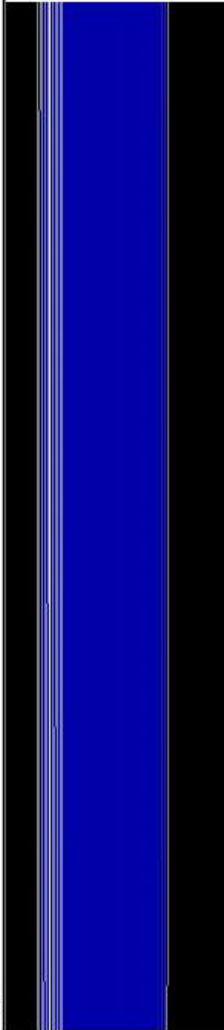
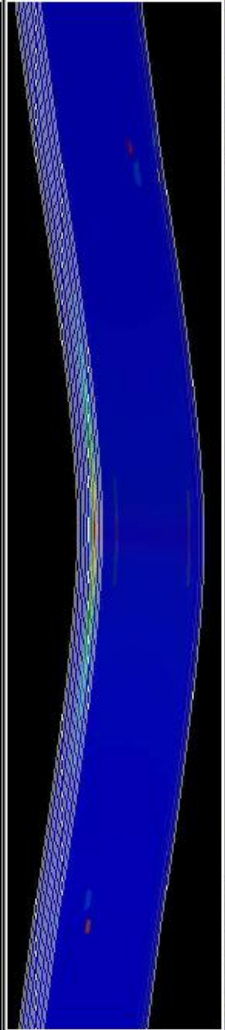
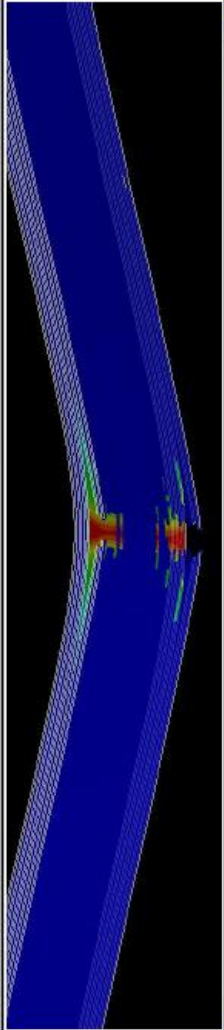
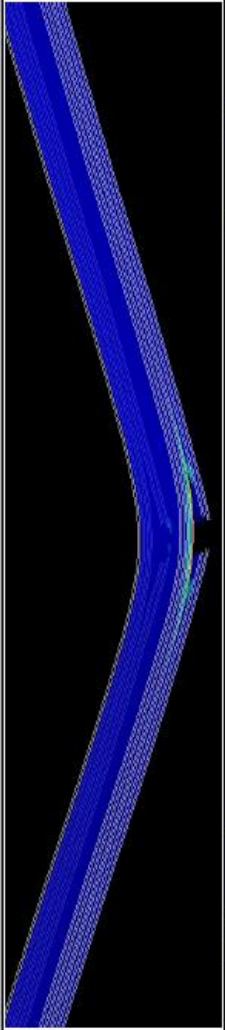
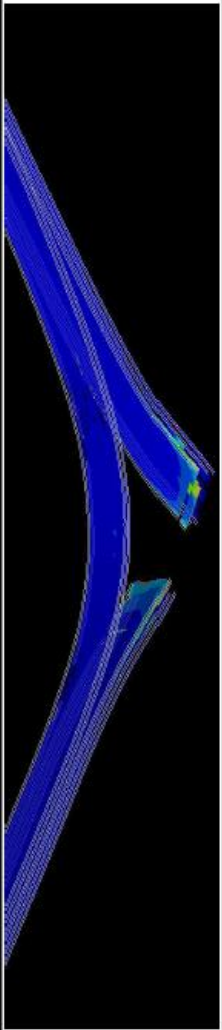


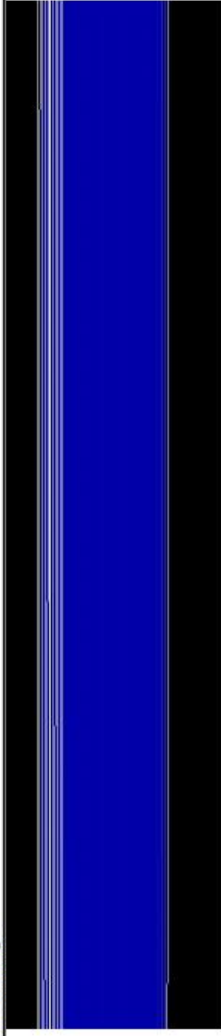
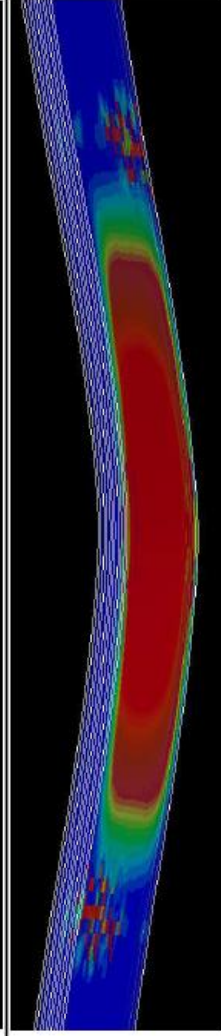
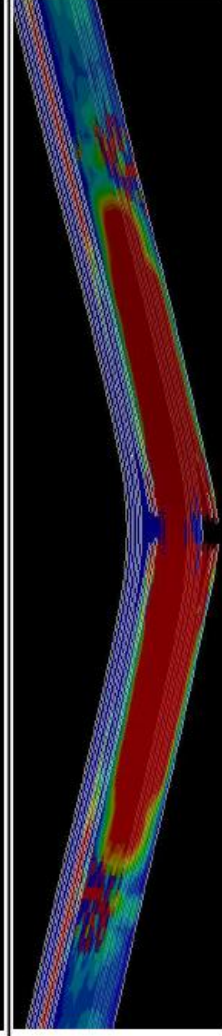
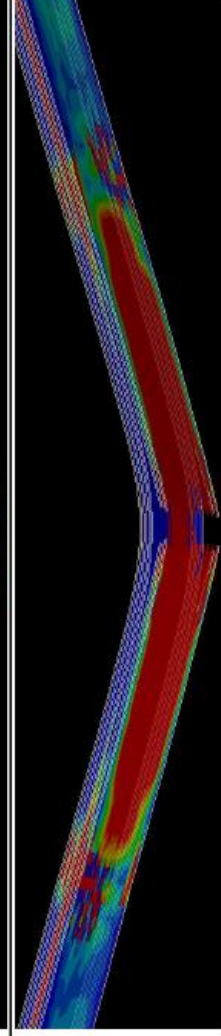
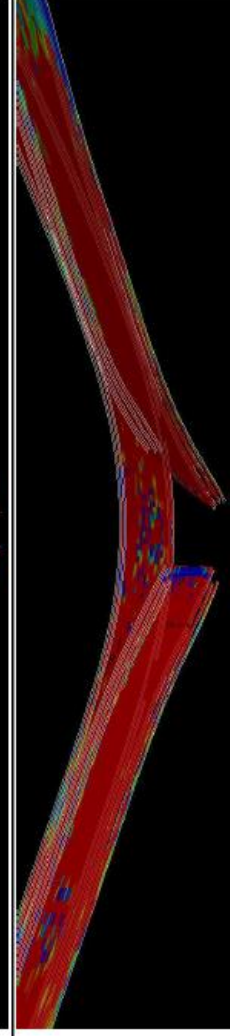
0.18 MVF TiGr Laminate Top View with Impactor Hidden

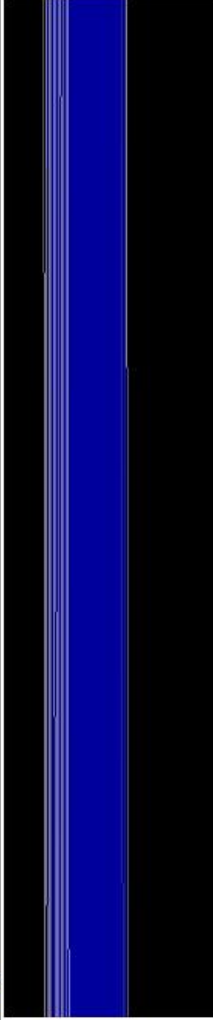
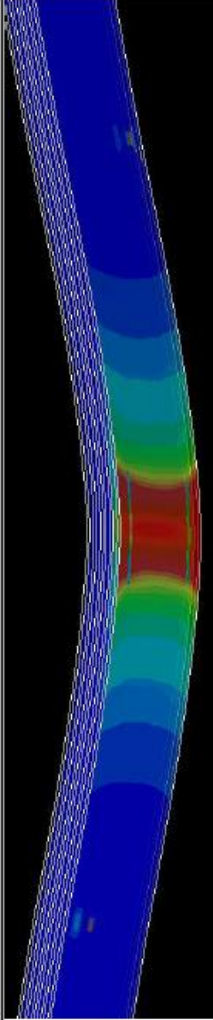
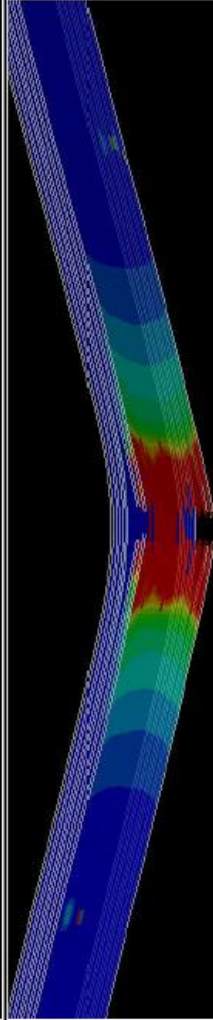
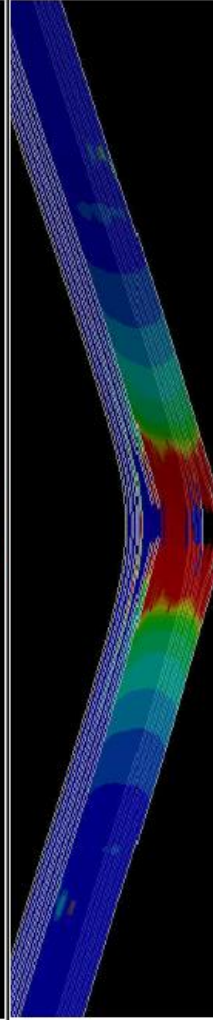
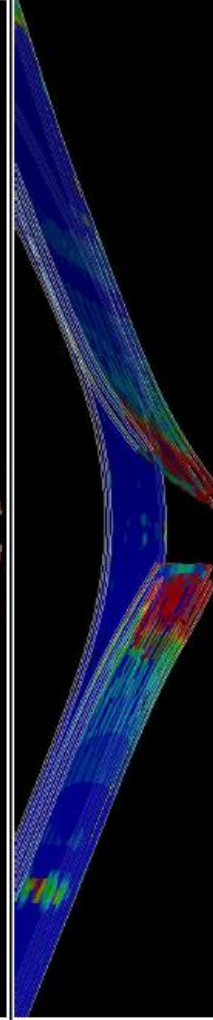


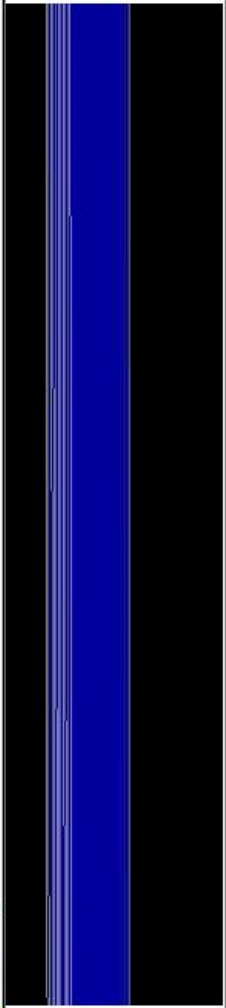
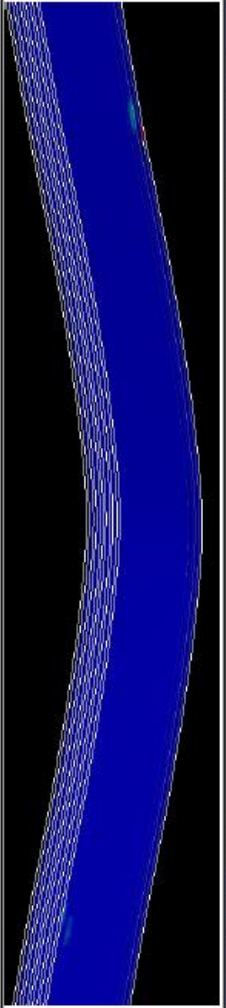
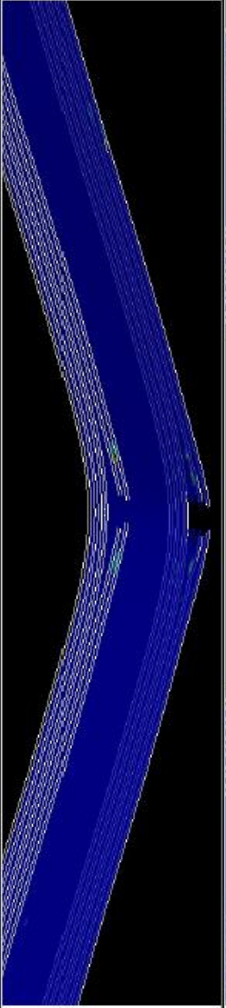
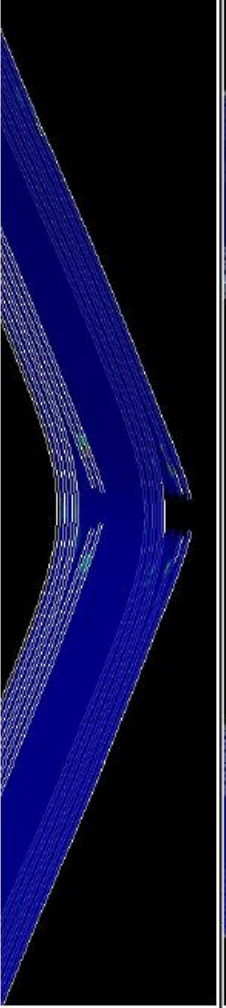
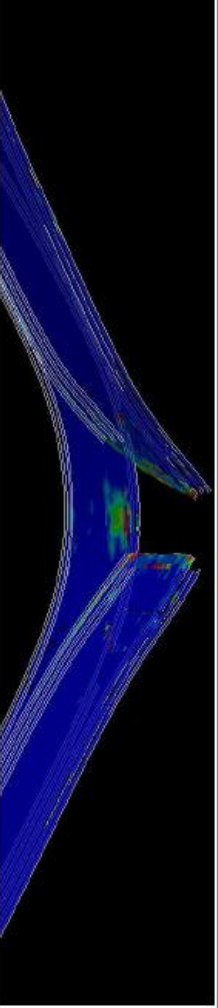
0.18 MVF TiGr Laminate View with Impactor Hidden

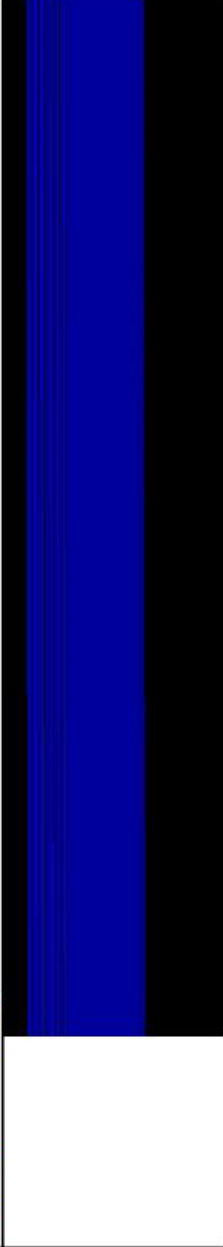
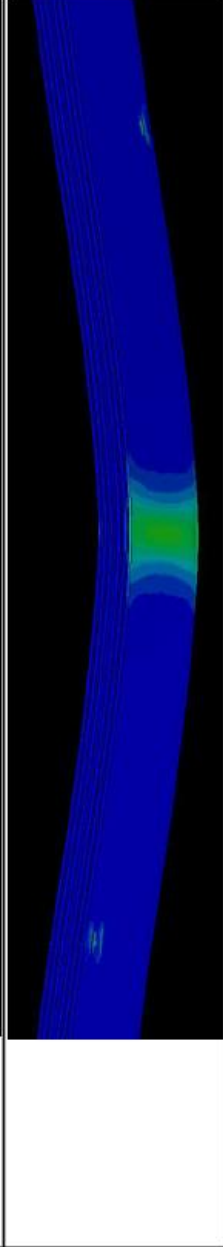
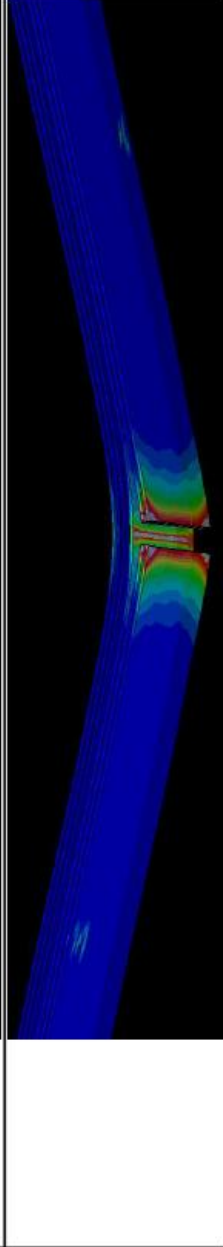
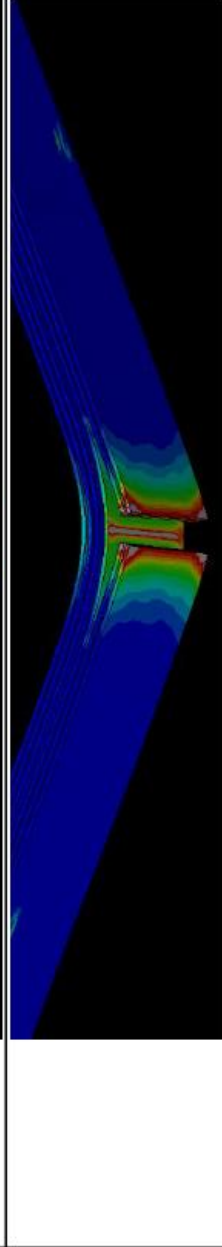
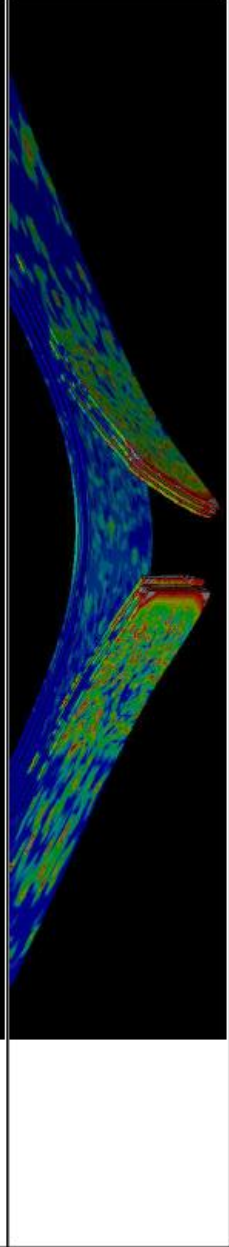
Vara Model .59 Metal Volume Fraction

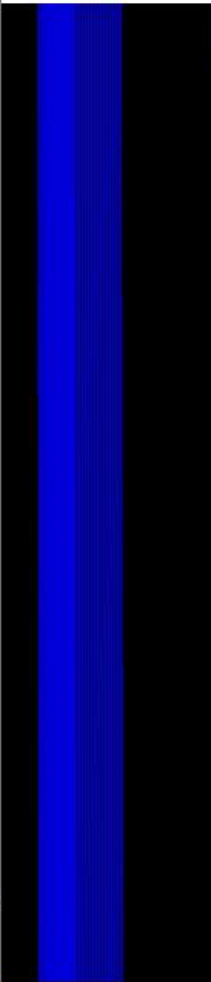
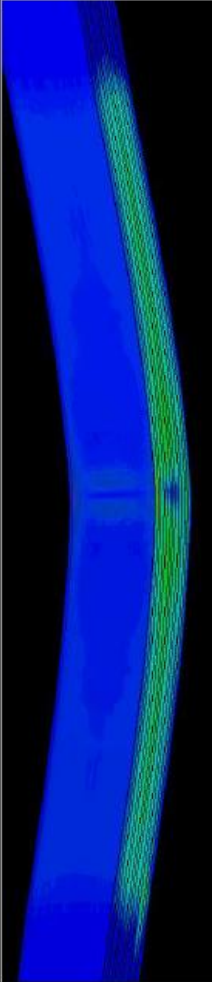
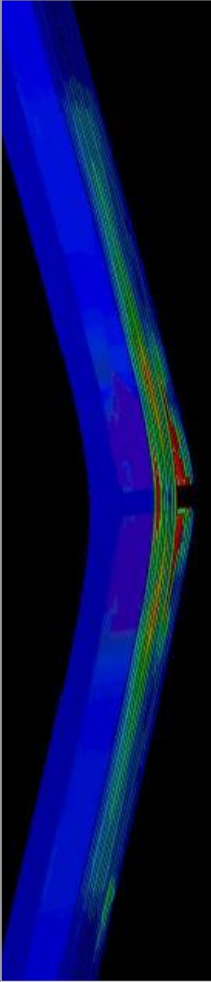
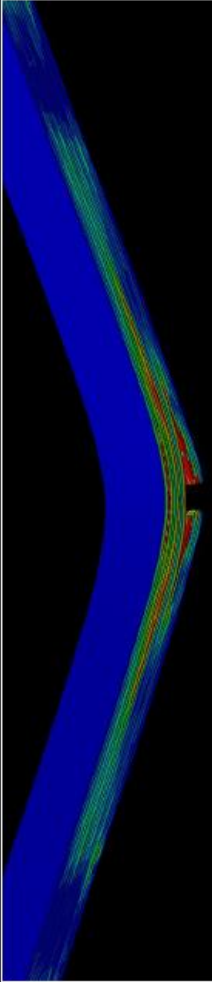
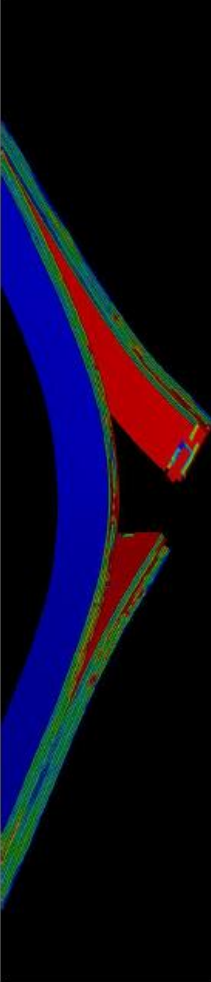
Extension (m)	Fiber Tension Damage
0.000	
0.003	
0.005	
0.007	
0.009	

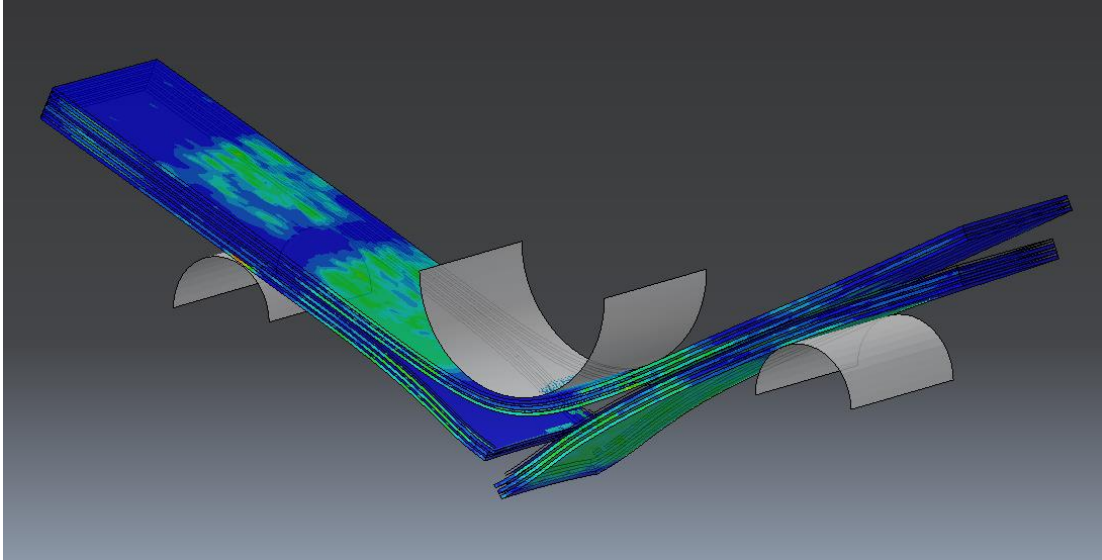
Extension (m)	Fiber Compression Damage
0.000	
0.003	
0.005	
0.007	
0.009	

Extension (m)	Matrix Tension Damage
0.000	
0.003	
0.005	
0.007	
0.009	

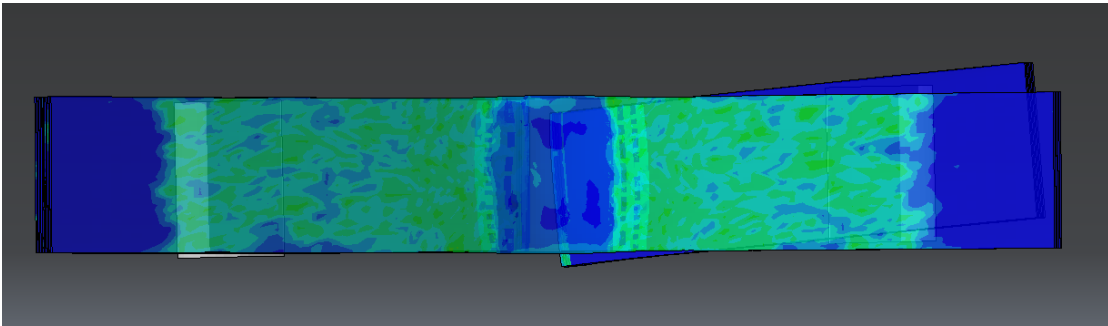
Extension (m)	Matrix Compression Damage
0.000	
0.003	
0.005	
0.007	
0.009	

Extension (m)	Johnson-Cook Damage
0.000	
0.003	
0.005	
0.007	
0.009	

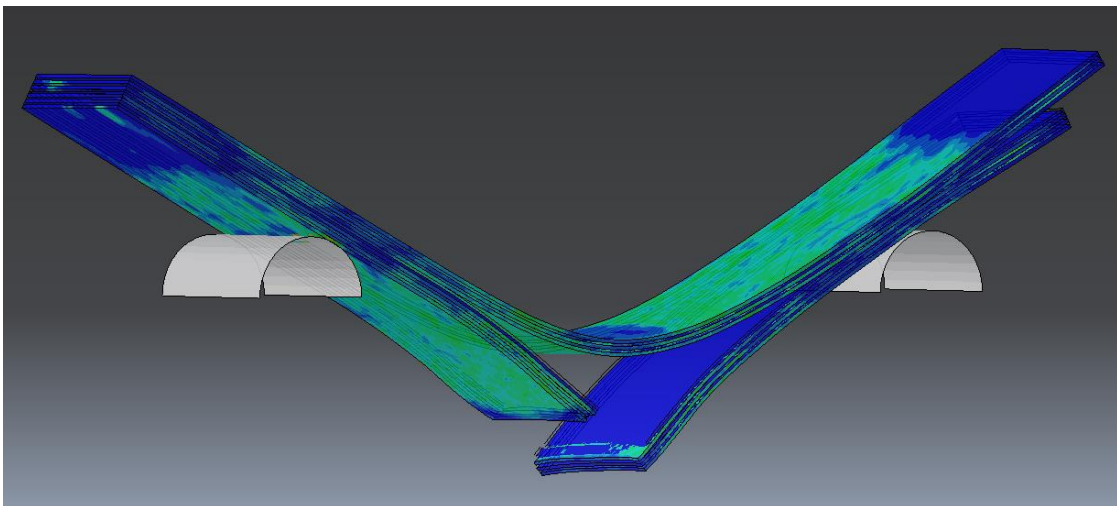
Extension (m)	Traction-Separation Damage
0.000	
0.003	
0.005	
0.007	
0.009	



0.59 MVF Laminate

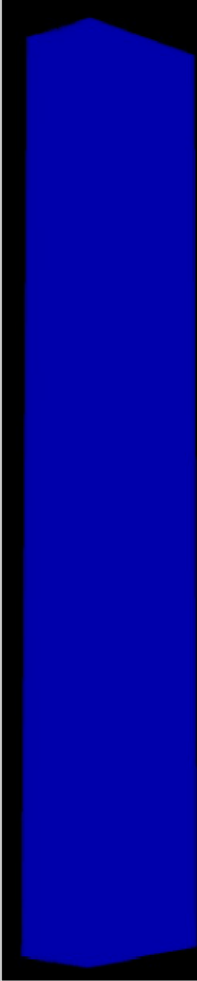

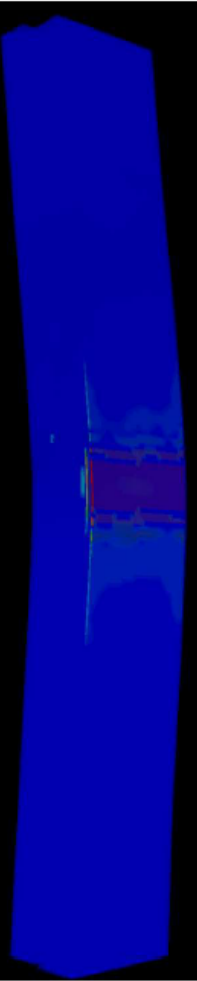
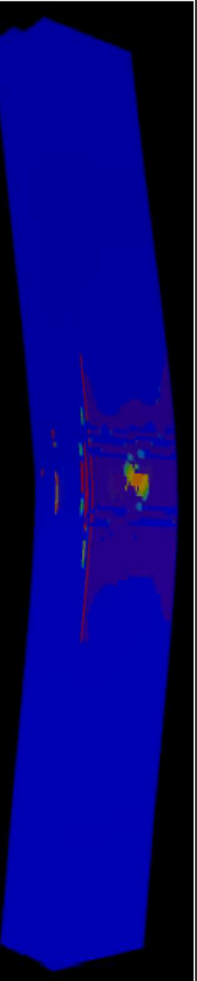
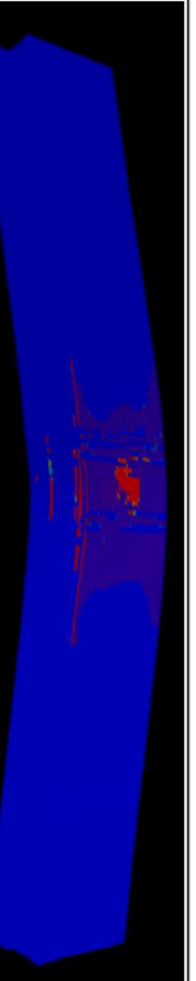


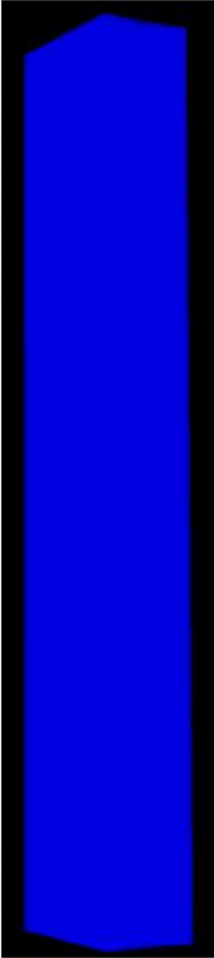
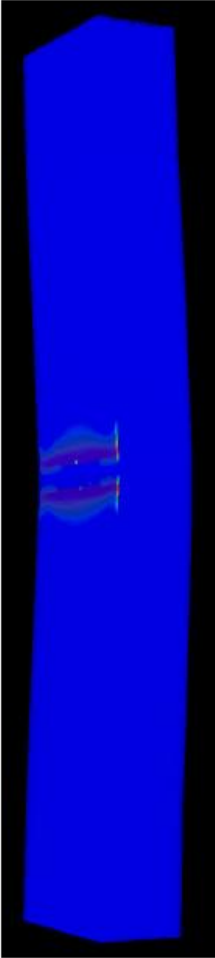
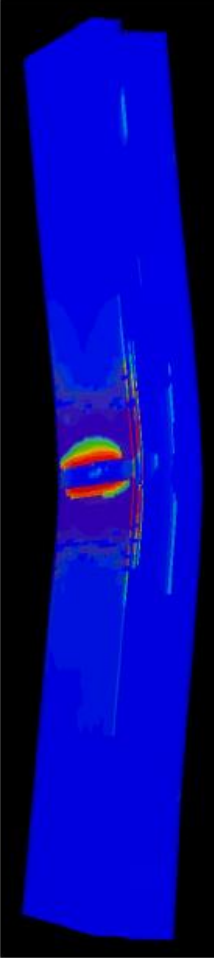
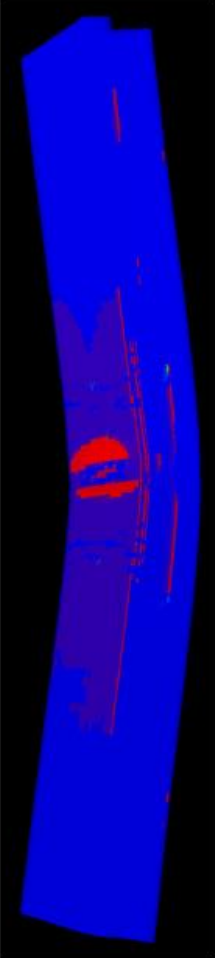
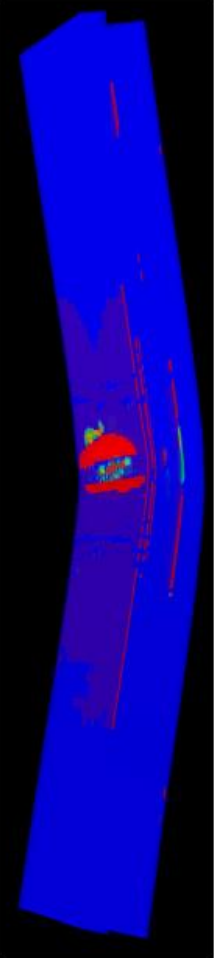
0.59 MVF Laminate Top View with Impactor Hidden


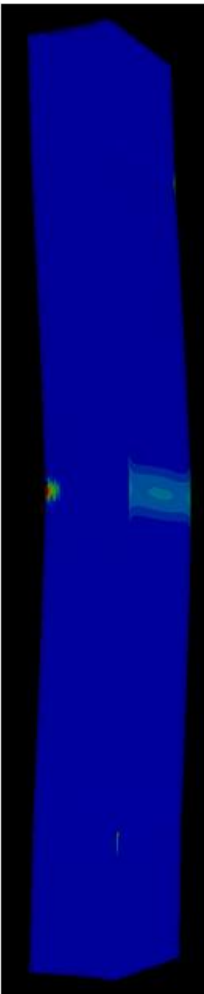
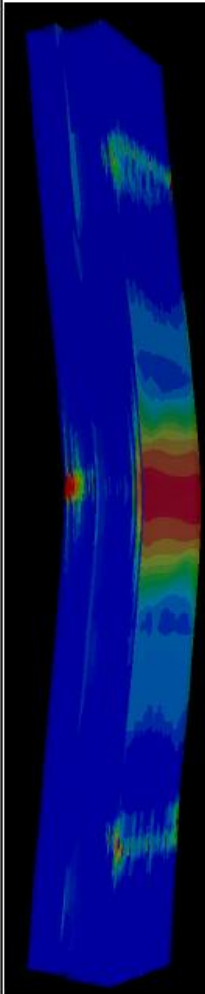
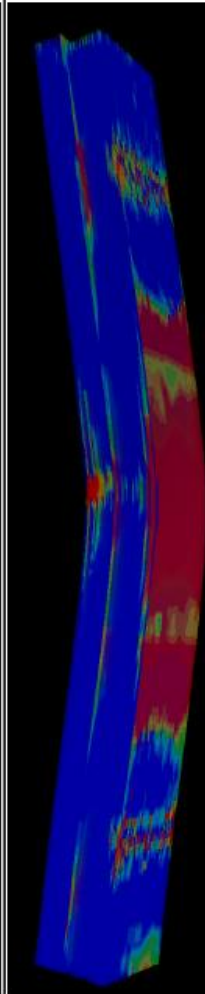
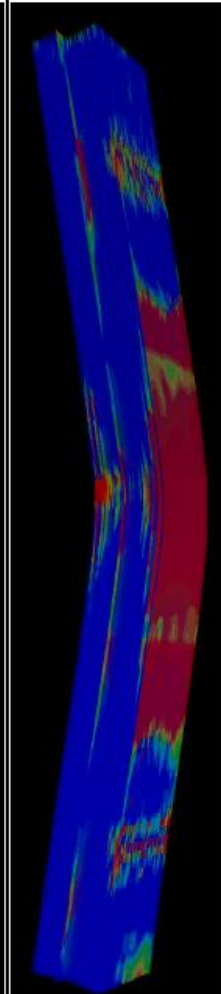


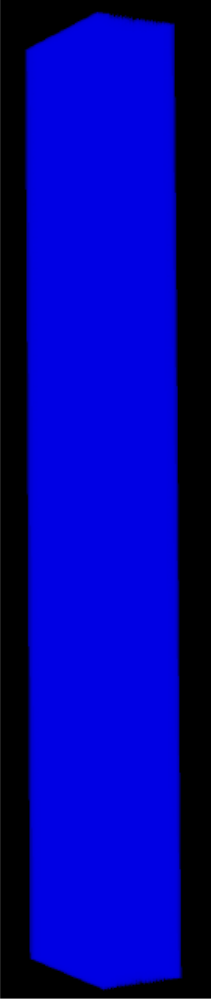
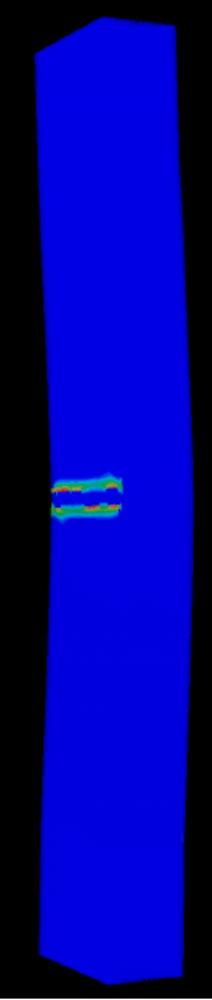
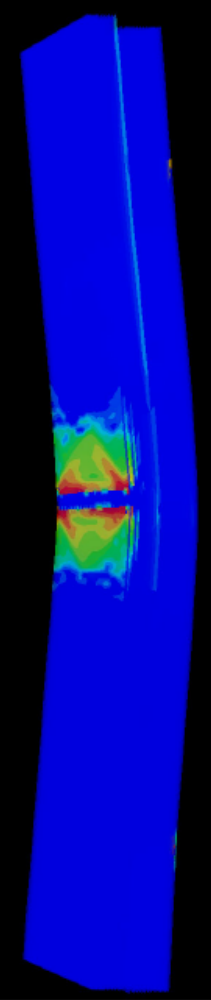
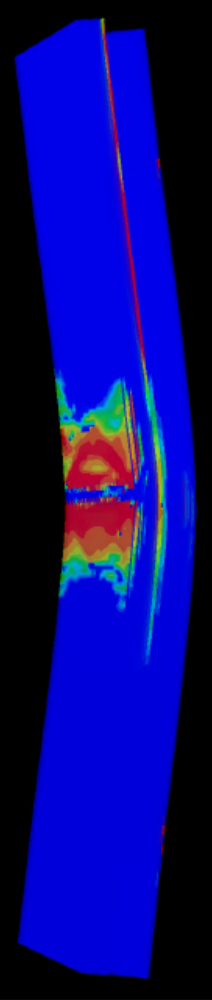
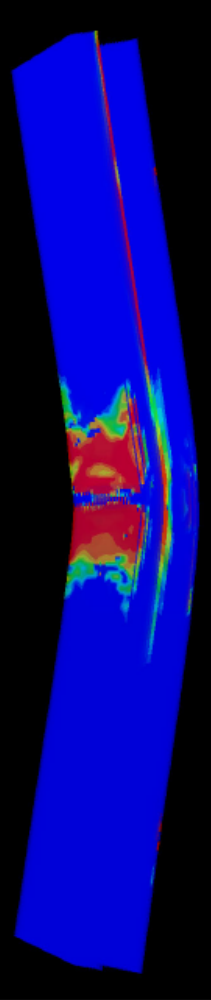
0.59 MVF Laminate View with Impactor Hidden

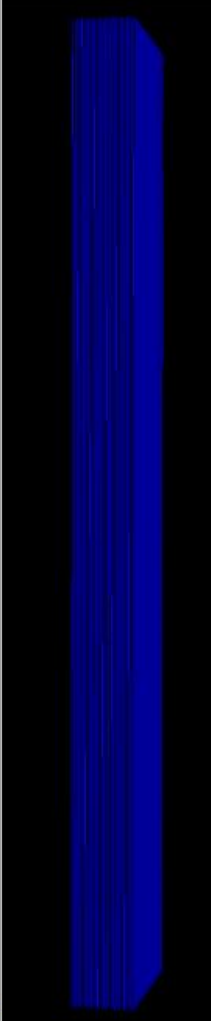
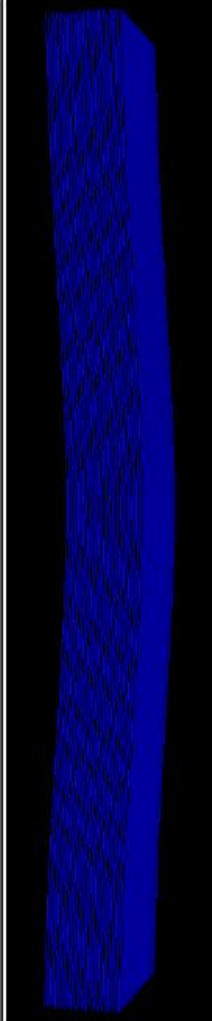
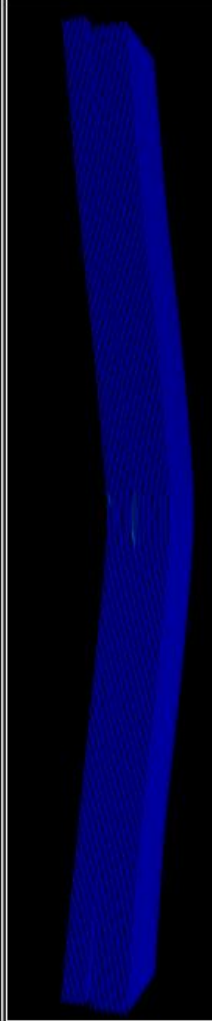
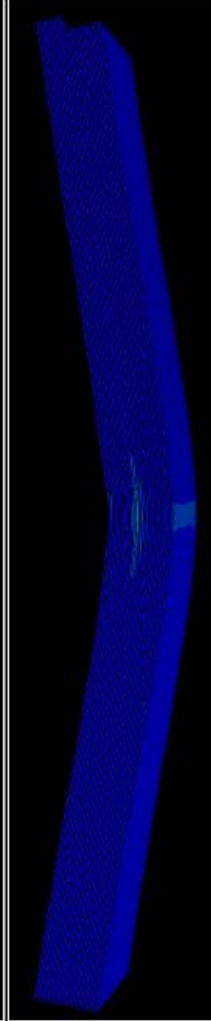
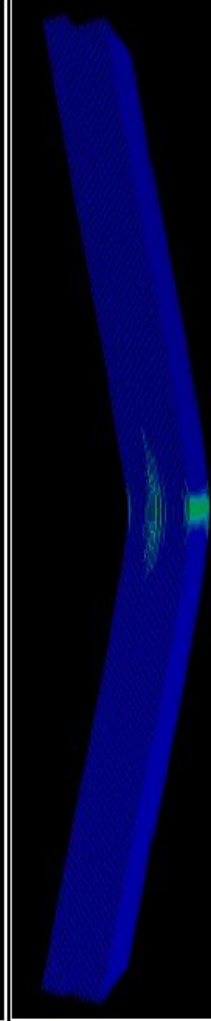
Thick Laminate Model - Static Load

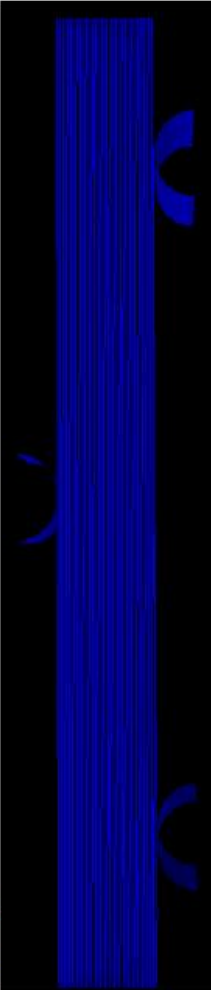
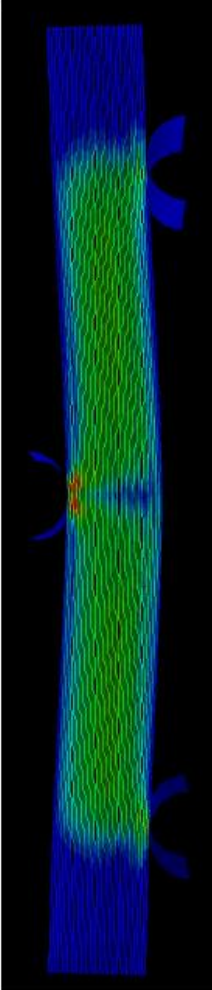
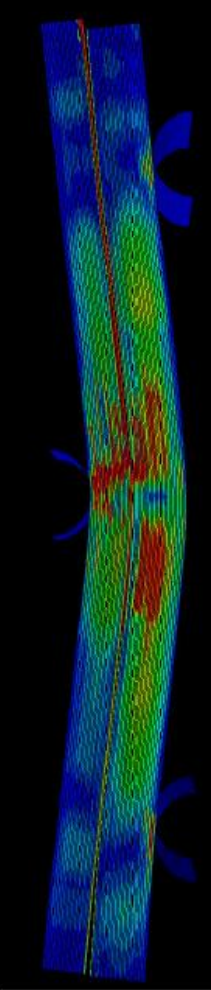
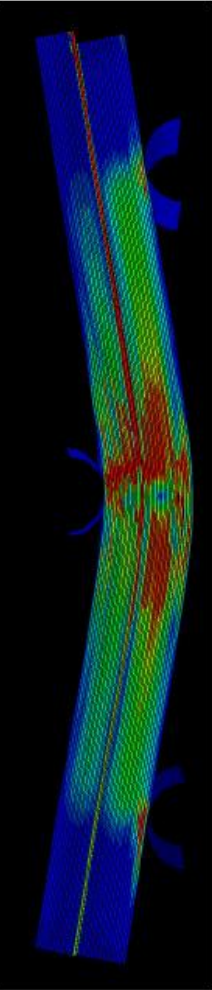
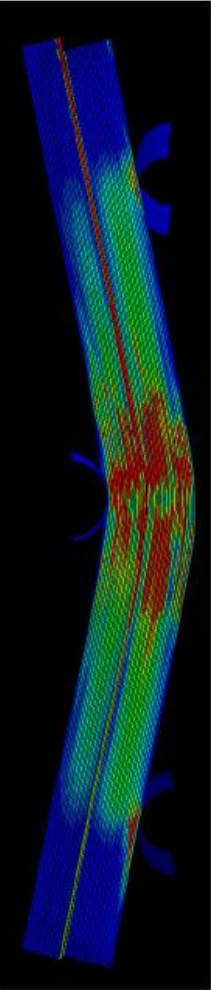
Extension (m)	Fiber Tension Damage
0.000	
0.004	
0.008	
0.012	
0.015	

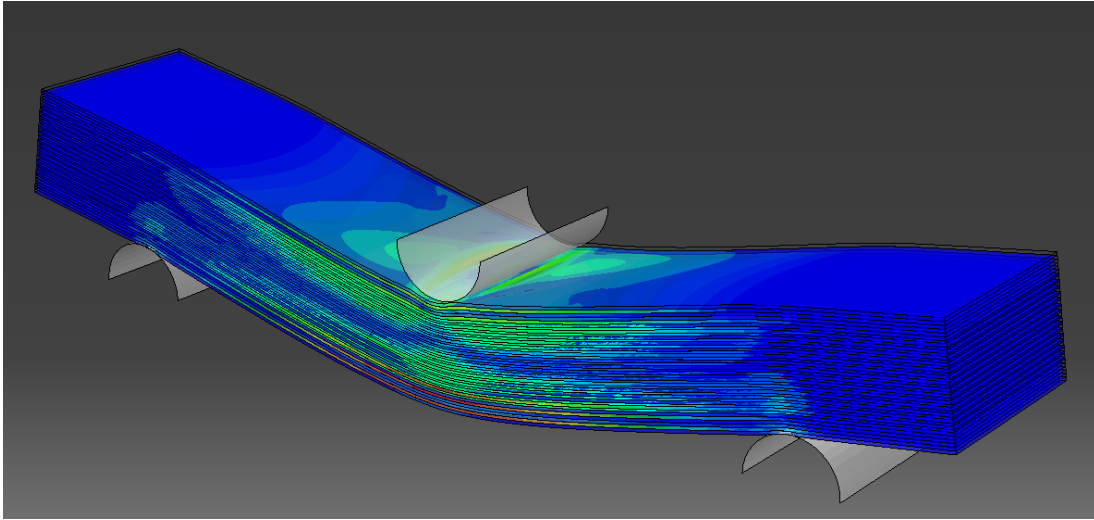
Extension (m)	Fiber Compression Damage
0.000	
0.004	
0.008	
0.012	
0.015	

Extension (m)	Matrix Tension Damage
0.000	
0.004	
0.008	
0.012	
0.015	

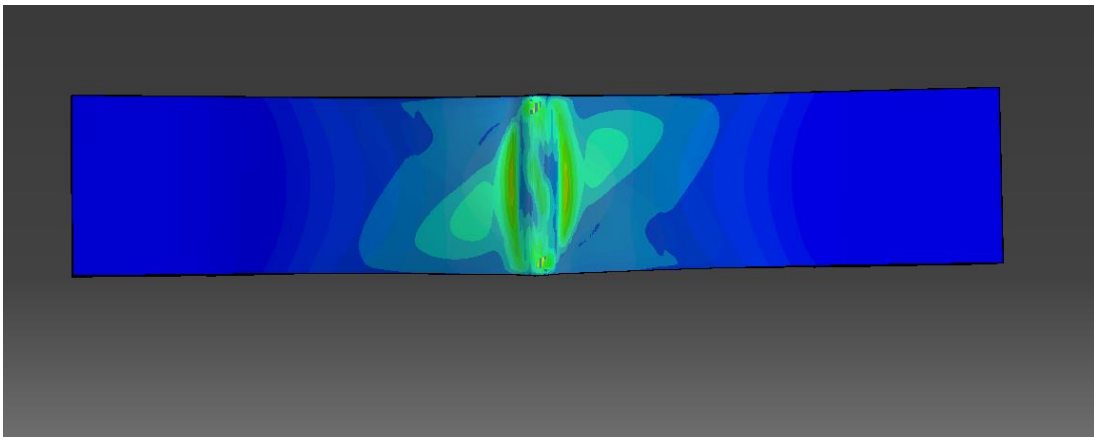
Extension (m)	Matrix Compression Damage
0.000	
0.004	
0.008	
0.012	
0.015	

Extension (m)	Johnson-Cook Damage
0.000	
0.004	
0.008	
0.012	
0.015	

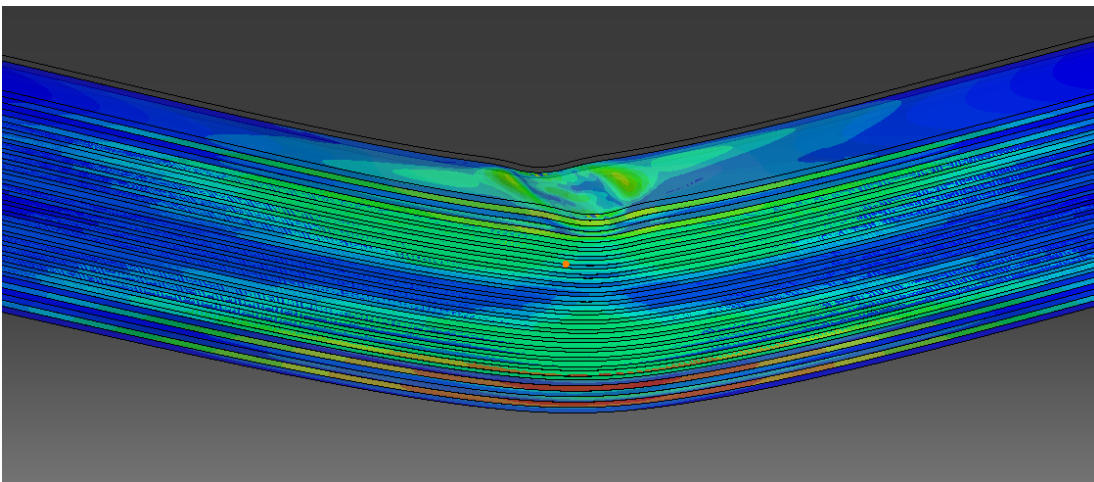
Extension (m)	Traction-Separation Damage
0.000	
0.004	
0.008	
0.012	
0.015	



Thick Laminate Model View



Thick Laminate Model Top View with Impactor Hidden



Thick Laminate Model View with Impactor Hidden

APPENDIX II: CLASSICAL LAMINATE THEORY, CALCULATION OF ELASTIC CONSTANTS

Bernhardt Laminate Analysis (CLT)

Material Properties:

CF/PEEK	Titanium 15-3-3-3
$E_{CF11} := 139\text{GPa}$	$E_{Ti} := 100.6\text{GPa}$
$E_{CF22} := 10\text{GPa}$	$\nu_{Ti12} := .36$
$\nu_{CF12} := .28$	
$G_{CF12} := 3.9\text{GPa}$	

1. Reduced stiffness matrix for each material

$$Q_{CF} := \begin{pmatrix} \frac{E_{CF11}^2}{E_{CF11} - \nu_{CF12}^2 \cdot E_{CF22}} & \frac{\nu_{CF12} \cdot E_{CF11} \cdot E_{CF22}}{E_{CF11} - \nu_{CF12}^2 \cdot E_{CF22}} & 0 \\ \frac{\nu_{CF12} \cdot E_{CF11} \cdot E_{CF22}}{E_{CF11} - \nu_{CF12}^2 \cdot E_{CF22}} & \frac{E_{CF11} \cdot E_{CF22}}{E_{CF11} - \nu_{CF12}^2 \cdot E_{CF22}} & 0 \\ 0 & 0 & G_{CF12} \end{pmatrix}$$

$$Q_{CF} = \begin{pmatrix} 141.858 & 2.816 & 0 \\ 2.816 & 10.057 & 0 \\ 0 & 0 & 3.9 \end{pmatrix} \cdot \text{GPa}$$

$$Q_{Ti} := \frac{E_{Ti}}{1 - \nu_{Ti12}^2} \begin{pmatrix} 1 & \nu_{Ti12} & 0 \\ \nu_{Ti12} & 1 & 0 \\ 0 & 0 & \frac{1 - \nu_{Ti12}}{2} \end{pmatrix} \quad Q_{Ti} = \begin{pmatrix} 115.579 & 41.608 & 0 \\ 41.608 & 115.579 & 0 \\ 0 & 0 & 36.985 \end{pmatrix} \cdot \text{GPa}$$

Calculate the transformed reduced stiffness matrix Q_{ij} for each ply based on the reduced stiffness matrix and fiber angle.

0 degree plies:

$$\theta := 0 \text{ deg}$$

$$\begin{aligned}
 Q_{11} &:= Q_{CF_{1,1}} \cdot \cos(\theta)^4 + 2 \cdot (Q_{CF_{1,2}} + 2 \cdot Q_{CF_{3,3}}) \cdot \cos(\theta)^2 \cdot \sin(\theta)^2 + Q_{CF_{2,2}} \cdot \sin(\theta)^4 \\
 Q_{12} &:= Q_{CF_{1,2}} \cdot (\cos(\theta)^4 + \sin(\theta)^4) + (Q_{CF_{1,1}} + Q_{CF_{2,2}} - 4 \cdot Q_{CF_{3,3}}) \cdot \cos(\theta)^2 \cdot \sin(\theta)^2 \\
 Q_{13} &:= (Q_{CF_{1,1}} - Q_{CF_{1,2}} - 2 \cdot Q_{CF_{3,3}}) \cdot \cos(\theta)^3 \cdot \sin(\theta) - (Q_{CF_{2,2}} - Q_{CF_{1,2}} - 2 \cdot Q_{CF_{3,3}}) \cdot \cos(\theta) \cdot \sin(\theta)^3 \\
 Q_{22} &:= Q_{CF_{1,1}} \cdot \sin(\theta)^4 + 2 \cdot (Q_{CF_{1,2}} + 2 \cdot Q_{CF_{3,3}}) \cdot \cos(\theta)^2 \cdot \sin(\theta)^2 + Q_{CF_{2,2}} \cdot \cos(\theta)^4 \\
 Q_{23} &:= (Q_{CF_{1,1}} - Q_{CF_{1,2}} - 2 \cdot Q_{CF_{3,3}}) \cdot \cos(\theta) \cdot \sin(\theta)^3 - (Q_{CF_{2,2}} - Q_{CF_{1,2}} - 2 \cdot Q_{CF_{3,3}}) \cdot \cos(\theta)^3 \cdot \sin(\theta) \\
 Q_{33} &:= (Q_{CF_{1,1}} + Q_{CF_{2,2}} - 2 \cdot Q_{CF_{1,2}} - 2 \cdot Q_{CF_{3,3}}) \cdot \cos(\theta)^2 \cdot \sin(\theta)^2 + Q_{CF_{3,3}} \cdot (\cos(\theta)^4 + \sin(\theta)^4)
 \end{aligned}$$

$$Q_{CF0ply} := \begin{pmatrix} Q_{11} & Q_{12} & Q_{13} \\ Q_{12} & Q_{22} & Q_{23} \\ Q_{13} & Q_{23} & Q_{33} \end{pmatrix} \quad Q_{CF0ply} = \begin{pmatrix} 141.858 & 2.816 & 0 \\ 2.816 & 10.057 & 0 \\ 0 & 0 & 3.9 \end{pmatrix} \cdot \text{GPa}$$

90 degree plies:

$$\theta := 90 \text{ deg}$$

$$\begin{aligned}
 Q_{11} &:= Q_{CF_{1,1}} \cdot \cos(\theta)^4 + 2 \cdot (Q_{CF_{1,2}} + 2 \cdot Q_{CF_{3,3}}) \cdot \cos(\theta)^2 \cdot \sin(\theta)^2 + Q_{CF_{2,2}} \cdot \sin(\theta)^4 \\
 Q_{12} &:= Q_{CF_{1,2}} \cdot (\cos(\theta)^4 + \sin(\theta)^4) + (Q_{CF_{1,1}} + Q_{CF_{2,2}} - 4 \cdot Q_{CF_{3,3}}) \cdot \cos(\theta)^2 \cdot \sin(\theta)^2 \\
 Q_{13} &:= (Q_{CF_{1,1}} - Q_{CF_{1,2}} - 2 \cdot Q_{CF_{3,3}}) \cdot \cos(\theta)^3 \cdot \sin(\theta) - (Q_{CF_{2,2}} - Q_{CF_{1,2}} - 2 \cdot Q_{CF_{3,3}}) \cdot \cos(\theta) \cdot \sin(\theta)^3 \\
 Q_{22} &:= Q_{CF_{1,1}} \cdot \sin(\theta)^4 + 2 \cdot (Q_{CF_{1,2}} + 2 \cdot Q_{CF_{3,3}}) \cdot \cos(\theta)^2 \cdot \sin(\theta)^2 + Q_{CF_{2,2}} \cdot \cos(\theta)^4 \\
 Q_{23} &:= (Q_{CF_{1,1}} - Q_{CF_{1,2}} - 2 \cdot Q_{CF_{3,3}}) \cdot \cos(\theta) \cdot \sin(\theta)^3 - (Q_{CF_{2,2}} - Q_{CF_{1,2}} - 2 \cdot Q_{CF_{3,3}}) \cdot \cos(\theta)^3 \cdot \sin(\theta) \\
 Q_{33} &:= (Q_{CF_{1,1}} + Q_{CF_{2,2}} - 2 \cdot Q_{CF_{1,2}} - 2 \cdot Q_{CF_{3,3}}) \cdot \cos(\theta)^2 \cdot \sin(\theta)^2 + Q_{CF_{3,3}} \cdot (\cos(\theta)^4 + \sin(\theta)^4)
 \end{aligned}$$

$$Q_{CF90ply} := \begin{pmatrix} Q_{11} & Q_{12} & Q_{13} \\ Q_{12} & Q_{22} & Q_{23} \\ Q_{13} & Q_{23} & Q_{33} \end{pmatrix} \quad Q_{CF90ply} = \begin{pmatrix} 10.057 & 2.816 & 0 \\ 2.816 & 141.858 & 8.036 \times 10^{-15} \\ 0 & 8.036 \times 10^{-15} & 3.9 \end{pmatrix} \cdot \text{GPa}$$

Calculate the A matrix

$$t := .125\text{mm}$$

$$\underline{\underline{A}} := (2 \cdot Q_{Ti} + 2Q_{CF90ply} + 6 \cdot Q_{CF0ply}) \cdot t$$

$$A = \begin{pmatrix} 137.802 & 13.218 & 0 \\ 13.218 & 71.902 & 2.009 \times 10^{-15} \\ 0 & 2.009 \times 10^{-15} & 13.146 \end{pmatrix} \cdot \text{GPa} \cdot \text{mm}$$

Matrix is symmetric, so B matrix is zero

Calculate the D matrix

$$D := 2 \cdot Q_{Ti} \left[t \cdot (.5625\text{mm})^2 + \frac{t^3}{12} \right] + 2 \cdot Q_{CF0ply} \left[t \cdot (.4375\text{mm})^2 + \frac{t^3}{12} \right] + 2 \cdot Q_{CF90ply} \left[t \cdot (.3125\text{mm})^2 + \frac{t^3}{12} \right] \dots \\ + 2 \cdot Q_{CF0ply} \left[t \cdot (.1875\text{mm})^2 + \frac{t^3}{12} \right] + 2 \cdot Q_{CF0ply} \left[t \cdot (.0625\text{mm})^2 + \frac{t^3}{12} \right]$$

$$D = \begin{pmatrix} 17.741 & 3.539 & 0 \\ 3.539 & 13.279 & 0 \\ 0 & 0 & 3.263 \end{pmatrix} \cdot \text{GPa} \cdot \text{mm}^3$$

Invert A and D matrices

$$A^{-1} = \begin{pmatrix} 7.387 \times 10^{-3} & -1.358 \times 10^{-3} & 0 \\ -1.358 \times 10^{-3} & 0.014 & 0 \\ 0 & 0 & 0.076 \end{pmatrix} \frac{1}{\text{GPa} \cdot \text{mm}}$$

$$D^{-1} = \begin{pmatrix} 0.06 & -0.016 & 0 \\ -0.016 & 0.08 & 0 \\ 0 & 0 & 0.307 \end{pmatrix} \frac{1}{\text{GPa} \cdot \text{mm}^3}$$

Effective In-Plane Laminate Constants:

$$H := 5.125 \text{ mm}$$

$$A_{\text{star}} := A^{-1} \quad A_{\text{star}} = \begin{pmatrix} 7.387 \times 10^{-3} & -1.358 \times 10^{-3} & 0 \\ -1.358 \times 10^{-3} & 0.014 & 0 \\ 0 & 0 & 0.076 \end{pmatrix} \frac{1}{\text{GPa} \cdot \text{mm}}$$

$$a_{\text{star}} := 2 \cdot H \cdot A_{\text{star}} \quad a_{\text{star}} = \begin{pmatrix} 9.234 \times 10^{-3} & -1.697 \times 10^{-3} & 0 \\ -1.697 \times 10^{-3} & 0.018 & 0 \\ 0 & 0 & 0.095 \end{pmatrix} \frac{1}{\text{GPa}}$$

$$E_x := \frac{1}{a_{\text{star}_{1,1}}} \quad E_x = 108.298 \text{ GPa}$$

$$E_y := \frac{1}{a_{\text{star}_{2,2}}} \quad E_y = 56.507 \text{ GPa}$$

$$G_{xy} := \frac{1}{a_{\text{star}_{3,3}}} \quad G_{xy} = 10.517 \text{ GPa}$$

$$\nu_{xy} := \frac{-a_{\text{star}_{1,2}}}{a_{\text{star}_{1,1}}} \quad \nu_{xy} = 0.184$$

$$\nu_{yx} := \frac{-a_{\text{star}_{1,2}}}{a_{\text{star}_{2,2}}} \quad \nu_{yx} = 0.096$$

Effective Flexural Engineering Constants

$$d_{\text{star}} := \frac{(2 \cdot H)^3}{12} D^{-1} \quad d_{\text{star}} = \begin{pmatrix} 9.69 \times 10^{-3} & -2.583 \times 10^{-3} & 0 \\ -2.583 \times 10^{-3} & 0.013 & 0 \\ 0 & 0 & 0.05 \end{pmatrix} \frac{1}{\text{GPa}}$$

$$E_{f,x} := \frac{1}{d_{\text{star}_{1,1}}} \quad E_{f,x} = 103.203 \text{ GPa}$$

$$E_{f,y} := \frac{1}{d_{\text{star}_{2,2}}} \quad E_{f,y} = 77.247 \text{ GPa}$$

$$G_{f,xy} := \frac{1}{d_{\text{star}_{3,3}}} \quad G_{f,xy} = 20.046 \text{ GPa}$$

$$\nu_{f,xy} := \frac{-d_{\text{star}_{1,2}}}{d_{\text{star}_{1,1}}} \quad \nu_{f,xy} = 0.267$$

$$\nu_{f,yx} := \frac{-d_{\text{star}_{1,2}}}{d_{\text{star}_{2,2}}} \quad \nu_{f,yx} = 0.2$$

Vara Laminate Analysis (CLT)

Material Properties:

CF/PEEK

$$E_{CF11} := 139 \text{ GPa}$$

$$E_{CF22} := 10 \text{ GPa}$$

$$\nu_{CF12} := .28$$

$$G_{CF12} := 3.9 \text{ GPa}$$

Titanium 15-3-3-3

$$E_{Ti} := 100.6 \text{ GPa}$$

$$\nu_{Ti12} := .36$$

1. Reduced stiffness matrix for each material

$$Q_{CF} := \begin{pmatrix} \frac{E_{CF11}^2}{E_{CF11} - \nu_{CF12}^2 E_{CF22}} & \frac{\nu_{CF12} E_{CF11} E_{CF22}}{E_{CF11} - \nu_{CF12}^2 E_{CF22}} & 0 \\ \frac{\nu_{CF12} E_{CF11} E_{CF22}}{E_{CF11} - \nu_{CF12}^2 E_{CF22}} & \frac{E_{CF11} E_{CF22}}{E_{CF11} - \nu_{CF12}^2 E_{CF22}} & 0 \\ 0 & 0 & G_{CF12} \end{pmatrix}$$

$$Q_{CF} = \begin{pmatrix} 141.858 & 2.816 & 0 \\ 2.816 & 10.057 & 0 \\ 0 & 0 & 3.9 \end{pmatrix} \cdot \text{GPa}$$

$$Q_{Ti} := \frac{E_{Ti}}{1 - \nu_{Ti12}^2} \begin{pmatrix} 1 & \nu_{Ti12} & 0 \\ \nu_{Ti12} & 1 & 0 \\ 0 & 0 & \frac{1 - \nu_{Ti12}}{2} \end{pmatrix}$$

$$Q_{Ti} = \begin{pmatrix} 115.579 & 41.608 & 0 \\ 41.608 & 115.579 & 0 \\ 0 & 0 & 36.985 \end{pmatrix} \cdot \text{GPa}$$

Calculate the transformed reduced stiffness matrix Q_{ij} for each ply based on the reduced stiffness matrix and fiber angle.

0 degree plies:

$$\theta := 0 \text{deg}$$

$$Q_{11} := Q_{CF_{1,1}} \cdot \cos(\theta)^4 + 2 \cdot (Q_{CF_{1,2}} + 2 \cdot Q_{CF_{3,3}}) \cdot \cos(\theta)^2 \cdot \sin(\theta)^2 + Q_{CF_{2,2}} \cdot \sin(\theta)^4$$

$$Q_{12} := Q_{CF_{1,2}} \cdot (\cos(\theta)^4 + \sin(\theta)^4) + (Q_{CF_{1,1}} + Q_{CF_{2,2}} - 4 \cdot Q_{CF_{3,3}}) \cdot \cos(\theta)^2 \cdot \sin(\theta)^2$$

$$Q_{13} := (Q_{CF_{1,1}} - Q_{CF_{1,2}} - 2 \cdot Q_{CF_{3,3}}) \cdot \cos(\theta)^3 \cdot \sin(\theta) - (Q_{CF_{2,2}} - Q_{CF_{1,2}} - 2 \cdot Q_{CF_{3,3}}) \cdot \cos(\theta) \cdot \sin(\theta)^3$$

$$Q_{22} := Q_{CF_{1,1}} \cdot \sin(\theta)^4 + 2 \cdot (Q_{CF_{1,2}} + 2 \cdot Q_{CF_{3,3}}) \cdot \cos(\theta)^2 \cdot \sin(\theta)^2 + Q_{CF_{2,2}} \cdot \cos(\theta)^4$$

$$Q_{23} := (Q_{CF_{1,1}} - Q_{CF_{1,2}} - 2 \cdot Q_{CF_{3,3}}) \cdot \cos(\theta) \cdot \sin(\theta)^3 - (Q_{CF_{2,2}} - Q_{CF_{1,2}} - 2 \cdot Q_{CF_{3,3}}) \cdot \cos(\theta)^3 \cdot \sin(\theta)$$

$$Q_{33} := (Q_{CF_{1,1}} + Q_{CF_{2,2}} - 2 \cdot Q_{CF_{1,2}} - 2 \cdot Q_{CF_{3,3}}) \cdot \cos(\theta)^2 \cdot \sin(\theta)^2 + Q_{CF_{3,3}} \cdot (\cos(\theta)^4 + \sin(\theta)^4)$$

$$Q_{CF0ply} := \begin{pmatrix} Q_{11} & Q_{12} & Q_{13} \\ Q_{12} & Q_{22} & Q_{23} \\ Q_{13} & Q_{23} & Q_{33} \end{pmatrix} \quad Q_{CF0ply} = \begin{pmatrix} 141.858 & 2.816 & 0 \\ 2.816 & 10.057 & 0 \\ 0 & 0 & 3.9 \end{pmatrix} \cdot \text{GPa}$$

90 degree plies:

$$\theta := 90 \text{deg}$$

$$Q_{11} := Q_{CF_{1,1}} \cdot \cos(\theta)^4 + 2 \cdot (Q_{CF_{1,2}} + 2 \cdot Q_{CF_{3,3}}) \cdot \cos(\theta)^2 \cdot \sin(\theta)^2 + Q_{CF_{2,2}} \cdot \sin(\theta)^4$$

$$Q_{12} := Q_{CF_{1,2}} \cdot (\cos(\theta)^4 + \sin(\theta)^4) + (Q_{CF_{1,1}} + Q_{CF_{2,2}} - 4 \cdot Q_{CF_{3,3}}) \cdot \cos(\theta)^2 \cdot \sin(\theta)^2$$

$$Q_{13} := (Q_{CF_{1,1}} - Q_{CF_{1,2}} - 2 \cdot Q_{CF_{3,3}}) \cdot \cos(\theta)^3 \cdot \sin(\theta) - (Q_{CF_{2,2}} - Q_{CF_{1,2}} - 2 \cdot Q_{CF_{3,3}}) \cdot \cos(\theta) \cdot \sin(\theta)^3$$

$$Q_{22} := Q_{CF_{1,1}} \cdot \sin(\theta)^4 + 2 \cdot (Q_{CF_{1,2}} + 2 \cdot Q_{CF_{3,3}}) \cdot \cos(\theta)^2 \cdot \sin(\theta)^2 + Q_{CF_{2,2}} \cdot \cos(\theta)^4$$

$$Q_{23} := (Q_{CF_{1,1}} - Q_{CF_{1,2}} - 2 \cdot Q_{CF_{3,3}}) \cdot \cos(\theta) \cdot \sin(\theta)^3 - (Q_{CF_{2,2}} - Q_{CF_{1,2}} - 2 \cdot Q_{CF_{3,3}}) \cdot \cos(\theta)^3 \cdot \sin(\theta)$$

$$Q_{33} := (Q_{CF_{1,1}} + Q_{CF_{2,2}} - 2 \cdot Q_{CF_{1,2}} - 2 \cdot Q_{CF_{3,3}}) \cdot \cos(\theta)^2 \cdot \sin(\theta)^2 + Q_{CF_{3,3}} \cdot (\cos(\theta)^4 + \sin(\theta)^4)$$

$$Q_{CF90ply} := \begin{pmatrix} Q_{11} & Q_{12} & Q_{13} \\ Q_{12} & Q_{22} & Q_{23} \\ Q_{13} & Q_{23} & Q_{33} \end{pmatrix} \quad Q_{CF90ply} = \begin{pmatrix} 10.057 & 2.816 & 0 \\ 2.816 & 141.858 & 8.036 \times 10^{-15} \\ 0 & 8.036 \times 10^{-15} & 3.9 \end{pmatrix} \cdot \text{GPa}$$

Calculate the A matrix

$$t := .125 \text{ mm}$$

$$\underline{\underline{A}} := (4 \cdot Q_{Ti} + 2 \cdot Q_{CF90ply} + 2 \cdot Q_{CF0ply}) \cdot t$$

$$A = \begin{pmatrix} 95.768 & 22.212 & 0 \\ 22.212 & 95.768 & 2.009 \times 10^{-15} \\ 0 & 2.009 \times 10^{-15} & 20.443 \end{pmatrix} \cdot \text{GPa} \cdot \text{mm}$$

Matrix is symmetric, so B matrix is zero

Calculate the D matrix

$$D := 2 \cdot Q_{Ti} \cdot \left[t \cdot (.4375 \text{ mm})^2 + \frac{t^3}{12} \right] + 2 \cdot Q_{CF90ply} \cdot \left[t \cdot (.3125 \text{ mm})^2 + \frac{t^3}{12} \right] \dots \\ + 2 \cdot Q_{Ti} \cdot \left[t \cdot (.1875 \text{ mm})^2 + \frac{t^3}{12} \right] + 2 \cdot Q_{CF0ply} \cdot \left[t \cdot (.0625 \text{ mm})^2 + \frac{t^3}{12} \right]$$

$$D = \begin{pmatrix} 7.055 & 2.457 & 0 \\ 2.457 & 10.144 & 0 \\ 0 & 0 & 2.221 \end{pmatrix} \cdot \text{GPa} \cdot \text{mm}^3$$

Invert A and D matrices

$$A^{-1} = \begin{pmatrix} 0.011 & -2.56 \times 10^{-3} & 0 \\ -2.56 \times 10^{-3} & 0.011 & 0 \\ 0 & 0 & 0.049 \end{pmatrix} \cdot \frac{1}{\text{GPa} \cdot \text{mm}}$$

$$D^{-1} = \begin{pmatrix} 0.155 & -0.037 & 0 \\ -0.037 & 0.108 & 0 \\ 0 & 0 & 0.45 \end{pmatrix} \cdot \frac{1}{\text{GPa} \cdot \text{mm}^3}$$

Effective In-Plane Laminate Constants:

$$H := 4.125 \text{ mm}$$

$$A_{\text{star}} := A^{-1} \quad A_{\text{star}} = \begin{pmatrix} 0.011 & -2.56 \times 10^{-3} & 0 \\ -2.56 \times 10^{-3} & 0.011 & 0 \\ 0 & 0 & 0.049 \end{pmatrix} \frac{1}{\text{GPa} \cdot \text{mm}}$$

$$a_{\text{star}} := 2 \cdot H \cdot A_{\text{star}} \quad a_{\text{star}} = \begin{pmatrix} 0.011 & -2.56 \times 10^{-3} & 0 \\ -2.56 \times 10^{-3} & 0.011 & 0 \\ 0 & 0 & 0.049 \end{pmatrix} \frac{1}{\text{GPa}}$$

$$E_x := \frac{1}{a_{\text{star}_{1,1}}} \quad E_x = 90.616 \text{ GPa}$$

$$E_y := \frac{1}{a_{\text{star}_{2,2}}} \quad E_y = 90.616 \text{ GPa}$$

$$G_{xy} := \frac{1}{a_{\text{star}_{3,3}}} \quad G_{xy} = 20.443 \text{ GPa}$$

$$\nu_{xy} := \frac{-a_{\text{star}_{1,2}}}{a_{\text{star}_{1,1}}} \quad \nu_{xy} = 0.232$$

$$\nu_{yx} := \frac{-a_{\text{star}_{1,2}}}{a_{\text{star}_{2,2}}} \quad \nu_{yx} = 0.232$$

Effective Flexural Engineering Constants

$$d_{\text{star}} := \frac{(2 \cdot H)^3}{12} \cdot D^{-1} \quad d_{\text{star}} = \begin{pmatrix} 0.013 & -3.125 \times 10^{-3} & 0 \\ -3.125 \times 10^{-3} & 8.972 \times 10^{-3} & 0 \\ 0 & 0 & 0.038 \end{pmatrix} \frac{1}{\text{GPa}}$$

$$E_{f,x} := \frac{1}{d_{\text{star}_{1,1}}} \quad E_{f,x} = 77.521 \text{ GPa}$$

$$E_{f,y} := \frac{1}{d_{\text{star}_{2,2}}} \quad E_{f,y} = 111.463 \text{ GPa}$$

$$G_{f,xy} := \frac{1}{d_{\text{star}_{3,3}}} \quad G_{f,xy} = 26.646 \text{ GPa}$$

$$\nu_{f,xy} := \frac{-d_{\text{star}_{1,2}}}{d_{\text{star}_{1,1}}} \quad \nu_{f,xy} = 0.242$$

$$\nu_{f,yx} := \frac{-d_{\text{star}_{1,2}}}{d_{\text{star}_{2,2}}} \quad \nu_{f,yx} = 0.348$$

Thick Laminate Analysis (CLT)

Material Properties:

CF/PEEK

$$E_{CF11} := 139 \text{ GPa}$$

$$E_{CF22} := 10 \text{ GPa}$$

$$\nu_{CF12} := .28$$

$$G_{CF12} := 3.9 \text{ GPa}$$

Titanium 15-3-3-3

$$E_{Ti} := 100.6 \text{ GPa}$$

$$\nu_{Ti12} := .36$$

1. Reduced stiffness matrix for each material

$$Q_{CF} := \begin{pmatrix} \frac{E_{CF11}^2}{E_{CF11} - \nu_{CF12}^2 \cdot E_{CF22}} & \frac{\nu_{CF12} \cdot E_{CF11} \cdot E_{CF22}}{E_{CF11} - \nu_{CF12}^2 \cdot E_{CF22}} & 0 \\ \frac{\nu_{CF12} \cdot E_{CF11} \cdot E_{CF22}}{E_{CF11} - \nu_{CF12}^2 \cdot E_{CF22}} & \frac{E_{CF11} \cdot E_{CF22}}{E_{CF11} - \nu_{CF12}^2 \cdot E_{CF22}} & 0 \\ 0 & 0 & G_{CF12} \end{pmatrix}$$

$$Q_{CF} = \begin{pmatrix} 141.858 & 2.816 & 0 \\ 2.816 & 10.057 & 0 \\ 0 & 0 & 3.9 \end{pmatrix} \cdot \text{GPa}$$

$$Q_{Ti} := \frac{E_{Ti}}{1 - \nu_{Ti12}^2} \begin{pmatrix} 1 & \nu_{Ti12} & 0 \\ \nu_{Ti12} & 1 & 0 \\ 0 & 0 & \frac{1 - \nu_{Ti12}}{2} \end{pmatrix}$$

$$Q_{Ti} = \begin{pmatrix} 115.579 & 41.608 & 0 \\ 41.608 & 115.579 & 0 \\ 0 & 0 & 36.985 \end{pmatrix} \cdot \text{GPa}$$

Calculate the transformed reduced stiffness matrix Q_{ij} for each ply based on the reduced stiffness matrix and fiber angle.

0 degree plies:

$$\theta := 0 \text{ deg}$$

$$Q_{11} := Q_{CF_{1,1}} \cdot \cos(\theta)^4 + 2 \cdot (Q_{CF_{1,2}} + 2 \cdot Q_{CF_{3,3}}) \cdot \cos(\theta)^2 \cdot \sin(\theta)^2 + Q_{CF_{2,2}} \cdot \sin(\theta)^4$$

$$Q_{12} := Q_{CF_{1,2}} \cdot (\cos(\theta)^4 + \sin(\theta)^4) + (Q_{CF_{1,1}} + Q_{CF_{2,2}} - 4 \cdot Q_{CF_{3,3}}) \cdot \cos(\theta)^2 \cdot \sin(\theta)^2$$

$$Q_{13} := (Q_{CF_{1,1}} - Q_{CF_{1,2}} - 2 \cdot Q_{CF_{3,3}}) \cdot \cos(\theta)^3 \cdot \sin(\theta) - (Q_{CF_{2,2}} - Q_{CF_{1,2}} - 2 \cdot Q_{CF_{3,3}}) \cdot \cos(\theta) \cdot \sin(\theta)^3$$

$$Q_{22} := Q_{CF_{1,1}} \cdot \sin(\theta)^4 + 2 \cdot (Q_{CF_{1,2}} + 2 \cdot Q_{CF_{3,3}}) \cdot \cos(\theta)^2 \cdot \sin(\theta)^2 + Q_{CF_{2,2}} \cdot \cos(\theta)^4$$

$$Q_{23} := (Q_{CF_{1,1}} - Q_{CF_{1,2}} - 2 \cdot Q_{CF_{3,3}}) \cdot \cos(\theta) \cdot \sin(\theta)^3 - (Q_{CF_{2,2}} - Q_{CF_{1,2}} - 2 \cdot Q_{CF_{3,3}}) \cdot \cos(\theta)^3 \cdot \sin(\theta)$$

$$Q_{33} := (Q_{CF_{1,1}} + Q_{CF_{2,2}} - 2 \cdot Q_{CF_{1,2}} - 2 \cdot Q_{CF_{3,3}}) \cdot \cos(\theta)^2 \cdot \sin(\theta)^2 + Q_{CF_{3,3}} \cdot (\cos(\theta)^4 + \sin(\theta)^4)$$

$$Q_{CF0ply} := \begin{pmatrix} Q_{11} & Q_{12} & Q_{13} \\ Q_{12} & Q_{22} & Q_{23} \\ Q_{13} & Q_{23} & Q_{33} \end{pmatrix} \quad Q_{CF0ply} = \begin{pmatrix} 141.858 & 2.816 & 0 \\ 2.816 & 10.057 & 0 \\ 0 & 0 & 3.9 \end{pmatrix} \cdot \text{GPa}$$

45 degree plies:

$$\theta := 45 \text{ deg}$$

$$Q_{11} := Q_{CF_{1,1}} \cdot \cos(\theta)^4 + 2 \cdot (Q_{CF_{1,2}} + 2 \cdot Q_{CF_{3,3}}) \cdot \cos(\theta)^2 \cdot \sin(\theta)^2 + Q_{CF_{2,2}} \cdot \sin(\theta)^4$$

$$Q_{12} := Q_{CF_{1,2}} \cdot (\cos(\theta)^4 + \sin(\theta)^4) + (Q_{CF_{1,1}} + Q_{CF_{2,2}} - 4 \cdot Q_{CF_{3,3}}) \cdot \cos(\theta)^2 \cdot \sin(\theta)^2$$

$$Q_{13} := (Q_{CF_{1,1}} - Q_{CF_{1,2}} - 2 \cdot Q_{CF_{3,3}}) \cdot \cos(\theta)^3 \cdot \sin(\theta) - (Q_{CF_{2,2}} - Q_{CF_{1,2}} - 2 \cdot Q_{CF_{3,3}}) \cdot \cos(\theta) \cdot \sin(\theta)^3$$

$$Q_{22} := Q_{CF_{1,1}} \cdot \sin(\theta)^4 + 2 \cdot (Q_{CF_{1,2}} + 2 \cdot Q_{CF_{3,3}}) \cdot \cos(\theta)^2 \cdot \sin(\theta)^2 + Q_{CF_{2,2}} \cdot \cos(\theta)^4$$

$$Q_{23} := (Q_{CF_{1,1}} - Q_{CF_{1,2}} - 2 \cdot Q_{CF_{3,3}}) \cdot \cos(\theta) \cdot \sin(\theta)^3 - (Q_{CF_{2,2}} - Q_{CF_{1,2}} - 2 \cdot Q_{CF_{3,3}}) \cdot \cos(\theta)^3 \cdot \sin(\theta)$$

$$Q_{33} := (Q_{CF_{1,1}} + Q_{CF_{2,2}} - 2 \cdot Q_{CF_{1,2}} - 2 \cdot Q_{CF_{3,3}}) \cdot \cos(\theta)^2 \cdot \sin(\theta)^2 + Q_{CF_{3,3}} \cdot (\cos(\theta)^4 + \sin(\theta)^4)$$

$$Q_{CF45ply} := \begin{pmatrix} Q_{11} & Q_{12} & Q_{13} \\ Q_{12} & Q_{22} & Q_{23} \\ Q_{13} & Q_{23} & Q_{33} \end{pmatrix} \quad Q_{CF45ply} = \begin{pmatrix} 43.287 & 35.487 & 32.95 \\ 35.487 & 43.287 & 32.95 \\ 32.95 & 32.95 & 36.571 \end{pmatrix} \cdot \text{GPa}$$

-45 degree plies:

$$\theta := -45 \text{ deg}$$

$$Q_{11} := Q_{CF_{1,1}} \cdot \cos(\theta)^4 + 2 \cdot (Q_{CF_{1,2}} + 2 \cdot Q_{CF_{3,3}}) \cdot \cos(\theta)^2 \cdot \sin(\theta)^2 + Q_{CF_{2,2}} \cdot \sin(\theta)^4$$

$$Q_{12} := Q_{CF_{1,2}} \cdot (\cos(\theta)^4 + \sin(\theta)^4) + (Q_{CF_{1,1}} + Q_{CF_{2,2}} - 4 \cdot Q_{CF_{3,3}}) \cdot \cos(\theta)^2 \cdot \sin(\theta)^2$$

$$Q_{13} := (Q_{CF_{1,1}} - Q_{CF_{1,2}} - 2 \cdot Q_{CF_{3,3}}) \cdot \cos(\theta)^3 \cdot \sin(\theta) - (Q_{CF_{2,2}} - Q_{CF_{1,2}} - 2 \cdot Q_{CF_{3,3}}) \cdot \cos(\theta) \cdot \sin(\theta)^3$$

$$Q_{22} := Q_{CF_{1,1}} \cdot \sin(\theta)^4 + 2 \cdot (Q_{CF_{1,2}} + 2 \cdot Q_{CF_{3,3}}) \cdot \cos(\theta)^2 \cdot \sin(\theta)^2 + Q_{CF_{2,2}} \cdot \cos(\theta)^4$$

$$Q_{23} := (Q_{CF_{1,1}} - Q_{CF_{1,2}} - 2 \cdot Q_{CF_{3,3}}) \cdot \cos(\theta) \cdot \sin(\theta)^3 - (Q_{CF_{2,2}} - Q_{CF_{1,2}} - 2 \cdot Q_{CF_{3,3}}) \cdot \cos(\theta)^3 \cdot \sin(\theta)$$

$$Q_{33} := (Q_{CF_{1,1}} + Q_{CF_{2,2}} - 2 \cdot Q_{CF_{1,2}} - 2 \cdot Q_{CF_{3,3}}) \cdot \cos(\theta)^2 \cdot \sin(\theta)^2 + Q_{CF_{3,3}} \cdot (\cos(\theta)^4 + \sin(\theta)^4)$$

$$Q_{CFneg45ply} := \begin{pmatrix} Q_{11} & Q_{12} & Q_{13} \\ Q_{12} & Q_{22} & Q_{23} \\ Q_{13} & Q_{23} & Q_{33} \end{pmatrix} Q_{CFneg45ply} = \begin{pmatrix} 43.287 & 35.487 & -32.95 \\ 35.487 & 43.287 & -32.95 \\ -32.95 & -32.95 & 36.571 \end{pmatrix} \cdot \text{GPa}$$

Calculate the A matrix

$$t_{ti} := .140\text{mm} \quad t_{cf} := .210\text{mm}$$

$$\underline{A} := 15 \cdot Q_{Ti} \cdot t_{ti} + 8 \cdot Q_{CF0ply} \cdot t_{cf} + 10Q_{CF45ply} \cdot t_{cf} + 8 \cdot Q_{CFneg45ply} \cdot t_{cf}$$

$$A = \begin{pmatrix} 644.66 & 226.247 & 13.839 \\ 226.247 & 423.234 & 13.839 \\ 13.839 & 13.839 & 222.458 \end{pmatrix} \cdot \text{GPa} \cdot \text{mm}$$

Matrix is symmetric, so B matrix is zero

Calculate the D matrix

$$\begin{aligned} D := & 2 \cdot Q_{CF45ply} \left[t_{cf} (3.675\text{mm})^2 + \frac{t_{cf}^3}{12} \right] + 2 \cdot Q_{CF0ply} \left[t_{cf} (3.465\text{mm})^2 + \frac{t_{cf}^3}{12} \right] \dots \\ & + 2 \cdot Q_{CFneg45ply} \left[t_{cf} (3.255\text{mm})^2 + \frac{t_{cf}^3}{12} \right] + 2 \cdot Q_{CF45ply} \left[t_{cf} (3.045\text{mm})^2 + \frac{t_{cf}^3}{12} \right] \dots \\ & + 2 \cdot Q_{CF0ply} \left[t_{cf} (2.835\text{mm})^2 + \frac{t_{cf}^3}{12} \right] + 2 \cdot Q_{CFneg45ply} \left[t_{cf} (2.625\text{mm})^2 + \frac{t_{cf}^3}{12} \right] \dots \\ & + 2 \cdot Q_{Ti} \left[t_{ti} (2.45\text{mm})^2 + \frac{t_{ti}^3}{12} \right] + 2 \cdot Q_{CF0ply} \left[t_{cf} (2.275\text{mm})^2 + \frac{t_{cf}^3}{12} \right] \dots \\ & + 2 \cdot Q_{Ti} \left[t_{ti} (2.1\text{mm})^2 + \frac{t_{ti}^3}{12} \right] + 2 \cdot Q_{CF45ply} \left[t_{cf} (1.925\text{mm})^2 + \frac{t_{cf}^3}{12} \right] \dots \\ & + 2 \cdot Q_{Ti} \left[t_{ti} (1.75\text{mm})^2 + \frac{t_{ti}^3}{12} \right] + 2 \cdot Q_{CFneg45ply} \left[t_{cf} (1.575\text{mm})^2 + \frac{t_{cf}^3}{12} \right] \dots \\ & + 2 \cdot Q_{Ti} \left[t_{ti} (1.4\text{mm})^2 + \frac{t_{ti}^3}{12} \right] + 2 \cdot Q_{CF45ply} \left[t_{cf} (1.225\text{mm})^2 + \frac{t_{cf}^3}{12} \right] \dots \\ & + 2 \cdot Q_{Ti} \left[t_{ti} (1.05\text{mm})^2 + \frac{t_{ti}^3}{12} \right] + 2 \cdot Q_{CF0ply} \left[t_{cf} (.875\text{mm})^2 + \frac{t_{cf}^3}{12} \right] \dots \\ & + 2 \cdot Q_{Ti} \left[t_{ti} (.7\text{mm})^2 + \frac{t_{ti}^3}{12} \right] + 2 \cdot Q_{CFneg45ply} \left[t_{cf} (.525\text{mm})^2 + \frac{t_{cf}^3}{12} \right] \dots \\ & + 2 \cdot Q_{Ti} \left[t_{ti} (.35\text{mm})^2 + \frac{t_{ti}^3}{12} \right] + 2 \cdot Q_{CF45ply} \left[t_{cf} (.175\text{mm})^2 + \frac{t_{cf}^3}{12} \right] \dots \\ & + 2 \cdot Q_{Ti} \left[t_{ti} (.035\text{mm})^2 + \frac{t_{ti}^3}{24} \right] \end{aligned}$$

$$D = \begin{pmatrix} 2.982 \times 10^3 & 950.432 & 107.617 \\ 950.432 & 1.543 \times 10^3 & 107.617 \\ 107.617 & 107.617 & 962.04 \end{pmatrix} \text{GPa} \cdot \text{mm}^3$$

Invert A and D matrices

$$A^{-1} = \begin{pmatrix} 1.91 \times 10^{-3} & -1.019 \times 10^{-3} & -5.542 \times 10^{-5} \\ -1.019 \times 10^{-3} & 2.911 \times 10^{-3} & -1.177 \times 10^{-4} \\ -5.542 \times 10^{-5} & -1.177 \times 10^{-4} & 4.506 \times 10^{-3} \end{pmatrix} \frac{1}{\text{GPa} \cdot \text{mm}}$$

$$D^{-1} = \begin{pmatrix} 4.175 \times 10^{-4} & -2.559 \times 10^{-4} & -1.808 \times 10^{-5} \\ -2.559 \times 10^{-4} & 8.099 \times 10^{-4} & -6.198 \times 10^{-5} \\ -1.808 \times 10^{-5} & -6.198 \times 10^{-5} & 1.048 \times 10^{-3} \end{pmatrix} \frac{1}{\text{GPa} \cdot \text{mm}^3}$$

Effective In-Plane Laminate Constants:

$$H := 3.78 \text{ mm}$$

$$A_{\text{star}} := A^{-1} \quad A_{\text{star}} = \begin{pmatrix} 1.91 \times 10^{-3} & -1.019 \times 10^{-3} & -5.542 \times 10^{-5} \\ -1.019 \times 10^{-3} & 2.911 \times 10^{-3} & -1.177 \times 10^{-4} \\ -5.542 \times 10^{-5} & -1.177 \times 10^{-4} & 4.506 \times 10^{-3} \end{pmatrix} \frac{1}{\text{GPa} \cdot \text{mm}}$$

$$a_{\text{star}} := 2 \cdot H \cdot A_{\text{star}} \quad a_{\text{star}} = \begin{pmatrix} 0.014 & -7.706 \times 10^{-3} & -4.19 \times 10^{-4} \\ -7.706 \times 10^{-3} & 0.022 & -8.899 \times 10^{-4} \\ -4.19 \times 10^{-4} & -8.899 \times 10^{-4} & 0.034 \end{pmatrix} \frac{1}{\text{GPa}}$$

$$E_x := \frac{1}{a_{\text{star}_{1,1}}} \quad E_x = 69.25 \text{ GPa}$$

$$E_y := \frac{1}{a_{\text{star}_{2,2}}} \quad E_y = 45.432 \text{ GPa}$$

$$G_{xy} := \frac{1}{a_{\text{star}_{3,3}}} \quad G_{xy} = 29.355 \text{ GPa}$$

$$\nu_{xy} := \frac{-a_{\text{star}_{1,2}}}{a_{\text{star}_{1,1}}} \quad \nu_{xy} = 0.534$$

$$\nu_{yx} := \frac{-a_{\text{star}_{1,2}}}{a_{\text{star}_{2,2}}} \quad \nu_{yx} = 0.35$$

Effective Flexural Engineering Constants

$$d_{\text{star}} := \frac{(2 \cdot H)^3}{12} D^{-1} \quad d_{\text{star}} = \begin{pmatrix} 0.015 & -9.213 \times 10^{-3} & -6.51 \times 10^{-4} \\ -9.213 \times 10^{-3} & 0.029 & -2.232 \times 10^{-3} \\ -6.51 \times 10^{-4} & -2.232 \times 10^{-3} & 0.038 \end{pmatrix} \frac{1}{\text{GPa}}$$

$$E_{f,x} := \frac{1}{d_{\text{star}_{1,1}}} \quad E_{f,x} = 66.523 \text{ GPa}$$

$$E_{f,y} := \frac{1}{d_{\text{star}_{2,2}}} \quad E_{f,y} = 34.29 \text{ GPa}$$

$$G_{f,xy} := \frac{1}{d_{\text{star}_{3,3}}} \quad G_{f,xy} = 26.49 \text{ GPa}$$

$$\nu_{f,xy} := \frac{-d_{\text{star}_{1,2}}}{d_{\text{star}_{1,1}}} \quad \nu_{f,xy} = 0.613$$

$$\nu_{f,yx} := \frac{-d_{\text{star}_{1,2}}}{d_{\text{star}_{2,2}}} \quad \nu_{f,yx} = 0.316$$

APPENDIX III: NUMERICAL MODELING CODE

Part geometry code omitted for brevity

** ASSEMBLY

**

*Assembly, name=Assembly

**

*Instance, name=Supports-1, part=Supports

0., 0.000891, -0.006635

*End Instance

**

*Instance, name=Impactor-1, part=Impactor

0., 0.012674, -0.006635

*End Instance

**

*Instance, name=GFRP-90-1, part=GFRP-90

-0.035, 0.004812, 0.002915

-0.035, 0.004812, 0.002915, -1.035, 0.004812, 0.002915, 90.

*End Instance

**

*Instance, name=GFRP-0-1, part=GFRP-0

-0.035, 0.005069, 0.002915

-0.035, 0.005069, 0.002915, -1.035, 0.005069, 0.002915, 90.

*End Instance

**

*Instance, name=GFRP-0-2, part=GFRP-0

-0.035, 0.005209, 0.002915

-0.035, 0.005209, 0.002915, -1.035, 0.005209, 0.002915, 90.

*End Instance

**

*Instance, name=Titanium-Tension1, part=Titanium-Tension

-0.035, 0.004952, 0.002915

-0.035, 0.004952, 0.002915, -1.035, 0.004952, 0.002915, 90.

*End Instance

**

*Instance, name=GFRP-90-2, part=GFRP-90

-0.035, 0.005466, 0.002915

-0.035, 0.005466, 0.002915, -1.035, 0.005466, 0.002915, 90.

*End Instance

**

*Instance, name=Titanium-Tension2, part=Titanium-Tension

-0.035, 0.004695, 0.002915

-0.035, 0.004695, 0.002915, -1.035, 0.004695, 0.002915, 90.

*End Instance

**

*Instance, name=Titanium-Compression-1, part=Titanium-Compression

-0.035, 0.005606, 0.002915

-0.035, 0.005606, 0.002915, -1.035, 0.005606, 0.002915, 90.

*End Instance

**

*Instance, name=Titanium-Compression-2, part=Titanium-Compression

-0.035, 0.005349, 0.002915

-0.035, 0.005349, 0.002915, -1.035, 0.005349, 0.002915, 90.

*End Instance

```

**
*Instance, name=GFRP-90-3, part=GFRP-90
  -0.035, 0.004555, 0.002915
  -0.035, 0.004555, 0.002915, -1.035, 0.004555, 0.002915, 90.
*End Instance
**
*Instance, name=Titanium-Tension-bottom, part=Titanium-Tension
  -0.035, 0.004438, 0.002915
  -0.035, 0.004438, 0.002915, -1.035, 0.004438, 0.002915, 90.
*End Instance
**
*Instance, name=GFRP-90-4, part=GFRP-90
  -0.035, 0.005723, 0.002915
  -0.035, 0.005723, 0.002915, -1.035, 0.005723, 0.002915, 90.
*End Instance
**
*Instance, name=Titanium-Compression-3, part=Titanium-Compression
  -0.035, 0.005863, 0.002915
  -0.035, 0.005863, 0.002915, -1.035, 0.005863, 0.002915, 90.
*End Instance
**
*Instance, name=GFRP-90-5, part=GFRP-90
  -0.035, 0.00598, 0.002915
  -0.035, 0.00598, 0.002915, -1.035, 0.00598, 0.002915, 90.
*End Instance
**
*Instance, name=Titanium-Compression-4, part=Titanium-Compression
  -0.035, 0.00612, 0.002915
  -0.035, 0.00612, 0.002915, -1.035, 0.00612, 0.002915, 90.
*End Instance
**
*Instance, name=GFRP-90-6, part=GFRP-90
  -0.035, 0.004298, 0.002915
  -0.035, 0.004298, 0.002915, -1.035, 0.004298, 0.002915, 90.
*End Instance
**
*Instance, name=Titanium-Tension-1, part=Titanium-Tension
  -0.035, 0.004181, 0.002915
  -0.035, 0.004181, 0.002915, -1.035, 0.004181, 0.002915, 90.
*End Instance
**
*Node
  1, 0., 0.0126740001, 0.00291500008
*Node
  2, -0.0199999996, 0.000890999974, 0.00291500008
*Node
  3, 0.0199999996, 0.000890999974, 0.00291500008
*Nset, nset=_PickedSet196, internal, instance=Supports-1
  7, 8, 9, 10, 11, 12, 85, 86, 87, 88, 89, 90, 91, 92, 93, 94
  95, 96, 97, 98, 99, 100, 101, 102, 103, 104, 105, 106, 107, 108, 109, 110
  111, 112, 113, 114, 115, 116, 117, 118, 119, 120, 121, 122, 123, 124, 125, 126
  127, 128, 129, 130, 131, 132, 133, 134, 135, 136, 137, 138, 139, 140, 141, 142
  143, 144, 145, 146, 147, 148, 149, 150, 151, 152, 153, 154, 155, 156, 499, 500
  501, 502, 503, 504, 505, 506, 507, 508, 509, 510, 511, 512, 513, 514, 515, 516
  517, 518, 519, 520, 521, 522, 523, 524, 525, 526, 527, 528, 529, 530, 531, 532
  533, 534, 535, 536, 537, 538, 539, 540, 541, 542, 543, 544, 545, 546, 547, 548

```

549, 550, 551, 552, 553, 554, 555, 556, 557, 558, 559, 560, 561, 562, 563, 564
565, 566, 567, 568, 569, 570, 571, 572, 573, 574, 575, 576, 577, 578, 579, 580
581, 582, 583, 584, 585, 586, 587, 588, 589, 590, 591, 592, 593, 594, 595, 596
597, 598, 599, 600, 601, 602, 603, 604, 605, 606, 607, 608, 609, 610, 611, 612
613, 614, 615, 616, 617, 618, 619, 620, 621, 622, 623, 624, 625, 626, 627, 628
629, 630, 631, 632, 633, 634, 635, 636, 637, 638, 639, 640, 641, 642, 643, 644
645, 646, 647, 648, 649, 650, 651, 652, 653, 654, 655, 656, 657, 658, 659, 660
661, 662, 663, 664, 665, 666, 667, 668, 669, 670, 671, 672, 673, 674, 675, 676
677, 678, 679, 680, 681, 682, 683, 684, 685, 686, 687, 688, 689, 690, 691, 692
693, 694, 695, 696, 697, 698, 699, 700, 701, 702, 703, 704, 705, 706, 707, 708
709, 710, 711, 712, 713, 714, 715, 716, 717, 718, 719, 720, 721, 722, 723, 724
725, 726, 727, 728, 729, 730, 731, 732, 733, 734, 735, 736, 737, 738, 739, 740
741, 742, 743, 744, 745, 746, 747, 748, 749, 750, 751, 752, 753, 754, 755, 756
757, 758, 759, 760, 761, 762, 763, 764, 765, 766, 767, 768, 769, 770, 771, 772
773, 774, 775, 776, 777, 778, 779, 780, 781, 782, 783, 784, 785, 786, 787, 788
789, 790, 791, 792, 793, 794, 795, 796, 797, 798, 799, 800, 801, 802, 803, 804
805, 806, 807, 808, 809, 810, 811, 812, 813, 814, 815, 816, 817, 818, 819, 820
821, 822, 823, 824, 825, 826, 827, 828, 829, 830, 831, 832, 833, 834, 835, 836
837, 838, 839, 840

*Elset, elset=_PickedSet196, internal, instance=Supports-1, generate
381, 760, 1

*Nset, nset=_PickedSet264, internal, instance=Impactor-1, generate
1, 4949, 1

*Elset, elset=_PickedSet264, internal, instance=Impactor-1, generate
1, 4800, 1

*Nset, nset=_PickedSet266, internal, instance=Supports-1
1, 2, 3, 4, 5, 6, 13, 14, 15, 16, 17, 18, 19, 20, 21, 22
23, 24, 25, 26, 27, 28, 29, 30, 31, 32, 33, 34, 35, 36, 37, 38
39, 40, 41, 42, 43, 44, 45, 46, 47, 48, 49, 50, 51, 52, 53, 54
55, 56, 57, 58, 59, 60, 61, 62, 63, 64, 65, 66, 67, 68, 69, 70
71, 72, 73, 74, 75, 76, 77, 78, 79, 80, 81, 82, 83, 84, 157, 158

159, 160, 161, 162, 163, 164, 165, 166, 167, 168, 169, 170, 171, 172, 173, 174
175, 176, 177, 178, 179, 180, 181, 182, 183, 184, 185, 186, 187, 188, 189, 190
191, 192, 193, 194, 195, 196, 197, 198, 199, 200, 201, 202, 203, 204, 205, 206
207, 208, 209, 210, 211, 212, 213, 214, 215, 216, 217, 218, 219, 220, 221, 222
223, 224, 225, 226, 227, 228, 229, 230, 231, 232, 233, 234, 235, 236, 237, 238
239, 240, 241, 242, 243, 244, 245, 246, 247, 248, 249, 250, 251, 252, 253, 254
255, 256, 257, 258, 259, 260, 261, 262, 263, 264, 265, 266, 267, 268, 269, 270
271, 272, 273, 274, 275, 276, 277, 278, 279, 280, 281, 282, 283, 284, 285, 286
287, 288, 289, 290, 291, 292, 293, 294, 295, 296, 297, 298, 299, 300, 301, 302
303, 304, 305, 306, 307, 308, 309, 310, 311, 312, 313, 314, 315, 316, 317, 318
319, 320, 321, 322, 323, 324, 325, 326, 327, 328, 329, 330, 331, 332, 333, 334
335, 336, 337, 338, 339, 340, 341, 342, 343, 344, 345, 346, 347, 348, 349, 350
351, 352, 353, 354, 355, 356, 357, 358, 359, 360, 361, 362, 363, 364, 365, 366
367, 368, 369, 370, 371, 372, 373, 374, 375, 376, 377, 378, 379, 380, 381, 382
383, 384, 385, 386, 387, 388, 389, 390, 391, 392, 393, 394, 395, 396, 397, 398
399, 400, 401, 402, 403, 404, 405, 406, 407, 408, 409, 410, 411, 412, 413, 414
415, 416, 417, 418, 419, 420, 421, 422, 423, 424, 425, 426, 427, 428, 429, 430
431, 432, 433, 434, 435, 436, 437, 438, 439, 440, 441, 442, 443, 444, 445, 446
447, 448, 449, 450, 451, 452, 453, 454, 455, 456, 457, 458, 459, 460, 461, 462
463, 464, 465, 466, 467, 468, 469, 470, 471, 472, 473, 474, 475, 476, 477, 478
479, 480, 481, 482, 483, 484, 485, 486, 487, 488, 489, 490, 491, 492, 493, 494
495, 496, 497, 498

*Elset, elset=_PickedSet266, internal, instance=Supports-1, generate
1, 380, 1

*Nset, nset=_PickedSet269, internal, instance=Impactor-1, generate

```

1, 4949, 1
*Elset, elset=_PickedSet269, internal, instance=Impactor-1, generate
1, 4800, 1
*Nset, nset=_PickedSet270, internal, instance=Supports-1, generate
1, 840, 1
*Elset, elset=_PickedSet270, internal, instance=Supports-1, generate
1, 760, 1
*Nset, nset=_PickedSet273, internal
1,
*Nset, nset=_PickedSet274, internal
1,
*Nset, nset=_PickedSet275, internal
1,
*Nset, nset=_PickedSet276, internal
1,
*Nset, nset=_PickedSet295, internal
2,
*Nset, nset=_PickedSet296, internal
3,
*Nset, nset=_PickedSet297, internal
2, 3
*Elset, elset=__PickedSurf261_SNEG, internal, instance=Impactor-1, generate
1, 4800, 1
*Surface, type=ELEMENT, name=_PickedSurf261, internal
__PickedSurf261_SNEG, SNEG
** Constraint: Constraint-1
*Rigid Body, ref node=_PickedSet295, elset=_PickedSet196, position=CENTER OF MASS
** Constraint: Constraint-4
*Coupling, constraint name=Constraint-4, ref node=_PickedSet275, surface=_PickedSurf261
*Kinematic
** Constraint: Constraint-5
*Rigid Body, ref node=_PickedSet296, elset=_PickedSet266, position=CENTER OF MASS
** Constraint: Constraint-12
*Rigid Body, ref node=_PickedSet276, elset=_PickedSet264, position=CENTER OF MASS
*End Assembly
**
** ELEMENT CONTROLS
**
*Section Controls, name=EC-1, ELEMENT DELETION=YES, MAX DEGRADATION=0.9,
hourglass=ENHANCED, second order accuracy=YES
1., 1., 1.
*Section Controls, name=EC-2, ELEMENT DELETION=YES, MAX DEGRADATION=0.98,
hourglass=ENHANCED, second order accuracy=YES
1., 1., 1.
*Section Controls, name=EC-3, ELEMENT DELETION=YES, MAX DEGRADATION=0.98, second order
accuracy=YES
1., 1., 1.
*Amplitude, name=Amp-1
0., 0., 0.01, 1.
**
** MATERIALS
**
*Material, name=GFRP
*Damage Initiation, criterion=HASHIN
3.6612e+10, 2e+08, 5e+07, 1.8202e+08, 5.9984e+07, 5.9984e+07
*Damage Evolution, type=ENERGY

```

128000.,135000., 5600., 9310.
 *Density
 1570.,
 *Elastic, type=LAMINA
 2.722e+11, 3.33e+09, 0.28, 1.358e+09, 1.358e+09, 1.25e+09
 *Material, name=Titanium-Compression
 *Damage Initiation, criterion=JOHNSON COOK
 0.19, 0., 0., 0., 0.,1669., 25., 1.
 *Damage Evolution, type=ENERGY
 16486.,
 *Density
 4430.,
 *Elastic
 1.0061e+11, 0.36
 *Plastic, hardening=JOHNSON COOK
 1.1e+09, 3.6e+08, 0.51, 1., 1669., 25.
 *Material, name=Titanium-Tension
 *Damage Initiation, criterion=JOHNSON COOK
 -0.04, 0.076, -0.48, -0.02, 3.87, 1669., 25., 1.
 *Damage Evolution, type=ENERGY
 16486.,
 *Density
 4430.,
 *Elastic
 1.0061e+11, 0.36
 *Plastic, hardening=JOHNSON COOK
 1.05e+09, 3.6e+08, 0.51, 1., 1669., 25.
 **
 ** INTERACTION PROPERTIES
 **
 *Surface Interaction, name=Cohesive
 *Cohesive Behavior, eligibility=ORIGINAL CONTACTS
 1e+13, 1e+13, 1e+13
 *Damage Initiation, criterion=MAXS
 6.23e+07, 9.23e+07, 9.23e+07
 *Damage Evolution, type=ENERGY, softening=EXPONENTIAL, mixed mode behavior=BK, power=2.284
 969.,1000.,1000.
 *Surface Interaction, name=IntProp-1
 *Friction
 0.2,
 *Surface Behavior, pressure-overclosure=HARD
 *Surface Interaction, name=Interlaminar
 *Cohesive Behavior, eligibility=ORIGINAL CONTACTS
 1e+16, 1e+16, 1e+16
 *Damage Initiation, criterion=MAXS
 1.37e+08, 1.37e+08, 1.37e+08
 *Damage Evolution, type=ENERGY, softening=EXPONENTIAL, mixed mode behavior=BK, power=1.45
 1200.,1800.,1800.
 ** -----
 **
 ** STEP: Step-1
 **
 *Step, name=Step-1, nlgeom=YES
 *Dynamic, Explicit
 , 0.5
 *Bulk Viscosity

```

0.06, 1.2
**
** BOUNDARY CONDITIONS
**
** Name: BC-1 Type: Velocity/Angular velocity
*Boundary, type=VELOCITY
_PickedSet273, 2, 2, -0.03
** Name: BC-2 Type: Symmetry/Antisymmetry/Encastre
*Boundary
_PickedSet270, ENCASTRE
** Name: BC-3 Type: Displacement/Rotation
*Boundary
_PickedSet274, 1, 1
_PickedSet274, 3, 3
_PickedSet274, 4, 4
_PickedSet274, 5, 5
_PickedSet274, 6, 6
** Name: BC-4 Type: Symmetry/Antisymmetry/Encastre
*Boundary
_PickedSet297, ENCASTRE
** Name: BC-7 Type: Displacement/Rotation
*Boundary
_PickedSet269, 1, 1
_PickedSet269, 3, 3
_PickedSet269, 4, 4
_PickedSet269, 5, 5
_PickedSet269, 6, 6
**
** INTERACTIONS
**
** Interaction: Int-4
*Contact, op=NEW
*Contact Inclusions, ALL EXTERIOR
*Contact Property Assignment
, , IntProp-1
Titanium-Tension2.Top , GFRP-90-1.Bottom , Cohesive
GFRP-90-1.Top , Titanium-Tension1.Bottom , Cohesive
Titanium-Tension1.Top , GFRP-0-1.Bottom , Cohesive
GFRP-0-1.Top , GFRP-0-2.Bottom , Cohesive
GFRP-0-2.Top , Titanium-Compression-2.Bottom , Cohesive
Titanium-Compression-2.Top , GFRP-90-2.Bottom , Cohesive
GFRP-90-2.Top , Titanium-Compression-1.Bottom , Cohesive
Titanium-Tension-bottom.Top , GFRP-90-3.Bottom , Cohesive
GFRP-90-3.Top , Titanium-Tension2.Bottom , Cohesive
Titanium-Compression-1.Top , GFRP-90-4.Bottom , Cohesive
GFRP-90-4.Top , Titanium-Compression-3.Bottom , Cohesive
Titanium-Compression-3.Top , GFRP-90-5.Bottom , Cohesive
GFRP-90-5.Top , Titanium-Compression-4.Bottom , Cohesive
Titanium-Tension-bottom.Bottom , GFRP-90-6.Top , Cohesive
GFRP-90-6.Bottom , Titanium-Tension-1.Top , Cohesive
**
** OUTPUT REQUESTS
**
*Restart, write, number interval=1, time marks=NO
**
** FIELD OUTPUT: F-Output-1

```

```
**
*Output, field, number interval=100
*Node Output
A, RF, U, V
*Element Output, directions=YES
CFAILURE, DAMAGEC, DAMAGEFC, DAMAGEFT, DAMAGEMC, DAMAGEMT, DAMAGESHR,
DAMAGET, DMICRT, DMICRTMAX, E, EDMICRTMAX, ER, ERPRATIO, EVF, LE
PE, PEEQ, PEEQVAVG, PEVAVG, S, SDEG, SHRRATIO, STATUS, SVAVG
*Contact Output
CFORCE, CSDMG, CSMAXSCRT, CSMAXUCRT, CSQUADSCRT, CSQUADUCRT, CSTRESS
**
** HISTORY OUTPUT: H-Output-1
**
*Output, history, time interval=0.005
*Energy Output
ALLAE, ALLCD, ALLCW, ALLDC, ALLDMD, ALLFD, ALLIE, ALLKE, ALLMW, ALLPD, ALLPW, ALLSE,
ALLVD, ALLWK, ETOTAL
*End Step
```

Stefan P. Hovik

Curriculum Vitae

28416 SE 43rd St.

Fall City, WA 98024

(206) 225-5228

stefan.p.hovik@gmail.com

Education:

University of Washington, Seattle, WA, 2019. *Doctor of Philosophy in Mechanical Engineering.*

Thesis Title: Experimental and Numerical Methods for Characterization of Impact Damage in Titanium-Graphite Laminates

University of Idaho, Moscow, ID, 2011. *Master of Science in Mechanical Engineering.*

Thesis Title: Improved Multi-Objective Genetic Algorithm for Geometric Optimization of FSAE Vehicle Suspension

University of Idaho, Moscow, ID, 2009. *Bachelor of Science in Mechanical Engineering.*

Experience:

TEST & EVALUATION ENGINEER, THE BOEING COMPANY, 2012-PRESENT

- Responsible for design, analysis, and fabrication oversight of test hardware for aerodynamic wind tunnel, propulsion, and full scale aircraft testing
- Principal investigator for remote-control actuators (RCA) technologies in wind tunnel models using shape memory alloy (SMA) actuators
- Extensive and detailed project management covering the entire product test lifecycle (PTLC)
- Responsible for development of statement-of-work (SOW) and requirements documents supporting internal and external customers

- Development of new testing methods and techniques, including Tuned-Mass-Dampers (TMD) in wind tunnel models and Structural-Health-Monitoring (SHM) systems among others

EQUIPMENT ENGINEER, THE BOEING COMPANY, 2011-2012

- Responsible for specification, procurement, installation, and qualification of machine tools and other capital equipment supporting the 787 aircraft program.
- Development of statement-of-work (SOW) documents for equipment reliability studies, equipment upgrades/modifications, and procurement projects.
- Composite fabrication equipment design, including development of proprietary hardware used for aircraft part fabrication (787 aircraft program).

Patents:

1. Hovik, S., Rueger, M., McGranahan, B., Gunter, I. Variable Spring Constant Tuned Mass Damper. US 20180045600 A1 U.S. Patent. February 15, 2018.
2. Griffin, S., Hovik, S. 2017. Semi-Active Tuned Mass Damper to Eliminate Limit-Cycle Oscillation. U.S. Patent Application, filed November, 2017. Patent Pending.

Selected Publications:

Hovik, S., Ramulu, M. (2017, May). *Experimental and Numerical Methods for Characterization of Impact Damage in Titanium-Graphite Laminates*. Paper presented at the SAMPE 2017 Conference, Seattle, WA.

Hovik, S., Ramulu, M., Isvonanda V. *Numerical Fracture Modeling of Quasi-Static Loading of Thin Titanium-Graphite Laminates* (Publication underway)

Hovik, S., Ramulu M., *Literature Review of TiGr* (Publication underway)

Hovik, S., Ramulu, M., *Numerical Fracture Modeling of Thin Titanium-Graphite Fiber-Metal Laminates* (Publication underway)

Hovik, S., Ramulu, M., Pahuja, R., *Numerical Modeling of Impact Behavior of Thick Titanium-Graphite Laminates* (Publication underway)